New Materials for Selective Separations at the Back End of the Nuclear Fuel Cycle

Jessica Veliscek Carolan

A thesis submitted in fulfilment of the requirements for the degree of Doctor of Philosophy

Faculty of Science

University of Sydney

2016

Declaration

This thesis describes research that is my own work and is, to the best of my knowledge, original. Full acknowledgement has been given where the previous work of others has been cited and a list of references is given. This work has not been submitted in any form for another degree or diploma at any university or other institute of tertiary education.

Publications Arising from this Thesis

Published papers in peer-reviewed academic journals:

1. J. Veliscek-Carolan, K.A. Jolliffe and T. L. Hanley, **2013**, "Selective Sorption of Actinides by Titania Nanoparticles Covalently Functionalised with Simple Organic Ligands", *ACS Appl. Mater. Interf.* 5, 11984-11944.

2. J. Veliscek-Carolan, T.L. Hanley and V. Luca, **2014**, "Zirconium Organophosphonates as High Capacity, Selective Lanthanide Sorbents", *Sep. Purif. Technol.* 129, 150-158.

3. J. Veliscek-Carolan, R. Knott and T. Hanley, **2015**, "Effects of Precursor Solution Aging and Other Parameters on Synthesis of Ordered, Mesoporous Titania Powders", *J. Phys. Chem. C.* 119, 7172-7183.

4. J. Veliscek-Carolan, K.A. Jolliffe and T.L. Hanley, **2015**, "Effective Am(III)/Eu(III) Separations using 2,6-bis(1,2,3-triazin-3-yl)pyridine (BTP) Functionalised Titania Particles and Hierarchically Porous Beads", *Chem. Commun.* 51, 11433-11436.

Oral presentations at scientific conferences and meetings:

1. J. Veliscek-Carolan, K.A. Jolliffe and T.L. Hanley, "Novel organic-functionalised porous titania materials for separations at the back end of the nuclear fuel cycle", Nuclear Chemistry for Sustainable Fuel Cycles (ATALANTE), No 5., France, September 2012.

2. J. Veliscek-Carolan, K.A. Jolliffe and T.L. Hanley, "Separations at the back end of the nuclear fuel cycle", Australian Synchrotron User Meeting, Australia, November 2013.

3. J. Veliscek-Carolan, R. Knott and T.L. Hanley, "Factors Controlling the Formation of Ordered, Mesoporous Bulk Phase Titania", Combined Australian Materials Societies (CAMS), No. 3, Australia, November 2014.

4. J. Veliscek-Carolan, K.A. Jolliffe and T.L. Hanley, "Materials for Selective Elemental Separations", Enabling Technologies Technical Exchange Meeting, United States of America, May 2015.

Abstract

Storage and recycling of nuclear waste are important issues that will increase in importance if nuclear power becomes more widely adopted worldwide. Recycling of used nuclear fuel is of benefit both in terms of increasing the nuclear lifetime (ie the number of years nuclear power will be a viable option for power generation) and decreasing the hazards (radiotoxicity, volume and longevity) of nuclear waste. Currently, most reprocessing of used nuclear fuel is performed using liquid-liquid extraction. However, use of solid sorbent materials has many advantages such the lack of organic solvent wastes. This research involves development of materials that are able to selectively remove specific target elements from solutions of used nuclear fuel. Once loaded with radionuclides, these materials may be utilised as transmutation matrices or wasteforms. Therefore, radiolytically and hydrolytically stable materials able to withstand the conditions of nuclear separations, such as titania and zirconia, have been targeted. Further, ordered porosity has been introduced into these titania and zirconia framework materials to improve their sorption capacity and kinetics. In order to impart selectivity to these materials, organic ligands are incorporated. Functional groups, including phosphonates, amines and peptides, have been chosen or designed based on their selectivity for elements relevant to the nuclear fuel cycle. Elements of interest include uranium, which constitutes >96% of used nuclear fuel and can be recycled; minor actinides, which contribute significantly to the radiotoxicity of nuclear waste and can also be recycled in fast neutron reactors; and lanthanides, which are targets for separation from the minor actinides as their high neutron absorption cross sections prevent transmutation of the minor actinides. Novel hybrid materials have been synthesized and their sorption characteristics, including selectivity, capacity and kinetics, evaluated.

Acknowledgements

I would first like to thank my supervisors Prof. Kate Jolliffe and Dr. Tracey Hanley, without whom this task would never have been completed. Kate, thank you very much for taking me on as a student in a field somewhat outside your area of interest. Your expertise and advice have been incredibly valuable. In addition, your dedication to, enthusiasm for and deep knowledge of chemistry are an inspiration. I hope I can continue to learn from you in my ongoing research career. Tracey, thank you for always being there to help me solve my problems, even if they did get harder as my PhD progressed, and supporting my development. Your breadth of knowledge is amazing. Your enthusiasm for science and for life make you a pleasure to work with; thank you for always having a million ideas (even in your dreams) and for always having a laugh (even when we wanted to cry instead). You are not just a supervisor and mentor but have also become a friend.

One of the highlights of my PhD experience was spending three months working at the CNEA in Argentina under the supervision of Dr Victor Luca. This was in large part due to the generosity and hospitality of Victor. Not many people would let a strange student and her boyfriend live in their house and treat them like family as you did. Victor, you have a huge heart, a wicked sense of humour and a first class science brain and I am so grateful I got the opportunity to work with you. Thanks also must go to Cristina, Agos, Stefo, Rodrigo and Ayelen for making me feel at home and showing me the sights.

So many people at ANSTO have helped me get through my PhD journey, both through scientific assistance and friendship. Thank you Dr Gordon Thorogood for endless cups of tea and chats (both scientific and not) and for your help with XRD. I feel very lucky to have got to know you over those amazing breakfasts overlooking Montpellier, for multiple reasons. Dr Massey De Los Reyes, thank you for your ridiculously enthusiastic support. I don't think I'll ever meet anyone who will scream as loudly as you when I tell them I've had a paper accepted. I'm sure we'll be friends for many years to come. Thank you Dr Robert Knott for maintaining the SAXS instrument that was so critical to my research and for always being so willing to help, especially if there was a cherry ripe to be had. Thank you Dr Inna Karatchevtseva for performing nitrogen porosimetry on some of my samples, for teaching me to use the FTIR and nanosizer and for always being friendly and generous with your time. Thanks also to Nick Scales for teaching me how to run ICP-MS, Dr Simon Middleburgh for teaching me how to use DMol^3, Joel Davis for SEM measurements and Rob Aughterson for TEM measurements. Thank you Dr Daniel Riley for always checking up on me. Thanks also to Dr Nigel Kirby and Dr Kathryn Spiers for their help with experiments at the Australian Synchrotron and to Ilkay Chironi and Grant Griffiths for maintaining the labs I worked in. Finally I would like to acknowledge that the work on conversion to a ceramic wasteform in *Chapter 3* was done by students Ms Margaux Tansu and Mr Jason Costa, with my supervision and the help of Drs Dan Gregg and Lou Vance.

Although I spent most of my time at ANSTO, I would like to thank Dr Rob Elmes, (nearly Dr) Karen Yuen, Dr Tien Ngo, Dr Deni Taleski and Dr Rob Thompson from the Jolliffe group as well as all the others in the lab for making me feel welcome and showing me the ropes when I was at Sydney Uni. Thanks also to Dr Nick Proschogo for mass spectrometry measurements. Thank you Dr Aditya Rawal and Dr James Hook at UNSW for your expertise and assistance with solid-state NMR measurements. I would also like to acknowledge the Microanalytical Unit at ANU and the Microanalysis Service at Macquarie University for percentage CHNP analysis.

I wish to acknowledge funds provided by Sydney University (postgraduate research support scheme), ANSTO (united uranium scholarship, travel bursary for Cheiron School and other travel funding), the Australian Synchrotron (travel bursary for user meeting) and Australian Ceramic Society (bursary for CAMS2014), which allowed me to attend conferences and workshops as well as to work overseas during my PhD candidature.

Although I cannot list here everyone who has supported me, if over the last five years you have said to me ‘you can do it’ in some form – thank you, it is truly appreciated. Special thanks in this regard must go to my family. To my parents, thank you for always encouraging me to pursue what I enjoy, for being interested in my work even when it involved unpronounceable words and for providing sage advice when things were hard. To Pete, your belief in the value of my work means so much to me, and helps me maintain mine, so thank you. Thanks also for believing in me, especially when I didn’t, and for all the hugs.

Table of Contents

List of Figures

List of Tables

List of Schemes

List of Abbreviations

ACN	Acetonitrile
AHA	Acetohydroxamic acid
An	Actinide elements
ATMP	Amino tris(methylene phosphonic acid)
ATR	Attenuated total reflectance
BET	Brunauer-Emmett-Teller
BJH	Barrett-Joyner-Halenda method
BPDC	2,2'-bipyridine-6,6'-dicarboxamides
BTBP	Bis-triazinyl bipyridine
BTP	Bis-triazinyl pyridine
CCD	Chlorinated cobalt dicarbollide
CD	Circular dichroism
CMPO	Carbamoylmethylphosphine oxide
CSA	Chemical shift anisotropy
D2EHPA	Di(2-ethylhexyl)phosphoric acid
DEDT-DPA	*N,N*-Diethyl-*N,N*-di(*p*-tolyl)pyridine-2,6-dicarboxamide
DFT	Density functional theory
DGA	Diglycolamide
DHOA	N,N-Dihexyl octanamide
DIAMEX	Diamide extraction
DIC	*N,N'*-Diisopropylcarbodiimide
DIPEA	*N,N'*-Diisopropylethylamine
DMAP	4-Dimethylaminopyridine
DMDBTDMA	*N, N'*-Dimethyl, *N, N'*-dibutyl tetradecyl malonamide
DMDOHEMA	*N,N'*–Dimethyl,*N,N'*-dioctylhexylethoxymalonamide
DMF	Dimethylformamide
DMSO	Dimethylsulfoxide
DPA	Dipicolinamide
DTPA	Diethylenetriaminepentaacetic acid
EDX	Energy dispersive x-ray analysis
EISA	Evaporation induced self-assembly
EO	Ethylene oxide
ESI-MS	Electrospray ionization mass spectra
EtOH	Ethanol
EXAFS	Extended x-ray absorption fine structure
Fmoc	Fluorenylmethyloxycarbonyl
FRs	Fast reactors
FS-13	Phenyltrifluoromethyl sulfone

FTIR	Fourier transform infra-red
FWHM	Full width at half maximum
HBTU	*O*-Benzotriazole-*N,N,N',N'*-tetramethyl-uronium-hexafluorophosphate
HDBP	Dibutyl phosphate
HEPES	4-(2-Hydroxyethyl)-1-piperazineethanesulfonic acid
HRMS	High resolution mass spectra
ICP-MS	Inductively coupled plasma mass spectrometry
I_{rel}	Relative intensity
K_d	Distribution coefficient
Ln	Lanthanide elements
LnBP	Lanthanide binding peptides
MA	Minor actinides
MAS	Magic angle spinning
MeOH	Methanol
MHI	Modulation of the hybrid interface
MOF	Metal-organic framework
MOX	Mixed oxide fuel
NMR	Nuclear magnetic resonance
Npts	Number of points
PAN	Polyacrylonitrile
PEO	Poly(ethylene oxide)
PO	Propylene oxide
ppm	parts per million
PPO	Poly(propylene oxide)
PSD	Pore size distribution
PTFE	Polytetrafluoroethylene
PyBOP	Benzotriazol-1-yloxytri(pyrrolidino)-phosphonium hexafluorophosphinate
PUREX	Plutonium and uranium extraction
R_g	Radius of gyration
RH	Relative humidity
RIR	Relative intensity ratio
SAXS	Small angle x-ray scattering
SAMMS	Self-assembled monolayers on mesoporous supports
SEM	Scanning electron microscopy
SF	Separation factor
SiO_2-P	Styrene-divinylbenzene polymer embedded in porous silica particles
TALSPEAK	Trivalent actinide lanthanide separation by phosphorus extractants and aqueous complexes
TBP	Tributyl phosphate
*t*Bu	*tert.*Butyl

terpy	2,2':6',2''-Terpyridine
TFA	Trifluoroacetic acid
TFAAD	Trifluroacetamide protected 10-amino-1-undecene
THF	Tetrahydrofuran
TIS	Triisopropylsilane
TODGA	*N,N,N',N'*-Tetraoctyl diglycolamide
TOPO	Trioctylphosphine oxide
TPH	Total petroleum hydrocarbons
TPTZ	2,4,6-Tripyridyl-1,3,5-triazine
TRUEX	Transuranic extraction
UNEX	Universal extraction
UREX	Uranium extraction
XAS	X-ray absorption spectroscopy
XRD	X-ray diffraction
ZrP	Zirconium organophosphonate

Chapter 1: Introduction

1.1 Context: Nuclear Separations

Separations processes are prevalent throughout the nuclear industry; within the nuclear fuel cycle, medical isotope production and for decontamination of environmental radioactivity. In terms of medical isotopes, production of technecium-99m (Tc-99m), the most commonly used medical isotope, requires separation from the parent nuclide molybdenum-99 (Mo-99) in generators.[1] The Mo-99 in turn is obtained via a separations process applied to irradiated uranium target plates[1] and the waste produced from this Mo-99 extraction may undergo further separations before immobilisation or recycling.[2,3] At the front end of the nuclear fuel cycle, nuclear separations are required for the extraction of uranium (U) and thorium (Th) from ores[4-6] as well as for enrichment.[7] At the back end of the nuclear fuel cycle, various separations are possible for reprocessing of used nuclear fuel.[8] These separations at the back end of the nuclear fuel cycle will be the focus of the present work.

Currently, nuclear power accounts for approx. 11 % of all electricity generated worldwide. There are 434 nuclear power plants currently in operation in 30 countries around the world and a further 72 power plants were under construction as of the end of 2013.[9] Global energy demands are likely to increase in future, due to an increasing population as well as improving quality of life in developing countries. Nuclear power is a potential candidate to provide much of this energy because it will become more economically viable as the cost of coal and gas increases, the technology is well developed and is able to provide baseload power and because nuclear power is an environmentally friendly option in terms of its greenhouse gas emissions. In fact, the life cycle greenhouse gas emissions for nuclear power (including construction, enrichment, waste management etc…) are similar to or less than those for renewable energy technologies such as photovoltaics, wind and hydroelectricity.[10]

Storage and recycling of nuclear waste are important issues that will increase in relevance if nuclear power becomes more widely adopted internationally. In some countries with nuclear power capability, such as the United States of America, the current policy for management of used nuclear fuel is storage in a deep geological repository, without any form of reprocessing.[11] In this scenario the used fuel will remain radioactive for hundreds of thousands of years as shown in Figure 1.1. Ensuring that there are no environmental or health risks from leakage of radioactive and/or toxic elements from the used nuclear fuel over this time period is both challenging and expensive, as is apparent in the fact that to date, no functioning deep geological repository for high level waste has been created anywhere in the world.[12] In addition, public perception of long term deep geological storage of radioactive waste is generally not positive.[13,14]

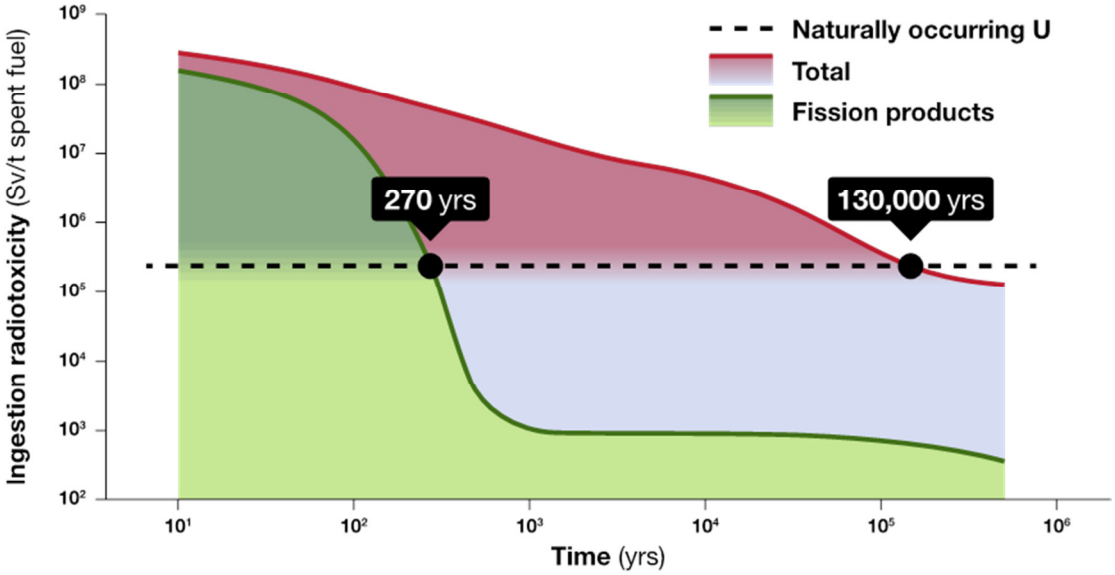

Figure 1.1: Evolution of the radiotoxicity of used nuclear fuel with and without reprocessing to separate and remove the actinides (U, Pu and MA). Figure adjusted from IAEA (2004).[15]

The alternative to deep geological disposal of used nuclear fuel is reprocessing. Approx. 95 % of used nuclear fuel consists of U and plutonium (Pu) (Figure 1.2), which can be recovered by reprocessing and subsequently converted into a Mixed OXide (MOX) material that can be recycled as fuel.[11] Reprocessing of used nuclear fuel to recover the U and Pu has been adopted by many countries with nuclear power capabilities, such as France, Japan, Russia and the United Kingdom.[16] In France and Japan, MOX fuel is also being fabricated and reused in light water nuclear reactors.[11] This means that more energy is being obtained from material previously considered 'nuclear waste'. From this it is clear that reprocessing used nuclear fuel to separate U and Pu from the fission products can increase the number of years nuclear power will be a viable option for power generation.

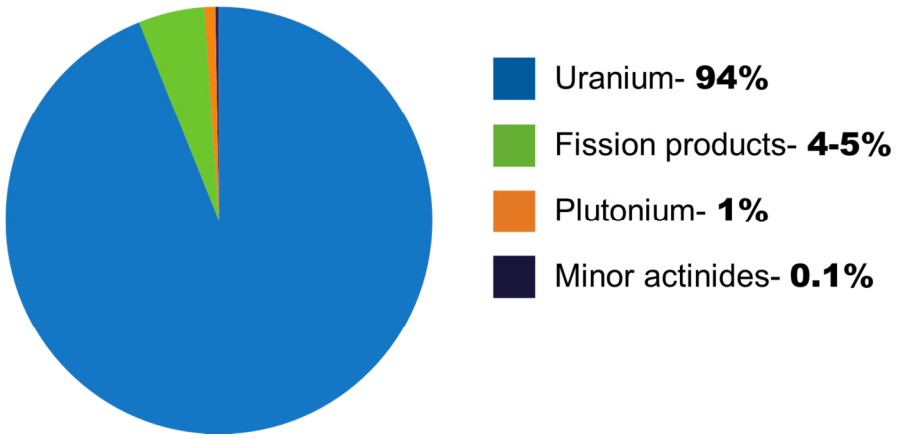

Figure 1.2: Approximate composition of used nuclear fuel. Figure adjusted from Hudson *et al.* (2013).[17]

A new class of 'generation IV' fast reactors (FRs) are currently under development that are able to utilise a greater proportion of the U-238 in fuel than 'generation III' reactors due to the higher energy of their 'fast' neutrons.[18] These FRs are also able to transmutate the minor actinides (MA) americium (Am), neptunium (Np) and curium (Cm) into less hazardous isotopes. Minor actinides and Pu are the major contributors to the long lifetime and radiotoxicity of used nuclear fuel,[19] so reprocessing to partition out Pu and MA would decrease the radiotoxicity, heat loading, volume and longevity of the remaining waste requiring long-term storage.[19,20] For example, Figure 1.1 shows how the radiotoxicity of light water reactor fuel (with 50 gigawatt-days/metric ton of heavy metal burn-up) would evolve over time with and without removal of Pu and MA.[15] Without any reprocessing, the waste would take 130 000 years to return to the radiotoxicity level of naturally occurring U. However, reprocessing the waste to remove all the actinides (An), leaving only the fission products, would decrease the lifetime of the waste to 270 years, after which time it would no longer require isolation from the environment. Therefore, in addition to increasing the nuclear lifetime, reprocessing and recycling of used nuclear fuel via the "partitioning and transmutation" method would dramatically decrease the hazardous nature of nuclear waste requiring long-term storage.[21] This is beneficial in terms of decreasing risk to the environment and public health as well as decreasing costs (due to storing reduced volumes of lower activity waste) and increasing public acceptance.

In order to decrease the lifetime of waste to be disposed, U, Pu and MA are targets for selective separation from solutions of dissolved used nuclear fuel, as they can be reused and/or transmutated in FRs. However, in order to transmutate MA they must be separated from the lanthanide fission products also present in used nuclear fuel. This separation is necessary because lanthanides (Ln) are present in substantially greater quantities than MA and, when present their higher neutron absorption cross-section results in preferential absorbtion of neutrons and prevents transmutation of MA.[17,22] Lanthanide elements themselves may also be considered targets for selective separations due to their importance in materials for clean energy technologies of the future such as wind turbines and electric vehicles, as well as their increasing industrial importance in applications such as catalysts, electronics and phosphors.[23,24] Unfortunately, the chemical similarity of Ln and MA makes their partitioning one of the most challenging hydrometallurgical separations known.[25] As a result, no process to separate MA from Ln has yet been implemented on an industrial scale.

Separation of cesium (Cs) and strontium (Sr) from used nuclear fuel is also a developing and topical area of research[26] as these elements contribute significantly to the heat production of used nuclear fuel (approx. 90 % in high level waste). Hence their removal from used nuclear fuel would reduce the volume of waste to be disposed and increase its ease of handling.[27] It may also be possible to re-use these elements, for example Cs-137 and Sr-90 can be used in various radiation therapies for cancer patients, food processing, industrial thickness and density gauges, sterilisation of medical supplies and irradiation processing of

sewage sludge.[27] Alternatively, Cs-137 and Sr-90 could simply be stored separately once recovered, as their relatively short half-lives of approx. 30 years means short-term storage only would be necessary. The radioactivity and radiotoxicity of the remaining (longer lived) waste would then be reduced and the volume required for repository type storage would be decreased.

1.2 Solvent Extraction Processes for Separations at the Back End of the Nuclear Fuel Cycle

Most commercial and developing processes for reprocessing of used nuclear fuel are presently solvent extraction processes. An organic solvent containing an extractant ligand is contacted with an aqueous solution of used nuclear fuel, usually dissolved in nitric acid. The organic extractant is chosen or designed to have the chemical ability to selectively partition the desired elements from the aqueous phase into the organic solvent. An ideal extractant should be efficient, selective, hydrolytically and radiolytically stable, soluble, give fast reaction kinetics and be easily synthesised.[28] The efficiency of extraction is measured using the distribution coefficient (K_d), which is the ratio of the concentration of the analyte in the organic phase (C_{org}) relative to the concentration of the analyte in the aqueous phase (C_{aq}) after contact. The selectivity of an extractant for one element (A) over another element (B) can then be evaluated using the separation factor, (SF_{AB}), which is the ratio of the distribution coefficients of element A ($K_d(A)$) and element B ($K_d(B)$).

$$K_d = \frac{C_{org}}{C_{aq}} \quad , \quad SF_{AB} = \frac{K_d(A)}{K_d(B)}$$

Extractants composed of only C, H, O and N atoms are often considered preferable in a nuclear context as they do not leave solid, radioactive residues when they are incinerated after being spent.[28] The radioactive residues produced from incineration of P and S containing extractants increase the volume of wastes to be processed and stored. This is referred to as the 'CHON' principle.

Due to the large number of elements present in used nuclear fuel, many varied solvent extraction processes have been developed to selectively extract different groups of elements. These processes may be classed into three groups corresponding to the three main sequential solvent extraction processes considered and utilised for reprocessing of used nuclear fuel. The initial step is to recover the U and perhaps also Pu for recycling as nuclear fuel. This process is presently performed on an industrial scale using solutions of used nuclear fuel dissolved in concentrated nitric acid. Therefore, the subsequent solvent extraction processes involving removal of both MA and Ln together from the remaining fission products in the raffinate after U and Pu removal must also be performed with nitric acid as the

aqueous phase. The final step then involves separation of MA from Ln, allowing the isolated MA to be transmutated into less hazardous materials.[17] Overviews of the solvent extraction processing technologies, available and postulated, for these three separations, are detailed in *sections 1.2.1, 1.2.2 and 1.2.3*, respectively.

1.2.1 Uranium and Plutonium Recovery

Currently, commercial reprocessing of used nuclear fuel is carried out in several countries including France, UK, Russia and Japan using the Plutonium and URanium Extraction (PUREX) process.[16] PUREX is a solvent extraction process utilising the organic ligand tributyl phosphate (TBP, 30 % in kerosene) to selectively extract Pu(IV) and U(VI) from a solution of used nuclear fuel dissolved in 3-6 M nitric acid. The chemical structure of the TBP extractant is shown in Figure 1.3. Oxalic and hydrofluoric acids can be added to prevent unwanted extraction of molybdenum (Mo) and zirconium (Zr). After the U(VI) and Pu(IV) are partitioned into the organic phase a reducing agent is added, causing formation of Pu(III) which is no longer complexed by TBP and can therefore be stripped with clean nitric acid. Uranium is protected from reduction using hydrazine, and is stripped from the organic phase subsequently at approx. 50 ^{o}C using dilute nitric acid.[16] The extracted Pu(IV) and U(VI) can then be converted to oxides to make MOX fuel which can be re-used in both current generation III reactors or FRs, as described in *section 1.1*.

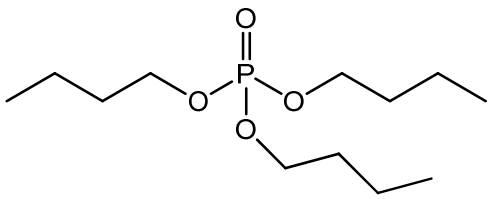

Figure 1.3: Organic extractant tributyl phosphate used in the PUREX process

Tributyl phosphate (Figure 1.3) is considered a good extractant molecule as it is simple, cheap and selective for the tetra- and hexa-valent An over the tri- and penta-valent An. It is also hydrolytically stable under the strong acidic conditions required for this process and is a very effective extractant.[16] However, TBP is not radiolytically stable and is degraded, predominantly forming dibutyl phosphate (HDBP), over time during the PUREX process.[16] This interferes with separation factors between U(VI)/Pu(IV) and other fission products since HDBP has different extraction behaviour to TBP and a particular affinity for Zr.[29] Washing with sodium carbonate can be performed to remove the degradation products. However, this costs time and money, generates waste and also becomes less effective over time. Partitioning of technetium (Tc) and neptunium (Np) is also difficult to control due to the large number of possible oxidation states of these elements.[16] Finally, as with most solvent extraction processes, PUREX can also encounter problems with third phase formation if the metal

loadings are too high. This third phase is a stable emulsion that forms between the organic and aqueous phases during solvent extraction such that the separation is compromised. The formation of HDBP, which is an alkyl phosphoric acid and hence acts as a surfactant, accentuates this problem.[29]

An alternative to the TBP extractant for recovery of U(VI) and Pu(IV) from solutions of used nuclear fuel is N,N-dihexyl octanamide (DHOA, Figure 1.4).[30] This extractant obeys the CHON principle, is readily solubilised in dodecane and does not cause third phase formation. It has also been shown to exhibit some superior properties to TBP, such as more efficient Pu(IV) extraction from 3 M nitric acid, lower partitioning of some contaminant elements and more efficient U(VI) stripping using 0.01 M nitric acid.[30] DHOA is however susceptible to radiolysis, as is TBP.

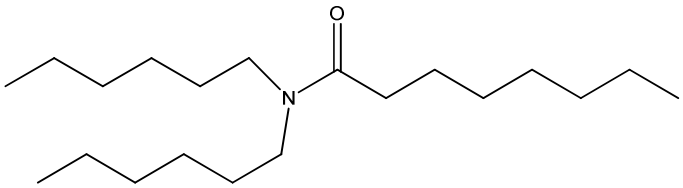

Figure 1.4: Organic extractant N,N-dihexyl octanamide used for U and Pu recovery

Another alternative to the PUREX process is the URanium EXtraction (UREX) process whereby Pu(IV) is deported to the raffinate with the remaining transuranic elements and fission products instead of being extracted with U(VI). This process is considered more proliferation resistant than the PUREX process because the Pu(IV) is not isolated at any point.[31] As with PUREX, 30% TBP in kerosene is used to extract U(VI) and Pu(IV) from dissolved used nuclear fuel. Then, a subsequent scrubbing of the loaded organic phase with 0.5 M acetohydroxamic acid (AHA) in 0.3 M nitric acid is used to return the Pu(IV) to the aqueous phase[31] since the AHA forms a strong complex with Pu(IV) but does not extract U(VI).[32] Substantial amounts of Tc are also extracted with the U(VI) into the organic phase, so the Tc is stripped using 6 M nitric acid before final conversion of the U(VI) to an oxide that can be re-enriched and re-used as fuel.[31]

1.2.2 Actinide Group Extractions

As described in *section 1.1*, other elements apart from U and Pu that are present in used nuclear fuel are also targets for separations. These include MA as well as Ln, Cs and Sr. Many solvent extraction processes have been developed to extract U, Pu, MA and Ln together, either with or without Cs and Sr. Once these elements are separated from the other fission products in used nuclear fuel, further processing to isolate individual elements is simplified. Such group actinide extraction processes could be applied directly to used nuclear fuel solutions or to PUREX raffinate solutions after U and Pu removal.[21]

The TRansUranic EXtraction (TRUEX) process is a modified PUREX process in which Np(V) and MA(III) are extracted as well as U(VI) and Pu(IV) due to the addition of a carbamoylmethylphosphine oxide (CMPO) extractant to the organic phase.[30] More specifically, the TRUEX process typically utilises an organic phase consisting of 0.2 M CMPO and 1.2 M TBP in paraffinic hydrocarbon diluent.[30] Phosphine oxides such as CMPO are known to form strong complexes with metals under acidic conditions[33] and were developed to overcome the relatively weak metal extraction properties of the carbamoylmethylphosphonate class of extractants.[34] Lanthanide elements and Tc are also extracted to a certain extent in the TRUEX process, depending on the processing conditions, but selectivity over other fission products is maintained.[35] The TRUEX process has been utilised successfully to decontaminate actinide-bearing wastes in the USA, Europe, Japan and India.[34]

The CMPO derivative typically used in the TRUEX process is octyl(phenyl)-*N,N*-diisobutyl-CMPO, shown in Figure 1.5, since it is easily synthesised, gives high MA distribution coefficients in the nitric acid concentration range 0.5 – 6 M and can tolerate higher metal loadings than several other CMPO derivatives tested without third phase formation.[35] As occurs for the TBP extractant in the PUREX process, CMPO degradation products form during processing which interfere with the desired properties of the process. Therefore, contact of the used organic phase with macroreticular anion exchange resins to remove the phosphonic and phosphinic acid degradation products followed by washing with dilute sodium carbonate solution (as for the PUREX process) is required before recycling is possible.[35]

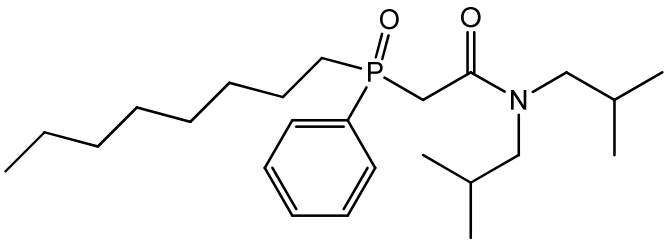

Figure 1.5: Organic extractant octyl(phenyl)-*N,N*-diisobutyl- carbamoylmethylphosphine oxide, used in the TRUEX process for group MA and Ln extraction

It has been demonstrated that improved performance of CMPO ligands can be obtained when they are preorganised onto tripodal scaffolds or calixarenes.[36] For example, improved extraction efficiency as well as MA-Ln selectivity was observed for CMPO groups attached to calix[4]arenes or triphenylmethane scaffolds.[37] Even small structural changes in the CMPO ligand, such as replacing the methylene bridge with an ethylene group, have been shown to have dramatic impact on extraction performance.[38] Of the scaffolds investigated, four CMPO units grafted to the wide rim of calix[4]arene gave the best extraction results, with partition coefficient K_d(Am) ~120 and separation factor $SF_{Am/Eu}$ ~10 for extraction from 3 M nitric acid into dichloromethane.[37]

Other organophosphorus extractants for group extraction of actinides have also been developed, including diisodecylphosphoric acid and trialkylphosphine oxides (Figure 1.6).[16] However, both of these extractants have a high affinity for nitrate anions such that at the high nitric acid concentrations relevant to nuclear fuel reprocessing their performance is compromised. Dilution and denitrification of used nuclear fuel would be necessary prior to utilising these extractants, which is an unattractive option due to the increased volume to be reprocessed and the associated increases in time and cost of reprocessing.

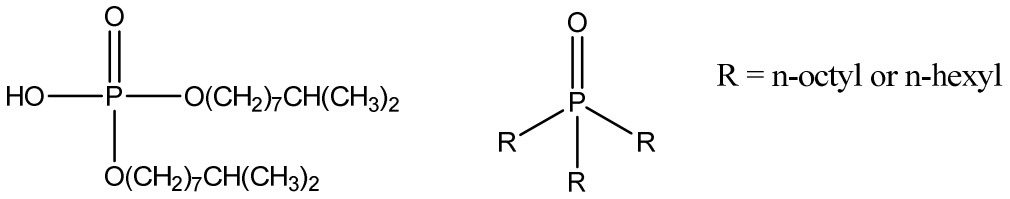

Figure 1.6: Organic organophosphorus extractants diisodecylphosphoric acid (left) and trialkylphosphine oxide (right), used for group actinide extraction

The DIAMide EXtraction (DIAMEX) process is another alternative for solvent extraction of all actinides from used nuclear fuel, in which the CHON principle is applied (unlike TRUEX). The extractant in the diamide process can be either a malonamide, as originally developed in France, or a diglycolamide (DGA). The original extractant used was 1 M *N, N'*-dimethyl, *N, N'*-dibutyl tetradecyl malonamide (DMDBTDMA, Figure 1.7) in normal paraffinic hydrocarbon diluent, which extracted Pu(IV) > U(VI) > Am(III) ~ Eu(III) ~ Fe(III) ~ Tc(VII) > Zr(IV) from 3-4 M nitric acid.[39] Formation of hydrolytic and radiolytic degradation products from DMDBTDMA does not detrimentally affect its extraction performance.[30] More recently, a different malonamide derivative *N,N'*–dimethyl,*N,N'*-dioctylhexylethoxymalonamide (DMDOHEMA, Figure 1.7) was developed, which exhibits higher lipophilicity and as a result limits third phase phenomena and facilitates removal of degradation products.[39] 1 M DMDOHEMA in n-dodecane has similar extraction properties to DMDBTDMA except that the preferential extraction of Pu(IV) over U(VI) is reversed. Both of these malonamide extractants exhibit K_d(Am) ~15 from 4 M nitric acid.[39]

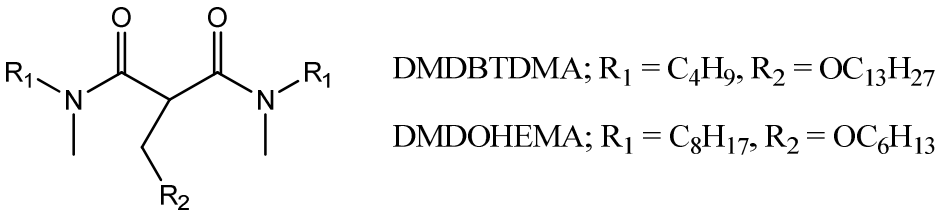

Figure 1.7: Organic extractants DMDBTDMA and DMDOHEMA, used in the DIAMEX process for group actinide extraction

Another class of diamide extractants used for the DIAMEX process is diglycolamides (DGA), which differ from malonamides primarily in that they have an ether oxygen atom between the two amine groups, as shown in Figure 1.8. This electron withdrawing oxygen atom decreases the basicity of the amide groups, making DGA extractants less acid sensitive than malonomides.[30] The oxygen atom also provides a third site for coordination of the metal, so that DGA ligands are tridentate, making them more efficient extractants than the bidentate malonamides.[40] As a result, lower concentrations of DGA extractants are required to achieve efficient extraction.[39]

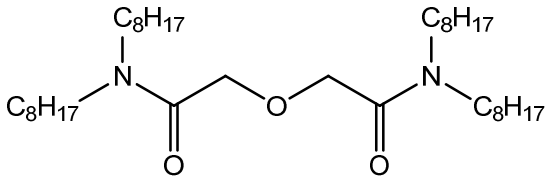

Figure 1.8: Organic extractant TODGA, used in the DIAMEX process for group actinide extraction

The most commonly used DGA ligand is *N,N,N',N'*-tetraoctyl diglycolamide (TODGA, Figure 1.8) due to its high solubility in n-dodecane and its high affinity for MA.[39] Many modifications of the TODGA ligand at the methylene between the amines and central oxygen or the oxygen itself have been shown to decrease its extraction efficiency.[40] Unfortunately, solvent extraction using TODGA requires a phase modifier, usually DHOA or TBP, to reduce third phase formation.[39] Specifically, 0.1 M TODGA with 0.5 M DHOA in n-dodecane extracts Am(III) ~ Eu(III) ~ Zr(IV) > Pu(IV) > U(VI) ~Tc(VII) > Mo(VI) ~ Sr(II) with K_d(Am) ~300 from 3 M nitric acid.

As described above for the CMPO ligand in the TRUEX process, preorganisation of DGA ligands onto tripodal scaffolds has been shown to improve their extraction efficiency.[41,42] CMPO and TODGA ligands have also been modified via covalent attachment to cobalt bis(dicarbollide) anions with diethylene glycol chains (in the case of CMPO on a calix[4]arene scaffold).[43,44] For both extractants this resulted in higher extraction efficiencies than when the ligand and cobalt bis(dicarbollide) anion were used together without covalent attachment. For the modified TODGA ligand the kinetics of extraction and $SF_{Eu/Am}$ were also enhanced, to 5.6 versus 2.0 from 3 M nitric acid, although the K_d(Eu) of 0.6 remained low at this acid concentration.[43] More recently, calixarene analogues called pillar[5]arenes functionalised with DGA ligands have demonstrated K_d(Eu) ~40 and $SF_{Eu/Am}$ of 4.8 from 3 M nitric acid.[45]

UNiversal EXtraction (UNEX) is a process for separation of An, Ln, Cs and Sr from other fission products in used nuclear fuel. The organic phase is composed of 0.08 M chlorinated cobalt dicarbollide (CCD) to extract Cs, 0.5 vol% polyethylene glycol (PEG-400) to extract Sr and 0.02 M diphenyl-N,N-di-n-butylcarbamoylmethylphosphine (Ph_2CMPO) to extract MA and Ln, in the stable diluent phenyltrifluoromethyl sulfone (FS-13).[46]

1.2.3 Minor Actinide-Lanthanide Separations

Separation of MA from Ln has not yet been achieved industrially due to the chemical similarity of these two classes of elements. Both MA and Ln are small, hard trivalent cations in solution. Lanthanides(III) generally have coordination numbers of 8 or more and their preferred geometry is tricapped trigonal prism.[33] Am(III) and Eu(III) are most commonly used to represent MA and Ln, respectively, when demonstrating selectivity.[47] Since transmutation of the MA elements is the end goal, it is generally considered preferable that selectivity for MA over Ln is demonstrated. Solvent extraction processes designed to separate MA from Ln are typically considered for use on PUREX raffinate solutions containing fission products, including Ln, Cs, Sr, Tc and iodine (I), as well as MA. Alternatively, MA-Ln separations may be performed on MA and Ln mixtures produced subsequent to a group An extraction process such as TRUEX or DIAMEX.

It has been demonstrated that use of extractants with soft donor atoms such as nitrogen or sulphur can provide MA-Ln selectivity.[22,33] The selectivity of soft donor ligands for MA over Ln has been postulated to arise from π back donation from the 5f orbitals in the trivalent MA ions to the π^* orbitals in the ligand, leading to covalency in the bonding that is absent with Ln.[28] Nitrogen donors are preferred over sulphur according to the CHON principle. Less basic nitrogen donors are also preferable as they perform better under the highly acidic conditions of nuclear reprocessing.

Some of the first ligands developed that demonstrated successful MA-Ln separation ($SF_{Am/Eu} > 10$) were N-donor ligands including 2,2':6',2''-terpyridine (terpy) and 2,4,6-tripyridyl-1,3,5-triazine (TPTZ), shown in Figure 1.9. However, these ligands required the presence of a hydrophobic, anionic synergist, such as α-bromodecanoic acid, to be effective. Also, extraction efficiencies were poor ($K_d(Am) < 1$) at acidities greater than 0.1 M nitric acid for terpy or 1 M nitric acid for TPTZ.[28,47] Subsequently extractants based on 2,6-bis(benzoxazol-2-yl)pyridine were developed, which demonstrated superior MA-Ln selectivity to terpy and TPTZ. The highest $SF_{Am/Eu}$ of 70 was achieved with 0.04 M 2,6-bis(benzoxazol-2-yl)-4-(2-decyl-1-tetradecyloxy)pyridine and 1 M α-bromodecanoic acid in total petroleum hydrocarbons (TPH) from 0.1 M nitric acid.[48] However, the extraction efficiency at this acid concentration was very low ($K_d(Am)$ ~0.1) and higher acidities could not be tolerated.

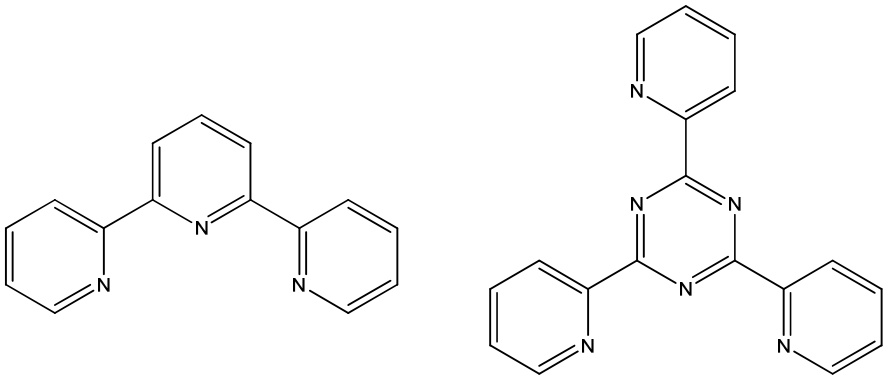

Figure 1.9: Early organic extractants for MA-Ln separation, terpy (left) and TPTZ (right)

In order to increase extraction affinities, extractant ligands were designed to incorporate both hard O-donor atoms and softer N-donor atoms to maintain selectivity. For example, many extractants based on the simple picolinamide moiety have been investigated based on the modest MA-Ln selectivity demonstrated by picolinic acid.[17] Several dipicolinamide (DPA) derivatives have been synthesised and the best performing derivative was *N*,*N*-diethyl-*N*,*N*-di(*p*-tolyl)pyridine-2,6-dicarboxamide (DEDT-DPA, Figure 1.10), which at a concentration of 0.1 M in chloroform was able to extract Am with K_d 11 and $SF_{Am/Eu}$ 3.9 from 6 M nitric acid,[49] with extraction increasing with nitric acid concentration. Adding a second pyridine group to the extractant structure to give 2,2'-bipyridine-6,6'-dicarboxamides (BPDC) resulted in increased SFs, but only in the presence of the lipophillic anionic synergist CCD. Directly comparable $SF_{Am/Eu}$ values for DPA versus BPDC are not available, but 0.03 M *N*,*N*-diethyl-*N*,*N*-dibenzyl-BPDC (DEDB-BPDC, Figure 1.10) and 0.01 M CCD in *meta*-nitrobenzotrifluoride (F-3) extracted Am from 1 M nitric acid with K_d ~7 and $SF_{Am/Eu}$ ~30. For this system, extraction efficiency decreased with increasing nitric acid concentration. Therefore it is questionable whether the addition of the second pyridine group was beneficial overall.

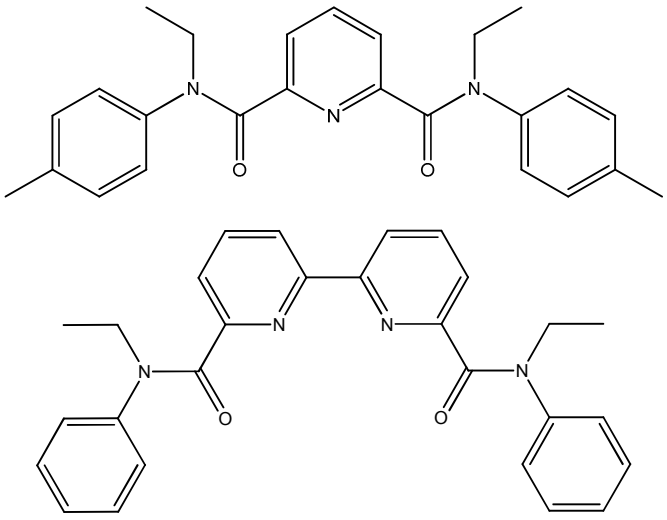

Figure 1.10: Organic picolinamide based extractants DEDT-DPA (above) and DEDB-BPDC (below) used for MA-Ln separations

Attaching picolinamide based ligands to a macrocyclic scaffold such as a calixarene can also improve their extraction efficiency.[33,50] From a series of picolinamide bearing calix[4]arenes, calix[6]arenes and calix[8]arenes synthesised by Casnati et al., an upper rim functionalised calix[4]arene (Figure 1.11, left) was demonstrated to exhibit the highest MA-Ln selectivity. For this extractant, K_d(Am) ~12 and $SF_{Am/Eu}$ ~14 from 0.001 M nitric acid were achieved using 0.01 M extractant and 0.003 M brominated CCD synergist in nitrophenyl hexyl ether.[50] However, picolinamide functionalised calixarenes were generally not effective for extractions from more acidic solutions (pH < 2) due to protonation of the extractant.[33] A picolinamide functionalised calix[6]arene (Figure 1.11, right, R = H) demonstrated the highest extraction efficiency and MA-Ln selectivity during extraction experiments from 0.01 M nitric acid, with 0.005 M extractant and 0.003 M brominated CCD synergist in nitrophenyl hexyl ether affording K_d(Am) ~9 and $SF_{Am/Eu}$ ~10.[50] Modification of picolinamide functionalised calixarenes by addition of electron withdrawing groups such as esters to the pyridine of the picolinamide decreases the basicity of the pyridine and as a result can improve extraction from more acidic solutions.[51] For example, 0.001 M methyl ester substituted picolinamide functionalised calix[6]arene (Figure 1.11, right, R = $COOCH_3$) with 0.003 M brominated CCD synergist demonstrated K_d(Am) ~40 and $SF_{Am/Eu}$ ~3 from 2 M nitric acid.

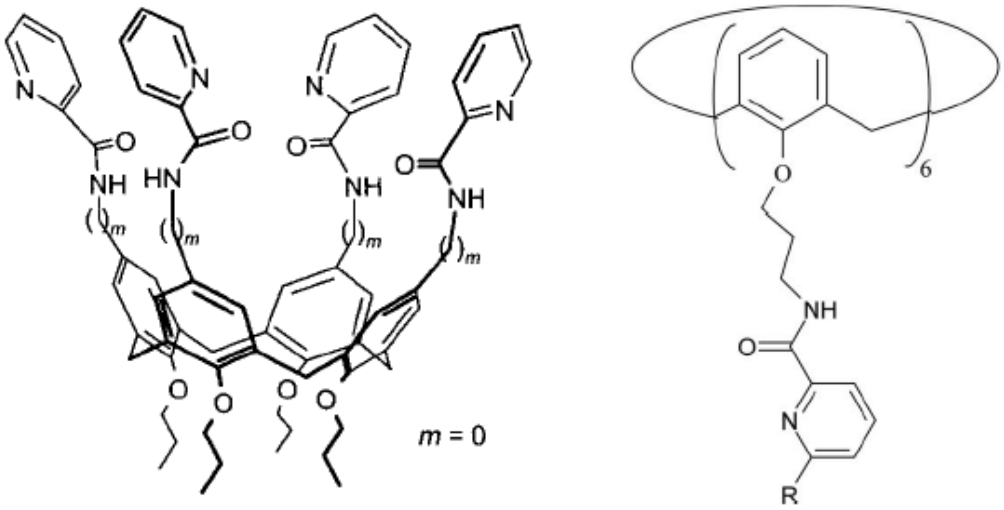

Figure 1.11: Picolinamide functionalised calixarene extractants for MA-Ln separation[50,51]

The sulphur based extractant bis(2,4,4-trimethylpentyl)dithiophosphinic acid is the active component of commercial extractant Cyanex 301, shown in Figure 1.12, and was originally developed for selective extraction of Zn(II),[52] but has demonstrated the highest known $SF_{Am/Eu}$ of approx. 40 000. This SF was achieved using 0.1 M Cyanex 301 + 0.02 M 2,2'-bipyridyl or 0.002 M 1,10-phenanthroline in toluene as the organic phase, extracting Am(III) and Eu(III) from 1 M $NaNO_3$ + 0.02 M sulfanilic acid at pH 3.2.[53] However, in the absence of the nitrogen donor co-extractants this selectivity is dramatically reduced; using 0.5 M Cyanex 301 in

kerosene as the organic phase, tracer levels of Am(III) and 0.3 M Eu(III) were extracted from 1 M $NaNO_3$ + 0.4 M formic acid at pH 3.7 with $SF_{Am/Eu}$ up to 10 000.[54] Although this extractant is able to provide excellent SF values, it is inappropriate for use under realistic nuclear reprocessing conditions due to its instability to oxidising conditions such as the presence of nitric acid. Under these conditions Cyanex 301 is oxidised to form first Cyanex 302 then Cyanex 272 (see Figure 1.12). Cyanex 302 demonstrates decreased $SF_{Am/Eu}$ values and Cyanex 272 preferentially extracts Ln over MA.[33] Also, even small amounts of impurities in the organic phase have a dramatic detrimental effect on the separation.[52]

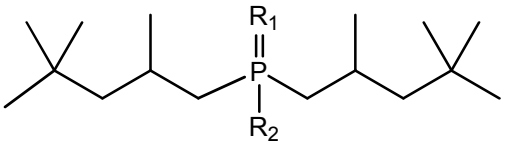

Cyanex 301; R_1 = S, R_2 = SH
Cyanex 302; R_1 = S, R_2 = OH
Cyanex 272; R_1 = O, R_2 = OH

Figure 1.12: Organic extractant Cyanex 301 and its oxidation products Cyanex 302 and Cyanex 272

In order to improve the hydrolytic and radiolytic stability of dithiophosphinic acid extractants, derivatives were prepared with trifluoromethylphenyl side chains,[55] since benzene rings can act as energy sinks and prevent radiolysis.[47] These aromatic dithiophosphinic acids demonstrated improved $SF_{Am/Eu}$ values relative to Cyanex 301 as well as improved stability. In fact, 0.1 M bis(o-trifluoromethylphenyl)-dithiophosphinic acid in FS-13 extracted Am(III) and Eu(III) from 0.01 M HNO_3 + 1 M $NaNO_3$ with $SF_{Am/Eu}$ of approx. 10 000 at pH 2.[55] The position of the trifluoromethyl group on the phenyl ring was observed to have a large impact on the separation performance of the ligand in this work. Further investigation into the effect of dithiophosphinic acids substitutents on their selectivity using x-ray absorption spectroscopy (XAS) and density functional theory (DFT) has suggested that the presence of ortho groups on the phenyl rings causes steric interactions such that the phenyl rings rotate around the P-C bond and the molecular symmetry of the extractant is decreased. This in turn increases the energy of the HOMO of the extractant molecule, making it more 'soft' and hence more selective.[56]

In order to extract MA from Ln under more strongly acidic conditions, it is possible to use dithiophosphinic acids synergistically with hard donor extractants.[57] In fact, under these conditions other An such as U and Pu may also be extracted. For example, 0.5 M bis(o-trifluoromethylphenyl)-dithiophosphinic acid and 0.1 M trioctylphosphine oxide (TOPO) in toluene selectivity extract U, Pu, Am and Np from 0.3 M nitric acid with $K_d > 6$, while Ln, Cs, Sr, Ba and Rb remained in the aqueous solution with $K_d < 0.2$.[58]

In the 1960s at Oak Ridge National Laboratory in the USA another process for MA-Ln separation was developed, namely the Trivalent Actinide Lanthanide Separation by Phosphorus Extractants and Aqueous Complexes (TALSPEAK) process. The TALSPEAK process typically uses 0.5 M di(2-ethylhexyl)phosphoric acid (D2EHPA) in

1,4-diisopropylbenzene to extract Ln from an aqueous phase consisting of 0.05 diethylenetriaminepentaacetic acid (DTPA) in 1 M lactic acid (pH ~3.5) and can achieve $SF_{Eu/Am}$ ~90.[59] The chemical structures of these extractants are shown in Figure 1.13. The DTPA is responsible for keeping MA in the aqueous solution, while the lactic acid acts as a buffer as well as improving the kinetics of extraction and reducing radiolytic degradation of the DTPA.[59,60]

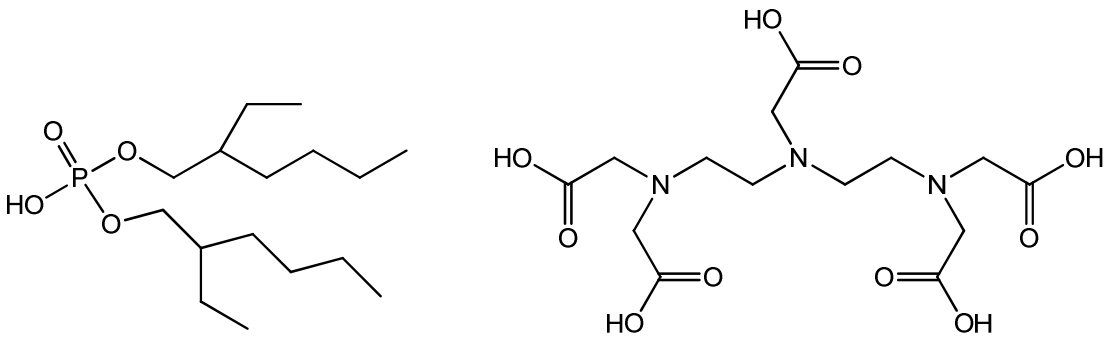

Figure 1.13: Organic extractants D2EHPA (left) and DTPA (right) used in the TALSPEAK process

Another class of extractants for MA-Ln separations is the bis-triazinyl pyridine (BTP) and bis-triazinyl bipyridine (BTBP) extractants. These are N-donor extractants and fulfil the CHON criteria. Discovery of the solvent extraction properties of the BTP class of extractants[61] represented a breakthrough in MA-Ln separation technology as this was the first class of extractants able to effectively separate MA from Ln in concentrated nitric acid solutions without the use of a synergist.[17] This new, desirable property of unassisted extraction from strongly acidic solutions can be explained by the fact that BTP extractants can complex MA as nitrate salts and that they are able to form 1:3 complexes, unlike most other N donor extractants which form 1:2 complexes.[28] In fact, extraction of MA increases with nitric acid concentration,[47] which has been suggested to result from the fact that protonation of BTP extractants causes them to adopt the 'cis' conformation which is conducive to metal binding.[62]

BTP ligands were developed before BTBPs and their properties depend significantly on what substituents are present at the 5,6 positions of the triazinyl rings. It was originally noted that branched alkyl substituents provided superior hydrolytic stability to unbranched substituents.[28,60] As a result, *iso*-propyl substituents became commonly used (*i*Pr-BTP, shown in Figure 1.14). Using 0.01 M *i*Pr-BTP + 0.5 M DMDOHEMA in n-octanol from 0.5 M nitric acid gave K_d(Am) 9 and $SF_{Am/Eu}$ 90.[28] Extraction from more acidic solutions was more efficient but less selective. In addition, the extraction kinetics were slow, hydrolysis was extensive in strong (3 M) nitric acid and > 80 % radiolysis occurred upon irradiation with 100 kGy gamma dose.[62] This is a significant disadvantage given that the annual dose to an organic phase in a

MA-Ln separation solvent extraction process plant has been estimated as 100 kGy – 1 MGy.[47]

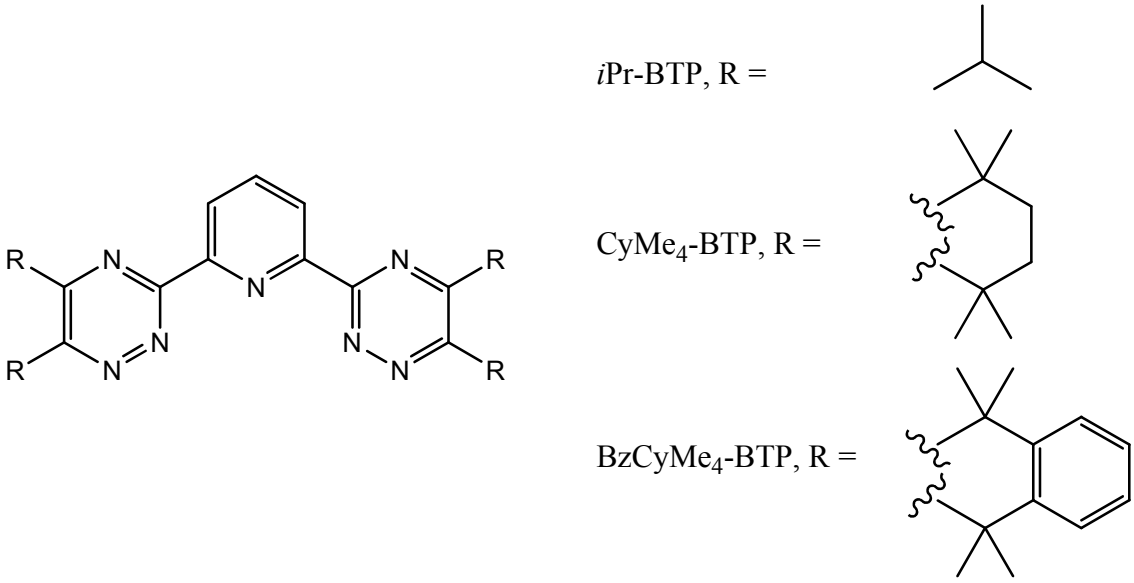

Figure 1.14: Organic BTP extractants used for MA-Ln separation

Later, the annulated ring $CyMe_4$ substituent was developed (see Figure 1.14). $CyMe_4$-BTP demonstrated improved acid stability (stable up to 24 h in 3 M nitric acid) [62] as well as increased efficiency and selectivity. Specifically, 0.01 M $CyMe_4$-BTP + 0.5 M DMDOHEMA in n-octanol exhibited K_d(Am) ~500 and $SF_{Am/Eu}$ ~5600 from 0.5 M nitric acid. The DMDOHEMA was added as a synergist in order to improve the kinetics of extraction[47] since the radiolytic stability and kinetics of extraction were still problematic for $CyMe_4$-BTP. In fact, $CyMe_4$-BTP demonstrated slower kinetics even that *i*Pr-BTP.[62] This is in accordance with the general pattern which has been noted that increasing the size and branching of substituents improves their hydrolytic and radiolytic stability but slows their rate of extraction.[28,63] To address the radiolytic stability of $CyMe_4$-BTP, a scavenger molecule such as nitrobenzene can be included in the organic phase of the solvent extraction system.[47] Alternatively, a conjugated ring can be appended to the $CyMe_4$ group to give $BzCyMe_4$-BTP, as shown in Figure 1.14.[62] However, this additional conjugated ring decreased the efficiency and selectivity of MA extraction. For 0.01 M extractant + 0.5 M DMDOHEMA in n-octanol from 0.5 M nitric acid, K_d(Am) was 500 and $SF_{Am/Eu}$ 1600 for $CyMe_4$-BTP while D_{Am} was 10 and $SF_{Am/Eu}$ 600 for $BzCyMe_4$-BTP.[62]

The high extraction efficiencies of BTPs can be problematic as it causes stripping of the metal from the organic phase to become extremely challenging.[47] This is a major problem since it prevents recycling of the organic solvent. Due to the prohibitively high extraction efficiencies of $CyMe_4$-BTP, the BTBP extractant, shown in Figure 1.15, was developed.[47] As well as facilitating stripping, BTBP extractants also demonstrate superior solubility, hydrolytic and radiolytic stability to BTP extractants.[63] In terms of radiolytic stability, $CyMe_4$-BTBP

(Figure 1.15) has been shown to withstand up to 20 kGy dose,[47] which would allow it to survive approximately two months in a MA-Ln separation solvent extraction process plant. The kinetics of extraction was still slow using $CyMe_4$-BTBP, for example extraction with 0.02 M $CyMe_4$-BTBP in octanol from 0.5 M nitric acid required more than 30 minutes to reach equilibrium.[64] Therefore addition of DMDOHEMA to the organic phase to act as a phase transfer agent was still beneficial, as with BTP extractants. However, increasing the DMDOHEMA concentration above 0.25 M caused a decrease in $SF_{Am/Eu}$ since the DMDOHEMA itself extracts MA and Ln non-selectively.[64] Using 0.01 M $CyMe_4$-BTBP and 0.25 M DMDOHEMA in octanol as the organic phase resulted in K_d(Am) ~10 and $SF_{Am/Eu}$ ~120 from 1 M nitric acid within 5 minutes of mixing.

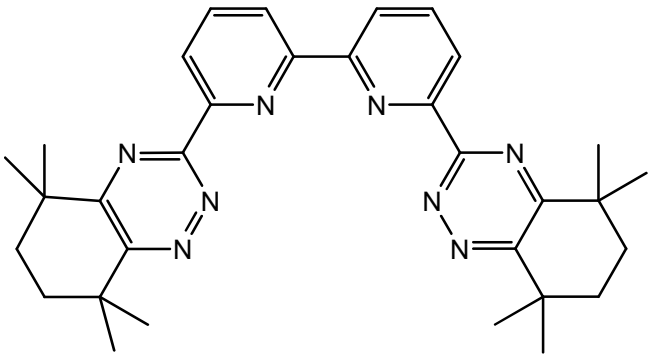

Figure 1.15: Organic extractant $CyMe_4$-BTBP used for MA-Ln separation

Successful MA-Ln separation has been demonstrated on a radioactive spent fuel solution using $CyMe_4$-BTBP. After PUREX and DIAMEX processing, a 2 M nitric acid aqueous solution containing MA and Ln underwent 9 extractions with 0.015 M $CyMe_4$-BTBP and 0.25 M DMDOHEMA in n-octanol to give a MA stream containing less than 0.1% Ln.[65] However, a slow flow rate was required due to the poor kinetics of the extractant and the loading capacity of the organic was also limited, making this MA-Ln separation process non-ideal for industrial use.[65]

It has been hypothesised that the reason for the slow kinetics of extraction by $CyMe_4$-BTBP could be that the more energetically favourable *trans* conformation must transform into the *cis* conformation in order to coordinate metal cations.[66] Therefore the 2,2'-bipyridine moiety of the BTBP extractant was replaced with 1,10-phenanthroline, affording the quadridentate bis-triazine extractant, $CyMe_4$-BTPhen (Figure 1.16), which is locked into a *cis* conformation. Solvent extraction studies with $CyMe_4$-BTPhen showed that it was able to quickly, effectively and selectively extract MA from Ln in concentrated nitric acid solutions without the use of a synergist, making it a highly suitable candidate for use under MA-Ln separation processing conditions. Specifically, 0.01 M $CyMe_4$-BTPhen in octanol extracted Am from 1 M nitric acid with K_d ~1000 and $SF_{Am/Eu}$ ~300.[66] This K_d(Am) value is approx. two orders of magnitude greater than was achieved using $CyMe_4$-BTBP and the SF is also

greater. Despite the high affinity of $CyMe_4$-BTPhen for MA, back extraction was possible using glycolic acid.[17] In terms of kinetics, extraction of Am reached equilibrium within approx. 15 min without the use of a phase transfer agent.[66] Furthermore, $CyMe_4$-BTPhen was more soluble in 1-octanol than $CyMe_4$-BTBP.[17]

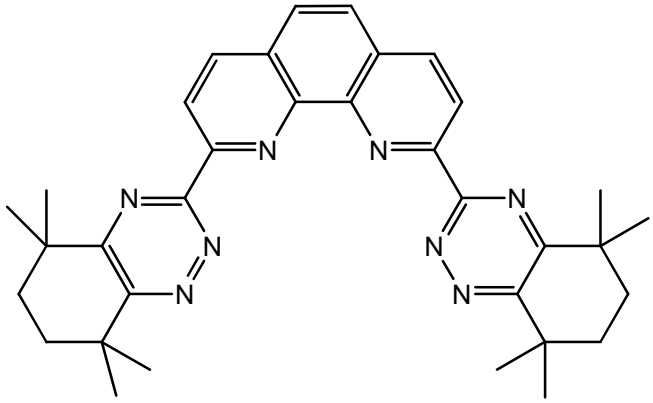

Figure 1.16: Organic extractant $CyMe_4$-BTPhen used for MA-Ln separation

1.2.4 Separation of Cesium

Calixarene crown ethers have been shown to be effective and selective extractants for Cs from used nuclear fuel solutions, typically performing better than mono-crown ethers.[67,68] In particular calix[4]arene-crown-6 ethers, such as calix[4]arene bis(*tert*-octlbenzo-crown-6), shown in Figure 1.17, are ideal for extraction of Cs from alkaline waste streams.[67] However, this extractant degrades under strongly acidic conditions, whereas calix[4]-bis-2,3-napthocrown-6, in which the *tert*-octylbenzo groups of the structure in Figure 1.17 have been replaced by naphthalene groups, demonstrated chemical stability in 3 M nitric acid over six months.[68] In terms of extraction performance, 2.5 mM calix[4]-bis-2,3-napthocrown-6 in nitrobenzene extracted Cs from 3 M nitric acid simulated high level liquid waste with K_d ~ 10 and was selective over fission products including Ln, Mo, Tc, Zr, Sr and others.

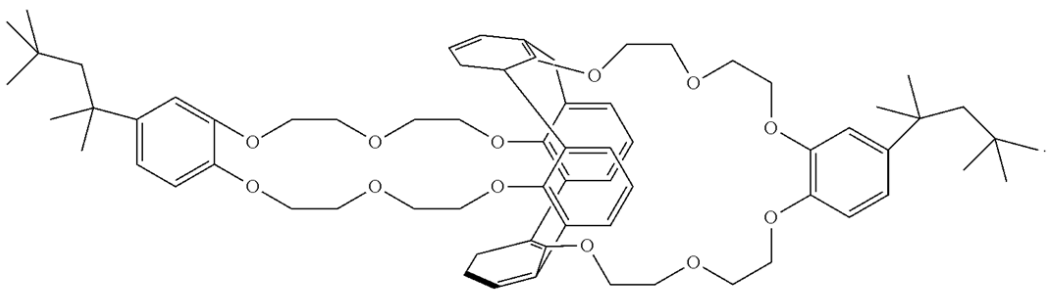

Figure 1.17: Calixarene crown ether extractant for selective Cs removal from alkaline solutions

1.3 Solid Materials for Separations at the Back End of the Nuclear Fuel Cycle

Currently, most commercial or proposed reprocessing of used nuclear fuel is performed using solvent extraction techniques, many of which are described above. However, use of solid sorbent materials as an alternative to solvent extraction has many advantages. These include the avoidance of organic solvents (which removes problems associated with chemical and radiolytic degradation of the diluent such as reduced performance and secondary waste generation),[28,69] faster kinetics in many cases,[63] the fact that the extractant molecule does not need to be designed to be soluble in an organic phase or obey the CHON principle, a phase modifier is never required and there is no possibility of third phase formation. Thus, using solid sorbent materials reduces the complexity of reprocessing relative to solvent extraction, which in turn reduces the time and cost required. In addition, the complexity necessarily introduced when designing a solvent extraction process can sometimes have negative consequences to the separation performance. For example, adding long chain alkyl groups to extractants in order to increase their solubility in organic diluents can make them more susceptible to protonation,[47] reduce their extraction efficiency[41] or cause undesirable aggregation at the solvent interface during extraction.[33] One final advantage of solid phase materials as sorbents for nuclear separations is that after loading with radionuclides the material can potentially be used as a wasteform precursor or transmutation matrix. Thus the time and cost associated with the extra processing steps of stripping and oxide conversion can be avoided.

It was therefore of interest to incorporate the active groups of extractants currently used in solvent extraction processes into solid-phase materials in order to produce sorbent materials for separations relevant to nuclear fuel reprocessing. Many such materials have been reported previously, in which the extractant ligand is impregnated or coated onto solid support structures such as polymer resins, porous silica, polymer membranes, metal oxide particles, clays, carbon-based materials or magnetic nanoparticles.[17,70,71] However, there are very few examples of solid phase materials used for nuclear separations at industrial or pilot scales.[72] Selected examples of materials with extractant ligands impregnated in polymer resins, silica or carbon materials are given in Table 1.1.[70]

Table 1.1: Solid-phase extractants used for preconcentration of An and Ln.[70,73]

Impregnation Extractant	Solid support	Recovered Elements	Conditions
TBP	Amberlite XAD-7	U(VI), Pu(IV), Am(III)	4 M HNO_3
	styrene-divinylbenzene copolymer	U(VI)	5.5 M HNO_3
	silica	Pu(IV), Am(III), Eu(III)	3 M HNO_3
	cellulose	U(VI), Th(IV)	2 M HNO_3
CMPO	Amberlite XAD-4 + XAD-7	U(VI), Am(III), Nd(III)	3 M HNO_3
	silica	U(VI), Pu(IV), Eu(III), Th(IV)	3 M HNO_3
	styrene-divinylbenzene copolymer in silica	Am(III), Cm(III)	3 M HNO_3
	polyacrylonitrile	U(VI), Pu(IV), Am(III), Eu(III)	0.1-5 M HNO_3
TOPO	C18-silica	U(VI)	0.5 M HNO_3
TODGA	silica	U(VI), Th(IV), Am(III), Cm(III)	3 M HNO_3
	Amberchrom CG-71	U(VI), Pu(IV), Am(III)	3 M HNO_3
	polypropylene fiber	Am(III), Ln(III)	3 M HNO_3
DEDT-DPA	polyacrylonitrile fiber	U(VI), Pu(IV), Am(III), Eu(III)	2-6 M HNO_3
p-butylcalix[4]arene	silica gel	U(VI)	pH 6
D2EHPA	Amberlite XAD-7	Ln(III)	pH 3.5
	Teflon	Ln(III)	pH 2-3
carboxylic acids	carbon	U(VI), Th(IV)	pH 1-2

In order to develop a sorbent material for nuclear separations, several factors must be considered. For example, sorbents for selective separation of targeted elements from highly acidic aqueous solutions of irradiated nuclear fuel should preferably exhibit favourable hydrolytic and radiolytic stability, as well as chemical stability. It is considered preferable for solid phase sorbents to have open, porous structures in order to provide high surface areas which result in more active sites per gram of material (high capacity) and facilitate rapid mass transport (fast kinetics).[74] In order for a solid phase sorbent to be practically useful in a flow-through column setup, it should also have a granular physical form with a particle size large enough to prevent issues with loss of pressure and clogging.[75]

1.3.1 Silica Based Sorbents

Many examples exist of organic extractant molecules from solvent extraction processes being incorporated into silica based solid sorbent materials. Some examples were given in Table 1.1. The relative ease of porous silica synthesis has led to a variety of silica based sorbent materials being used for nuclear separations, including porous silica loaded with extractant impregnated polymers,[76] functionalised via silanes[77] or magnetised via

incorporation of iron oxide.[78] However, silica based materials are not ideal for separations in a nuclear context as they demonstrate relatively poor hydrolytic[79] and radiolytic[80] stability.

Extractants including but not limited to BTP, TODGA, CMPO, DTPA have been impregnated into styrene-divinylbenzene polymer which is in turn embedded into porous silica particles to make sorbent materials (SiO_2-P) for selective MA extraction or separation of Ln and An from simulated high level waste.[69,72,81-83] Calix[4]arene-crown impregnated SiO_2-P materials have also been developed for selective Cs extraction from nitric acid solutions.[26] These materials were able to perform the desired separations, for example *i*Bu-BTP impregnated SiO_2-P achieved K_d(Am) ~ 20,000 and $SF_{Am/Gd}$ ~70 from 3 M nitric acid[70a] and CMPO impregnated SiO_2-P achieved K_d(Ln) ~ 50 with selectivity (SF > 50) over Na, K, Cs, Sr, Ba and Ru.[69] However, since the extractants are anchored to the solid via intermolecular forces only in these materials, the extractant leaks relatively easily from the solid sorbent material. For example, treating TODGA/SiO_2-P with 3 M nitric acid at 80 ^oC for 100 h or irradiation with 3 MGy gamma dose decreased the amount of neodymium (Nd) sorbed by this material by more than half.[82] Similar decreases in sorption capacity upon gamma irradiation were seen for CMPO/SiO_2-P.[72]

More sophisticated solid phase materials for separations can be synthesised by functionalisation of silica based framework materials via covalent silane anchor groups.[77,84,85] These silica framework materials have previously been synthesised with ordered or disordered porosity. Several carboxylate and phosphonate functionalised disordered porous silica materials have been shown to extract Ln from pH 3-6 aqueous solutions.[86] These materials were then fused via heat treatment to immobilise the Ln ions within the structure and produce a glass wasteform. Silica gel functionalised with carboxylate appended macrocycles has also been show to successfully decontaminate solutions of U, Pu and Am[87] and malonamide functionalised mesoporous silica has been shown to extract Pu(IV) > Am(III) ~ Ln(III) from 3.5 M nitric acid.[88]

Functionalised ordered porous silica frameworks have been synthesised in the form of 'self-assembled monolayers on mesoporous supports' (SAMMS, Figure 1.18) and used for separation of radionuclides present in used nuclear fuel.[89-92] For example, a silica SAMMS functionalised with acetamide phosphonate was shown to extract Eu(III) from 3 M nitric acid with K_d ~200 and selectivity over divalent transition metal cations as well as K and Ca at pH 2.[91] This same material was shown to extract Pu(IV) from 0.1 M nitric acid/1 M sodium nitrate with K_d ~20,000 and selectivity over a variety of di, tri and tetravalent metal cations.[92] In addition, silica SAMMS functionalised with hydroxypyridinones were able to selectively extract Pu(IV) and U(VI) from acidic solutions.[89] Pu(IV) was extracted from 0.1 M nitric acid/1 M sodium nitrate with K_d ~80,000 and selectivity over Fe, Al, Zr and Mo, while U(VI) was extracted from 0.2 M nitric acid with K_d ~4000 (selectivity not reported). However, self-assembled monolayers of organosilanes on silica surfaces have been shown to undergo radiolysis upon gamma doses of 500 kGy.[93]

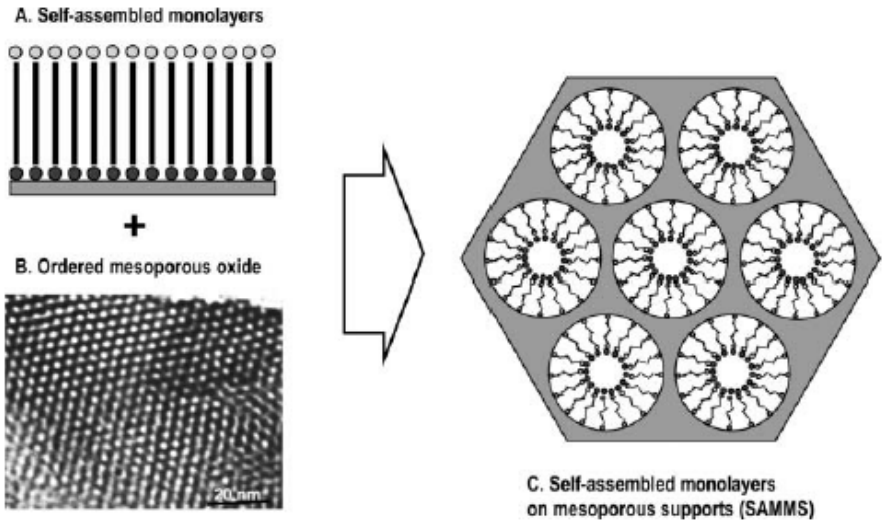

Figure 1.18: Self-assembled monolayers on mesoporous supports (SAMMS)[91]

Magnetic nanoparticles are another alternative solid phase sorbent that has been investigated for separations at the back end of the nuclear fuel cycle, as they allow easy separation of the solid and liquid phases using magnetic fields.[78] Magnetic silica particles, consisting of iron oxide in porous silica, coated in starburst dendrimers with terminal amino groups were functionalised with CMPO, picolinamide or DGA ligands to produce materials for MA-Ln separations from pH 1 nitric acid.[94] The picolinamide functionalised particles performed poorly at this low pH, but CMPO and DGA functionalised materials afforded K_d(Am) of 80 or 200 and $SF_{Am/Eu}$ 2 or 0.4, respectively. Another example of dendrimer coated magnetic silica particles functionalised with tripodal CMPO ligands showed the opposite selectivity under the same sorption conditions; Eu was extracted preferentially over Am, with K_d(Am) 60 and $SF_{Am/Eu}$ 0.3.[95]

1.3.2 Polymer Resins

Extraction chromatographic resins consisting of extractant molecules immobilised in non-reactive macroporous polymer supports have also been widely adopted for separations at the back end of the nuclear fuel cycle,[72] although they are more commonly used for analytical purposes than full-scale processing due to their chemical instability.[34] An example of an extraction chromatographic resin being used for processing of used nuclear fuel solutions is the Plutonium and Uranium Recovery On CHROMatographic EXtraction columns (PUROCHROMEX) process. This is a solid phase version of the PUREX process whereby light water reactor fuel dissolved in 5-6 M nitric acid is passed through a silica column followed by three columns consisting of 60 wt% TBP in polystyrene-divinylbenzene copolymer beads.[72] The major concern with this process was the hydrolytic and radiolytic instability of the polymeric sorbents.

Extractant molecules may either be impregnated into polymer resins via intermolecular forces or covalent attachment. Covalent attachment of extractant ligands to the polymer

support may be considered preferable as it minimises loss of the extractant during processing, but the alternative of physical impregnation is a simpler and more versatile option.[96] Some examples of impregnated materials were given in Table 1.1. In addition to this list, Cyanex 301 has been impregnated into various polymers including an alginate biopolymer,[72] styrene-divinylbenzene resins XAD-4 and Chromosorb 102, and acrylic ester resin XAD-7.[96] A transuranic specific (TRU Spec) resin composed of CMPO and TBP impregnated in Amberchrom CG-71 acrylic ester resin beads has demonstrated extraction of Pu(IV) and Np(IV) with K_d ~10^5, Th(IV) with K_d ~10^4, U(VI) with K_d ~10^3 and Am(III) with K_d ~10^2 from 1-4 M nitric acid.[97] Selectivity over Tc(VII) and Fe(III) in this acidity range was also demonstrated. CMPO has also been impregnated into several other polymer matrices including polyacrylonitrile (PAN), polyacrylate and polystyrene and the sorption performance of the resulting materials investigated.[96] The differing extraction efficiencies and sorption kinetics of these various CMPO impregnated materials demonstrated that the choice of polymer matrix can have a significant impact on sorption performance, which can be attributed to differences in the porosity and functionality of the polymer frameworks. TODGA impregnated into Amberchrom CG-71 resin beads demonstrated extraction of Pu(IV), Th(IV), Am(III) and Ln(III) from 1-4 M nitric acid with K_d 10^3-10^4 and equilibrium was reached within 10 minutes.[98] Hydrolytic stability and selectivity over Sr(II), Fe(III) and Al(III) was also demonstrated for this resin, but selectivity over Zr(IV) was poor from 4 M nitric acid.

In terms of covalently functionalised polymer resins, Merrifield chloromethylated styrene-divinylbenzene resin has been covalently modified with CMPO and the resulting material was able to sorb Ln with K_d ~100 as well as U(VI) and Th(IV) with K_d ~1000 from 4 M nitric acid within 10 minutes.[99] Separation of these elements was then possible using various eluents. Other examples of covalently functionalised polymer resins for sorption of An and Ln from concentrated nitric acid solutions include malonamide and phosphonic acid functionalised polystyrene.[96] The commercial resin Diphonix, which is a styrene-divinylbenzene sulfonated ion exchange resin containing gem-diphosphonic acid groups (Figure 1.19), has been shown to be able to extract U(VI), Th(IV), Pu(IV), Np(V) and Am(III) with K_d values greater than 100 from 0.1-10 M nitric acid.[100] The demonstrated ability of Diphonix to extract An from highly acidic solutions was attributed to the presence of the diphosphonic acid groups.

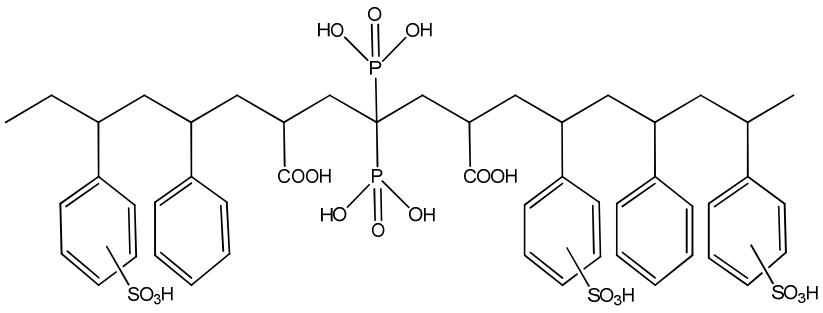

Figure 1.19: Structure of the commercially available Diphonix resin, used for An sorption[101]

Gamma irradiation of some polymer resins, including Diphonix, with 0.25-2 MGy in nitric acid was observed to decrease their efficiency or capacity. However, the kinetics of sorption by the polymer resins were relatively unaffected by gamma irradiation, while silica based sorbents that were also evaluated exhibited both decreased efficiency and kinetics of sorption upon irradiation.[102]

1.3.3 Metal Oxide Materials

Group IV metal oxides such as titania and zirconia demonstrate superior hydrolytic and radiolytic stability to silica and polymer based materials[102,103] and are therefore preferable as framework materials for separations in a nuclear context. Titania or zirconia based sorbents could also potentially be used, post-sorption, for waste immobilisation or as transmutation matrices.[104] As wasteforms, titania or zirconia based ceramics may be considered superior to vitrified silica as they are more leach resistant.[105,106] Other advantages of titania and zirconia include ready availability, cost effectiveness and non-toxicity.

Organo-functionalised group IV metal oxide sorbent materials are substantially less common than their silica or polymer resin counterparts, but examples do exist.[103,107-110] In most cases the desired functional group is anchored to the surface by ionic bonding of phosphate, phosphonate or carboxylate groups.[85,111] This surface complexation process is shown in Figure 1.20 for a phosphate group. Phosphate or phosphonate groups are considered preferable to carboxylate groups as they bind to titania and zirconia with superior strength and selectivity.[103,107,112] However, grafting of monophosphonate groups has relatively little utility unless the phosphonate provides unbound groups for potential binding to metal cations. Therefore, polyphosphonate functionalised metal(IV) oxide materials have been developed. These materials have the potential to offer strong surface anchoring via multiple phosphonate groups but at the same time free phosphonate or other functional groups useful for cation binding.[103] It has also been shown that polyphosphonates bound to zirconia surfaces mitigate leaching of framework elements.[113]

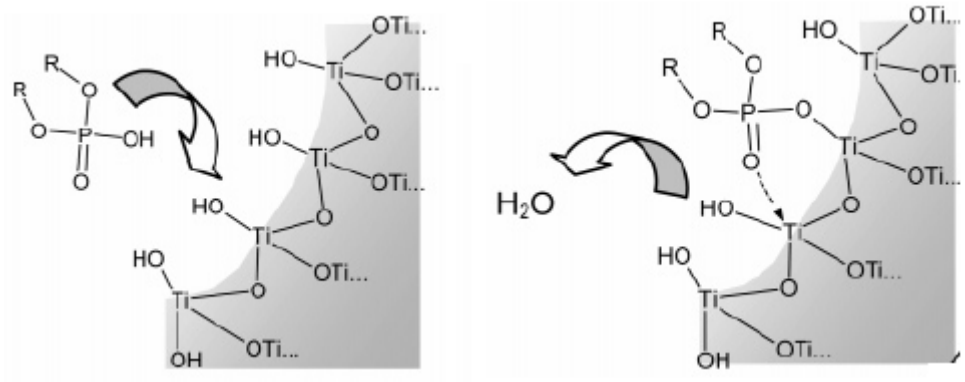

Figure 1.20: Post synthetic grafting of phosphate to a titania surface.[114]

Post synthetic grafting of functional groups to metal oxide surfaces has the disadvantage that the limited surface functionality of the metal oxide materials limits the capacity of the material for the functional group and hence for the species of interest to be sorbed. In many cases even monolayer coverage cannot be achieved, particularly for bulk materials, due to inaccessibility of the pores to the grafting molecule and/or pore blockage by strong grafting groups.[114,115] An alternative method of synthesis for functionalised metal oxide materials is co-condensation of the metal oxide and functional group such that the functional group is incorporated into the structure of the material. Via this strategy, if the molar ratio of the functional group ligand to Zr or Ti is greater than 1, a large number of available functional groups should be produced which are able to bind metal cations from solution. For example, titanium phosphate or zirconium phosphate-phosphonate materials synthesised by co-condensation have been shown to efficiently extract U from nitric acid solutions with pH ≥ 1[116] and to extract Pu, Np and Nd from pH 2 nitric acid.[110] Also, titanium and zirconium organophosphonates synthesised using diethylene triamine pentamethylene phosphonate (Figure 1.21) have demonstrated extraction of Th(IV), U(VI) and to a lesser extent Ln(III) from 0.2 M nitric acid.[117]

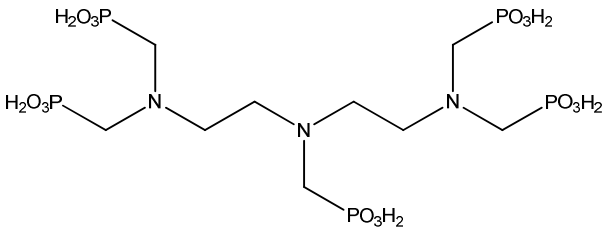

Figure 1.21: Diethylene triamine pentamethylene phosphonate used for functionalization of titania and zirconia to produce sorbent materials

Independent of their synthesis method, all phosphonate functionalised metal oxide materials suffer the disadvantage that under strongly acidic conditions, such as are required for nuclear reprocessing, some phosphonate groups are cleaved from the surface of titania and zirconia materials.[118] As an alternative, covalent attachment of an organic extractant to the surface of titania or zirconia via a long-chain alkene that self-assembles on the surface[119] should result in Ti-O-C or Zr-O-C bonds that are impervious to hydrolytic cleavage. Also, using a direct covalent linkage via an alkene should allow closer, more ordered packing and hence higher loading of the organic extractant, relative to phosphonate groups which have a large surface area (0.25 nm^2) that impedes close packing.[120] However, no known examples exist of covalent functionalization of chemically stable titania or zirconia with extractant ligands for nuclear separations. Therefore, this is a major aim of the current work.

1.4 Environmental Remediation

Recovery of radionuclides such as An from nuclear and industrial wastewater either before or after release into the environment is another important and topical area of research due to their radioactivity which is often coupled with heavy metal toxicity.[77,121,122] Typically solid phase sorbent materials are more effective for preconcentration or analysis of dilute environmental radionuclide solutions than solvent extraction.[17] Solvent extraction processes are impractical for environmental cleanup due to the large volumes of aqueous solutions involved as well as the requirement to perform the separation 'on-site'.

An investigation of An and Ln removal from freshwater and seawater environments using conventional ion exchange and chelating resins versus SAMMS and nanoporous manganese dioxide particles showed that 3,4-hydroxypyridinone functionalised SAMMS and small manganese dioxide particles exhibited the most consistent high efficiency sorption.[122] Many polymeric resins for An and Ln separation from environmental samples have also been developed.[96,123,124] For example, the Dipex resin is a commercially available extraction chromatographic resin consisting of bis(2-ethylhexyl)methane-diphosphonic acid impregnated into Amberchrom CG-71ms acrylic ester resin beads which can effectively extract An including U(VI), Th(IV), Pu(IV) and Am(III) from chloride solutions with varying acidity.[123] Selectivity for Am(III) over potential interfering cations such as Fe(III) and Al(III) was also demonstrated by this resin. Several carbon-based nanomaterials have also been investigated for environmental remediation of radionuclides.[83] Finally, a variety of sorbent materials, including functionalised mesoporous silica,[125,126] metal-organic frameworks (MOFs)[127], ion-exchange and chelating resins[128] have been investigated specifically for U extraction.

1.5 Overview of Thesis

This thesis will describe the development of hybrid inorganic-organic materials that are able to selectively remove specific target elements from solutions of used nuclear fuel in nitric acid. Justification for the development of solid phase sorbent materials rather than the presently predominant technology of solvent extraction is provided in *section 1.3*. The metal oxides titania and zirconia were chosen as the inorganic framework materials for these hybrid solid phase sorbent materials due to their enhanced radiolytic and hydrolytic stability relative to silica or polymer based materials.[102,103] This chemical stability is essential for separations in a nuclear context. Functionalisation of the titania and zirconia framework materials with organic ligands, in order to impart selectivity for metal species of interest at the back end of the nuclear fuel cycle, will then be performed and the sorption properties of the resulting hybrid materials described. The elements targeted for separation from solutions of used nuclear fuel include An and Ln. Actinides are targets for removal as they are the main contributors to the hazards of used nuclear fuel and they can be recycled. Lanthanides are targets for removal because they must be separated from MA to enable MA transmutation and Ln are also highly valuable for other applications such as electronics and catalysis.[24]

Generally, the organic ligands chosen for functionalization will be based on extractants used in known solvent extraction processes. For example, a ligand based on TBP will be used to functionalise a material designed for selective U sorption. Two different types of functionalization will be investigated; functionalisation via co-condensation of organic ligands with zirconia (*Chapter 3*) and covalent functionalization via self-assembly of organic ligands on titania surfaces followed by post-synthetic grafting (*Chapters 4, 5 and 7*). Functionalisation via co-condensation is explored because this method of functionalization allows a large number of functional groups to be introduced. This is expected to result in materials with a high capacity for the targeted element. On the other hand, covalent functionalization via post-synthetic grafting is investigated as the C-O-metal bonds created should provide chemical stability as well as access to a wide range of functional groups.

Titania nanoparticles will be used initially as the framework material for post-synthetic covalent functionalization, to provide proof-of concept. These nanoparticles will be functionalized with different organic ligands depending on the element targeted for separation; an amine or phosphate for U (*Chapter 4*), peptide for Ln (*Chapter 5*) and picolinamide or BTP for the more challenging MA-Ln separation (*Chapters 4 and 7*). Sorption behavior in nitric acid solutions of varying pH will be explored for all of these organo-functionalised titania nanoparticle materials in order to determine whether the functionalization imparts selectivity for the targeted element.

More complex titania framework materials with hierarchical and/or ordered porosity will then be prepared and functionalized. Introduction of ordered mesoporosity into titania powders will first be developed then translated into synthesis of titania beads as this is a more practical morphology for packing of chromatographic columns (*Chapter 6*). Finally, a comparison of the selectivity, capacity and kinetics of sorption using titania nanoparticles versus porous titania beads functionalized with the same BTP ligand will be performed (*Chapter 7*). This will determine whether the more complex inorganic framework produces materials with improved sorption properties.

1.6 References

(1) van der Walt, T. N.; Coetzee, P. P. *Radiochim. Acta* **2004**, *92*, 251.

(2) Hang, T. *Ion Exchange Modelling of Crystalline Silicotitanate (Ionsiv IE-911) Column for Cesium Removal from Argentine Waste (U)*, Westinghouse Savannah River Company, 2003.

(3) Hladik, O.; Bernhard, G.; Boessert, W.; Grahnert, T.; Munze, R. *Appl Radiat Isotopes* **1987**, *38*, 619.

(4) Crouse Jr., D. J. B., K.B. *Industrial and Engineering Chemistry* **1959**, *51*, 1461.

(5) Nasab, M. E.; Sam, A.; Milani, S. A. *Hydrometallurgy* **2011**, *106*, 141.

(6) International Atomic Energy Agency, I. *Uranium Extraction Technology*, 1993.

(7) Greenland, P. T. *Contemp Phys* **1990**, *31*, 405.
(8) International Atomic Energy Agency, I. *Spent Fuel Reprocessing Options*, 2008.
(9) International Atomic Energy Agency, I. *Energy, Electricity and Nuclear Power Estimates for the Period up to 2050*, 2014.
(10) International Atomic Energy Agency, I. *Climate Change and Nuclear Power*, IAEA, 2009.
(11) Feiveson, H. M., Z.; Ramana, M.V.; von Hippel, F. *Managing Spent Fuel from Nuclear Power Reactors: Experience and Lessons from Around the World*, The International Panel on Fissile Materials (IPFM), 2011.
(12) Bates, E. A.; Driscoll, M. J.; Lester, R. K.; Arnold, B. W. *Energ Policy* **2014**, *72*, 186.
(13) Kugo, A.; Yoshikawa, H.; Shimoda, H.; Wakabayashi, Y. *J Nucl Sci Technol* **2005**, *42*, 755.
(14) Poumadere, M.; Bertoldo, R.; Samadi, J. *Wires Clim Change* **2011**, *2*, 712.
(15) International Atomic Energy Agency, I. *Implications of Partitioning and Transmutation in Radioactive Waste Management*, IAEA, 2004.
(16) Paiva, A. P.; Malik, P. *J. Radioanal. Nucl. Chem.* **2004**, *261*, 485.
(17) Hudson, M. J.; Harwood, L. M.; Laventine, D. M.; Lewis, F. W. *Inorganic Chemistry* **2013**, *52*, 3414.
(18) Khodarev, E. *IAEA Bulletin* **1978**, *20*, 29.
(19) Salvatores, A. *Nucl Eng Des* **2005**, *235*, 805.
(20) Nilsson, M.; Nash, K. L. *Solvent Extr. Ion Exch.* **2007**, *25*, 665.
(21) Modolo, G.; Wilden, A.; Geist, A.; Magnusson, D.; Malmbeck, R. *Radiochim. Acta* **2012**, *100*, 715.
(22) Lewis, F. W.; Hudson, M. J.; Harwood, L. M. *Synlett* **2011**, 2609.
(23) Puchy, B. *Briefing Paper: Rare Earth Elements*, Department of Environmental Quality, 2011.
(24) Jordens, A.; Cheng, Y. P.; Waters, K. E. *Miner Eng* **2013**, *41*, 97.
(25) Nash, K. L. *Solvent Extr. Ion Exch.* **1993**, *11*, 729.
(26) Zhang, A. Y.; Chai, Z. F. *Ind Eng Chem Res* **2012**, *51*, 6196.
(27) International Atomic Energy Agency, I. *Feasibility of Separation and Utilization of Caesium and Strontium from High Level Liquid Waste*, IAEA, 1993.
(28) Kolarik, Z. *Chemical Reviews* **2008**, *108*, 4208.
(29) Mincher, B. J.; Mezyk, S. P.; Martin, L. R. *J Phys Chem A* **2008**, *112*, 6275.
(30) Manchanda, V. K.; Pathak, P. N. *Sep. Purif. Technol.* **2004**, *35*, 85.
(31) Olander, D. *J Nucl Mater* **2009**, *389*, 1.
(32) Tkac, P.; Paulenova, A. *Separation Science and Technology* **2008**, *43*, 2670.
(33) Dam, H. H.; Reinhoudt, D. N.; Verboom, W. *Chemical Society Reviews* **2007**, *36*, 367.
(34) Mathur, J. N.; Murali, M. S.; Nash, K. L. *Solvent Extr. Ion Exch.* **2001**, *19*, 357.
(35) Horwitz, E. P.; Kalina, D. G.; Diamond, H.; Vandegrift, G. F.; Schulz, W. W. *Solvent Extr. Ion Exch.* **1985**, *3*, 75.

(36) Dam, H. H.; Reinhoudt, D. N.; Verboom, W. *New Journal of Chemistry* **2007**, *31*, 1620.

(37) Rudzevich, V.; Schollmeyer, D.; Braekers, D.; Desreux, J. F.; Diss, R.; Wipff, G.; Bohmer, V. *Journal of Organic Chemistry* **2005**, *70*, 6027.

(38) Peters, C.; Braekers, D.; Kroupa, J.; Kasyan, O.; Miroshnichenko, S.; Rudzevich, V.; Bohmer, V.; Desreux, J. F. *Radiochim. Acta* **2008**, *96*, 203.

(39) Ansari, S. A.; Pathak, P.; Mohapatra, P. K.; Manchanda, V. K. *Sep. Purif. Rev.* **2011**, *40*, 43.

(40) Iqbal, M.; Huskens, J.; Verboom, W.; Sypula, M.; Modolo, G. *Supramol Chem* **2010**, *22*, 827.

(41) Matloka, K.; Gelis, A.; Regalbuto, M.; Vandegrift, G.; Scott, M. J. *Separation Science and Technology* **2006**, *41*, 2129.

(42) Janczewski, D.; Reinhoudt, D. N.; Verboom, W.; Hill, C.; Allignol, C.; Duchesne, M. T. *New Journal of Chemistry* **2008**, *32*, 490.

(43) Gruner, B.; Kvicalova, M.; Selucky, P.; Lucanikova, M. *Journal of Organometallic Chemistry* **2010**, *695*, 1261.

(44) Mikulasek, L.; Gruner, B.; Danila, C.; Bohmer, V.; Caslavsky, J.; Selucky, P. *Chem Commun* **2006**, 4001.

(45) Wu, L.; Fang, Y. Y.; Jia, Y. M.; Yang, Y. Y.; Liao, J. L.; Liu, N.; Yang, X. S.; Feng, W.; Ming, J. L.; Yuan, L. H. *Dalton T* **2014**, *43*, 3835.

(46) Romanovskiy, V. N.; Smirnov, I. V.; Babain, V. A.; Todd, T. A.; Herbst, R. S.; Law, J. D.; Brewer, K. N. *Solvent Extr. Ion Exch.* **2001**, *19*, 1.

(47) Ekberg, C.; Fermvik, A.; Retegan, T.; Skarnemark, G.; Foreman, M. R. S.; Hudson, M. J.; Englund, S.; Nilsson, M. *Radiochim. Acta* **2008**, *96*, 225.

(48) Drew, M. G. B.; Hill, C.; Hudson, M. J.; Iveson, P. B.; Madic, C.; Vaillant, L.; Youngs, T. G. A. *New Journal of Chemistry* **2004**, *28*, 462.

(49) Babain, V. A. A., M.Y.; Smirnov, I.V.; Shadrin, A.Y. *Radiochemistry* **2006**, *48*, 369.

(50) Casnati, A.; Della Ca', N.; Fontanella, M.; Sansone, F.; Ugozzoli, F.; Ungaro, R.; Liger, K.; Dozol, J. F. *European Journal of Organic Chemistry* **2005**, 2338.

(51) Macerata, E.; Sansone, F.; Baldini, L.; Ugozzoli, F.; Brisach, F.; Haddaoui, J.; Hubscher-Bruder, V.; Arnaud-Neu, F.; Mariani, M.; Ungaro, R.; Casnati, A. *European Journal of Organic Chemistry* **2010**, 2675.

(52) Zhu, Y. J.; Chen, J.; Jiao, R. Z. *Solvent Extr. Ion Exch.* **1996**, *14*, 61.

(53) Bhattacharyya, A.; Mohapatra, P. K.; Manchanda, V. K. *Solvent Extr. Ion Exch.* **2006**, *24*, 1.

(54) Chen, J.; Zhu, Y. J.; Jiao, R. Z. *Separation Science and Technology* **1996**, *31*, 2723.

(55) Peterman, D. R.; Greenhalgh, M. R.; Tillotson, R. D.; Klaehn, J. R.; Harrup, M. K.; Luther, T. A.; Law, J. D. *Separation Science and Technology* **2010**, *45*, 1711.

(56) Daly, S. R.; Keith, J. M.; Batista, E. R.; Boland, K. S.; Clark, D. L.; Kozimor, S. A.; Martin, R. L. *J. Am. Chem. Soc.* **2012**, *134*, 14408.

(57) Modolo, G.; Odoj, R. *Solvent Extr. Ion Exch.* **1999**, *17*, 33.

(58) Zalupski, P. R.; Ensor, D. D.; Riddle, C. L.; Peterman, D. R. *Solvent Extr. Ion Exch.* **2013**, *31*, 430.

(59) Nilsson, M.; Nash, K. L. *Solvent Extr. Ion Exch.* **2009**, *27*, 354.

(60) Mincher, B. J.; Modolo, G.; Mezyk, S. P. *Solvent Extr. Ion Exch.* **2010**, *28*, 415.

(61) Kolarik, Z.; Mullich, U.; Gassner, F. *Solvent Extr. Ion Exch.* **1999**, *17*, 1155.

(62) Hudson, M. J.; Boucher, C. E.; Braekers, D.; Desreux, J. F.; Drew, M. G. B.; Foreman, M. R. S.; Harwood, L. M.; Hill, C.; Madic, C.; Marken, F.; Youngs, T. G. A. *New Journal of Chemistry* **2006**, *30*, 1171.

(63) Hubscher-Bruder, V.; Haddaoui, J.; Bouhroum, S.; Arnaud-Neu, F. *Inorganic Chemistry* **2010**, *49*, 1363.

(64) Geist, A.; Hill, C.; Modolo, G.; Foreman, M. R. S. J.; Weigl, M.; Gompper, K.; Hudson, M. J. *Solvent Extr. Ion Exch.* **2006**, *24*, 463.

(65) Magnusson, D.; Christiansen, B.; Foreman, M. R. S.; Geist, A.; Glatz, J. P.; Malmbeck, R.; Modolo, G.; Serrano-Purroy, D.; Sorel, C. *Solvent Extr. Ion Exch.* **2009**, *27*, 97.

(66) Lewis, F. W.; Harwood, L. M.; Hudson, M. J.; Drew, M. G. B.; Desreux, J. F.; Vidick, G.; Bouslimani, N.; Modolo, G.; Wilden, A.; Sypula, M.; Vu, T. H.; Simonin, J. P. *J. Am. Chem. Soc.* **2011**, *133*, 13093.

(67) Harmon, B. W.; Ensor, D. D.; Delmau, L. H.; Moyer, B. A. *Solvent Extr. Ion Exch.* **2007**, *25*, 373.

(68) Raut, D. R.; Mohapatra, P. K.; Ansari, S. A.; Manchanda, V. K. *Separation Science and Technology* **2009**, *44*, 3664.

(69) Zhang, A. Y.; Hu, Q. H.; Wang, W. H.; Kuraoka, E. *Ind Eng Chem Res* **2008**, *47*, 6158.

(70) Mokhodoeva, O. B. M., G.V.; Zakharchenko, E.A. *Radiochemistry* **2011**, *53*, 35.

(71) Ding, C. C.; Cheng, W. C.; Sun, Y. B.; Wang, X. K. *Dalton T* **2014**, *43*, 3888.

(72) Tranter, T. J. In *Advanced Separation Techniques for Nuclear Fuel Reprocessing and Radioactive Waste Treatment*; Nash, K. L. L., G.J, Ed.; Woodhead Publishing Limited: Cambridge, 2011.

(73) Kamenik, J. *Czech J Phys* **2006**, *56*, D493.

(74) Lehman, S. E.; Larsen, S. C. *Environ-Sci Nano* **2014**, *1*, 200.

(75) Hua, M.; Zhang, S. J.; Pan, B. C.; Zhang, W. M.; Lv, L.; Zhang, Q. X. *J Hazard Mater* **2012**, *211*, 317.

(76) Wei, Y. Z.; Zhang, A. Y.; Kumagai, M.; Watanabe, M.; Hayashi, N. *J Nucl Sci Technol* **2004**, *41*, 315.

(77) Fryxell, G. E.; Mattigod, S. V.; Lin, Y. H.; Wu, H.; Fiskum, S.; Parker, K.; Zheng, F.; Yantasee, W.; Zemanian, T. S.; Addleman, R. S.; Liu, J.; Kemner, K.; Kelly, S.; Feng, X. D. *J Mater Chem* **2007**, *17*, 2863.

(78) Kaur, M.; Zhang, H. J.; Martin, L.; Todd, T.; Qiang, Y. *Environ Sci Technol* **2013**, *47*, 11942.

(79) Iler, R. K. *The Chemistry of Silica: Solubility, Polymerisation, Colloid and Surface Properties and Biochemistry of Silica*; Wiley-Interscience: New York, 1979.

(80) Etienne, M.; Walcarius, A. *Talanta* **2003**, *59*, 1173.

(81) Hoshi, H.; Wei, Y. Z.; Kumagai, M.; Asakura, T.; Morita, Y. *Journal of Alloys and Compounds* **2006**, *408*, 1274.

(82) Zhang, A. Y.; Wei, Y. Z.; Hoshi, H.; Kumagai, M.; Kamiya, M.; Koyama, T. *Radiat Phys Chem* **2005**, *72*, 669.

(83) Shi, W. Q.; Yuan, L. Y.; Li, Z. J.; Lan, J. H.; Zhao, Y. L.; Chai, Z. F. *Radiochim. Acta* **2012**, *100*, 727.

(84) Walcarius, A.; Mercier, L. *J Mater Chem* **2010**, *20*, 4478.

(85) Soler-Illia, G. J. A. A.; Azzaroni, O. *Chemical Society Reviews* **2011**, *40*, 1107.

(86) Shkrob, I. A.; Tisch, A. R.; Marin, T. W.; Muntean, J. V.; Kaminski, M. D.; Kropf, A. J. *Ind Eng Chem Res* **2011**, *50*, 4686.

(87) Barbette, F.; Rascalou, F.; Chollet, H.; Babouhot, J. L.; Denat, F.; Guilard, R. *Anal Chim Acta* **2004**, *502*, 179.

(88) Bourg, S.; Broudic, J. C.; Conocar, O.; Moreau, J. J. E.; Meyer, D.; Man, M. W. C. *Chem Mater* **2001**, *13*, 491.

(89) Lin, Y. H.; Fiskum, S. K.; Yantasee, W.; Wu, H.; Mattigod, S. V.; Vorpagel, E.; Fryxell, G. E.; Raymond, K. N.; Xu, J. D. *Environ Sci Technol* **2005**, *39*, 1332.

(90) Yantasee, W.; Fryxell, G. E.; Addleman, R. S.; Wiacek, R. J.; Koonsiripaiboon, V.; Pattamakomsan, K.; Sukwarotwat, V.; Xu, J.; Raymond, K. N. *J Hazard Mater* **2009**, *168*, 1233.

(91) Fryxell, G. E.; Wu, H.; Lin, Y. H.; Shaw, W. J.; Birnbaum, J. C.; Linehan, J. C.; Nie, Z. M.; Kemner, K.; Kelly, S. *J Mater Chem* **2004**, *14*, 3356.

(92) Fryxell, G. E.; Lin, Y. H.; Fiskum, S.; Birnbaum, J. C.; Wu, H.; Kemner, K.; Kelly, S. *Environ Sci Technol* **2005**, *39*, 1324.

(93) Le Caer, S.; Brunet, F.; Chatelain, C.; Ladevie, L.; Durand, D.; Dauvois, V.; Renault, J. P.; Charpentier, T. *J Phys Chem C* **2013**, *117*, 23258.

(94) Gruttner, C.; Bohmer, V.; Casnati, A.; Dozol, J. F.; Reinhoudt, D. N.; Reinoso-Garcia, M. M.; Rudershausen, S.; Teller, J.; Ungaro, R.; Verboom, W.; Wang, P. S. *Journal of Magnetism and Magnetic Materials* **2005**, *293*, 559.

(95) Reinoso-Garcia, M. M.; Janczewski, D.; Reinhoudt, D. N.; Verboom, W.; Malinowska, E.; Pietrzak, M.; Hill, C.; Baca, J.; Gruner, B.; Selucky, P.; Gruttner, C. *New Journal of Chemistry* **2006**, *30*, 1480.

(96) Yang, Y. J.; Alexandratos, S. D. *Ind Eng Chem Res* **2009**, *48*, 6173.

(97) Horwitz, E. P.; Chiarizia, R.; Dietz, M. L.; Diamond, H. *Anal Chim Acta* **1993**, *281*, 361.

(98) Horwitz, E. P.; McAlister, D. R.; Bond, A. H.; Barrans, R. E. *Solvent Extr. Ion Exch.* **2005**, *23*, 319.

(99) Raju, C. S. K.; Subramanian, M. S. *J Hazard Mater* **2007**, *145*, 315.

(100) Horwitz, E. P.; Chiarizia, R.; Diamond, H.; Gatrone, R. C.; Alexandratos, S. D.; Trochimczuk, A. Q.; Crick, D. W. *Solvent Extr. Ion Exch.* **1993**, *11*, 943.

(101) Chiarizia, R.; Horwitz, E. P.; Alexandratos, S. D.; Gula, M. J. *Separation Science and Technology* **1997**, *32*, 1.

(102) Chiarizia, R.; Horwitz, E. P. *Solvent Extr. Ion Exch.* **2000**, *18*, 109.

(103) Griffith, C. S.; De Los Reyes, M.; Scales, N.; Hanna, J. V.; Luca, V. *Acs Appl Mater Inter* **2010**, *2*, 3436.

(104) Gregg, D. J.; Karatchevtseva, I.; Triani, G.; Lumpkin, G. R.; Vance, E. R. *J Nucl Mater* **2013**, *441*, 203.

(105) Donald, I. W.; Metcalfe, B. L.; Taylor, R. N. J. *J Mater Sci* **1997**, *32*, 5851.

(106) Leturcq, G.; Advocat, T.; Hart, K.; Berger, G.; Lacombe, J.; Bonnetier, A. *Am Mineral* **2001**, *86*, 871.

(107) HailuTaffa, D.; Kathiresan, M.; Walder, L. *Langmuir* **2009**, *25*, 5371.

(108) Rehor, I.; Kubicek, V.; Kotek, J.; Hermann, P.; Szakova, J.; Lukes, I. *Eur J Inorg Chem* **2011**, 1981.

(109) Shah, B.; Chudasama, U. *Desalin Water Treat* **2012**, *38*, 227.

(110) Burns, J. D.; Clearfield, A.; Borkowski, M.; Reed, D. T. *Radiochim. Acta* **2012**, *100*, 381.

(111) Clifford, J. N.; Martinez-Ferrero, E.; Viterisi, A.; Palomares, E. *Chemical Society Reviews* **2011**, *40*, 1635.

(112) Pawsey, S.; McCormick, M.; De Paul, S.; Graf, R.; Lee, Y. S.; Reven, L.; Spiess, H. W. *J. Am. Chem. Soc.* **2003**, *125*, 4174.

(113) de los Reyes, M.; Majewski, P. J.; Scales, N.; Luca, V. *Acs Appl Mater Inter* **2013**, *5*, 4120.

(114) Angelome, P. C.; Soler-Illia, G. J. D. A. A. *Chem Mater* **2005**, *17*, 322.

(115) Lim, M. H.; Stein, A. *Chem Mater* **1999**, *11*, 3285.

(116) Fouad, H. K.; Bishay, A. F. *J. Radioanal. Nucl. Chem.* **2010**, *283*, 765.

(117) Patel, P. R. C., U.V. *Desalin Water Treat* **2014**, *52*, 481.

(118) Marcinko, S.; Fadeev, A. Y. *Langmuir* **2004**, *20*, 2270.

(119) Li, B.; Franking, R.; Landis, E. C.; Kim, H.; Hamers, R. J. *Acs Appl Mater Inter* **2009**, *1*, 1013.

(120) Gao, W.; Dickinson, L.; Grozinger, C.; Morin, F. G.; Reven, L. *Langmuir* **1997**, *13*, 115.

(121) Lopes, C. B. L., P.F.; Cardoso, S.P.; Pereira, E.; Duarte, A.C.; Silva, C.M. In *Ion Exchange Technology II*; Inamuddin, M. L., Ed.; Springer Science & Business Media: New York, 2012.

(122) Johnson, B. E.; Santschi, P. H.; Chuang, C. Y.; Otosaka, S.; Addleman, R. S.; Douglas, M.; Rutledge, R. D.; Chouyyok, W.; Davidson, J. D.; Fryxell, G. E.; Schwantes, J. M. *Environ Sci Technol* **2012**, *46*, 11251.

(123) Horwitz, E. P.; Chiarizia, R.; Dietz, M. L. *React Funct Polym* **1997**, *33*, 25.

(124) Dev, K.; Pathak, R.; Rao, G. N. *Talanta* **1999**, *48*, 579.

(125) Vivero-Escoto, J. L.; Carboni, M.; Abney, C. W.; deKrafft, K. E.; Lin, W. B. *Micropor Mesopor Mat* **2013**, *180*, 22.

(126) Yuan, L. Y.; Liu, Y. L.; Shi, W. Q.; Lv, Y. L.; Lan, J. H.; Zhao, Y. L.; Chai, Z. F. *Dalton T* **2011**, *40*, 7446.

(127) Carboni, M.; Abney, C. W.; Liu, S. B.; Lin, W. B. *Chem Sci* **2013**, *4*, 2396.

(128) Phillips, D. H.; Gu, B.; Watson, D. B.; Parmele, C. S. *Water Res* **2008**, *42*, 260.

Chapter 2: General Methods

2.1 Nuclear Magnetic Resonance (NMR)

Solution NMR ^{1}H and ^{13}C spectra were recorded using a Bruker AV400 NMR Spectrometer, a Bruker Avance DPX 300 spectrometer or a Bruker Avance DPX 200 spectrometer, and were reported as parts per million (ppm) downfield shift using deuterochloroform ($CDCl_3$, δ 7.26 ppm for ^{1}H, 77.16 ppm for ^{13}C), deuteromethanol (MeOH-d_4, δ 3.31 ppm for ^{1}H, 49.00 ppm for ^{13}C), or deuterated dimethyl sulfoxide (DMSO-d_6, δ 2.50 ppm for ^{1}H) as internal references. The data are reported as chemical shift (δ), multiplicity (br = broad, s = singlet, d = doublet, t = triplet, q = quartet, dt = doublet of triplets, m = multiplet), coupling constant (*J* Hz) and relative integral.

Cross-polarised ^{13}C-^{1}H and ^{31}P-^{1}H solid-state NMR spectra were recorded on a Bruker Biospin Avance III solid state 300 MHz instrument using a Bruker 4 mm double resonance magic-angle spinning (MAS) probehead with a MAS frequency of 12 kHz. Spectral deconvolution of these one-dimensional NMR spectra was performed using GRAMS/AI™ spectroscopy software. Directly polarised ^{31}P NMR spectra, two-dimensional ^{1}H-^{31}P HetCor NMR spectra, spin relaxation (T1) experiments, ^{31}P-^{1}H recoupling experiments and ^{31}P chemical shift anisotropy (CSA) recoupling experiments were also recorded using the instrument described above as well as a Bruker Avance III solid state 700 MHz NMR spectrometer.

2.2 Mass Spectrometry

Low resolution electrospray ionization mass spectra (ESI-MS) were recorded on a 4000 QTrap AB SCIEX Mass Spectrometer or a Thermo Finnigan LCQ Deca Ion Trap mass spectrometer. High resolution mass spectra (HRMS) were recorded on a Bruker BioApex Fourier Transform Ion Cyclotron Resonance mass spectrometer (FT-ICR) with an analytical ESI source, operating at 4.7 T.

2.3 Spectroscopic Methods

2.3.1 Fourier Transform Infra-Red (FTIR) Spectroscopy

Fourier Transform Infra-Red (FTIR) spectra were obtained on a Nicolet Nexus 8700 FTIR Spectrometer (Thermo Electron Corporation) using the Smart iTR attenuated total reflection (ATR) accessory. Measurements were performed in absorbance mode from 700 – 4000 cm^{-1}, with a step size of 0.5 cm^{-1}. All spectra shown have been background subtracted. Spectral deconvolution of FTIR data was performed using GRAMS/AI™ spectroscopy software.

2.3.2 Fluorescence Spectroscopy

Fluorescence spectroscopy titrations were performed using a Cary Eclipse Fluorescence Spectrometer, typically in phosphorescence mode from 550 to 750 nm using an excitation wavelength of 345 nm, PMT voltage 800 V, excitation slit 20 nm, emission slit 5 nm, emission filter open, excitation filter on automatic. The delay time was 0.1 ms, flash count was 1, total decay time was 0.02 s and gate time was 0.01 s. The scan averaging time was 0.1 s and the data interval was 1 nm. A Savitzky-Golay smoothing factor of 5 was applied.

The fluorescence titration of LLLL-Glu-OH, without a naphthalimide tag, was performed in phosphorescence mode from 550 to 750 nm using an excitation wavelength of 282 nm (the observed absorbance peak in the uv-visible spectrum of the peptide:Eu complex). The PMT voltage was set at 800 V, excitation slit 20 nm, emission slit 10 nm, emission filter open, excitation filter on automatic. The scan averaging time was 0.03 s and the data interval was 0.5 nm. A Savitzky-Golay smoothing factor of 9 was applied.

To determine equilibrium constants from the fluorescence titration data, global analysis of the spectrophotometric data was carried out using a non-linear least-squares fitting procedure using the commercially available software program HypSpec® (Hyperquad® package). This application assumes that the spectral intensity of each chemical species is proportional to the concentration of that species in solution.

Luminescence decay rates were measured on a Cary Eclipse Fluorescence Spectrometer in phosphorescence mode using 50 cycles with an excitation wavelength of 345 nm and an emission wavelength of 592 nm. The PMT voltage was 800 V, excitation slit was 20 nm, emission slit was 10 nm, delay time was 0.1 ms, flash count was 1, total decay time was 0.005 s and gate time was 0.02 s.

2.3.3 Circular Dichroism (CD)

Circular Dichroism (CD) measurements were performed on a JASCO J-710 Spectropolarimeter. CD spectra were measured via 8 accumulations from 180 to 260 nm with a step resolution of 0.5 nm and a speed of 100 nm/min. The response time was 4 s, the bandwidth was 1 nm and the sensitivity was 50 mdeg. The CD spectrum of 10 mM HEPES buffer was measured as a blank and automatically subtracted from the spectra of the samples. Raw data was collected in units of ellipticity (mdeg) and was converted to molar ellipticity using the formula

$$[\theta] = \frac{\theta}{10cnl}$$

Where [θ] is the molar ellipticity (deg.cm^2/decimole), θ is the ellipticity (mdeg), c is the concentration of the sample (M), n is the number of peptide bonds in the sample and l is the pathlength (cm).[1] In this case the path length was 0.1 cm.

Fitting of the data to determine the alpha helix, beta sheet and random coil content of the peptides was not performed as the peptides (2-4mers) were too short to form these structures and the concentration of the solutions (30-60 µM) were too low for self-assembled structures to form.

2.4 Nitrogen Porosimetry

Nitrogen adsorption-desorption isotherms were obtained by multipoint nitrogen gas sorption experiments at 77 K after degassing at 150 °C on a Micromeritics ASAP 2020 adsorption analyser (Norcross, GA). Surface areas were estimated according to the Brunauer-Emmett-Teller (BET) method while pore volume and pore size distributions were calculated using the Barrett-Joyner-Halenda (BJH) method based on the desorption branch of the isotherm.

2.5 Electron Microscopy

2.5.1 Scanning Electron Microscopy (SEM)

Scanning electron microscopy (SEM) images were collected using a Zeiss Ultra Plus electron microscope operating at 10-15 kV. Titania beads (*Chapter 6*) were broken in half by applying gentle pressure to individual beads prior to deposition on double sided carbon tape and coating with 2-3 nm platinum, while zirconium organophosphonate powders (*Chapter 3*) and titania powders (*Chapter 4*) were simply directly applied to the carbon tape before platinum coating and imaging.

2.5.2 Transmission Electron Microscopy (TEM)

Transmission electron microscopy *(*TEM) samples consisted of crushed specimen dispersed in ethanol then dispensed onto holey carbon film supported on a TEM copper mesh grid. A JEOL 2010F operated at 200 keV was used to characterise the samples via bright field imaging and selected area electron diffraction.

2.6 X-Ray Characterisation Methods

2.6.1 X-Ray Diffraction (XRD)

X-ray diffraction (XRD) patterns were measured with a PANalytical X'Pert Pro diffractometer (Almelo, the Netherlands) using Cu Kα radiation (λ = 1.54 Á) at 40 kV and 30 mA. The data for mesoporous titania powders and beads (*Chapters 4 and 6*) were recorded from 5–80° and 10-80° respectively, with a step size of 0.02°. The data for amorphous zirconium organophosphonates (*Chapter 3*) were recorded from 0-60° while the data for the crystalline ceramic materials synthesised by sintering of Eu loaded zirconium organophosphonate materials were recorded from 5-140°, both with a step size of 0.03°. Phase identification and relative intensity ratio (RIR) calculations were performed using X-Pert HighScore software.

2.6.2 Small Angle Scattering

Titania and zirconium organophosphonate (ZrP) powder samples (*Chapters 4 and 6*) were prepared for small angle x-ray scattering (SAXS) measurements by applying a small amount of powder between two pieces of Scotch™ MagicTape or kapton tape. Titania beads (*Chapter 6*) were crushed into powder and similarly measured. Zirconium organophosphonate slurry samples in 0.1 M

nitric acid (*Chapter 3*) were also measured in kapton tape with a drop of 0.1 M nitric acid being added to the ZrP powder between the two pieces of tape. Peptide solutions (*Chapter 5*) were measured in quartz capillaries.

Most SAXS measurements were performed on a Bruker NanoSTAR SAXS camera (Bruker-AXS, Karlsruhe), with 3 pin-hole collimation for point focus geometry. The instrument source was a copper rotating anode (0.3 mm filament) operating at 45 kV and 110 mA, fitted with Montel mirrors, resulting in Cu Kα radiation of wavelength 1.54 Å. The SAXS camera was fitted with a Vantec2000 2D detector. The sample to detector distance was chosen to be 730 mm which provided a Q-range of 0.01 to 0.39 $Å^{-1}$ ($Q= (4\pi\sin\theta)/\lambda$ where 2θ is the scattering angle and λ is the wavelength of the incident X-rays).

Small angle x-ray scattering (SAXS) measurements on ZrP slurries in 0.1 M nitric acid (*Chapter 3*) and peptide solutions (*Chapter 5*) were performed at the SAXS/WAXS beamline at the Australian Synchrotron. The beamline source was an in-vacuum undulator with a 22 mm period, 3 m length and K_{max} 1.56. The operating energy was 11 keV. The beamline was fit with a cryo-cooled Si(111) double crystal monochromators as well as horizontal and vertical focussing mirrors with three mirror stripes (Si, Rh and Pt). The detector used was a Dectris – Pilatus 1 M detector of size 170 x 170 mm with 6 orders of magnitude dynamic range and a 10 Hz frame rate. The sample to detector distance was chosen to be 500 mm, which provided a Q-range of 0.02 to 1.1 $Å^{-1}$.

D-spacings for the SAXS data are reported with an error value of 10 Å as this was the maximum resolution of the instrument. All presented SAXS data were background subtracted using an appropriate blank cell (constant configuration without a sample). SAXS data of mesoporous titania precursor solutions (*Chapter 6*) was also placed on an absolute scale using the absolute intensity of water reported by Orthaber et al.[2] For mesoporous titania powder and bead samples, it was not possible to place the data on an absolute scale as the path length could not be quantitatively determined, but the amount of sample in the beam was adjusted so that transmission values were comparable between samples. Therefore the degree of order could only be treated as relative variations. Relative intensities of correlation peaks in the SAXS data were calculated based on the number of counts at the peak position divided by background counts at that position.

Guinier fitting of SAXS data was performed, using PRIMUS software,[3] to afford values for the radius of gyration (R_g) of scattering structures. The R_g is the root mean square distance of an object's parts from its centre of mass and as such gives a shape-independent indication of the size and density of an object. Fitting of SAXS data using power law, Debye, excluded volume polymer fit and various peak models was performed using SasView 2.2.0 software. Details of the fitting models used are provided below:

Guinier: Guinier analysis allows determination of the radius of gyration, R_g, because at low q the form factor of the SAXS data can be approximated by the equation:

$$I(q) = I_0 \exp\left(\frac{-R_g^2 q^2}{3}\right)$$

Therefore a plot of Ln(I(q)) against q^2 has the slope $-(R_g)^2/3$ as long as $qR_g \leq 1.3$.[4]

Debye Model: The Debye model is a form factor for a linear polymer chain given by the equation:

$$I(q) = \frac{2 \times A(e^{-x} + x - 1)}{x^2} + B$$

Where $x = (qR_g)^2$, R_g = radius of gyration (Å), A = scale and B = background (cm^{-1}).[5]

Excluded Volume Polymer Model: The excluded volume polymer model is a form factor for polymer chain conformations in which the Porod exponent, m, can vary from 1.6 to 3 rather than being limited to a value of 2. As a result, non-Gaussian polymer chains such as those with excluded volume effects or branching are also described. The fit function is given by the equation:

$$I(q) = \frac{A}{nU^{\frac{1}{2n}}}\gamma\left(\frac{1}{2n}, U\right) - \frac{1}{nU^{\frac{1}{n}}}\gamma\left(\frac{1}{n}, U\right) + B$$

Where A = scale, B = background (cm^{-1}), n = excluded volume parameter = 1/m, $U = \frac{q^2 R_g^2 (2n+1)(2n+2)}{6}$, R_g = radius of gyration (Å) and γ(x, U) is the incomplete gamma function $\int_0^U e^{-t} t^{x-1}\, dt$.[6,7]

Lorentz Peak Model: This model describes a Lorentzian shaped peak with a flat background and is given by the equation:

$$I(q) = \frac{A}{\left(1 + \left(\frac{q - q_0}{B}\right)^2\right)} + C$$

Where A = scale, q_0 = peak position ($Å^{-1}$) which is equivalent to the d-spacing or correlation length of the repeating unit, B = half-width-half-maximum of the peak ($Å^{-1}$) and C = background (cm^{-1}).

Gauss Peak Model: This model describes a Gaussian shaped peak with a flat background and is given by the equation:

$$I(q) = Aexp\left[\frac{-(q - q_0)^2}{2B^2}\right] + C$$

Where A = scale, q_0 = peak position ($Å^{-1}$) which is equivalent to the d-spacing or correlation length of the repeating unit, 2.354*B = full-width-half-maximum of the peak ($Å^{-1}$) and C = background (cm^{-1}).

Broad Peak Model: An empirical function that describes a broad shaped scattering peak on a power law background and is given by the equation:

$$I(q) = \frac{A}{q^n} + \frac{B}{1 + \left((q - q_0)\xi\right)^m} + C$$

Where A = scale for the power law function, B = scale for the broad peak function, C = background (cm^{-1}), n = exponent of the power law function, m = exponent of the broad peak function which controls the peak shape (if m = 2 peak is Lorentzian in shape), q_0 = peak position ($Å^{-1}$) which is equivalent to the d-spacing or correlation length of the repeating unit and ξ = peak width (Å).

2.6.3 X-Ray Absorption Spectroscopy (XAS)

The extended x-ray absorption fine structure (EXAFS) spectrum from any element in a sample is the absorption spectrum above the energy of the absorption edge. Detailed discussion of EXAFS theory will not be provided here, but can be found in 'X-Ray Absorption' by Koningsberger and Prins (1988).[8] As x-rays are absorbed by the atoms of the targeted element, in this case Zr, photoelectrons are emitted and scatter from the surrounding atoms. The interference of these scattering photoelectrons with each other produces the oscillating signal in the absorption spectrum, which contains information about the type, number and distances of the atoms surrounding the absorbing atom.

Extended x-ray absorption fine structure (EXAFS) measurements at the Zr *K* edge were performed at the Australian National Beamline Facility (ANBF) within the Photon Factory at Tsukuba, Japan. Energy selection was accomplished using a water cooled monochromators with Si(111) crystals. Harmonic rejection was achieved by 50% detune on the second crystal. Measurements were performed in transmission mode at 20 K with Oken ionisation chambers used as detectors. The absorption spectrum of Zr foil was recorded as an energy calibration at the same time as sample spectra were collected. The energy of a monoclinic zirconia standard was calibrated by assigning the maximum inflection point of the Zr *K* edge in a monoclinic zirconia standard as 17998 eV. The EXAFS spectra of all the zirconium organophosphonate samples were then aligned with that of the monoclinic zirconia standard.

The collected EXAFS data was processed using the Athena program. Each data set was normalised to a unit edge step and background subtracted using the spline function, R_{bkg}, to determine the maximum frequency of the background. Fitting of the EXAFS data was then performed using the Artemis program. The fits were performed in R space obtained by taking the Fourier transform (FT) of the χ(k) data within a specified Hanning window. Since there was no crystallographic data available for these novel amorphous materials, the theoretical EXAFS models for fitting were constructed by the program FEFF on the basis of the crystal structure of $Zr(HPO_4)_2(H_2O)$ or monoclinic ZrO_2. Two single scattering paths from the theoretical EXAFS model constructed by FEFF were then used to fit the experimental data. The first scattering path was always single scattering from O with the shortest path length, and the second scattering path was either from P (if using the EXAFS model based on $Zr(HPO_4)_2(H_2O)$) or Zr (if using the EXAFS model based on monoclinic ZrO_2), also with the shortest path length. The output parameters from this fitting included:[9]

- S_0^2; passive electron reduction factor, constrained to one value for both scattering paths
- ΔE_0; energy shift of the photoelectron, constrained to one value for both scattering paths
- ΔR; change in the path length, variable for each scattering path
- σ^2; dampening of oscillations due to disorder, variable for each scattering path

- N; degeneracy of the path (coordination number in the case of single scattering paths), varied manually between 1, 2, 4, 6 and 8 to obtain the best fit

The goodness-of-fit values given for the fits in this work included the R factor and reduced chi squared (χ_v^2) values. The R-factor simply indicates the percentage of misfit between the experimental data and the calculated fit, for example an R-factor of 0.01 indicates 1 % misfit. On the other hand, χ_v^2 is the fitting metric that is actually minimised during the fit via least-squares minimisation. The χ_v^2 value represents the misfit relative to the estimated uncertainty, divided by the number of degrees of freedom in the fit.[9]

2.7 Elemental Analysis

2.7.1 CHNP Microanalysis

Elemental microanalyses of C, H, and N content for the mesoporous titania samples in *Chapter 6* as well as the functionalised titania materials in *Chapters 4 and 5* were performed using a Model PE2400 CHNS/O elemental analyser, PE Datamanager 2400 for Windows™ and a PerkinElmer AD-6 Ultra Micro Balance (CHNS/O Microanalysis Service at Macquarie University). The samples were combusted in oxidisable metal containers and the combustion products, after scrubbing and oxidation, are quantitatively measured using frontal gas chromatography.

Elemental microanalyses of C, H, N and P content for the zirconium organophosphonate materials in *Chapter 3* as well as the organic ligands and the functionalised titania materials in *Chapter 4* were performed by the Microanalytical Unit at the Australian National University. C, H, N analysis was performed using a Carlo Erba 1106 analyser. The sample was combusted, and the gases, after scrubbing and reducing, were separated on a gas chromatography column and measured at the detector. Phosphorus determinations were made after oxidative digestion by comparative UV spectrophotometric measurements of the yellow vanadomolybdophosphate complex. A variety of methods are used for decomposition of the sample to minimise chemical interferences.

2.7.2 Inductively Coupled Plasma Mass Spectrometry (ICP-MS)

Elemental concentrations of solutions were measured ICP-MS with a Varian 820-MS instrument equipped with nickel cones, Micromist low flow nebuliser, double-glass Scott spray chamber, and SPS3 autosampler. The resolution, mass calibration, sensitivity and stability of the ICP-MS instrument were checked and optimisation of the instrument parameters to maximise the sensitivity of the mass spectrometer and minimise the formation of oxides and double charged ions was performed prior to each analysis. Samples were prepared for ICP-MS analysis by dilution to < 1 ppm in 3 % nitric acid. Quantitative analysis was achieved by measurement of a nine-point calibration curve from 0 to 1000 ppb for each element to be analysed, using commercially available multi-element standard solutions. Internal standards of Sc, Y, In, Tb and Bi (to cover the range of masses being analysed) at a concentration of 5 ppb each were also added to each sample and calibration standard in order to correct for any loss of analytes during sample preparation or measurement. After analysing approximately 20 samples, reagent blank solutions as well as 10 ppb and 500 ppb standard solutions

were measured, to ensure quality control and detect any carry-over effects. Reported error values were calculated by assuming 5 % error in the average of the duplicate or triplicate measured ICP-MS values, unless the standard deviation of the triplicate samples was greater than 5 % of the average, in which case the standard deviation was used.

2.8 Radioanalytical Methods

Gamma counting was performed using a Wallac Wizard^{TM} 3" 1480 automatic gamma counter (PerkinElmer). Background correction, crosstalk correction and spillover corrections were all applied. For Am-241 the energy window used was 50-80 keV and there was no decay correction used. For Eu-152 the entire energy window of 10-1800 keV was used because the relatively low concentration of the Eu-152 spike meant that measuring a single peak resulted in poor count rates and no other elements were present in solution to provide interference. A counting time of 1 h for each sample was used. Samples of known concentration were used to calibrate the gamma counter and the limits of linearity were tested by serial dilution. Reported error values were calculated using the standard deviation of the duplicate samples measured.

2.9 Other Characterisation Methods

Nanoparticle size and zeta potential measurements were performed using a Nano Series ZS Zen 3600. Size measurements were performed at room temperature using dynamic light scattering with Mark-Houwink parameters and a 173 ^{o} backscatter angle of detection. Attenuator position and time of measurement were chosen automatically by the software. The cuvettes used were Plastibrand 2.5 mL disposable cuvettes (DTS0012) and three measurements were performed for each sample. Zeta potential measurements were performed at room temperature by applying a known electric field to the sample then measuring the electrophoretic mobility and calculating the zeta potential using the Helmholtz-Smoluchowski equation. Attenuator position, voltage and the number of runs were chosen automatically by the software. The cuvettes used were Malvern folded capillary cells (DTS1061) and three measurements were performed for each sample.

Viscosity measurements were performed using an Ubbelohde size 1 Ostwald glass viscometer. Measurements using the Ostwald glass viscometer were performed once at 24 ^{o}C as the relatively long experiment times resulted in evaporation of the solutions increasing the viscosity between measurements.

Melting points were obtained using a Stanford Research Systems Optimelt melting point apparatus and are uncorrected.

Optical rotations were obtained using a Perkin Elmer model 341 polarimeter at 589 nm and 20 ^{o}C, using the indicated spectroscopic grade solvent.

2.10 Density Functional Theory (DFT) Modelling

All structure optimisations were performed using the DFT program DMol[3],[10] which is part of the Materials Studio modelling software distributed by Accelrys. This program uses a basis set of numeric atomic functions for the atoms. For this work, the double numeric polarised (DNP) basis set with a cutoff radius of 3.5 Å was chosen and the generalised gradient approximation (GGA/PBE) functional[11] was used. Core electron potentials were represented using DFT semi-core pseudopotentials. Thermal smearing of 0.01 Hartree (Ha) was used. Atom-centred grids were used for the numerical integration with increasing numbers of grid points for the 'coarse' and 'medium' geometry optimisations, respectively. Spins were unrestricted for structures containing Eu. All self-consistent field (SCF) calculations were performed with a final convergence criterion of 2×10^{-5} Ha for the energy.

Simulated annealing was performed using molecular dynamics, again as part of the DMol[3] program within Materials Studio. The coarse geometry optimised structures of the peptide:Eu complexes were subjected to 500 temperature cycles from 0 to 300 K using constant volume/constant temperature (NVT) conditions. At the end of each annealing cycle the structures were again energy minimised to converge below 10^{-4} Ha and the energy minimised structures used for further modelling. Thermal smearing of 0.01 Ha and a simple NH thermostat were also used for the molecular dynamics simulated annealing.

2.11 Sorption

2.11.1 Sorption Methods

In general, solutions for sorption were prepared using metal nitrate salts of each element and MilliQ water or nitric acid then pH adjusted to the appropriate value using nitric acid and/or ammonium hydroxide. Solutions and solid-phase sorbent materials were contacted in 7 mL plastic screw-cap vials. Samples were shaken on a horizontal mixer at a constant speed of 140 rpm for a period of 24 h, unless indicated otherwise. After sorption, each sample was filtered through an individual 0.45 µm syringe filter, except the titania beads in *Chapter 7* for which the liquid from the suspensions was decanted off using a glass pipette. The resulting liquids after filtration or decanting were analysed by ICP-MS or gamma counting. Initial concentrations before sorption were measured from samples shaken and filtered as described above but in the absence of any sorbent material (as a control) to ensure that metal sorption to the plastic vial or filter did not affect the reported results. Measurements of the controls were the same as the concentrations measured of the original metal solutions that were not shaken and filtered.

2.11.2 Sorption Calculations

Percentage extraction and distribution coefficients (K_d) were calculated by measuring the concentration of the analyte before and after sorption by ICP-MS;

$$K_d = \frac{C_f - C_i}{C_f} \times \frac{V}{m}$$

Where C_f is the final concentration of the analyte after sorption (mg/L), C_i is the initial concentration before sorption (mg/L), V is the volume of solution added during the sorption experiment (mL) and m is the mass of sorbent material used (g). The partition coefficients (mL/g) of particular analytes can then be used to calculate separation factors:

Separation Factor $SF_{AB} = \frac{K_d(A)}{K_d(B)}$

2.11.3 Kinetics Models[12]

The pseudo first-order kinetic model assumes the rate of sorption of an analyte onto a surface is proportional to the amount of the analyte that has been sorbed from the solution phase and is given by the equation:

$$\frac{dq_t}{dt} = k_1(q_e - q_t)$$

Where q_e and q_t are the sorption capacity (mmol/g) of the analyte at equilibrium and at time t, respectively, and k_1 is the rate constant for pseudo-first order sorption.

The pseudo second-order kinetic model assumes the rate of sorption of an analyte onto a surface is proportional to the square of the amount of the analyte that has been sorbed from the solution phase and is given by the equation:

$$\frac{dq_t}{dt} = k_2(q_e - q_t)^2$$

Where k_2 is the rate constant for pseudo-second order sorption.

2.11.4 Sorption Isotherm Models [13,14]

Equilibrium adsorption isotherms plot the concentration of the analyte that has been adsorbed (C_{ads}, mg/g) against the final equilibrium analyte concentration (C_{eq}, mg/L) and give an indication of the total sorbent capacity of a material. The two most commonly used models for equilibrium adsorption isotherms are the Langmuir and Freundlich models. The *Langmuir* model isotherm assumes the sorbent material has a limited (monolayer) capacity and that all adsorption sites are identical. It has the form;

$$C_{ads} = \frac{bC_mC_{eq}}{1 + bC_{eq}}$$

Where C_m represents the maximum adsorption capacity (mg/g) and *b* is the Langmuir equilibrium constant (L/mg). The *Freundlich* model isotherm is an empirical model for multilayer sorption with the form;

$$C_{ads} = bC_{eq}^{n}$$

Where *b* is the Freundlich constant and *n* the Freundlich exponent. The Langmuir and Freundlich models are the most commonly used two-parameter adsorption models. Other two parameter models include the *Temkin* model isotherm, which has the form;

$$C_{ads} = \frac{RT \ln(\, bC_{eq})}{a}$$

Where *R* is the gas constant (8.314 J/mol K), *T* is the temperature (K), *a* is the Temkin constant (related to the heat of sorption, J/mol) and *b* is the Temkin isotherm constant (L/g). Another two-parameter model is the *Dubinin-Radushkevich* isotherm model, which has the form;

$$C_{ads} = C_m exp\left\{-b\left[RT \ln\left(1 + \frac{1}{C_{eq}}\right)\right]^2\right\}$$

Where *b* is the Dubinin-Radushkevich model constant (mol^2/kJ^2). Several other three-parameter models were also used to fit the experimental data, such as the *Redlich-Peterson* isotherm model[1], which combines features of the Langmuir and Freundlich isotherms and has the form;

$$C_{ads} = \frac{aC_{eq}}{1 + bC_{eq}^{n}}$$

Where *a* is the Redlich-Peterson model isotherm constant (L/g), *b* is the Redlich-Peterson model constant (L/mg) and *n* is the Redlich-Peterson model exponent. The *Sips* isotherm model is another three-parameter model representing a combination of the Langmuir (at high concentrations) and Freundlich (at low concentrations) models and has the form;

$$C_{ads} = \frac{aC_{eq}^{n}}{1 + bC_{eq}^{n}}$$

Where *a* is the Sips model isotherm constant (L/g), *b* is the Sips model constant (L/mg) and *n* is the Sips model exponent For both the Redlich-Peterson and Sips isotherm models, the constant *n* has a value between 0 and 1 and gives an indication of whether the adsorption behaviour has the Langmuir form ($n = 1$) or Freundlich form ($n = 0$). The final three-parameter model used for fitting the experimental data was the Toth isotherm model, which is derived from potential theory and has the form;

$$C_{ads} = \frac{C_m a C_{eq}}{\left[1 + \left(aC_{eq}\right)^n\right]^{1/n}}$$

Where *a* is the Toth model constant and *n* is the Toth model exponent. The Toth model isotherm describes adsorption to a heterogeneous surface where the majority of sorption sites have an energy less than the mean.

2.12 References

(1) *Circular Dichroism and the Conformational Analysis of Biomolecules*; Fasman, G. D., Ed.; Plenum Press: New York, 1996.

(2) Orthaber, D.; Bergmann, A.; Glatter, O. *J Appl Crystallogr* **2000**, *33*, 218.

(3) Konarev, P. V.; Volkov, V. V.; Sokolova, A. V.; Koch, M. H. J.; Svergun, D. I. *J Appl Crystallogr* **2003**, *36*, 1277.

(4) Higgins, J. S. B., H.C. *Polymers and Neutron Scattering*; Oxford University Press: Oxford, 1996.

(5) Roe, R.-J. *Methods of X-Ray and Neutron Scattering in Polymer Science*; Oxford University Press: New York, 2000.

(6) Benoit, H. *Comptes Rendus* **1957**, *245*, 2244

(7) Hammouda, B. *Adv Polym Sci* **1993**, *106*, 87.

(8) *X-Ray Absorption: Principles, Applications, Techniques of EXAFS, SEXAFS and XANES*; Koningsberger, D. C.; Prins, R., Eds.; John Wiley & Sons: New York, 1988; Vol. 92.

(9) Kelly, S. D.; Kemner, K. M.; Fein, J. B.; Fowle, D. A.; Boyanov, M. I.; Bunker, B. A.; Yee, N. *Geochim Cosmochim Ac* **2002**, *66*, 3855.

(10) Delley, B. *J Chem Phys* **2000**, *113*, 7756.

(11) Perdew, J. P.; Burke, K.; Ernzerhof, M. *Phys Rev Lett* **1996**, *77*, 3865.

(12) Ho, Y. S.; McKay, G. *Adsorpt Sci Technol* **2002**, *20*, 797.

(13) Ho, Y. S.; Porter, J. F.; Mckay, G. *Water Air Soil Poll* **2002**, *141*, 1.

(14) Limousin, G.; Gaudet, J. P.; Charlet, L.; Szenknect, S.; Barthes, V.; Krimissa, M. *Appl Geochem* **2007**, *22*, 249.

Chapter 3: Zirconium Organophosphonates

Hybrid inorganic-organic materials for selective separations of lanthanide elements (Ln) from solutions of used nuclear fuel were synthesised via co-condensation of zirconia and an organophosphonate. As described in *Chapter 1*, Ln are targets for selective separation from used nuclear fuel due to their high neutron absorption cross-section, which means they must be separated from actinide elements (An) before the An can be recycled and transmutated.[1] Lanthanides are also targets for separations due to their broad industrial value in applications such as magnets and phosphors.[2] A zirconia based material was chosen for investigation due to the hydrolytic and radiolytic stability of zirconia.[3] The organic ligand chosen for functionalization of zirconia was an organic phosphonate because the strong affinity of organophosphorus compounds for Ln is well known. This is evidenced by the number of organophosphorus compounds, such as tributyl phosphate (TBP) and carbamoylmethylphosphine oxide (CMPO), used to extract Ln in solvent extraction processes[4,5] and chromatographic resins.[6-8] In addition, zirconia and phosphate based materials have the potential to be converted into stable ceramic waste forms after sorption for immobilisation of the radionuclides.[3,9,10]

Since the pioneering work of Alberti and Clearfield on pillared zirconium(IV) phosphonates,[11,12] a wide range of other Zr(IV) metal organic frameworks based on phosphonate motifs have been developed having structures that range from amorphous to highly crystalline.[13-20] Porous zirconium organophosphonate (ZrP) materials have been synthesised previously using surfactant or small molecule templates.[15,16] However, templated synthesis of mesoporous metal organophosphonates can encounter problems with degradation of the organophosphonate during removal of the template by thermal treatment[16] or incomplete template removal by solvent extraction.[21] Therefore, no templating was used for synthesis of the coordination networks in this study.

Most previously synthesised ZrP materials have used mono- or bis-phosphonates to form either amorphous porous structures[15,16] or crystalline layered/pillared structures.[17-20] However, in an attempt to provide a higher number of unbound phosphonate groups for Ln binding from solution, the use of higher order polyphosphonates was targeted in this work. Recently a tris-phosphonate; amino tris(methylene phosphonic acid) (ATMP, Figure 3.1), was used to functionalise pre-assembled mesoporous zirconium titanium oxide. The ATMP imparted significant selectivity for Ln and mitigated leaching of the framework elements.[22] However, these materials had a low phosphonate loading as the partially condensed metal oxide framework had only a limited number of surface sites to which phosphonates could bind; hence they demonstrated a very limited capacity for Ln.[23] Therefore in the present work, materials were synthesised with ATMP incorporated into the framework. This was achieved via co-condensation of zirconia and ATMP during hydrothermal synthesis, to give a higher density of evenly distributed phosphonate groups.

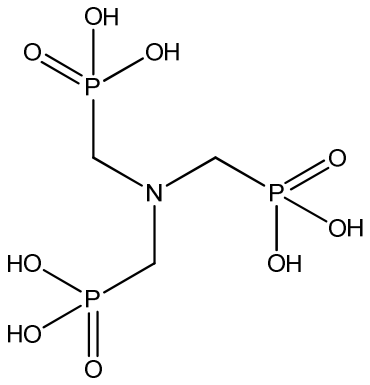

Figure 3.1: Chemical structures of amino tris(methylene phosphonic acid) (ATMP)

Few studies have considered ZrP materials for the sorption of Ln or An[14,18-20] despite the known affinity of organophosphorus based extractants for Ln and An cations. The aim of the present work was to develop novel ZrP phases with high capacity and selectivity for Ln. This was undertaken by varying the synthesis parameters and investigating what effect this had on the structure, chemical composition and sorption properties of the ZrP materials. Specifically, the effects of varying the Zr precursor, Zr:P ratio, pH and temperature of hydrothermal synthesis were measured. In terms of sorption properties, the capacity and kinetics of Ln sorption were explored, as well as the selectivity of the ZrP materials. Sorption experiments were performed with the fission products lanthanum (La), neodymium (Nd), europium (Eu), holmium (Ho), ytterbium (Yb), cesium (Cs) and strontium (Sr) as well as activation product cobalt (Co), in order to determine the selectivity of the ZrP materials for Ln over other elements present in solutions of used nuclear fuel as well as within the Ln series. Investigation of the mode of binding by solid-state nuclear magnetic resonance (NMR) and fourier transform infra-red (FTIR) spectroscopy was also performed.

3.1 Experimental Methods

3.1.1 Sorbent Materials Synthesis

All reactants were purchased from Sigma Aldrich and were reagent grade or higher. Reagents were used as supplied without further purification. Aqueous ATMP (50 wt%) was mixed with MilliQ water to make a total volume of 10.0 mL. Zirconium(IV) was then added as either the chloride or propoxide (70 wt% in 1-propanol). If zirconium tetrachloride ($ZrCl_4$) was used, it was dissolved in 3.5 mL tetrahydrofuran (THF) before addition to the aqueous ATMP solution to slow the hydrolysis rate of Zr and hence favour formation of a mesoporous structure.[24] The pH was adjusted by addition of potassium hydroxide (KOH) solution (2.0 M). The resulting suspension was then stirred at room temperature for 1 h in a plastic beaker before transfer to a parr reactor vessel for hydrothermal treatment at 120 or 160 ^{o}C for 24 h. After cooling, the products were vacuum filtered through qualitative filter paper, washed with MilliQ water and air dried. The resulting white solid was ground to a fine powder in a mortar and pestle. Eight series of samples were synthesised and are described in Table 3.1.

Table 3.1. Synthesis conditions for ZrP materials.

Series #	Sample name	Zr precursor	Temp (°C)	pH adjust*	Zr:P stoichiometries
1	ZrPA	chloride	120	N (~1)	1:1, 3:4, 1:2, 1:3, 1:4
2	-	chloride	120	Y (4-5)	1:1, 3:4, 1:2, 1:4
3	-	chloride	160	Y (4-5)	1:1, 3:4, 1:2, 1:4
4	-	chloride	160	Y (6-7)	1:1, 1:2, 1:4, 1:8
5	ZrPB	propoxide	120	N (1-2)	1:1, 3:4, 1:2, 1:3, 1:4
6	-	propoxide	120	Y (<1)	1:1, 3:4, 1:2, 1:4
7	-	propoxide	160	N (1-2)	1:2, 1:4, 1:8, 1:10
8	ZrPC	propoxide	160	Y (4-5)	1:1, 3:4, 1:2, 1:3, 1:4, 1:8

*N = No, Y = Yes

In order to capture a range of different synthesis conditions, series 1, 5 and 8 were chosen for further investigation and designated ZrPA, ZrPB and ZrPC, respectively. Details of pH measurements and yields of samples with Zr:P molar ratios 1:1, 3:4, 1:2, 1:3 and 1:4 within these series are listed in Table 3.2. Yields were calculated as the percentage of the Zr added that was present in the final material.

Table 3.2: Measured pH during synthesis of ZrPA, ZrPB and ZrPC samples

sample	Zr:P molar ratio added	2M KOH (mL)	Final pH	Yield (%)
ZrPA-1	1:1	-	1.2	70
ZrPA-2	3:4	-	1.1	78
ZrPA-3	1:2	-	1.1	70
ZrPA-4	1:3	-	1.0	77
ZrPA-5	1:4	-	1.0	72
ZrPB-1	1:1	-	1.9	88
ZrPB-2	3:4	-	1.5	86
ZrPB-3	1:2	-	1.4	83
ZrPB-4	1:3	-	1.3	84
ZrPB-5	1:4	-	1.2	88
ZrPC-1	1:1	0.7	4.3	76
ZrPC-2	3:4	1.0	4.5	63
ZrPC-3	1:2	1.4	4.3	61
ZrPC-4	1:3	2.4	4.6	62
ZrPC-5	1:4	3.5	4.2	59

3.1.2 Sorption Methodology

Selective sorption of fission products La, Nd, Eu, Ho, Yb, Cs, Sr and activation product Co at a concentration of 0.1 mmol/L each was investigated via competitive sorption experiments in 0.1 M nitric acid. These batch sorption experiments were performed in triplicate using a constant volume-to-mass ratio of 100. Kinetic measurements were

performed in duplicate using 100 ppm Eu in 0.1 M nitric acid. Sorption isotherm measurements to determine capacity were performed in duplicate using solutions of Eu in 0.1 M nitric acid with an initial Eu concentration ranging from 1 to 1000 ppm.

3.2 Results

3.2.1 Effects of Varying Synthesis Conditions

The results of nitrogen porosimetry and preliminary sorption testing with La, Nd and Gd on all the materials listed in Table 3.1 are given in Appendix A. From this data, the effect of individual synthesis parameters could be determined. For example, the Zr propoxide precursor produced materials with generally higher surface area and higher Ln sorption than the Zr chloride precursor. Also, higher temperature hydrothermal treatment produced materials with higher surface area but lower Ln sorption independent of whether the propoxide or chloride precursor was used. Finally, synthesis at higher pH consistently produced materials with higher Ln sorption but had no consistent effect on surface area. Despite this promising trend, synthesis of ZrP materials at pH 6-7 was not pursued because (i) if the molar ratio P/Zr added during synthesis was more than 2 at pH 6-7, no material precipitated, and (ii) the materials that could be made at low molar ratio P/Zr were difficult to handle and filter, presumably due to an extremely small particle size.

Increasing the length or temperature of hydrothermal treatment to 4 days or 200 ^{o}C, respectively, was also attempted but did not produce crystalline samples. Reaction temperatures of 200 ^{o}C or greater resulted in degradation of the organophosphonate as indicated by a change in sample colour from white to brown. Samples were also prepared using zirconium propoxide precipitated in water and stirred without pH adjustment or at pH 4-5 before addition of ATMP followed by hydrothermal treatment at 160 ^{o}C. These materials showed the same properties as those synthesised by addition of zirconium propoxide to an ATMP solution. Thus, the time of ATMP addition before hydrothermal treatment did not affect the material properties.

3.2.2 X-Ray Diffraction

X-ray diffraction (XRD) of all the synthesised ZrP materials showed a single broad peak in the 2θ range of 17-40^{o}, indicating that they consisted of an amorphous framework. A representative sample is shown in Figure 3.2.

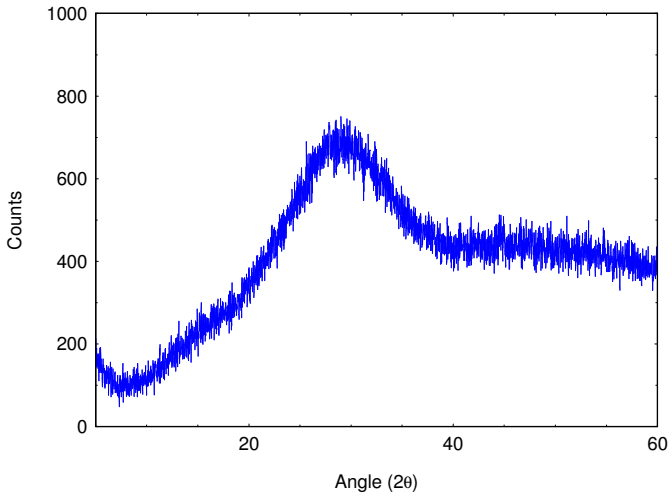

Figure 3.2: XRD pattern of ZrPC-1

3.2.3 Nitrogen Porosimetry

Nitrogen adsorption-desorption isotherms were measured for all of the synthesised ZrP materials. The calculated BET surface area, micropore surface area, pore volume and pore diameters from these isotherms[25] are listed in Table 3.3. From this data it is clear that highly porous materials have been synthesised without the use of templates.

Table 3.3: Physicochemical properties of ZrP materials

Sample	***BET Surface Area (m^2/g)***	***Micropore Surface Area (m^2/g)***	***Pore Volume (mL/g)***	***Pore Diameter (nm)***
ZrPA-1	203	54	0.54	<2, ~40
ZrPA-2	237	73	0.71	<2, ~40
ZrPA-3	316	99	0.90	<2, ~40
ZrPA-4	125	9	0.63	<2. ~40
ZrPA-5	78	4	0.50	~40
ZrPB-1	427	48	0.54	<2, ~20
ZrPB-2	299	49	0.40	<2, ~20
ZrPB-3	105	14	0.26	<2, ~20
ZrPB-4	41	3	0.20	~20
ZrPB-5	33	2	0.18	~20
ZrPC-1	500	53	0.51	<2
ZrPC-2	435	87	0.40	<2
ZrPC-3	303	80	0.27	<2
ZrPC-4	25	11	0.03	<2
ZrPC-5	1	-	-	-

For the ZrPA series, surface area, microporosity and pore volume increased with the molar ratio P/Zr in the samples up to ZrPA-3 but then underwent an abrupt, dramatic decrease when P/Zr was further increased for ZrPA-4. In addition, while for ZrPA-1, -2 and -3 the proportion of the surface area due to microporosity was approx. 30 %, this decreased to

approx. 5 % for ZrPA-4 and -5. Despite this, the shape of the nitrogen adsorption-desorption isotherms were similar for all the samples in this series, and are represented by the data for ZrPA-2 in Figure 3.3. This isotherm was classified as Type II, which represents unrestricted monolayer-multilayer adsorption and is obtained for macroporous adsorbents. The isotherm also contained a H3 hysteresis loop, indicating capillary condensation in slit-shaped mesopores formed due to aggregation of plate-like particles.[25] As such, the ZrPA materials had hierarchical porosity with micropores, mesopores and macropores apparent. The inset to Figure 3.3 shows the pore size distribution (PSD) for ZrPA-2. The large peak at low pore diameter (< 2 nm) was attributed to the presence of micropores and there was also a broad peak centred at approx. 40 nm from mesopores. Similar PSD plots were seen for ZrPA-1 and -3. However, for ZrPA-4 and -5, the peak at < 2 nm pore diameter was greatly reduced, due to the loss of microporosity in these samples (Table 3.3).

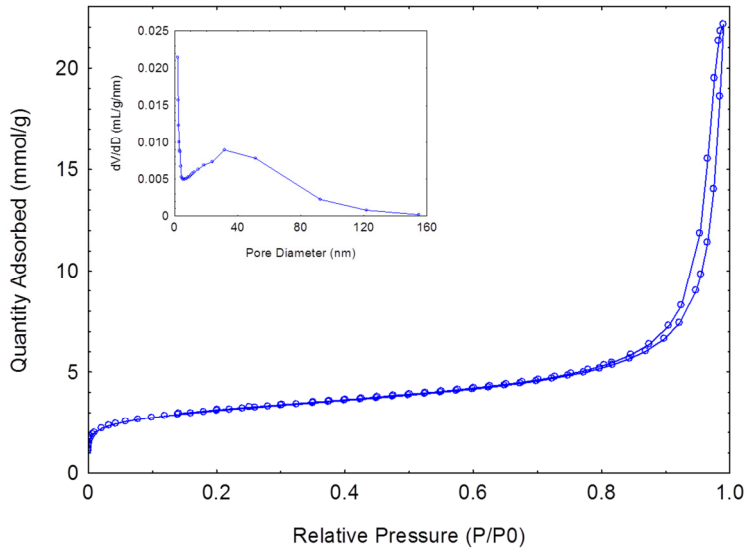

Figure 3.3: Nitrogen adsorption-desorption isotherm for ZrPA-2. Inset: PSD.

For the ZrPB series, surface area, microporosity and pore volume all decreased with increasing molar ratio P/Zr. The decrease was approx. linear from ZrPB-1 to -3 then reached a plateau at ZrPB-4. The shape of the nitrogen adsorption-desorption isotherms were similar across the ZrPB series and are represented by the data for ZrPB-3 in Figure 3.4. The isotherms for the ZrPB materials were classified as Type II with H3 hysteresis, similar to the ZrPA materials. Thus, the ZrPB materials also demonstrated hierarchical porosity with macropores, mesopores and micropores. The PSD was similar for ZrPB-1, -2 and -3 and is shown as the inset to Figure 3.4. Although the PSD was dominated by the peak at < 2 nm, mesopores of approx. 20 nm diameter were also present across the ZrPB series. For ZrPB-4 and -5, almost all the microporosity was lost and consequently the PSD of these materials did not have a peak at < 2 nm and the broad peak due to mesopores of approx. 20 nm diameter predominated.

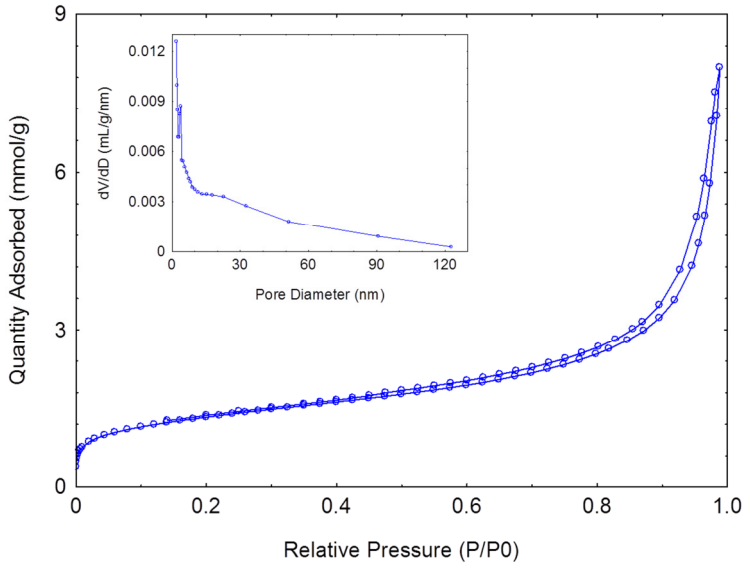

Figure 3.4: Nitrogen adsorption-desorption isotherm for ZrPB-3. Inset: PSD.

For the ZrPC series, surface area and pore volume decreased with the molar ratio P/Zr until ZrPC-5, which demonstrated negligible surface area and pore volume. The decrease was approx. linear from ZrPC-1 to -3 but was followed by a substantial step decrease to ZrPC-4. Micropore surface area increased from ZrPC-1 to ZrPC-2 before decreasing across the remainder of the series. As a result, the proportion of the total surface area due to microporosity increased across the series and was approx. 10, 20, 30 and 40 % for ZrPC-1, -2, -3 and -4, respectively. The shape of the nitrogen adsorption-desorption isotherm was consistent across the ZrPC series; a Type II isotherm with H3 hysteresis. Thus, the ZrPC materials also had hierarchical porosity with macropores, mesopores and micropores, as was observed for the ZrPA and ZrPB series. The representative isotherm for the ZrPC series, ZrPC-2, is shown in Figure 3.5. The inset to Figure 3.5 shows the PSD, which indicated a pore diameter of < 2 nm was the only pore size present. Pore size distibution was also consistent across the ZrPC series except for ZrPC-5, which was not porous.

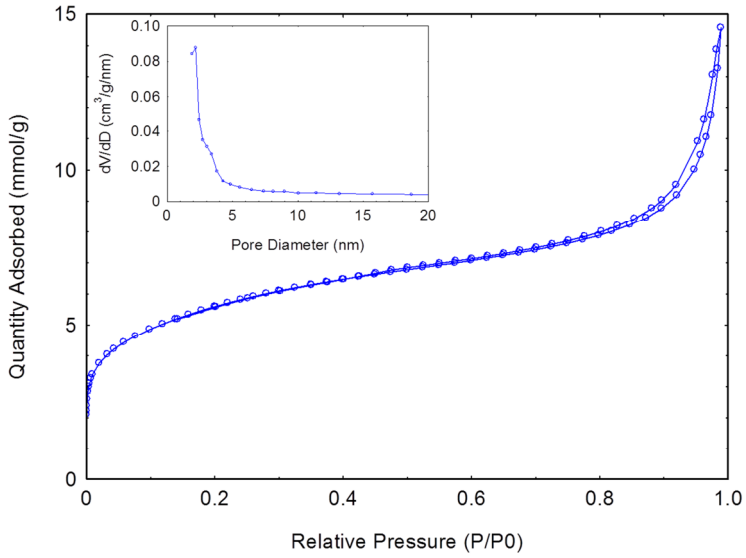

Figure 3.5: Nitrogen adsorption-desorption isotherm for ZrPC-2. Inset: PSD.

3.2.4 Elemental Analysis

Elemental analysis of the ZrP materials was performed via two methods and the results are shown in Table 3.4. Digestion in concentrated sulphuric acid followed by inductively coupled plasma mass spectrometry (ICP-MS) was used to measure the %Zr and %P in all the samples, while %CHNP was also determined by microanalysis for the end members of the three series ZrPA, ZrPB and ZrPC. The difference between the %P values as determined by ICP-MS and microanalysis was consistently less than 2 %, which suggests that the results can be viewed with confidence. The data in Table 3.4 shows that as the molar ratio P/Zr increased the %Zr in the samples decreased and the %P (as well as %CHN) increased, as expected. The total percentage of Zr + P was 37 % for ZrPA-1, 41 % for ZrPB-1 and 33 % for ZrPC-1 and a similar trend of ZrPB > ZrPA ≥ ZrPC was seen for all stoichiometries.

Table 3.4: Elemental analysis of ZrP materials

Sample	ICP-MS		Microanalysis				Molar P/Zr	
	%Zr	%P	%C	%H	%N	%P	expected	measured
ZrPA-1	26.9	9.9	5.4	2.0	2.3	9.9	1.0	1.1
ZrPA-2	25.7	11.5					1.3	1.3
ZrPA-3	19.3	13.2					2.0	2.0
ZrPA-4	17.6	18.2					3.0	3.0
ZrPA-5	15.4	17.5	8.6	2.9	4.0	19.4	4.0	3.5
ZrPB-0	46.1	-					0	0
ZrPB-1	29.7	10.5	5.2	2.8	1.5	11.2	1.0	1.0
ZrPB-2	27.5	14.1					1.3	1.5
ZrPB-3	23.7	17.1					2.0	2.1
ZrPB-4	21.7	19.3					3.0	2.6
ZrPB-5	21.7	20.6	9.6	2.8	3.2	20.5	4.0	2.8
ZrPC-1	24.4	8.3	3.8	2.8	1.4	9.1	1.0	1.0
ZrPC-2	24.0	9.7					1.3	1.2
ZrPC-3	21.4	13.4					2.0	1.8
ZrPC-4	18.0	15.1					3.0	2.5
ZrPC-5	15.5	17.0	6.1	2.7	2.4	15.8	4.0	3.2

The expected molar ratio P/Zr, based on the amount of Zr precursor and ATMP that were added to the reaction mixture, is also listed in Table 3.4 for each sample, along with the experimentally measured value. For the ZrPA series, the expected and experimental values matched well (± 0.2) until ZrPA-5. For the ZrPB series, lower than expected molar P/Zr ratios were measured for both ZrPB-4 and -5. In addition, the difference observed between the expected and measured values were larger than was seen in the ZrPA series. For the ZrPC series, the onset of the mismatch between the expected and experimental molar P/Zr values occurred at the same point as the ZrPB series. However, the molar P/Zr ratio still increased substantially between ZrPC-4 and ZrPC-5, unlike the ZrPB series. As a result, ZrPC-5 had a higher molar P/Zr ratio than ZrPB-5, but ZrPA-5 has the highest molar P/Zr ratio of all.

3.2.5 Scanning Electron Microscopy

Scanning electron microscopy (SEM) images of ZrP powders from the ZrPA series are shown in Figure 3.6. All the powders had a similar morphology consisting of agglomerated spherical particles approx. 50 nm in diameter.

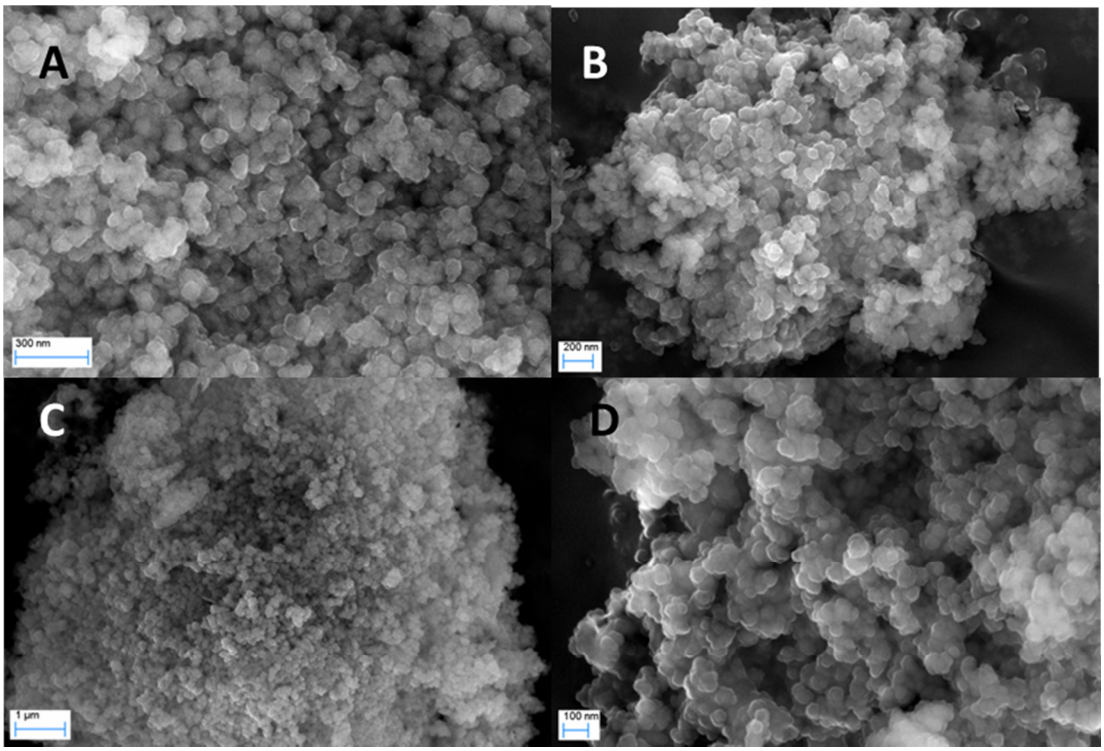

Figure 3.6: SEM images of ZrPA-1 (A), -3 (B), -4 (C) and -5 (D).

Representative SEM images of ZrP powders from the ZrPB series are shown in Figure 3.7. The SEM image of ZrPB-2 on the left indicates the presence of both unstructured powders and micron-sized particles with large honeycomb-shaped pores in these materials. The SEM images in the middle and right of Figure 3.7 show that both the unstructured powders and honeycomb shaped particles consisted of smaller agglomerated particles approx. 50 nm in diameter.

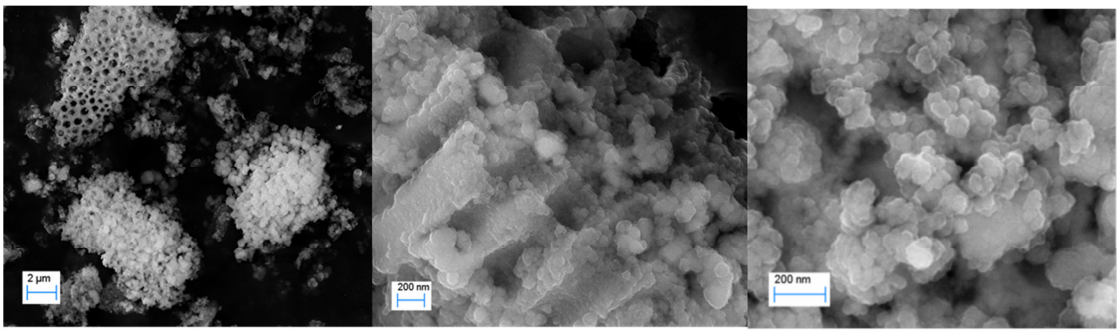

Figure 3.7: SEM images of ZrPB-1 (middle) and -2 (left and right).

Representative SEM images of ZrP powders from the ZrPC series are shown in Figure 3.8. ZrPC-1, -2, -3 and -4 all showed a similar morphology of agglomerated spherical particles approx. 50 nm in diameter, represented by images A and B in Figure 3.8. Unlike the ZrPC samples with lower molar P/Zr ratios, ZrPC-5 consisted of solid micron-sized particles with a possible layered morphology on the nanoscale, as shown in images C and D of Figure 3.8.

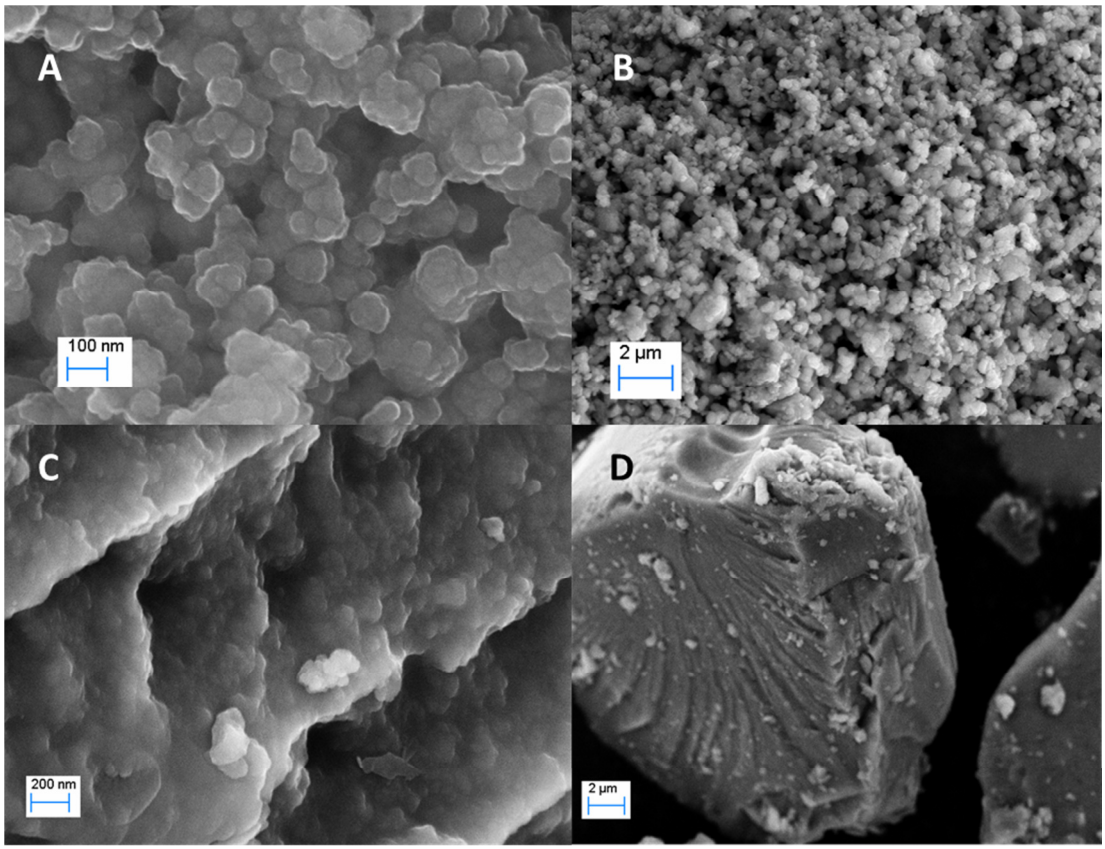

Figure 3.8: SEM images of ZrPC-2 (A), -4 (B) and -5 (C and D).

3.2.6 Competitive Sorption

The results of competitive sorption experiments for the ZrPA series are shown in Figure 3.9. ZrPA-1 and -2 did not show any sorption but as the molar ratio P/Zr was further increased, sorption also increased for all the elements apart from Cs. Cs was not substantially extracted by any of the ZrPA materials. For ZrPA-3, Ln sorption ranged from 13 to 27 % while Cs, Sr and Co remained in solution. When the molar P/Zr ratio was further increased to give ZrPA-4, Ln sorption became almost quantitative and sorption of Sr and Co also increased to approx. 20 %. A minimal increase in Ln sorption was observed as the molar P/Zr ratio was again increased to give ZrPA-5, since sorption was already 98 to 99 % for ZrPA-4. Sorption of Sr and Co increased to approx. 50 % for ZrPA-5. Some bell-shaped intra-Ln selectivity was also observed for the ZrPA materials, with sorption increasing across the Ln series from La to Eu, then decreasing again to Yb. ZrPA-3 showed the highest intra-Ln selectivity of all the ZrPA samples, with separation factor $SF_{Eu/Ln}$ ranging from 1.6 to 2.4.

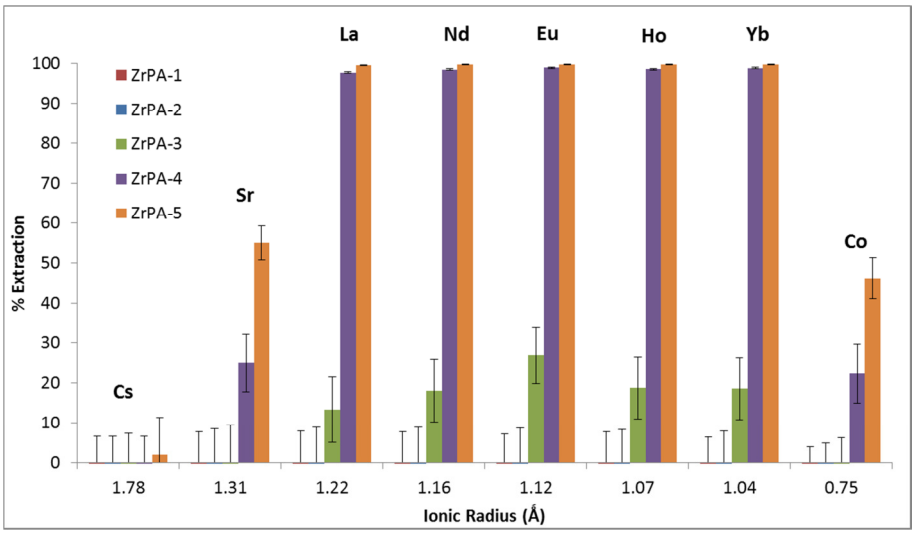

Figure 3.9: Competitive sorption efficiencies of 0.1 mM Co, Sr, Cs and Ln from 0.1 M nitric acid using ZrPA materials.

The extraction efficiencies of the ZrPB series are shown in Figure 3.10. As for the ZrPA series, the material with the lowest molar P/Zr ratio, ZrPB-1, did not show any sorption but as the molar ratio P/Zr increased, sorption also increased. ZrPB-2 sorbed between 7 and 17 % of the Ln elements without sorbing any Cs, Sr or Co. Similar intra-Ln selectivity to what was observed for ZrPA-3 (Figure 3.9) was also present for ZrPB-2, which showed $SF_{Eu/Ln}$ ranging from 1.7 to 2.7. This was the highest intra-Ln selectivity observed amongst the ZrPB samples. Increasing the molar P/Zr ratio to give ZrPB-3 caused Ln sorption to increase up to 40 % for La, 55 % for Nd and 60-70 % for Eu, Ho and Yb. ZrPB-3 still showed no sorption of Cs, Sr or Co. Further increasing the molar P/Zr ratio to give ZrPB-4 and -5 had no significant impact on the sorption properties of the materials.

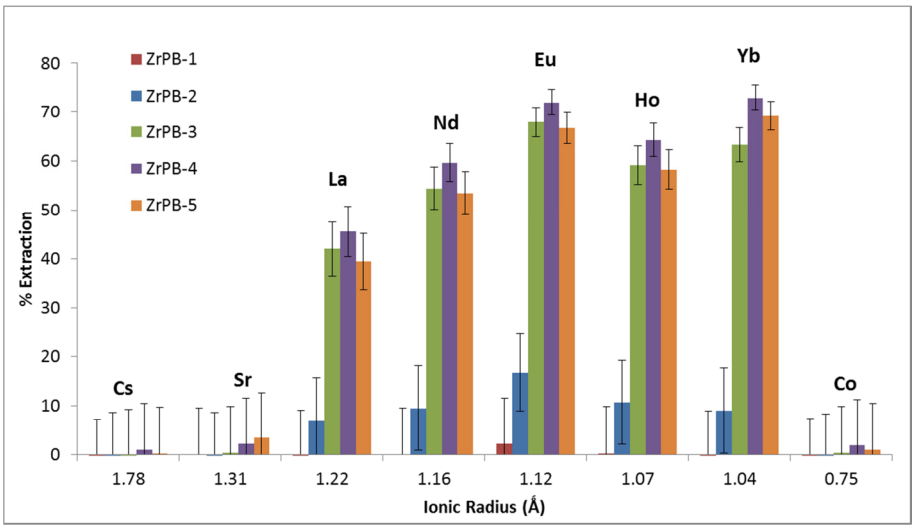

Figure 3.10: Competitive sorption efficiencies of 0.1 mM Co, Sr, Cs and Ln from 0.1 M nitric acid using ZrPB materials.

The extraction efficiencies of the ZrPC series are shown in Figure 3.11. Extraction of Ln again increased with the molar ratio P/Zr in the samples but for the ZrPC series even the sample with the lowest molar P/Zr ratio, ZrPC-1, showed substantial Ln extraction of 35 to 57 %. Extraction of Ln then increased to between 66 and 84 % for ZrPC-2, 97 and 99 % for ZrPC-3 and was quantitative for ZrPC-4 and -5. Selectivity for Ln was again evident in the ZrPC series as no significant sorption of Cs was observed for any of the samples and sorption of Sr and Co was negligible for ZrPC-1, -2 and -3 then increased to between 20 and 30 % for ZrPC-4 and -5. In addition, bell-shaped intra-Ln selectivity was again observed for ZrPC-1 and -2, with ZrPC-2 producing the best intra-Ln separation factors of the ZrPC series, ranging from 1.4 ($SF_{Eu/Ho}$) to 2.7 ($SF_{Eu/La}$).

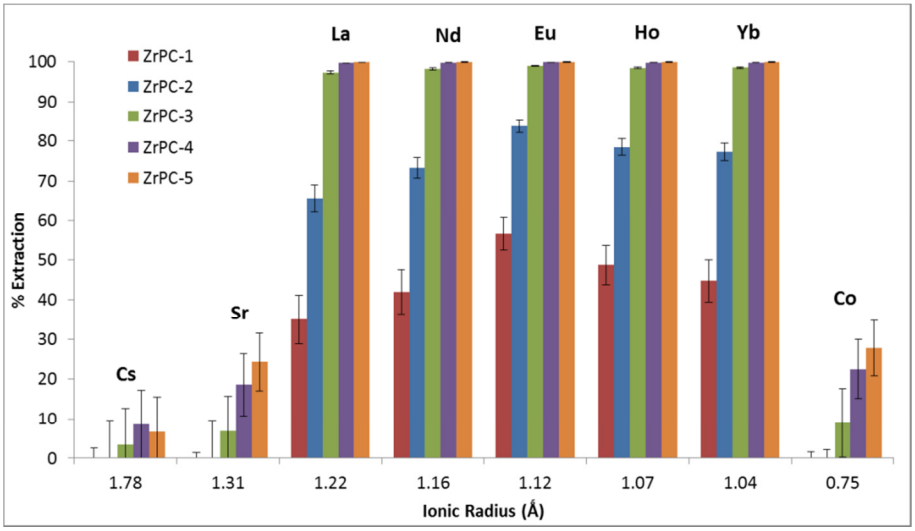

Figure 3.11: Competitive sorption efficiencies of 0.1 mM Co, Sr, Cs and Ln from 0.1 M nitric acid using ZrPC materials.

3.2.7 Sorption Capacity

Since ZrPA-5 as well as ZrPC-3, -4 and -5 all showed quantitative Ln sorption during the competitive sorption experiments; their equilibrium sorption isotherms were measured and are shown in Figure 3.12. These sorption isotherms were fitted with the commonly used Langmuir and Freundlich sorption isotherm models as well as Redlich-Peterson, Toth, Temkin, Sips and Dubinin-Radushkevich sorption isotherm models.[26,27] Mathematical descriptions of these models are given in *Chapter 2*. The model isotherm constants as well as goodness of fit values for each isotherm model are reported in Table 3.5. The ZrPA-5 experimental data was best fit with the Redlich-Peterson isotherm model (as determined by the r^2 value), which is shown as a solid line in Figure 3.12. The Redlich-Peterson isotherm model is a combination of the Langmuir and Freundlich isotherms. The Langmuir isotherm assumes monolayer capacity and identical sorption sites while the Freundlich isotherm is an empirical model for multilayer sorption. For ZrPC-3, -4 and -5, the Toth isotherm model consistently provided the best or equal best fit (as determined by the r^2 value) to the experimental data and is shown as a dashed line in Figure 3.12. The Toth isotherm assumes an asymmetrical quasi-Gaussian

energy distribution in which the majority of sorption sites have a sorption energy lower than the mean.

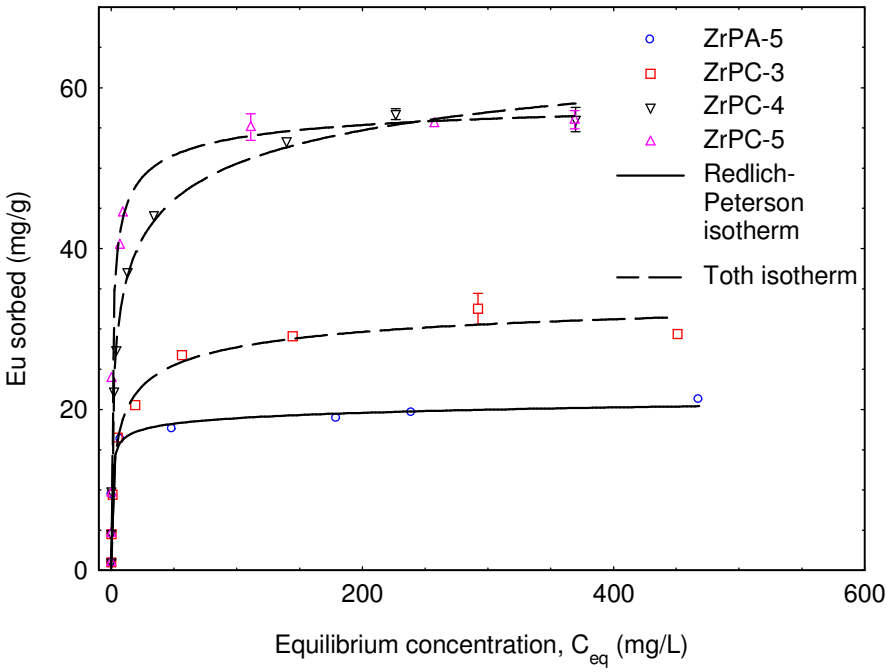

Figure 3.12: Equilibrium sorption isotherms and model fits of ZrPA-5, ZrPC-3, -4 and -5 with Eu in 0.1 M nitric acid.

Table 3.5: Model isotherm constants for ZrPA-5, ZrPC-3, -4 and -5.

Model		ZrPA-5	ZrPC-3	ZrPC-4	ZrPC-5
Langmuir	C_m	19.2	29.6	54.4	52.3
	b	1.66	0.26	0.25	1.60
	r^2	*0.976*	*0.955*	*0.964*	*0.957*
Freundlich	b	8.75	10.6	20.2	23.7
	n	0.15	0.19	0.19	0.16
	r^2	*0.873*	*0.929*	*0.968*	*0.888*
Temkin	a	818	746	416	461
	b	7.13	31.8	39.8	164
	r^2	*0.727*	*0.973*	*0.984*	*0.960*
Dubinin-Radushkevich	C_m	18.7	28.1	49.5	55.5
	b	0.0002	0.008	0.003	0.007
	r^2	*0.963*	*0.842*	*0.863*	*0.835*
Redlich-Peterson	a	14.6	21.8	25.2	121.8
	b	2.81	1.32	4.72	3.30
	n	0.95	0.90	0.86	0.94
	r^2	*0.992*	*0.984*	*0.990*	*0.982*
Sips	a	24.6	5.07	24.7	44.0
	b	1.25	0.15	0.36	0.75
	n	0.75	0.54	0.46	0.58
	r^2	*0.980*	*0.990*	*0.998*	*0.982*
Toth	C_m	20.1	37.3	81.9	60.0
	a	3.29	2.48	13.3	6.49
	n	1.62	2.60	0.27	0.46
	r^2	*0.983*	*0.990*	*0.997*	*0.982*

The Redlich-Peterson isotherm model that provided the best fit to the experimental equilibrium sorption isotherm for ZrPA-5, does not have sorption capacity, C_m, as one of its fitted parameters. However, all three of the isotherm models that do have sorption capacity as one of the fitted parameters (Langmuir, Dubinin-Radushkevich and Toth) provided a reasonable fit to the experimental data ($r^2 > 0.95$) and consistently suggested a sorption capacity of 19-20 mg Eu/g for ZrPA-5 (Table 3.5). This value is also consistent with the sorption capacity that would be estimated based on a visual inspection of the experimental data in Figure 3.12. The sorption capacities of ZrPC-3, -4 and -5, according to the Toth isotherm model, were 37, 82 and 60 mg Eu/g, respectively. Thus, ZrPA-5 had the lowest sorption capacity of the materials tested and ZrPC-4 had the highest.

The value of the constant *n* in the Redlich-Peterson model of ZrPA-5 was close to one (Table 3.5), indicating that the sorption behaviour more closely resembled the Langmuir model than the Freundlich model. This was consistent with the value of *n* for the fitted Sips model isotherm and with the fact that the Langmuir model itself provided a better fit to the experimental data of ZrPA-5 ($r^2 = 0.98$) than the Freundlich model ($r^2 = 0.87$). Thus, all the

sorption sites on ZrPA-5 are likely to be similar and form a monolayer capacity. The fact that the Toth isotherm provided the best or equal best fit to the experimental sorption isotherms of ZrPC-3, -4 and -5 data indicates that the sorbing surface of these ZrPC materials was energetically heterogeneous.

3.2.8 Sorption Kinetics

The kinetics of Eu sorption from 0.1 M nitric acid were investigated for the ZrP materials from each series that demonstrated the highest sorption in the competitive sorption experiments (*section 3.2.6*). Hence, the sorption kinetics of ZrPA-5, ZrPB-5 as well as ZrPC-3, -4 and -5 were measured and the results are shown in Table 3.6. For all of these ZrP materials, equilibrium was reached within 24 h. Within 30 minutes, 86 % of the total uptake was achieved for ZrPA-5, 82 % of the total uptake was achieved for ZrPB-5 and 98-100 % of the total uptake was achieved for ZrPC-3, -4 and -5.

Table 3.6: Percentage extraction of 100 ppm Eu from 0.1 M nitric acid over time with ZrPA-5, ZrPB-5, ZrPC-3, -4 and -5.

Time (h)	***% extracted***				
	ZrPA-5	**ZrPB-5**	**ZrPC-3**	**ZrPC-4**	**ZrPC-5**
0	0.0 ± 0.3	0.0 ± 0.3	0.0 ± 0.3	0.0 ± 0.3	0.0 ± 0.3
0.03			69.3 ± 10.2		62.4 ± 2.8
0.08	69.9 ± 0.3	35.2 ± 2.1	87.1 ± 4.3	98.7 ± 0.1	79.5 ± 8.5
0.17			94.3 ± 1.0		84.8 ± 0.7
0.25		39.7 ± 2.2		99.3 ± 0.01	
0.5	86.0 ± 0.7	41.3 ± 1.6	97.9 ± 0.1	99.5 ± 0.02	98.3 ± 0.3
1	92.0 ± 0.1	42.7 ± 0.6		99.6 ± 0.04	
2		45.9 ± 0.9	98.9 ± 0.1	99.7 ± 0.02	99.8 ± 0.03
4	97.2 ± 0.1	46.9 ± 0.7		99.7 ± 0.02	
8	98.9 ± 0.2	50.3 ± 1.1		99.5 ± 0.2	
16	99.4 ± 0.04	50.0 ± 0.5		99.8 ± 0.02	
24	99.5 ± 0.03	50.5 ± 2.0	98.9 ± 0.1	99.8 ± 0.1	99.8 ± 0.1

Pseudo first-order and second-order kinetics models were used to fit the experimental data in Table 3.6. Mathematical descriptions of these models are given in *Chapter 2*. All of the samples fit the pseudo-second-order kinetic model as indicated by the fact that a plot of t/q_t versus t was linear (Figure 3.13).[28] The calculated rate constant for ZrPA-5 was 0.023 g/mg min and for ZrPB-5 was 0.027 g/mg min. The calculated rate constants for ZrPC-3, -4 and -5 were 0.21, 0.58 and 0.11 g/mg min, respectively. Thus, ZrPA-5 and ZrPB-5 showed similar sorption kinetics, which were both substantially slower than the ZrPC materials. ZrPC-4 showed the fastest sorption kinetics.

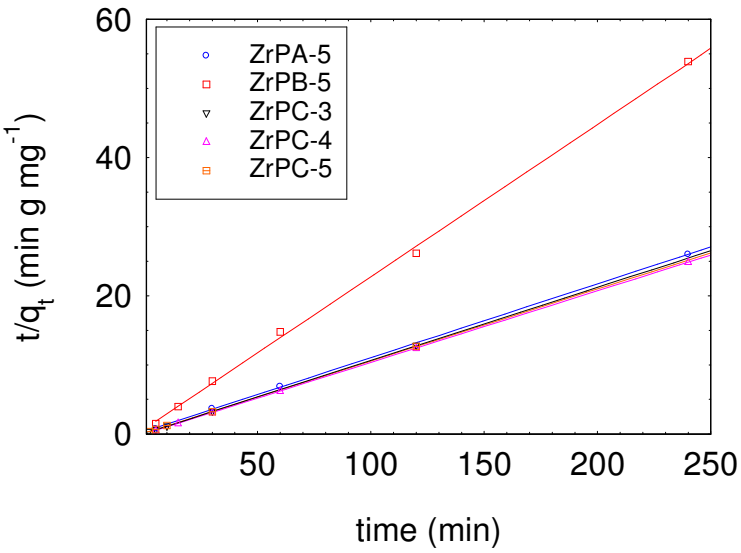

Figure 3.13: Linear fit of the pseudo-second-order rate equation to sorption kinetics data for ZrPA-5, ZrPB-5, ZrPC-3, -4 and -5.

3.2.9 Fourier Transform Infra-Red (FTIR) Spectroscopy

Fourier transform infra-red (FTIR) spectra of the ZrPA series are shown in Figure 3.14. Absorbance bands were observed at 1640, 1430, 1320 and 1270 cm^{-1} and were assigned to the water bending, P-CH_2 stretch, Zr-OH bending (in-plane) and P=O stretch, respectively.[29,30] The dominant broad absorbance band from approx. 900 to 1250 cm^{-1} was at the characteristic frequency of the P-O stretch.[31] Spectral deconvolution of the broad P-O absorbance band indicated the presence of three bands, the peak positions of which are given in Table 3.7. Assignments of these absorbance bands are also given in Table 3.7. Unfortunately, the relative intensities of these bands could not be established since several different intensity fits gave similar goodness-of-fit values.

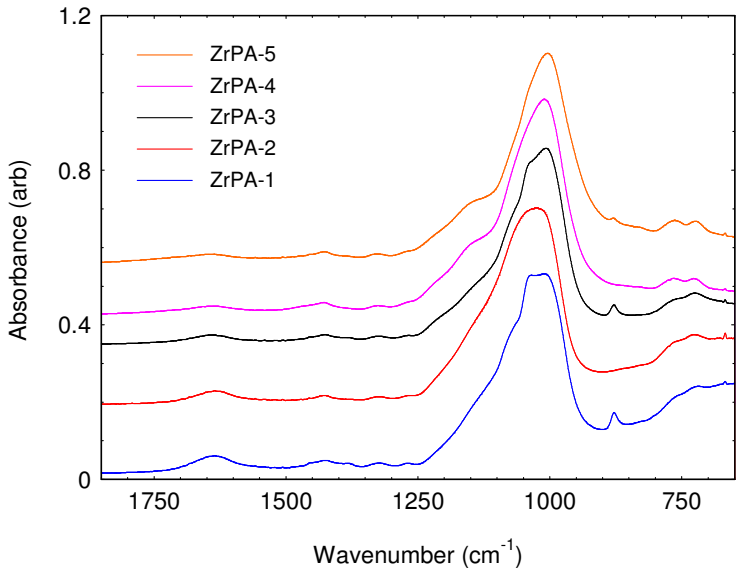

Figure 3.14: FTIR spectra of ZrPA samples.

Table 3.7: Wavenumbers and assignments of FTIR absorbance bands in P-O stretch region of ZrP materials

	band I (cm^{-1})	**band II (cm^{-1})**	**band III (cm^{-1})**
ZrPA	1000-1005	1055-1060	1140-1155
ZrPB	1000-1030	1060-1075	1130-1140
ZrPC	1000-1010	1060-1070	1130-1150
assignment	$PO_3^{2-}{}_{sym}$ (920-990)[29] P-OH (910-1040)[29]	$PO_3^{2-}{}_{asym}$ (970-1090)[29]	P-O-Zr (1100-1030)[32]

The FTIR spectra of the ZrPB series are shown in Figure 3.15. The same absorbance bands are visible in these spectra as were described above for the ZrPA series. Spectral deconvolution of the broad P-O absorbance band of the ZrPB samples again indicated the presence of three bands, the peak positions of which are given in Table 3.7. As for the ZrPA series, the relative intensity of the three absorbance bands in the P-O stretch region could not be determined as there was insufficient structure in the spectral envelope.

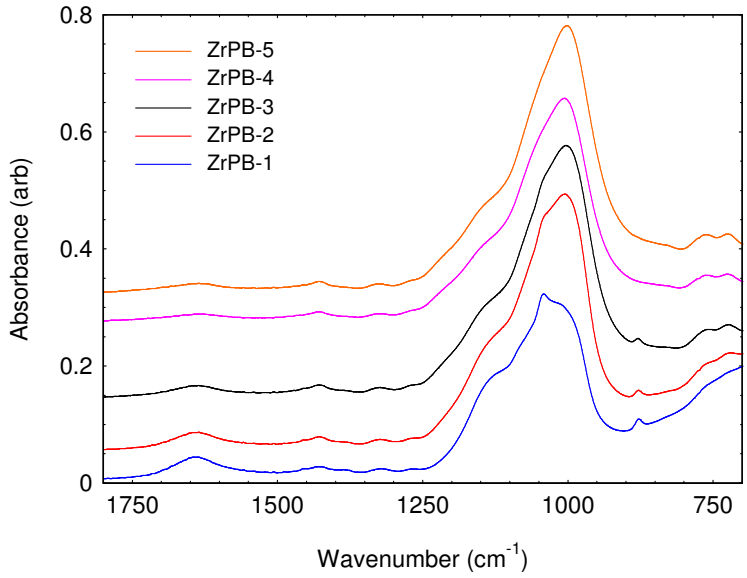

Figure 3.15: FTIR spectra of ZrPB samples.

The FTIR spectra of the ZrPC series are shown in Figure 3.16. The same absorbance bands are again visible in these spectra. Spectral deconvolution of the broad P-O absorbance band of the ZrPC samples indicated the presence of three bands, the peak positions of which are given in Table 3.7. Although the relative intensity of these deconvolved absorbance bands could still not be determined for the ZrPC materials, a shift in the peak position of the overall P-O absorbance band to lower wavenumber (1030 to 960 cm^{-1}) was observed as the molar P/Zr ratio of the materials was increased (Figure 3.16). Since P-OH stretching vibrations appear at the low wavenumber end of the P-O stretch region, this trend suggested that the amount of free P-OH groups increased with the molar ratio P/Zr. The shape of the P-O

absorbance band in Figure 3.16 was also observed to change with the molar ratio P/Zr. Specifically, the ratio of the absorbance band at 960 - 1030 cm^{-1} to that of the shoulder at 1130 cm^{-1} increased from 1.5 for ZrPC-1, 1.7 for ZrPC-2, 2.1 for ZrPC-3, 2.5 for ZrPC-4 to 3.1 for ZrPC-5. This also suggested that as the molar ratio P/Zr in the samples increased the amount of PO_3^{2-} and P-OH groups relative to P-O-Zr groups increased. A similar change in shape occurred in the FTIR spectra of the ZrPA and ZrPB series with increasing molar P/Zr ratio (Figures 3.14 and 3.15), but was less obvious because the P-O absorbance band in the FTIR spectra of the ZrPA and ZrPB series were broader than for the ZrPC series.

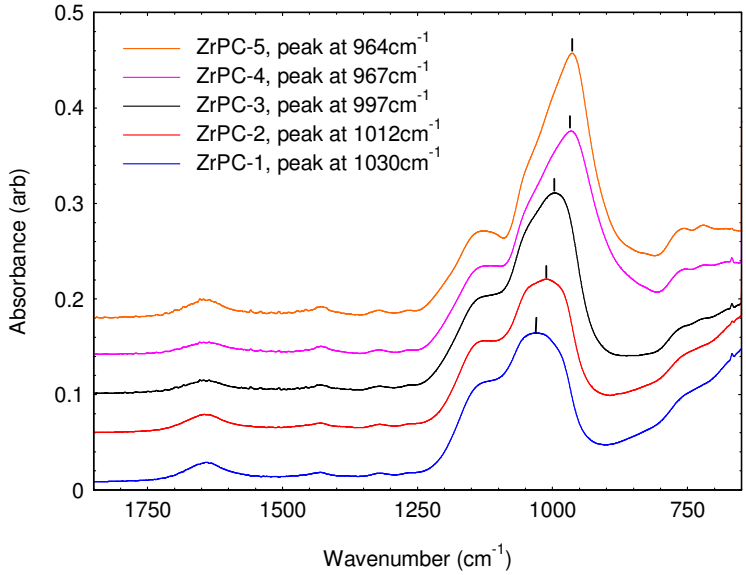

Figure 3.16: FTIR spectra of ZrPC samples.

The FTIR spectra of ZrPC-5 before and after Eu sorption are shown in Figure 3.17. Spectral deconvolution of the three bands in the P-O stretching region was possible for these samples as a higher degree of structural resolution was present in the data. The most intense band, which appeared at 967 and 976 cm^{-1} before and after Eu sorption, respectively, was assigned as the symmetric stretch of PO_3^{2-} or P-OH stretching (or both).[29] The absorbance band at 1041-1045 cm^{-1} was assigned as the asymmetric stretch of PO_3^{2-} and did not change substantially upon Eu sorption. The final band, which was assigned as P-O groups coordinated to metal centres,[32] was of most interest as it shifted substantially from 1141 to 1125 cm^{-1} and its relative intensity increased approx. 60 % upon Eu sorption. The wavenumber shift and increase in intensity of the P-O-metal absorbance band upon Eu sorption provides strong evidence that the sorbed Eu was coordinated by the phosphonate groups within the ZrP materials.

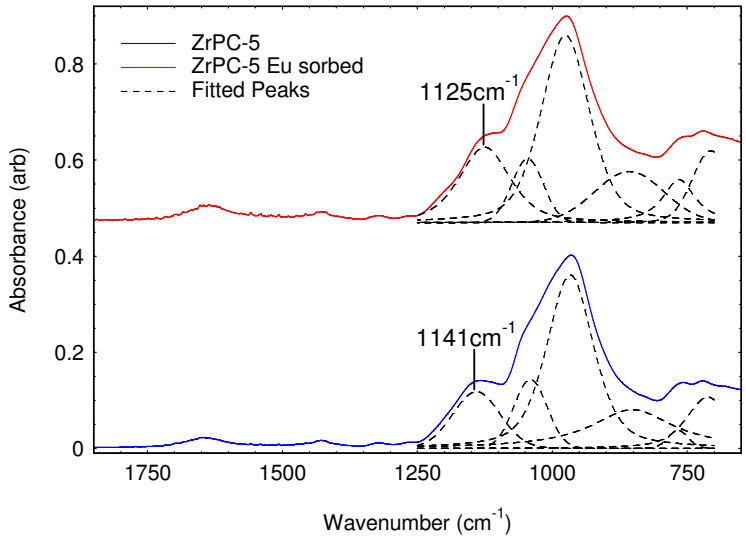

Figure 3.17: FTIR spectra of ZrPC-5 before and after Eu sorption.

3.2.10 Solid-State Nuclear Magnetic Resonance

3.2.10.1 ^{13}C Magic Angle Spinning Nuclear Magnetic Resonance

Figure 3.18 shows the ^{13}C magic angle spinning nuclear magnetic resonance (MAS NMR) spectrum of ZrPA-3, which was chosen to be representative of all the ZrP samples. The ^{13}C MAS NMR spectrum contains three shifts at 27, 54 and 61 ppm. The shifts at 27 and 61 ppm are residual solvent peaks from isopropanol that was generated during synthesis. The major peak at 54 ppm is attributed to the methylene group of ATMP, since similar chemical shifts have previously been shown to correspond to a methylene group between a tertiary amine and a phosphonic acid.[24,33,34]

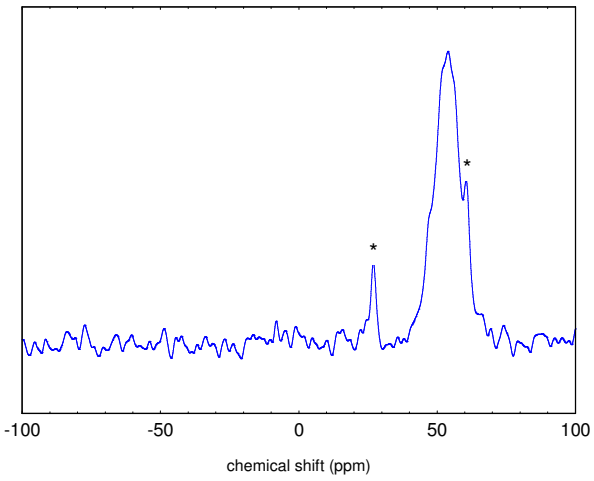

Figure 3.18: ^{13}C MAS-NMR spectrum of ZrPA-3 (* = residual solvent peaks)

3.2.10.2 ^{31}P Magic Angle Spinning Nuclear Magnetic Resonance

The ^{31}P MAS NMR spectra of selected ZrPA, ZrPB and ZrPC series materials were measured and all consisted of relatively broad but structured resonances. The ^{31}P MAS NMR spectra of ZrPA-3 and -4 are shown in Figure 3.19. Deconvolution of the spectral envelope of ZrPA-3 indicated four shifts at -3.5, 4.8, 11.2 and 19.3 ppm while the ^{31}P NMR spectral envelope of ZrPA-4 was fitted with three shifts at -3.2, 4.0 and 10.0 ppm. The relative intensities of the fitted peaks are given in Table 3.8. Increasing the molar ratio P/Zr from ZrPA-3 to ZrPA-4 decreased the number of signals in the ^{31}P MAS NMR spectrum as the peak with chemical shift 19.3 ppm in ZrPA-3 was no longer present in ZrPA-4. However, the peak with chemical shift 10.0 ppm in the ZrPA-4 spectrum was substantially broader than the peak with a similar chemical shift of 11.2 ppm in the ZrPA-3 spectrum (FWHM 13.4 versus 10.1 ppm). Thus, it is possible that the fourth peak was still present in the ZrPA-4 spectrum but due to a change in its chemical shift or a decrease in its size, it could no longer be resolved.

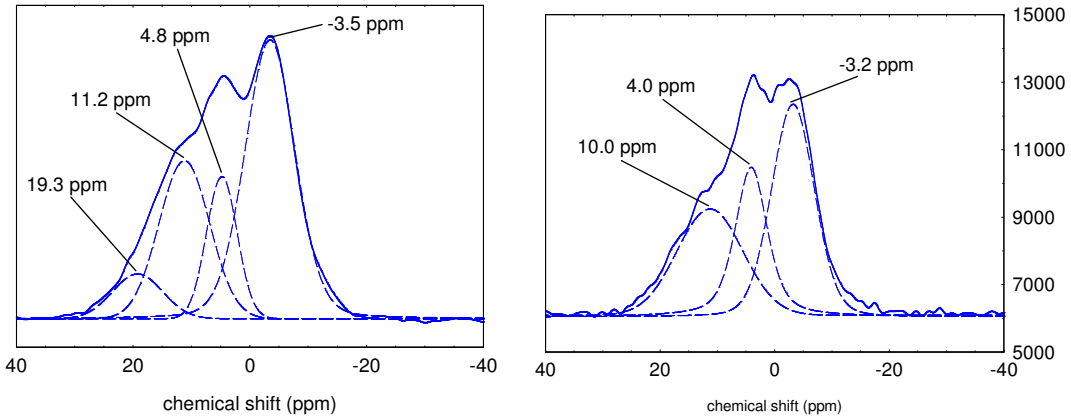

Figure 3.19: ^{31}P MAS NMR spectra of ZrPA-3 (left) and ZrPA-4 (right) with fitted peaks.

Table 3.8: Relative intensities of deconvolved peaks in ^{31}P MAS NMR spectra of ZrP materials

chemical shift (ppm)	ZrPA-3	ZrPA-4	ZrPB-4	ZrPC-3	ZrPC-5
18 to 20	0.07			0.27	0.12
10 to 11	0.27	0.38	0.35	0.15	0.50
3 to 5	0.15	0.18	0.17	0.37	0.16
-2 to -4	0.51	0.44	0.49	0.21	0.21
-25					0.01

The ^{31}P MAS NMR spectrum of ZrPB-4 is shown in Figure 3.20. The spectral envelope of ZrPB-4 was fitted with three peaks at -3.3, 4.0 and 9.6 ppm and their relative intensities are given in Table 3.8. The ^{31}P MAS NMR spectra of ZrPC-3 and -5 are shown in Figure 3.21. Spectral deconvolution of the ^{31}P MAS NMR spectrum of ZrPC-3 suggested the spectral envelope contained four peaks at -2.3, 2.9, 10.3 and 17.5 ppm while the ^{31}P NMR spectral

envelope of ZrPC-5 was more complex but better defined, and so could be satisfactorily fitted with five chemical shifts at -25.0, -1.6, 3.2, 10.1 and 19.9 ppm. The relative intensities of the fitted peaks are given in Table 3.8.

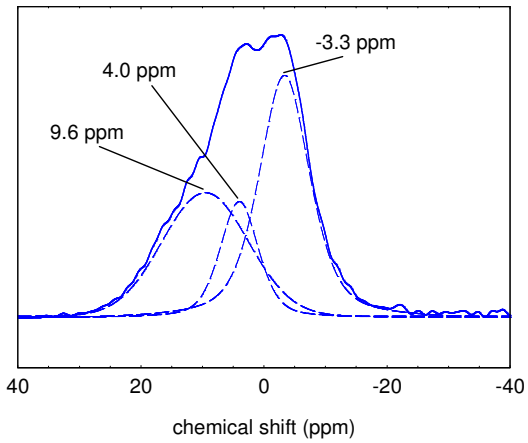

Figure 3.20: ^{31}P MAS NMR spectra of ZrPB-4 with fitted peaks

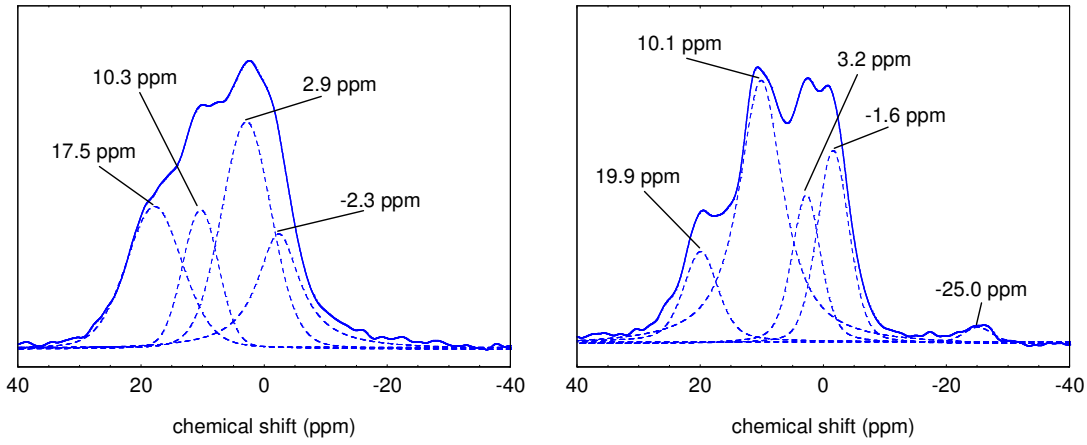

Figure 3.21: ^{31}P MAS NMR spectra of ZrPC-3 (left) and ZrPC-5 (right) with fitted peaks.

Further NMR experiments were performed on ZrPA-3 and ZrPC-5 to elucidate more about the structural differences between ZrP materials that demonstrated low Ln sorption (ZrPA-3) and high Ln sorption (ZrPC-5). Directly polarised ^{31}P MAS NMR of ZrPC-5 showed all the same peaks as cross-polarised spectrum in Figure 3.21, indicating that all the P environments were close to H atoms. This was expected given that all the P atoms in ATMP are nearest neighbours with a CH_2 group. Further evidence of the correlation between the CH_2 group in ATMP, which has a ^{1}H chemical shift of ~4 ppm, and all four phosphonate P signals in ZrPC-5 was provided by the 2D ^{1}H-^{31}P HetCor NMR of ZrPC-5 in Figure 3.22. This data also suggested that the different phosphonate signals had varying degrees of hydration and that the P environment at -2 to -4 ppm was the most hydrated. 2D ^{1}H-^{31}P HetCor NMR of ZrPA-3 showed the same result.

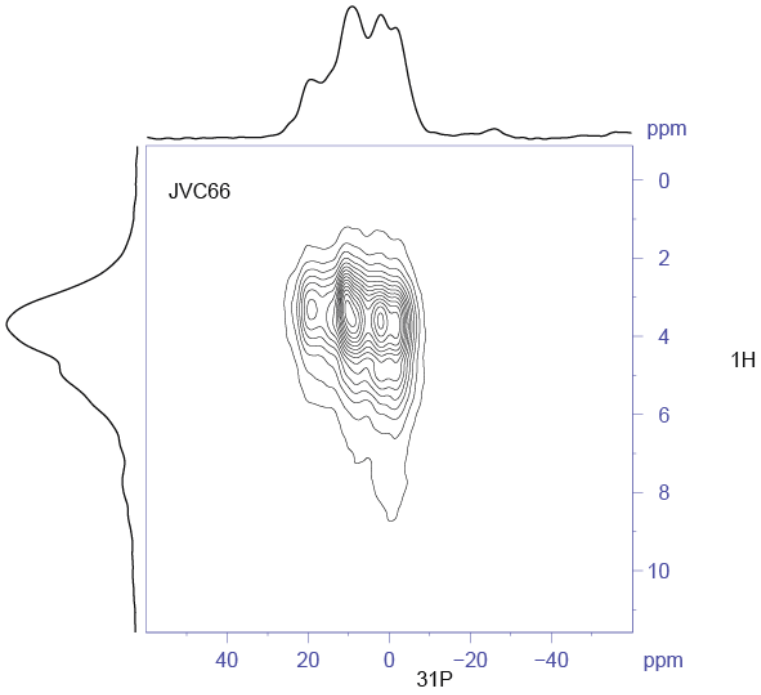

Figure 3.22: 2D ^{1}H-^{31}P HetCor NMR of ZrPC-5

Spin relaxation time (T1) experiments on ZrPC-5 showed that all the P signals in the 20 to -2 ppm envelope relaxed at a similar rate and were therefore the same phase. However, the signal at -25 ppm relaxed more slowly which suggested that this signal was due to a small amount of a secondary phase. A ^{31}P-^{1}H recoupling experiment also showed that all the P signals in the 20 to -2 ppm envelope of ZrPC-5 were suppressed at a similar rate while the signal at -25 ppm was more slowly supressed. Thus, the secondary phase was further from H atoms than the other P environments. Finally, ^{31}P chemical shift anisotropy (CSA) recoupling experiments on ZrPC-5 showed that the signal at -25 ppm decayed more slowly than the signals in the 20 to -2 ppm envelope, which suggested the P environment with chemical shift -25 ppm was symmetrical. ^{31}P CSA experiments on ZrPA-3 showed that the signals at -2 to -4 ppm and 18 to 20 ppm decayed more quickly and hence were less symmetrical than those at 3 to 5 ppm and 10 to 11 ppm.

T1 relaxation measurements were also performed on ZrPA-3 and ZrPC-5 after contact with Eu solutions in 0.1 M nitric acid. ZrPA-3 had an unchanged 10-30 s relaxation time before and after contact with Eu, indicating that minimal Eu was sorbed by this material. On the other hand, the relaxation time of ZrPC-5 decreased from approx. 100 s to approx. 10 s after contact with Eu, uniformly across all the phosphonate signals. This indicated that Eu was sorbed by ZrPC-5 and that the sorbed Eu was within 1 nm of all the measured P environments. This result also confirmed that all the phosphonate environments were closely integrated within the ZrP materials, not in separated domains.

3.2.11 Small Angle X-Ray Scattering

In general, the small angle x-ray scattering (SAXS) data of the ZrP materials was consistent with scattering from three dimensional particles at low Q and porous structures at high Q, suggesting porous particles. Also, it should be noted that the SAXS data of the slurry samples in 0.1 M nitric acid extend to higher Q than the dry powder samples as the slurry samples were measured at the Australian Synchrotron rather than using a lab based SAXS instrument. There was a difference in contrast factor between the ZrP materials and their medium for the dry powder samples, which were measured under vacuum, and the slurry samples, which were measured in 0.1 M nitric acid. Since scattering intensity is proportional to the contrast factor,[35,36] the intensity of the scattering from the ZrP materials when dry and when wet were not directly comparable. Furthermore, the SAXS data was not able to be placed on an absolute scale because the path length could not be quantitatively determined. As a result, the data was only able to be analysed qualitatively rather than quantitatively.

The SAXS patterns of the ZrPA materials are shown in Figure 3.23. All the SAXS patterns of the ZrPA materials showed a Q^{-x} dependence with x = 3.4 to 4.0 at low Q (0.02 to 0.11 $Å^{-1}$) and x = 1.2 to 2.5 at high Q (0.24 to 0.39 $Å^{-1}$). The specific power law exponents are given in Table 3.9. The power law dependence at low Q was indicative of the presence of large three-dimensional scattering objects with varying degrees of surface roughness.[37] The fact that no turnover was observed in in the data measured from 0.01 $Å^{-1}$ suggested that these three-dimensional particles were large in size, greater than approx. 600 Å. The power law dependence at high Q indicated that on a smaller scale there were polymer-like scattering structures for ZrPA-1 and -5 and higher dimensional scattering structures for ZrPA-3 and -4.[36] The Q range of these scatterers suggested that they were all less than approx. 50 Å in size.

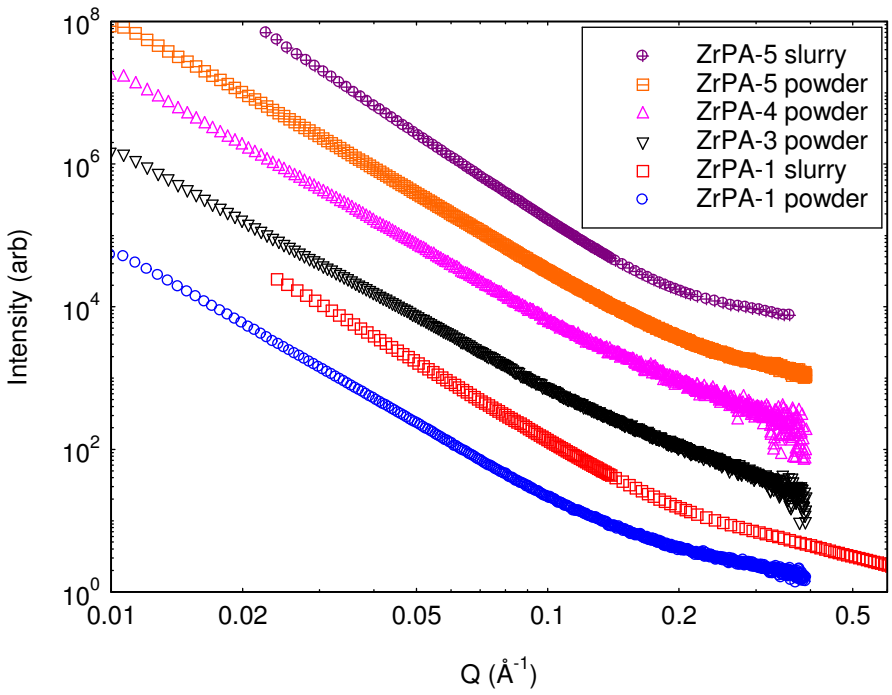

Figure 3.23: SAXS data of ZrPA materials. Traces have been offset for clarity.

Table 3.9: Power law exponents from SAXS data of ZrPA samples

	low Q power law exponent (0.02 – 0.11 Å)	**high Q power law exponent (0.24 – 0.39 Å)**
ZrPA-1 powder	-3.5	-1.5
ZrPA-1 slurry	-3.6	-1.6
ZrPA-3 powder	-3.4	-2.4
ZrPA-4 powder	-3.5	-2.5
ZrPA-5 powder	-3.5	-1.6
ZrPA-5 slurry	-4.0	-1.2

The SAXS patterns of the ZrPB materials are shown in Figure 3.24. Similar to the ZrPA samples, the SAXS patterns of the ZrPB dry powders showed a Q^{-x} dependence with x = 3.4 to 4.0 at low Q (0.01 to 0.04 $Å^{-1}$) and x = 1.2 to 2.5 at intermediate Q (0.20 to 0.39 $Å^{-1}$). For the ZrPB slurry samples, the SAXS data extended to higher Q so a third power law exponent was observed from 0.40 to 1.14 $Å^{-1}$. The specific power law exponents are given in Table 3.10. The power law dependence at low Q again indicated that large (> 600 Å) three-dimensional scattering objects with varying degrees of surface roughness were present in all these samples.[37] The power law dependence at intermediate Q indicated that there were also scattering structures on the 10-100 Å scale that decreased in dimensionality across the ZrPB series. Finally, the power law dependence at high Q suggested that approx. < 15 Å scattering structures were present in the slurry samples. These small scatterers were globular in nature for the ZrPB-1 slurry and swollen polymer-like for the ZrPB-4 slurry.[36,37]

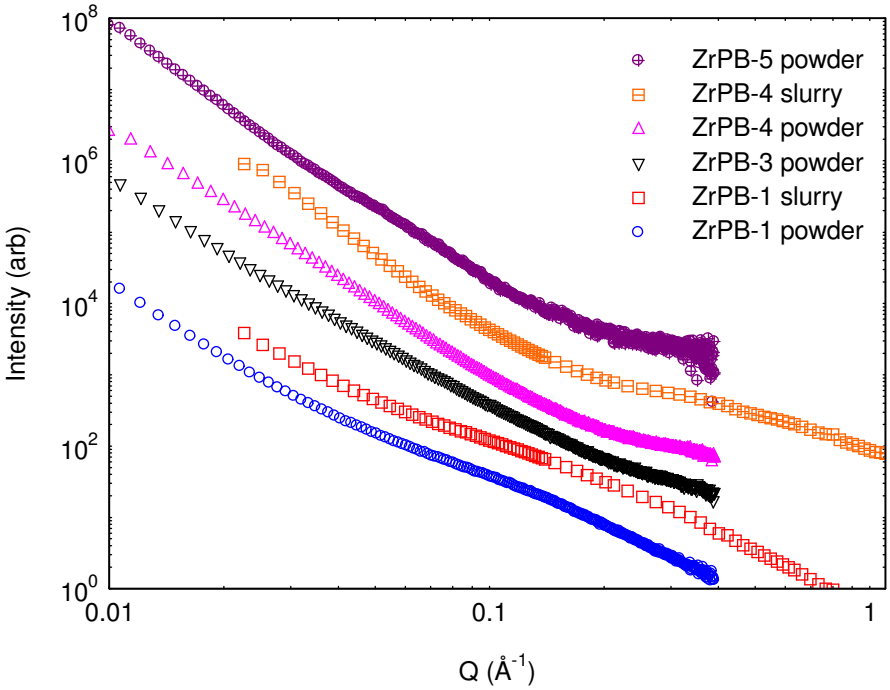

Figure 3.24: SAXS data of ZrPB materials. Traces have been offset for clarity.

Table 3.10: Power law exponents from SAXS data of ZrPB samples

	low Q power law exponent (0.01 – 0.04 Å)	**medium Q power law exponent (0.20 – 0.39 Å)**	**high Q power law exponent (0.40 – 1.14 Å)**
ZrPB-1 powder	-3.4	-2.5	
ZrPB-1 slurry	-2.7	-2.2	-2.9
ZrPB-3 powder	-3.4	-1.6	
ZrPB-4 powder	-3.5	-1.2	
ZrPB-4 slurry	-4.0	-1.0	-1.5
ZrPB-5 powder	-4.0	-1.2	

The SAXS patterns of the ZrPC series dry powder samples are shown in Figure 3.25. All the SAXS data for the dry powder samples showed a Q^{-x} dependence with x = 3.3 to 4.2 at low Q (0.01 to 0.04 $Å^{-1}$) and a substantially more variable x = 0.7 to 3.0 at high Q (0.22 to 0.39 $Å^{-1}$). The specific power law exponents are given in Table 3.11. As for the ZrPA and ZrPB series, the power law dependence at low Q indicated the presence of large (> 600 Å) three-dimensional scattering objects with varying degrees of surface roughness. The power law exponent at high Q for the ZrPC dry powders indicated the presence of smaller (< 100 Å) scattering structures that decreased in dimensionality from three dimensional particles with rough surfaces for ZrPC-1 to rod-like structures for ZrPC-5.

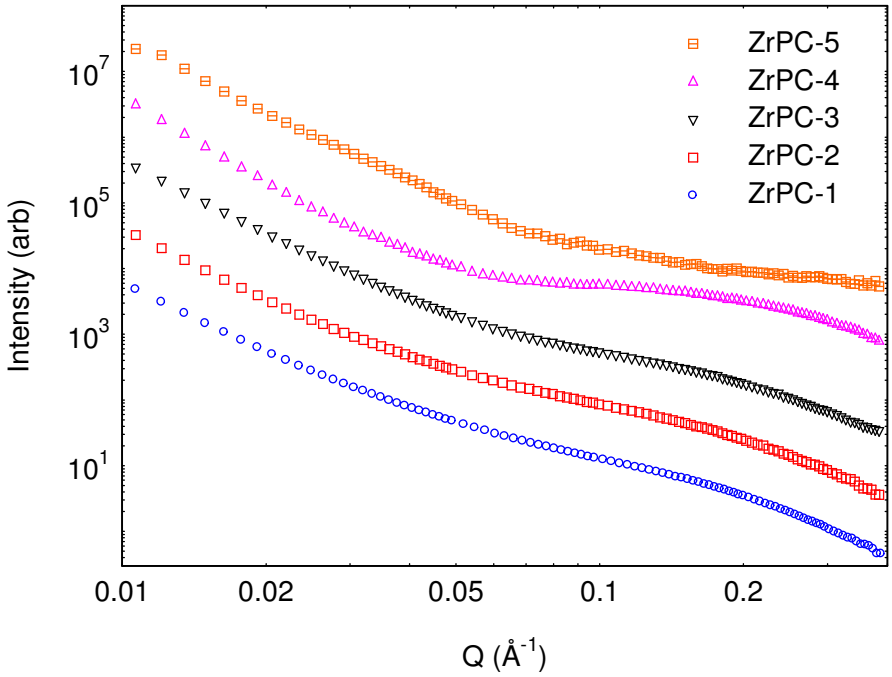

Figure 3.25: SAXS data of ZrPC materials as dry powders. Traces have been offset for clarity.

Table 3.11: Power law exponents from SAXS data of ZrPC dry powder samples

	low Q power law exponent (0.01 – 0.04 Å)	**high Q power law exponent (0.22 – 0.39 Å)**
ZrPC-1 powder	-3.3	-3.0
ZrPC-2 powder	-3.4	-2.8
ZrPC-3 powder	-3.6	-2.6
ZrPC-4 powder	-4.2	-2.0
ZrPC-5 powder	-3.8	-0.7

The SAXS patterns of the ZrPC slurry samples are shown in Figure 3.26. The ZrPC-1 slurry showed a Q^{-x} dependence with x = 2.6 at low Q (0.02 to 0.35 $Å^{-1}$) and x = 3.1 at high Q (0.45 to 1.14 $Å^{-1}$). The SAXS patterns of the ZrPC-3, -4 and -5 slurries on the other hand showed correlation peaks. Although these peaks appear as single peaks via visual inspection, the peak shape could not be fit with a single peak model. Thus, both broad and Lorentzian peaks were fit to the data on a power law background and the parameters of these model fits are given in Table 3.12. As for the dry powder samples, the ZrPC slurries consisted of large three-dimensional particles, as indicated by their power law exponents of -2.6 to -3.8 at low Q. The power law exponents of the ZrPC slurries were consistently lower than their corresponding dry powder samples, suggesting an increase in the surface roughness of these particles when wet. The appearance of correlation peaks in the SAXS patterns of the ZrPC-3, -4 and -5 slurries also suggested that these materials showed increased porosity when wet.

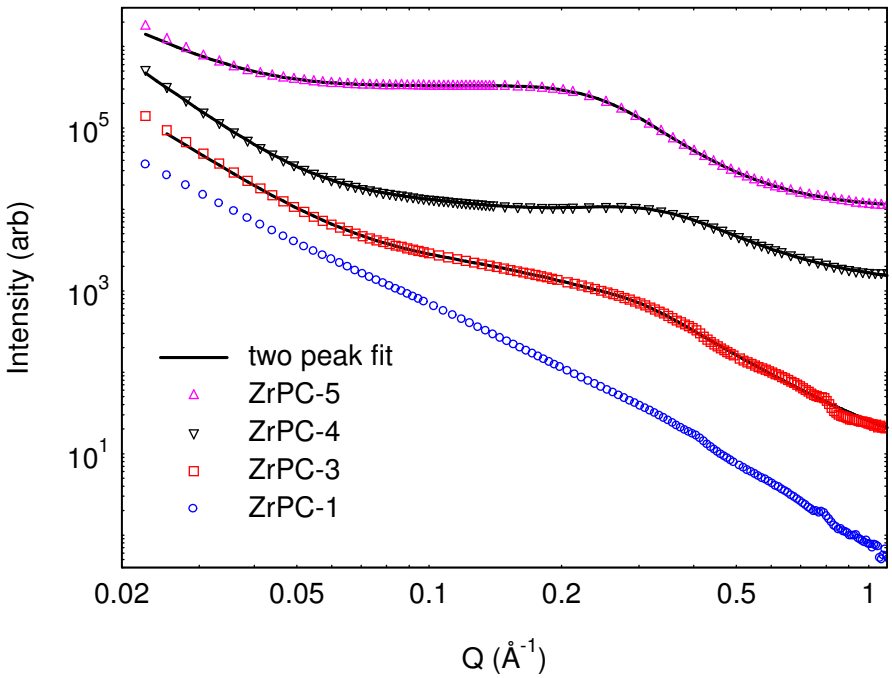

Figure 3.26: SAXS data of ZrPC materials as slurries in 0.1 M nitric acid. Traces have been offset for clarity.

Table 3.12: Parameters of broad and Lorentzian peak fit for ZrPC-3, -4 and -5 slurries

	power law exponent	peak type	d-spacing (Å)*	peak width ($Å^{-1}$)	broad peak exponent	χ^2/Npts
ZrPC-3	3.4	broad	>600	0.18 ± 0.002	3.0	61
		Lorentzian	23 ± 5	0.10 ± 0.001		
ZrPC-4	3.8	broad	95 ± 10	0.10 ± 0.001	1.8	40
		Lorentzian	22 ± 5	0.17 ± 0.0002		
ZrPC-5	2.8	broad	52 ± 5	0.13 ± 0.001	2.9	39
		Lorentzian	26 ± 5	0.09 ± 0.0003		

*D-spacing errors assumed to be 10 Å below 0.1 $Å^{-1}$ and 5 Å above

For the ZrPC-3 slurry, the broad peak had a large d-spacing (> 600 Å) and large width, suggesting that this peak represented large, polydisperse particles.[36] The broad peaks in the ZrPC-4 and -5 slurries had substantially smaller d-spacings and were not as wide as for ZrPC-3. Therefore, these broad peaks were hypothesised to represent mesoporous structures that developed in these materials when wet. Given the large width of these broad peaks, wormhole mesoporosity with a large range of pore sizes was implicated.[38] The Lorentzian peaks in the ZrPC-3, -4 and -5 slurries all had similar d-spacings of approx. 20-25 Å, again indicative of mesopores. Thus, small 20-25 Å mesopores were present in the ZrPC-3, -4 and -5 slurries while larger (50-100 Å) mesopores were also present in the ZrPC-4 and -5 slurries. Again, the large width of these smaller mesopores indicated disordered, wormhole mesoporosity.

3.2.12 Extended X-ray Absorption Fine Structure (EXAFS) Spectroscopy

The Extended X-ray Absorption Fine Structure (EXAFS) spectra for the Zr *K* edge of a selection of ZrP materials covering the range of synthesis conditions; ZrPA-1, -3, -4, -5, ZrPB-1, -3, -4, ZrPC-1, -2, -3 and -5, were measured at the Photon Factory, Tsukuba, Japan. The measured edge steps for ZrPA-5 and ZrPB-3 were less than 0.5 so these data were excluded from analysis. The remaining EXAFS spectra were observed to fall into one of two different shape categories, designated A and B and represented by ZrPA-1 and ZrPA-4, respectively, in *Figure 3.27*. The EXAFS data of ZrPA-1, ZrPB-1, ZrPB-4, ZrPC-1, ZrPC-2 and ZrPC-3 were closer to shape 'A' while ZrPA-3, ZrPA-4 and ZrPC-5 were closer to shape 'B'.

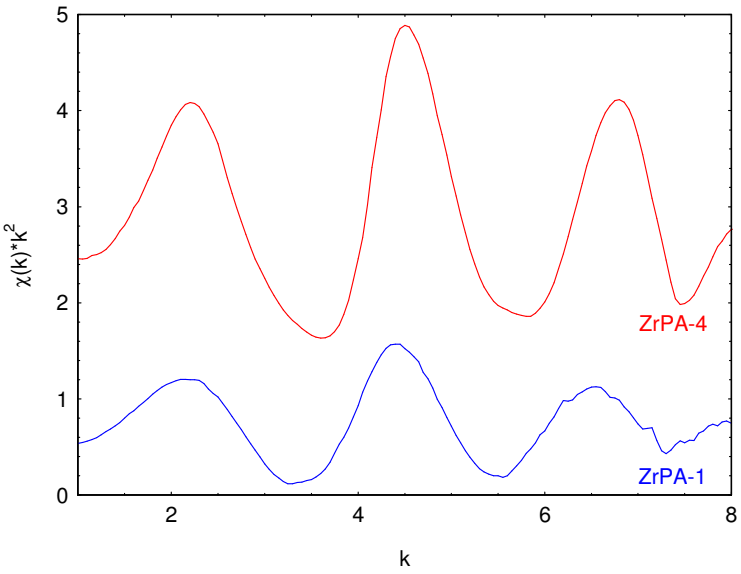

Figure 3.27: EXAFS spectra of Zr K edge for ZrPA-1 (shape 'A') and ZrPA-4 (shape 'B'). Traces have been offset for clarity.

The EXAFS spectrum of ZrPA-1 (shape 'A') was background subtracted with a R_{bkg} value of 0.79 using the data processing program Athena.[39] A Fourier transform was then applied to the aligned and background subtracted data in the k-range 2.0 to 7.5 using a Hanning window with a window sill width (dk) of 1.5, to give χ(R). Finally, the R-range 0.8 to 3.3 Å was fit to a theoretical model based on the crystal structure of hydrated zirconium phosphate ($Zr(HPO_4)_2(H_2O)$) using Artemis software.[39] The number of independent points in the fit was 9 and the number of variables in the fit was 6. The best calculated fit (R-factor 0.011, χ_v^2 1642) is shown in Figure 3.28 and the fit parameters are given in Table 3.13. This R-factor indicated that the degree of mismatch between the experimental data and the model fit was 1.1 %. Fitting data for the other ZrP samples with shape 'A' using the same theoretical model are given in Appendix A.

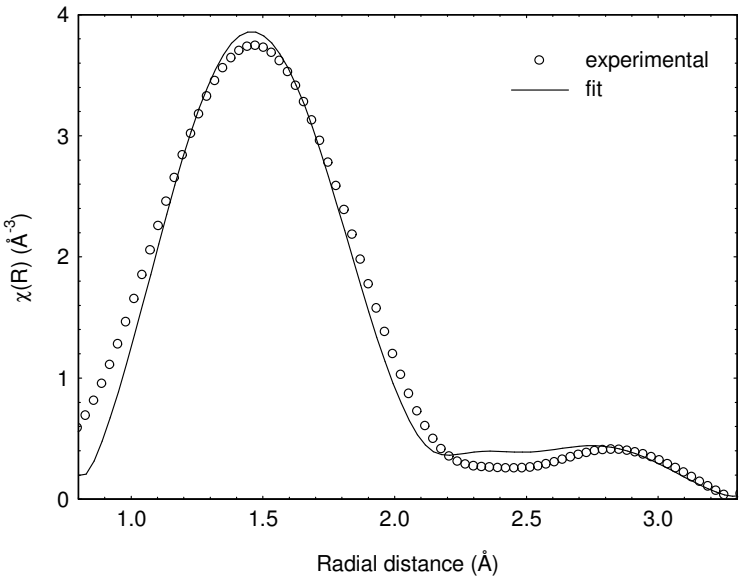

Figure 3.28: Experimental and calculated Fourier transforms of ZrPA-1 EXAFS from FEFF code for $Zr(HPO_4)_2(H_2O)$ with single scattering from inner-shell O and P.

Table 3.13: Fitting parameters of Zr EXAFS for ZrPA-1 (shape 'A') and ZrPA-4 (shape 'B')

Sample	Path	S_0^2	E_0	N	R (Å)	σ^2 (Å^2)
ZrPA-1	Zr-O	1.0 ± 0.2	-3.0 ± 1.7	4	2.09 ± 0.02	0.006 ± 0.003
	Zr-P			2	3.72 ± 0.10	0.021 ± 0.020
ZrPA-4	Zr-O	1.3 ± 0.2	-3.8 ± 1.3	6	2.04 ± 0.01	0.004 ± 0.002
	Zr-P			6	3.60 ± 0.02	0.008 ± 0.003

The best-fit model of ZrPA-1 (shape 'A') consisted of single scattering from a first coordination sphere of 4 O atoms and 2 P atoms. Fitting the ZrPA-1 EXAFS data with a theoretical model based on the crystal structure of monoclinic ZrO_2 gave fitting parameters consistent with those in Table 3.13 for the Zr-O path. However, the σ^2 value for the scattering from the Zr-Zr path was very high (0.034 ± 0.029) and the overall fit was poorer than that shown in Figure 3.28. Thus, the first coordination sphere of the Zr atoms in ZrPA-1 has been shown to consist of O and P atoms rather than O and Zr atoms.

The EXAFS spectrum of ZrPA-4 (shape 'B') was background subtracted using a R_{bkg} value of 0.79 using the data processing program Athena.[39] A Fourier transform was then applied to the aligned and background subtracted data in the k-range 2.0 to 8.9 using a Hanning window with dk 1.1, to give χ(R). Finally, the R-range 0.8 to 3.2 Å was fit to the theoretical model based on the crystal structure of hydrated zirconium phosphate ($Zr(HPO_4)_2(H_2O)$) using Artemis software.[39] The number of independent points in the fit was 10 and the number of variables in the fit was 6. The best calculated fit (R-factor 0.011, χ_v^2 5751) is shown in Figure 3.29 and the fit parameters are given in Table 3.13. Fitting data for the other ZrP samples with shape 'B' using the same theoretical model are given in Appendix A.

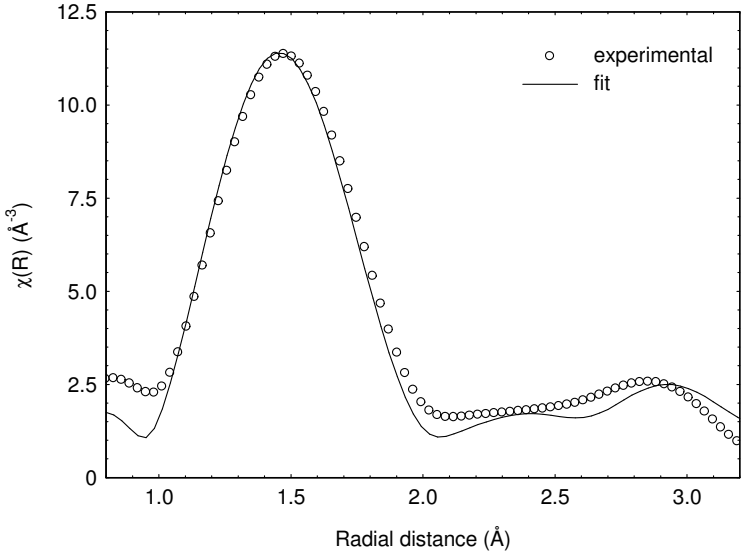

Figure 3.29: Experimental and calculated Fourier transforms of ZrPA-4 EXAFS from FEFF code for $Zr(HPO_4)_2(H_2O)$ with single scattering from inner-shell O and P.

The best-fit model of ZrPA-4 (shape 'B') consisted of single scattering from a first coordination sphere of 6 O atoms and 6 P atoms. Fitting the ZrPA-4 EXAFS data with a theoretical model based on the crystal structure of monoclinic ZrO_2 gave a σ^2 value for the Zr-O path with an error larger than the value itself and an overall fit that was poorer than that shown in Figure 3.29. Thus, as for ZrPA-1, the first coordination sphere of the Zr atoms in ZrPA-4 has been shown to consist of O and P atoms rather than O and Zr atoms.

The amplitudes (S_0^2) for the model fits of both EXAFS data types A and B were consistent (Table 3.13 and Appendix A). However, the modelled coordination numbers for shape B were higher than those modelled for shape A, and the radial distances Zr-O were consistently slightly shorter for shape 'B' than shape 'A'. In addition, while the σ^2 values for the Zr-O paths were within error of each other for both spectrum shapes, the σ^2 value for the Zr-P path was consistently higher for shape 'A' than for shape 'B'. Thus, the modelling of the EXAFS data suggested that there were more atoms in the first coordination sphere of Zr for shape 'B' than for shape 'A' and that these atoms were more closely bound.

3.3 Discussion

4.3.1 NMR Assignments

All the ^{31}P chemical shifts of the NMR signals for the ZrP materials fit into 5 broad categories of (1) 18 to 20 ppm, (2) 10 to 11 ppm, (3) 3 to 5 ppm, (4) -2 to -4 ppm and (5) -25 ppm. The ^{31}P chemical shift at -25 ppm was observed only in ZrPC-5 and was consistent with the chemical shift of a zirconium phosphate group.[11,40] This assignment was supported by spin relaxation time and ^{31}P-^{1}H recoupling experiments on ZrPC-5, which

showed that the signal at -25 ppm was from a different phase to the other signals and was further from H atoms. ^{31}P CSA recoupling experiments also indicated that this P environment was symmetrical ($POZr_4$). Thus, it appears that a small amount of phosphate formed via decomposition of the ATMP during hydrothermal treatment to synthesise ZrPC-5. However, the low relative intensity of the signal at -25.0 ppm (0.01) indicated that the amount of this degradation was minimal.

The remaining ^{31}P chemical shifts were assigned as phosphonate signals,[17,40,41] but their degree of coordination was unknown. Literature suggests that the ^{31}P chemical shift of a phosphonate becomes more upfield shifted as metal coordination increases.[42-44] According to this hypothesis the most downfield signal in the ^{31}P NMR spectra of the ZrP materials, with chemical shift 18 to 20 ppm, should correspond to the "free" phosphonate without Zr coordination $P(O)(OH)_2$. However, the intensity of this signal decreased when the ratio P/Zr was increased and the FTIR data (*section 3.2.9*) suggested that increasing the ratio P/Zr in the ZrP materials increased the number of P-OH groups. Thus, the hypothesis of phosphonate ^{31}P signals being shifted upfield upon metal coordination was inconsistent with the FTIR results and was not adopted.

Grossmann et al. (2004) in their NMR investigations of ATMP found that in the solid state the chemical shift of fully protonated ATMP was 12.5 ppm.[41] This value shifted upfield as the ATMP was titrated with Na or Li only until the ATMP became fully coordinated by the metal, at which point the chemical shift became suddenly and dramatically shifted downfield to between 19 and 24 ppm. From this, the signal with chemical shift 10 to 11 ppm was assigned as $P(O)(OH)_2$ (Figure 3.30) because it was closest to the measured literature value of 12.5 ppm for fully protonated ATMP. In addition, this signal demonstrated the least variation in its chemical shift value between the ZrP samples and the broader chemical shift range of the other signals can be attributed to coordination of Zr ions by the P-O groups with different degrees of affinity. The signal with chemical shift 3 to 5 ppm was assigned as P(O)(OH)(OZr) and the signal with chemical shift -2 to -4 ppm was assigned as $P(O)(OZr)_2$ (Figure 3.30) since metal coordination has previously been shown to cause upfield shifts in NMR signals.[41,44] Finally, the signal with chemical shift 18 to 20 ppm was assigned as $P(OZr)_3$ (Figure 3.30) because it has been previously demonstrated that upon complete metal coordination, the ^{31}P chemical shift of solid-state ATMP is shifted downfield.[41] ^{31}P CSA recoupling experiments on ZrPA-3 showed that the $P(O)(OZr)_2$ and $P(OZr)_3$ phosphonate environments, that is those with the highest degree of Zr coordination, were the most unsymmetrical.

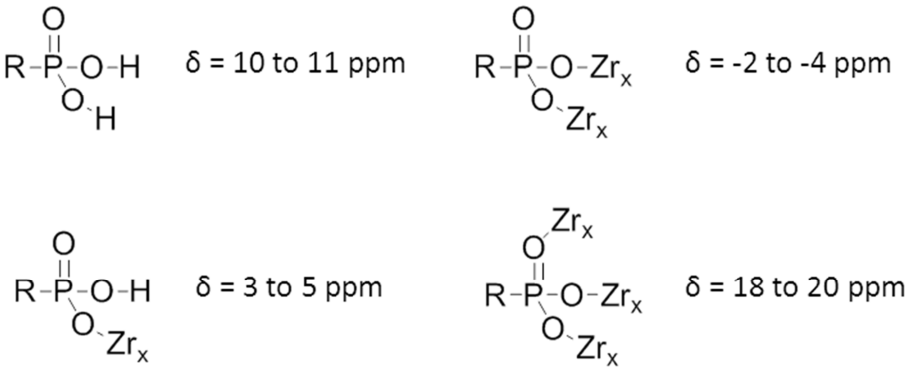

Figure 3.30: ^{31}P MAS NMR chemical shift assignments

3.3.2 Effects of Varying Synthesis Conditions

Independent of the synthesis conditions used, all the ZrP materials were amorphous and showed hierarchical porosity with micro, meso and macropores as well as PSDs dominated by <2 nm (except ZrPB-4 and -5 which only had 20 nm pores). The amorphous nature of the ZrP materials was expected as metal phosphonates tend naturally to be poorly crystalline, especially those based on tri- or tetra-valent metals.[45] Attempts to synthesise crystalline materials were unsuccessful, but amorphous compounds may be preferable in any case as they are generally more reactive and have higher surface areas.[17] All the ZrP materials that showed sorption also showed selectivity for Ln over Co, Cs and Sr, as well as a slight bell-shaped intra-Ln selectivity across the Ln series such that Eu was the most efficiently extracted Ln. This bell-shaped intra-Ln selectivity has been observed previously and was attributed to a combination of electrostatic attraction and dehydration enthalpy of the Ln cations.[46]

3.3.2.1 Increasing the Molar P/Zr Ratio

Elemental analysis showed that the molar P/Zr ratio of the ZrP materials increased as more ATMP was added during synthesis, as expected. This was supported by the EXAFS data, which showed that increasing the molar P/Zr ratio of the ZrP materials caused their Zr *K* edge EXAFS spectra to change from shape 'A' to 'B'. Since the shape 'A' spectrum represented a structure in which the first coordination sphere of Zr contained on average 2 P atoms rather the 6 P atoms represented by shape 'B', the EXAFS data indicated that adding more ATMP during synthesis increased the amount of phosphonate groups coordinated to Zr atoms in the resulting ZrP materials. Elemental analysis also showed that at high molar P/Zr ratios not all of the ATMP added was incorporated into the final product. This effect was the most pronounced for the ZrPB series, followed by the ZrPC series then the ZrPA series (Table 3.4). Again, this was consistent with the EXAFS data, which showed that the molar P/Zr ratio at which the change from shape 'A' to shape 'B' occurred was lower for the ZrPA series than for the ZrPB and ZrPC series.

Substantial changes in the sorption properties, structure and chemical composition of the ZrP materials were observed as the molar P/Zr ratio increased. In general, increasing the

molar P/Zr ratio in the ZrP materials increased their Ln capacity but decreased their selectivity. Also, nitrogen porosimetry showed that in general increasing the molar P/Zr ratio of the ZrP materials decreased their surface area, except between ZrPA-1 and -3. The resulting inverse relationship between surface area and sorption capacity was unexpected and is discussed further in *section 3.3.3* below.

Although increasing the molar P/Zr ratio generally caused a decrease in surface area, this decrease was not linear. The ZrPA, B and C series each showed a discontinuity in their surface area data between molar P/Zr ratio of 2 and 3, although they manifested in different ways, as shown in Figure 3.31. For the ZrPA series, the surface area decreased by approx. two thirds whereas previously it had been increasing. For the ZrPB series, the decrease in surface area became less pronounced and reached a plateau. For the ZrPC series, the decrease in surface area became larger such that ZrPC-5 (with molar P/Zr ratio 3.2) had no measurable surface area whatsoever. The SEM images of ZrPC-5 also showed evidence of densification and agglomeration of the smaller particles to give a more bulk solid morphology, consistent with this porosimetry data. Overall, a structural change occurred in the Zr-O-P network when the molar P/Zr ratio was increased above 2.

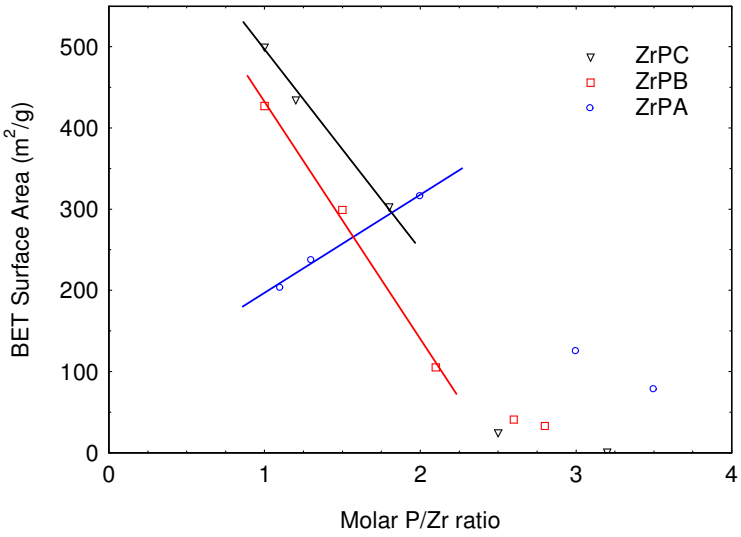

Figure 3.31: Changes in BET surface area with increasing molar P/Zr ratio

The results of SAXS experiments on the ZrPC powder materials provided more information about how the porosity decreased with increasing molar P/Zr ratio for this series. The sizes of the substructures of the particles in ZrPC-1 to -4 according to SAXS were consistent with the pore size from nitrogen porosimetry, so these substructures were assigned as pores. Thus, SAXS showed that the dimensionality of the pores decreased from three dimensional with rough surfaces (ZrPC-1) to polymer-like (ZrPC-4) as the molar ratio P/Zr increased (Table 3.11). This explains the observed decrease in surface area with increasing molar ratio P/Zr. Also, the decrease in the dimensionality of the pores was greatest between ZrPC-3 and -4 (Table 3.11), which corresponds to the largest decrease in surface

area for the ZrPC series between the molar P/Zr ratio of 2 and 3 (Figure 3.31). For the ZrPC-5 powder, the smaller rod-like substructures observed via SAXS were representative of the ZrP material itself as this sample was non-porous according to nitrogen porosimetry and SEM.

A comparison of the ^{31}P MAS-NMR data of ZrPA-3 versus -4 and ZrPC-3 versus -5 provided further insight into the effect of increasing the molar P/Zr ratio on the structure and composition of the ZrP materials. For both the ZrPA and ZrPC series, increasing the molar P/Zr ratio increased the number of $P(O)(OH)_2$ environments with chemical shift 10 to 11 ppm and decreased the number of $P(OZr)_3$ environments with chemical shift 18 to 20 ppm. In addition, for the ZrPA series the $P(O)(OZr)_2$ environment with chemical shift -2 to -4 ppm was decreased and for the ZrPC series the P(O)(OH)(OZr) environment with chemical shift 3 to 5 ppm was decreased (Table 3.8). This was consistent with the FTIR results which also indicated that increasing the P/Zr ratio increased the number of P-OH groups relative to P-O-Zr. It was as expected that with increasing molar P/Zr ratio, the Zr atoms became coordinatively saturated and so the number of free phosphonate groups, uncoordinated by Zr, increased.

3.3.2.2 Differences Between ZrPA, ZrPB and ZrPC Series

Although the ZrPA and ZrPB series were synthesised under very similar conditions, with the only difference being the Zr precursor used, substantial differences were observed in their sorption behaviour and structure. In terms of sorption, the ZrPA materials had lower Ln capacities than the ZrPB series when the molar P/Zr ratio was low. This was because the chloride precursor of the ZrPA series resulted in more acidic synthesis conditions and hence more protonated phosphonate groups unavailable to bind Ln. However, for the high molar P/Zr ratio materials (-4 and -5 samples), the reverse was observed. This was because the difference in the pH of synthesis between the A and B series was smaller for these samples (Table 3.2) and the ZrPB materials had lower 'actual' molar P/Zr ratios (Table 3.4). For example, ZrPA-5 was synthesised at pH 1.0, had a molar P/Zr ratio of 3.5 and sorbed Eu quantitatively while ZrPB-5 was synthesised at pH 1.2 but had a molar P/Zr ratio of 2.8 and so sorbed only 70 % Eu.

Another difference between the sorption properties of the ZrPA and ZrPB series was that Ln sorption increased across the ZrPA series but reached a maximum at ZrPB-3 for the ZrPB series. An increase in Ln sorption with increasing molar P/Zr ratio was expected due to the increasing number of free phosphonate groups available to bind Ln, as described above. However, between ZrPB-3 and -5 the increase in the molar P/Zr ratio appeared to be offset by the decrease in the pH of synthesis (1.4 to 1.2) and the decrease in surface area (105 to 33 m^2/g), resulting in similar sorption for these three samples. The ZrPB materials were also more selective for Ln over Co, Cs and Sr than the ZrPA series and had higher intra-Ln selectivity. Intra-Ln separation to isolate individual elements within the Ln series is challenging but of significant industrial value.[47,48] Thus, the ZrPB materials may be more appropriate for

applications in which selectivity is more critical than capacity, such as environmental applications in which concentrations are generally low.

In terms of structural and compositional differences between the ZrPA and ZrPB series, the ^{31}P NMR spectra of ZrPA-4 and ZrPB-4 were very similar, indicating that the Zr precursor used did not significantly impact the type or number of P environments in the ZrP material produced. There were however substantial differences in the surface areas of the ZrPA materials relative to the ZrPB materials, as shown in Figure 3.31. Thus, the Zr precursor used during synthesis had a large impact on the size and number of pores formed.

The ZrPC series showed more substantial differences to the ZrPA and ZrPB series, as expected given that the ZrPC series was synthesised at higher temperature (160 versus 120 ^{o}C) and higher pH (4-5 versus 1-2). In terms of sorption behaviour, the ZrPC materials demonstrated higher Ln sorption capacities than the ZrPA and ZrPB series, which was attributed to their higher pH of synthesis resulting in more deprotonated phosphonate groups available to bind Ln. In terms of sorption kinetics, the ZrPA-5 and ZrPB-5 materials had similar sorption kinetics but were both slower to sorb Eu than the ZrPC-3, -4 and -5 materials. As a result, the ZrPC materials have the best potential for deployment in columns with relatively fast flow rates. The sorbent with the fastest kinetics was ZrPC-4, which had a rate constant more than an order of magnitude greater than that of ZrPA-5 or ZrPB-5. Given that ZrPC-4 also showed the highest sorption capacity of all the materials tested, ZrPC-4 was considered to have the best Ln sorption properties of all the ZrP materials synthesised. However, the ZrPB series materials were able to provide superior selectivity for Ln over Co, Cs and Sr relative to ZrPC-4.

There were also substantial differences in the structure of the ZrPC materials relative to the ZrPA and ZrPB series. For example, small (< 5 nm) mesopores were the only pores present in the ZrPC materials, while the ZrPA and ZrPB materials also contained larger pores of approx. 40 nm for the ZrPA series and approx. 20 nm for the ZrPB series. Overall, pore size increased in the order ZrPC < ZrPB < ZrPC, which explains why ZrPA-3, ZrPB-2 and ZrPC-3 all had a surface area of approx. 300 m^2/g but their pore volumes were 0.90, 0.40 and 0.27 mL/g, respectively.

3.3.3 Structural Change Upon Wetting

An interesting aspect of the present ZrP materials was the fact that increasing the molar P/Zr ratio generally decreased surface area (as measured by nitrogen porosimetry) but increased Ln sorption capacity. This inverse relationship between surface area and sorption capacity was intuitively contradictory but may be explained by the increased amount of free phosphonate groups available to coordinate Ln at higher molar P/Zr ratios. In some cases however, the presence of increased free phosphonate groups was not sufficient to explain the observed behaviour. For example, ZrPC-5 demonstrated a surface area of 1 m^2/g and Eu capacity of 60 mg/g. The surface area measured by nitrogen access to the pores in this material clearly did not reflect its ability to sorb ions from solution. There were two possible

explanations for this behaviour; (i) the materials exhibited different structures when dry than when wet or (ii) the nitrogen porosimetry results were not indicative of the true surface areas of the materials due to blocked pore entrances. Blockage of pore entrances may be due to very small pore sizes as in the case of MOF materials[49] or be the result of some form of soluble material that blocks pore entrances when dry but allows ionic access when wet.

In order to investigate whether any structural changes took place in the ZrP materials when they were contacted with 0.1 M nitric acid, as occurred in the sorption experiments, SAXS measurements were performed on slurries of the ZrP materials in 0.1 M nitric acid. For the ZrPA series, no substantial changes were observed in the SAXS data of the ZrPA materials when they were wet relative to when they were dry. For this series, the surface area of the ZrPA material with the highest molar P/Zr ratio, ZrPA-5, was still a substantial 78 m^2/g. Thus, it is reasonable to assume that the increasing amount of free phosphonate available to coordinate Ln as the molar P/Zr ratio increased compensated for the decrease in surface area for the ZrPA series.

For the ZrPB series, no substantial changes were observed in the SAXS data at low Q upon wetting, indicating that the large particles (50-70 nm) remained relatively unchanged. However, the smaller scale structures seen at intermediate Q in the SAXS data did change shape upon wetting, as indicated by a decrease in their power law exponents (Table 3.10). These subtle structural changes do not explain the observed trend of increasing sorption with decreasing surface area, which was observed for the ZrPB series between the -1 and -3 samples. Thus, increased free phosphonate groups must again account for this behaviour. However, when the surface area decreased further from 105 m^2/g for ZrPB-3 to 33 m^2/g for ZrPB-5, there was no increase in sorption despite the molar P/Zr ratio increasing from 2.1 to 2.8. This suggests that when the surface area became low enough, increasing free phosphonate groups could no longer compensate for the decreased surface area.

The SAXS data of the ZrPC materials all changed upon wetting, indicating that these materials underwent a change in structure when wet. The SAXS data of the ZrPC-1 material showed that its particles changed shape when wet but no development of increased porosity was observed. For ZrPC-3, its particles increased in size when wet but its approx. 2 nm mesopores underwent minimal change. ZrPC-4 also maintained its approx. 2 nm mesopores but also developed larger, approx. 10 nm mesopores upon wetting. Finally, ZrPC-5, which showed no porosity whatsoever as a dry powder, showed both approx. 2 nm mesopores as well as larger, approx. 5 nm mesopores when wet. Although the absolute intensity of the correlation peaks in the SAXS data could not be determined (the path length of the samples was not defined), it was clear from visual inspection of the data (Figure 3.26) that the intensity of the correlation peaks in the wet samples increased with the molar ratio P/Zr. Thus, the mesoporosity introduced in the wet samples was more prevalent for the samples with a higher molar P/Zr ratio. This development of porosity in the ZrPC materials when they were contacted with 0.1 M nitric acid explains the observed high Ln sorption capacity of the ZrPC-4 and -5 samples, despite their negligible BET surface areas. This result has important and

wide-ranging implications as it demonstrates that, contrary to popular belief, surface area as measured by nitrogen porosimetry is not a reliable tool to predict the sorption capacity of materials.

3.3.4 Comparison with Other Materials for Selective Ln Sorption

All of the ZrP materials synthesised that showed sorption also demonstrated selectivity for Ln over Cs, Sr and Co. This selectivity was expected as zirconium phosphonate materials have previously been shown to sorb Ln preferentially over alkali and alkaline earth metals,[19] divalent transition metals and thorium.[14] The Ln sorption properties of the ZrP materials in this work compare favourably with other metal phosphonate type materials. Tin and zirconium phosphate-phosphonate materials have been shown to extract La from 1 % NaCl solution at pH 3,[18] Ln from approx. pH 3 solution[19] and Nd from 0.1 M nitric acid,[20] but kinetics and capacities were not determined in any of these studies. A similar Zr-ATMP material has been shown to sorb Ce selectively over various divalent transition and heavy metal ions as well as Th, although these sorption studies were performed using individual elements rather than the competitive sorption that was utilised in this work.[14] In addition, the selectivity of the present materials is substantially greater, since $SF_{Ce/Co}$ of the previous Zr-ATMP material was of the order of 10-20 whereas the present ZrP materials demonstrate $SF_{La/Co}$ ranging from 350 to 1400. When taking into consideration the different methodologies of synthesis (sol-gel versus hydrothermal) as well as the different elemental compositions and morphologies of the previous and current ZrP materials it must be concluded that the ZrP materials synthesised in this work are substantially different to previously synthesised materials and also demonstrate superior Ln sorption properties.

The sorption kinetics of the ZrP materials in this study were also substantially faster than the previously synthesised Zr-ATMP material, as approx. 30 min rather than 6 h was required to attain equilibrium.[14] The kinetics of the ZrP materials in this study also compare favourably with other materials used for Ln sorption. The ZrP materials in this study exhibited similar or faster kinetics than silica-based materials functionalised with phosphonates or carboxylates.[48,50,51] For example, the rate of Ln uptake by phosphoric acid loaded silica particles was only 2.6×10^{-4} g/mg min,[51] more than three orders of magnitude slower than ZrPC-4. Biopolymers, based on dried bacterial cells, have been shown to sorb Ln with very slow kinetics at pH 2.[52] Finally, Ln sorption by polymer resins functionalised with carboxylates, phosphonates or phosphine oxides occurred on similar or slower timescales to the ZrP materials in this study.[6-8,53-55]

The Ln capacities of the ZrP materials in this work also compare favourably with the previously synthesised Zr-ATMP material described above. The distribution coefficient of Ce sorption from 0.02 M nitric acid with the previous Zr-ATMP material was more than an order of magnitude less than was achieved for La by the ZrP materials in this study.[14] Therefore, it can be confidently stated that the Ln capacity of the ZrP materials in this study were superior to previously synthesised Zr-ATMP materials despite the fact that sorption capacities were not

explicitly measured in the previous study. The ZrP materials in this work also displayed capacities nearly two orders of magnitude higher than mesoporous zirconium titanates functionalised with ATMP post-synthesis, which showed capacities at pH 2 of approx. 0.83 mg Gd/g, despite having surface areas three orders of magnitude greater than ZrP-0.76.[23] The superior capacities of the present ZrP materials may be attributable to the higher ATMP loading (>14 % vs 2 %) and corresponding higher proportion of free phosphonate groups. This hypothesis is supported by the NMR and FTIR data shown above.

The capacity of the ZrP materials in this study were also superior to other types of materials used for Ln sorption. The ZrP materials in this study exhibited substantially greater capacities, at similar acidities, to silica-based materials functionalised with phosphonates or carboxylates.[48,50,51] For example, diphosphonic acid functionalised mesoporous silica had a Pr capacity of 37 mg/g in 0.01 M hydrochloric acid.[50] Carboxylate functionalised polymer resins showed poor Ln sorption at low pH[53,54] and a phosphonic acid functionalised Merrifield resin sorbed approx. 15 mg/g Eu from pH 1.2 nitric acid,[6] but was still inferior to the ZrP materials synthesised in this study. On the other hand, a phosphine oxide functionalised styrene-based resin (Figure 3.32) showed a similar Ln capacity to ZrPC-4, of 72 mg/g at 4 M nitric acid.[55] Commercial resins DIPEX® (diphosphonic acid impregnated into acrylate polymer) and Tulsion CH-93 (aminophosphonic acid functionalised resin) demonstrated Ln capacities of 45 mg/g in 1 M hydrochloric acid and 11 mg/g in 0.1 M phosphoric acid, respectively.[7,8] Thus, some polymer resins demonstrate similar capacities for Ln to the ZrP materials in this work, under strong acid conditions. However, the selectivity of these polymer resins over fission products such as Cs and Se was not reported. Also, the present ZrP materials retain the advantages of hydrolytic and radiolytic stability (which is poor for polymer resins [56,57]) and simple, relatively inexpensive synthesis.

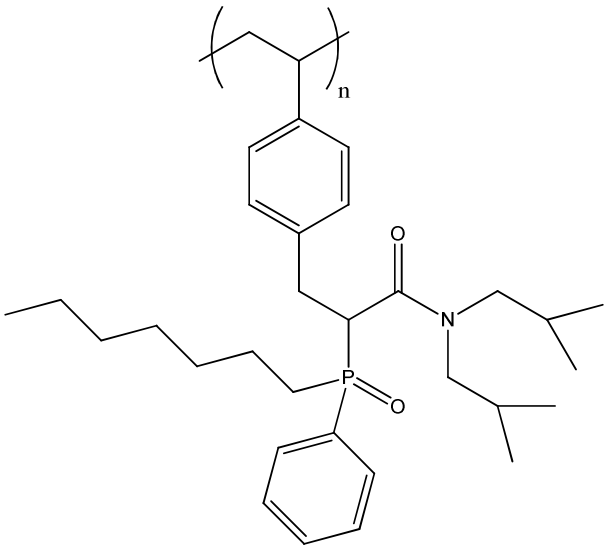

Figure 3.32: Chemical structure of phosphine oxide modified styrene polymer for Ln sorption

3.4 Conversion to a Ceramic Wasteform

After loading with Ln, conversion of the ZrP sorbent into a stable ceramic wasteform would immobilise the encapsulated Ln, which in the case of used nuclear fuel reprocessing could be radioactive Ln fission products or the chemically similar MA. Ceramic wasteforms are of interest as they can provide superior properties to vitreous wasteforms, such as chemical durability.[3] Some collaborative work outside the scope of this thesis has shown that ZrPC-4 can be loaded with Eu and converted to a ceramic by sintering at 1300 °C, without requiring addition of any additives. This resulted in a highly durable ceramic consisting of 7:3 ZrP_2O_7 (zirconium pyrophosphate):$EuPO_4$ (monazite) (Figure 3.33) with a waste loading of approx. 19 wt%.

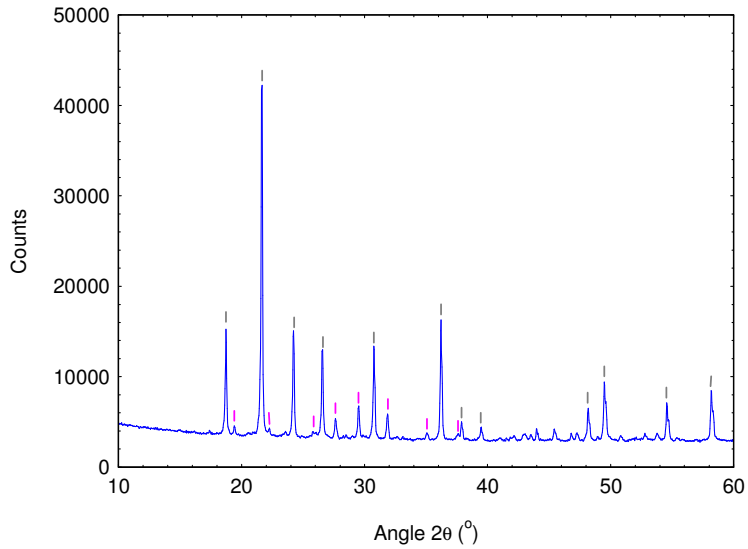

Figure 3.33: XRD pattern of Eu loaded ZrPC-4 after calcination at 700 °C for 4 h followed by sintering at 1300 °C for 12 h. The phases present were ZrP_2O_7 (grey) and $EuPO_4$ (pink).

3.5 Conclusions

Novel porous ZrP materials have been synthesised via simple hydrothermal treatment of zirconium precursors and varying amounts of commercially available ATMP without the inclusion of any template. As such, a simplified synthesis method for porous ZrP materials without any need for template removal has been developed. Three series of samples were investigated in detail; ZrPA series synthesised using Zr chloride at pH 1 and hydrothermal treatment at 120 °C, ZrPB series synthesised using Zr propoxide at pH 1-2 and hydrothermal treatment at 120 °C, ZrPC series synthesised using Zr propoxide at pH 4-5 and hydrothermal treatment at 160 °C. Five samples with varying molar P/Zr ratio were synthesised and characterised within each of these series.

All of the ZrP materials had some similar characteristics, independent of the synthesis conditions used. For example, XRD showed all the ZrP materials to be amorphous and SEM

indicated a morphology consisting of agglomerated spherical particles approx. 50-70 nm in diameter. In addition, nitrogen adsorption-desorption isotherms were similar in shape for all the ZrP materials measured and indicated hierarchical porosity. Finally, fitting of EXAFS data from selected ZrP materials across each series showed that for all the samples the Zr nearest neighbour environment consisted of O and P atoms and that the Zr-O distance was between 2.0 and 2.1 Å.

For all three ZrP series, changes were observed in the structure and sorption of the materials as the molar P/Zr ratio increased. Elemental composition of the ZrP materials was measured by microanalysis. As well as confirming that the molar P/Zr ratio increased as more ATMP was added during synthesis, this elemental analysis indicated that there was a maximum P/Zr ratio in the ZrP materials such that further additions of ATMP were not incorporated into the product. This maximum P/Zr ratio was different for the three ZrP series and increased in the order ZrPB < ZrPC < ZrPA. In terms of porosimetry, surface area generally decreased as the molar ratio P/Zr increased, due to a loss of micro- and mesoporosity. Nevertheless, sorption of Ln increased with the molar ratio P/Zr in the ZrP materials. This was explained by NMR and FTIR characterisation of the ZrP materials, which both showed that the amount of free phosphonate groups, uncoordinated by Zr and thus available to bind Ln, increased with the molar ratio P/Zr in the materials. In addition, SAXS data showed that the structure of the ZrPC materials was changed when they were wet, as was the case during sorption experiments. The ZrPC materials with high P/Zr molar ratios in particular appeared to develop wormhole mesoporosity upon wetting. Thus, the low measured BET surface areas of the dry ZrPC materials with high P/Zr molar ratios were not indicative of the available surface area for sorption when the materials were wet. This was an important result with potentially wide-ranging implications.

In terms of differences between the three ZrP series, again both structure and sorption behaviour were found to be affected by the synthesis conditions. In terms of structure, the largest difference between the three ZrP series was their porosity. For example, the ZrPA and ZrPB series materials had different surface areas and pore sizes, which must be attributed to the Zr precursor used as this was the only difference between these series. In terms of sorption, the ZrPB series materials showed the most selective Ln sorption but had lower capacities than the other ZrP series. The ZrPC series materials demonstrated the highest sorption capacities and faster sorption kinetics than the ZrPA and ZrPC series, as well as superior selectivity to the ZrPA series. Thus, the ZrPC series was considered to have best sorption properties of all the ZrP materials investigated. Of the ZrPC series, ZrPC-4 demonstrated the highest Ln sorption capacity and the fastest kinetics, making it the optimal composition. Other ZrP materials, similar to those described here, have been synthesised previously, but demonstrated inferior Ln sorption properties to the present materials.[14] Overall, the ZrP materials in this work, in particular ZrPC-4, show great promise as sorbents for Ln separations at the back end of the nuclear fuel cycle as they have multiple desirable

characteristics such easy synthesis with inexpensive reagents, high Ln selectivity in acidic media, high sorption capacity, and fast kinetics.

3.6 References

(1) Hudson, M. J.; Harwood, L. M.; Laventine, D. M.; Lewis, F. W. *Inorganic Chemistry* **2013**, *52*, 3414.

(2) Puchy, B. *Briefing Paper: Rare Earth Elements*, Department of Environmental Quality, 2011.

(3) Donald, I. W.; Metcalfe, B. L.; Taylor, R. N. J. *J Mater Sci* **1997**, *32*, 5851.

(4) Paiva, A. P.; Malik, P. *J. Radioanal. Nucl. Chem.* **2004**, *261*, 485.

(5) Nilsson, M.; Nash, K. L. *Solvent Extr. Ion Exch.* **2007**, *25*, 665.

(6) Abderrahim, O.; Ferrah, N.; Didi, M. A.; Villemin, D. *J. Radioanal. Nucl. Chem.* **2011**, *290*, 267.

(7) Horwitz, E. P.; Chiarizia, R.; Dietz, M. L. *React Funct Polym* **1997**, *33*, 25.

(8) Radhika, S.; Nagaraju, V.; Kumar, B. N.; Kantam, M. L.; Reddy, B. R. *J Rare Earth* **2012**, *30*, 1270.

(9) Park, T. J.; Garino, T. J.; Nenoff, T. M.; Rademacher, D.; Navrotsky, A. *J Am Ceram Soc* **2011**, *94*, 3053.

(10) Gregg, D. J.; Karatchevtseva, I.; Triani, G.; Lumpkin, G. R.; Vance, E. R. *J Nucl Mater* **2013**, *441*, 203.

(11) Alberti, G.; Murcia-Mascaros, S.; Vivani, R. *J. Am. Chem. Soc.* **1998**, *120*, 9291.

(12) Clearfield, A.; Wang, Z. K. *J Chem Soc Dalton* **2002**, 2937.

(13) Jia, Y. J.; Zhang, Y. J.; Wang, R. W.; Yi, J. J.; Feng, X.; Xu, Q. H. *Ind Eng Chem Res* **2012**, *51*, 12266.

(14) Shah, B.; Chudasama, U. *Desalin Water Treat* **2012**, *38*, 227.

(15) Perry, H. P.; Law, J.; Zon, J.; Clearfield, A. *Micropor Mesopor Mat* **2012**, *149*, 172.

(16) Shi, X.; Liu, J.; Li, C.; Yang, Q. *Inorganic Chemistry* **2007**, *46*, 7944.

(17) Clearfield, A. In *Progress in Inorganic Chemistry*; Karlin, K. D., Ed.; John Wiley & Sons, Inc.: 1998; Vol. 47, p 371.

(18) Moller, T.; Bestaoui, N.; Wierzbicki, M.; Adams, T.; Clearfield, A. *Appl Radiat Isotopes* **2011**, *69*, 947.

(19) Cahill, R., Shpeizer, B., Peng, G.-Z., Bortun, L., Clearfield, A. In *Separations of f elements*; Nash, K. L., Choppin, G.R., Ed.; Plenum Press: New York, 1995, p 165.

(20) Burns, J. D.; Clearfield, A.; Borkowski, M.; Reed, D. T. *Radiochim. Acta* **2012**, *100*, 381.

(21) Tsai, C. T.; Pan, Y. C.; Ting, C. C.; Vetrivel, S.; Chiang, A. S. T.; Fey, G. T. K.; Kao, H. M. *Chem Commun* **2009**, 5018.

(22) de los Reyes, M.; Majewski, P. J.; Scales, N.; Luca, V. *Acs Appl Mater Inter* **2013**, *5*, 4120.

(23) Griffith, C. S.; De Los Reyes, M.; Scales, N.; Hanna, J. V.; Luca, V. *Acs Appl Mater Inter* **2010**, *2*, 3436.

(24) Shi, X.; Li, J. P.; Tang, Y.; Yang, Q. H. *J Mater Chem* **2010**, *20*, 6495.

(25) Sing, K. S. W., Everett, D.H., Haul, R.A.W., Moscou, L., Pierotti, R.A., Rouquerol, J., Siemieniewska, T. *Pure & Applied Chemistry* **1985**, *57*, 603.

(26) Ho, Y. S.; Porter, J. F.; Mckay, G. *Water Air Soil Poll* **2002**, *141*, 1.

(27) Limousin, G.; Gaudet, J. P.; Charlet, L.; Szenknect, S.; Barthes, V.; Krimissa, M. *Appl Geochem* **2007**, *22*, 249.

(28) Ho, Y. S.; McKay, G. *Adsorpt Sci Technol* **2002**, *20*, 797.

(29) Colthup, N. B., Wiberley, S.E., Daly, L.H. *Introduction to Infrared and Raman Spectroscopy*; Academic Press: New York, 1964.

(30) Pradhan, D., National Institute of Technology Rourkela, 2009.

(31) Nakamoto, K. *Infrared and Raman Spectra of Inorganic and Coordination Compounds*; Fourth Edition ed.; John Wiley and Sons, Inc.: New York, 1986.

(32) Dahl, G. H., Block, B.P *Inorganic Chemistry* **1967**, *6*, 5.

(33) Ma, T. Y.; Zhang, X. J.; Yuan, Z. Y. *J Phys Chem C* **2009**, *113*, 12854.

(34) Ma, T. Y.; Zhang, X. J.; Yuan, Z. Y. *Micropor Mesopor Mat* **2009**, *123*, 234.

(35) Stuhrmann, H. B. In *Small Angle X-ray Scattering*; Glatter, O. K., O., Ed.; Academic Press Inc.: London, 1982, p 197.

(36) Hammouda, B.; National Institute of Standards and Technology: Gaithersburg, 2010.

(37) Higgins, J. S. B., H.C. *Polymers and Neutron Scattering*; Oxford University Press: Oxford, 1996.

(38) Pauly, T. R.; Liu, Y.; Pinnavaia, T. J.; Billinge, S. J. L.; Rieker, T. P. *J. Am. Chem. Soc.* **1999**, *121*, 8835.

(39) Ravel, B.; Newville, M. *J Synchrotron Radiat* **2005**, *12*, 537.

(40) Clayden, N. J. *J Chem Soc Dalton* **1987**, 1877.

(41) Grossmann, G.; Burkov, K. A.; Hagele, G.; Myund, L. A.; Hermens, S.; Verwey, C.; Aratool, S. M. *Inorg Chim Acta* **2004**, *357*, 797.

(42) Cabeza, A.; Gomez-Alcantara, M. D.; Olivera-Pastor, P.; Sobrados, I.; Sanz, J.; Xiao, B.; Morris, R. E.; Clearfield, A.; Aranda, M. A. G. *Micropor Mesopor Mat* **2008**, *114*, 322.

(43) Gomez-Alcantara, M. D.; Cabeza, A.; Olivera-Pastor, P.; Fernandez-Moreno, F.; Sobrados, I.; Sanz, J.; Morris, R. E.; Clearfield, A.; Aranda, M. A. G. *Dalton T* **2007**, 2394.

(44) Lin, X. Z.; Yuan, Z. Y. *Eur J Inorg Chem* **2012**, 2661.

(45) Gagnon, K. J.; Perry, H. P.; Clearfield, A. *Chemical Reviews* **2012**, *112*, 1034.

(46) Yang, Y. J.; Alexandratos, S. D. *Inorganic Chemistry* **2010**, *49*, 1008.

(47) Hwang, J.; Kim, J.; Ramasamy, E.; Choi, W.; Lee, J. *Micropor Mesopor Mat* **2011**, *143*, 149.

(48) Fryxell, G. E.; Chouyyok, W.; Rutledge, R. D. *Inorg Chem Commun* **2011**, *14*, 971.

(49) Park, K. S.; Ni, Z.; Cote, A. P.; Choi, J. Y.; Huang, R. D.; Uribe-Romo, F. J.; Chae, H. K.; O'Keeffe, M.; Yaghi, O. M. *P Natl Acad Sci USA* **2006**, *103*, 10186.

(50) Yantasee, W.; Fryxell, G. E.; Addleman, R. S.; Wiacek, R. J.; Koonsiripaiboon, V.; Pattamakomsan, K.; Sukwarotwat, V.; Xu, J.; Raymond, K. N. *J Hazard Mater* **2009**, *168*, 1233.

(51) Park, H. J.; Tavlarides, L. L. *Ind Eng Chem Res* **2010**, *49*, 12567.

(52) Texier, A. C.; Andres, Y.; Le Cloirec, P. *Environ Sci Technol* **1999**, *33*, 489.

(53) Dev, K.; Pathak, R.; Rao, G. N. *Talanta* **1999**, *48*, 579.

(54) Kaur, H.; Agrawal, Y. K. *React Funct Polym* **2005**, *65*, 277.

(55) Raju, C. S. K.; Subramanian, M. S. *J Hazard Mater* **2007**, *145*, 315.

(56) Chiarizia, R.; Horwitz, E. P. *Solvent Extr. Ion Exch.* **2000**, *18*, 109.

(57) Traboulsi, A.; Dupuy, N.; Rebufa, C.; Sergent, M.; Labed, V. *Anal Chim Acta* **2012**, *717*, 110.

Chapter 4: Titania Nanoparticles Covalently Functionalised with Simple Organic Ligands

As an alternative to co-condensation, functionalization of inorganic framework materials via post-synthetic grafting was investigated and the resulting materials used for selective separation of actinides (An) from solutions of used nuclear fuel. Specifically, ligands based on functional groups from organic extractants of known solvent extraction processes were used to functionalise titania nanoparticles. Titania nanoparticles were initially chosen as the solid phase framework material to be functionalised because titania is readily available, cost effective, non-toxic, hydrolytically and radiolytically stable.[1] Also, ceramic matrices containing titania are more leach resistant than vitrified silica,[2] so titania based sorbents could potentially be used, post-sorption, for waste immobilisation or as transmutation matrices. Nanoparticles of titania were used for initial proof of concept functionalization and sorption experiments due to their ease of preparation and ready surface availability relative to more complex porous structures.

Although functionalisation of titania is commonly performed using phosphate, phosphonate or carboxylic acid anchor groups,[3,4] functionalization via an alkene was investigated in the present work as it was considered likely to produce more hydrolytically stable covalent bonds. Covalent functionalization of titania via an alkene has been achieved previously via irradiation with ultraviolet light,[5] but in this work a more simple method of functionalization using heat was developed. A schematic representation of the ligands used for functionalization of the titania nanoparticles is shown in Figure 4.1. These ligands consisted of an alkene group for covalent attachment to the titania surface as well as a free functional group for selective sorption of metal cations. The alkene and the functional group were linked by an aliphatic alkyl chain which induced self-assembly of the ligands on the nanoparticle surface.

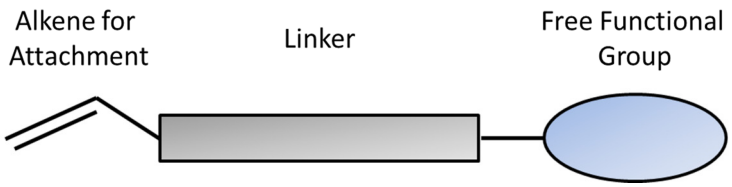

Figure 4.1: Schematic representation of organic ligands for covalent functionalisation

One of the main elements of interest for selective removal from solutions of used nuclear fuel is uranium (U), due to its potential for reuse as fuel in nuclear reactors.[6] Recovery of U from nuclear and industrial wastewater is another important potential application for these sorbent materials due to the heavy metal toxicity and radioactivity of U.[6] In *Chapter 1* the high

affinity of phosphonate groups for the uranyl cation was established. Therefore, a novel alkylphosphate ligand **1** (Figure 4.2) was synthesised, to mimic the behaviour of the tributylphosphate (TBP) ligand that is used in the commercial PUREX process for U extraction. However, under different conditions of pH and nitrate concentration, resins with either phosphonic acid, carboxylic acid or amino functional groups have been shown to provide the most effective U extraction.[7] Therefore, a simple alkylamine ligand **2** (Figure 4.2) was also synthesised for functionalization of the titania nanoparticles.

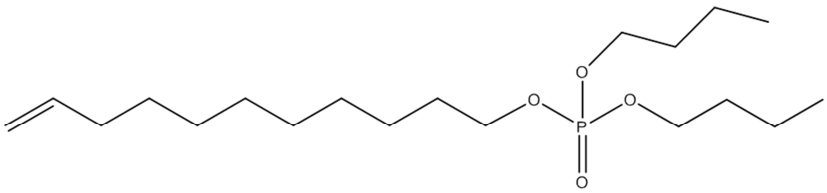

1

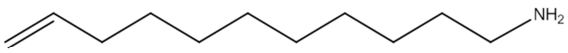

2

Figure 4.2: Chemical structure of novel alkylphosphate ligand **1** and alkylamine ligand **2** for selective sorption of U

Another class of elements that are targets for selective separations from used nuclear fuel are the minor actinides (MA), due to their radiotoxicity and long lifetimes.[8] Picolinamides are simple ligands with the potential to achieve the challenging separation of MA from the lanthanide (Ln) fission products.[9] Therefore, a third ligand was synthesised for titania nanoparticle functionalization based on the picolinamide functional group (**3**, Figure 4.3).

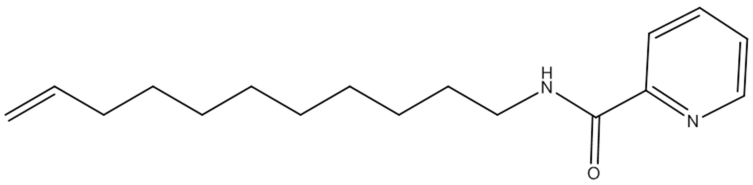

3

Figure 4.3: Chemical structure of novel picolinamide ligand **3** for selective sorption of MA

In this chapter, a description of the synthesis and characterisation of organic ligands **1**, **2** and **3** and how they were used to covalently functionalise titania nanoparticles is given. In addition, the sorption behaviour of the hybrid inorganic-organic materials produced towards a range of elements relevant to the nuclear fuel cycle with varied pH in nitrate media was

investigated. Specifically, sorption of the fission products cerium (Ce), europium (Eu), ytterbium (Yb), cesium (Cs), strontium (Sr) and molybdenum (Mo) as well as the actinides uranium (U) and americium (Am) to the functionalised titania nanoparticles was measured. The aim was to develop a material able to selectively extract the actinides (either U or Am) from the other elements present in a competitive environment.

4.1 Experimental Methods

4.1.1 Titania Nanoparticles Synthesis

Titanium(IV) isopropoxide (35.51 g, 125 mmol) and glacial acetic acid (7.49 g, 125 mmol) were mixed vigorously for 30 s followed by addition of MilliQ water (125 mL) to give a white precipitate. The suspension was stirred for a further 30 minutes then allowed to settle and the liquid removed. The solid was then washed with MilliQ water (5 x 125 mL). After the final wash, the solid was suspended in nitric acid (0.2 M, 125 mL) and stirred for 15 minutes at room temperature and then for a further 24 h at 70 ^{o}C, maintaining the volume at approx. 125 mL. The resulting stable sol was decanted into a petri dish and allowed to evaporate to dryness. The resulting solid was ground in a mortar and pestle to give a fine white powder which was thermally treated at 150 ^{o}C for 5 h then at 400 ^{o}C for 24 h, both with a ramp rate of 2 ^{o}C/min, then heated to 600 ^{o}C for 10 minutes, with a ramp rate of 10 ^{o}C/min, affording titania nanoparticles (8.1 g, 101 mmol). High temperature (600 ^{o}C) thermal treatment was required to ensure a clean nanoparticle surface for the subsequent functionalization step.

4.1.2 Organic Ligands Synthesis

N-Undecylenyl phthalimide (**4**):

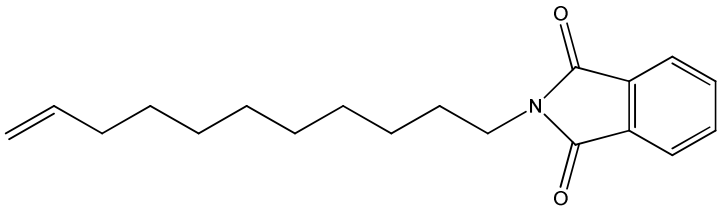

Potassium phthalimide (5.55 g, 30.0 mmol) was added to a solution of 11-bromo-1-undecene (5.0 mL, 23.0 mmol) in dimethylformamide (DMF, 13 mL) under nitrogen and the reaction mixture was stirred at 90 ^{o}C for 24 h. MilliQ water (37 mL) was added to the cooled reaction mixture and the resulting solution was extracted with diethyl ether (1 x 37 mL, 2 x 15 mL). The combined organic layers were evaporated under vacuum to afford the crude product as a yellow solid. Recrystallisation from methanol (MeOH) afforded the pure product as an off-white solid (3.79 g, 55 % yield). ^{1}H NMR (400 MHz, MeOD) δ (ppm): 7.83 (m, 2H), 7.76 (m, 2H), 5.79 (m, 1H), 4.91 (m, 2H), 3.62 (t, *J* = 7.3Hz, 2H), 2.01 (dt, *J* = 7.0Hz, 6.8Hz, 2H), 1.63 (m, 2H), 1.41-1.20 (m, 12H). Characterisation data was consistent with previously reported results.[10]

1-Amino-10-undecene (**2**, Figure 4.2):

Deprotection of compound **4** was achieved by refluxing with hydrazine monohydrate in ethanol (EtOH) followed by acidification to pH 1 with hydrochloric acid (HCl, 1 M). The precipitate formed was filtered and washed twice with HCl (1 M). Sodium hydroxide pellets were added to the combined filtrate and washings to give a pH of 10. This solution was concentrated under reduced pressure, affording a gelatinous white liquid which was extracted four times with diethyl ether. The combined ether extracts were washed with sodium hydroxide solution (0.2 M) and brine then dried over sodium sulphate. Removal of the solvent under reduced pressure afforded the crude aminoalkene as a yellow oil (1.05 g, 91 % yield). ^{1}H NMR (400 MHz, $CDCl_3$) δ (ppm): 5.81 (m, 1H), 4.96 (m, 2H), 2.83 (t, *J* = 7.4 Hz, 2H), 2.03 (dt, *J* = 6.8, 7.1Hz, 2H), 1.61 (m, 2H), 1.42-1.21 (m, 12H). Characterisation data was consistent with previously reported results.[10]

10-N-Boc-amino-undec-1-ene (**5**):

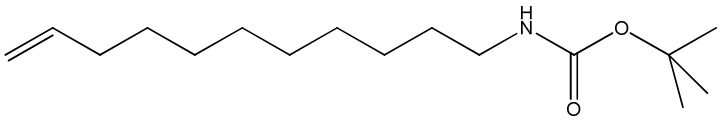

To a solution of compound **2** (0.30 g, 1.8 mmol) in chloroform (CH_2Cl_2, 5 mL) was added a solution of sodium hydrogen carbonate (0.15 g, 1.8 mmol) in MilliQ water (4 mL). Sodium chloride (0.32 g, 5.5 mmol) and di-*tert*-butyl dicarbonate (0.40 g, 1.8 mmol) were added to the reaction mixture, which was then refluxed for 90 min. After cooling to room temperature, the reaction mixture was extracted with diethyl ether (2 x 4 mL) and the combined organic layers were dried over sodium sulphate. Removal of the solvent under reduced pressure afforded the crude product as a yellow oil (0.24 g, 48 % yield). ^{1}H NMR (400 MHz, $CDCl_3$) δ (ppm): 5.80 (m, 1H), 4.94 (m, 2H), 3.09 (m, 2H), 2.03 (dt, *J* = 6.8, 7.1Hz, 2H), 1.57 (m, 2H), 1.43 (s, 9H), 1.40-1.18 (m, 12H). Characterisation data was consistent with previously reported results.[11]

Trifluoroacetamide-protected 10-amino-1-undecene (TFAAD, **6**):

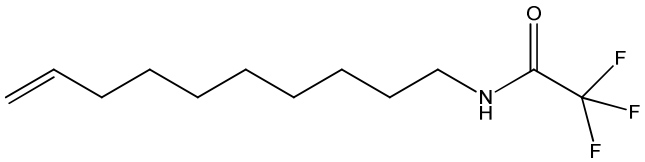

Tetrapropylammonium bromide (22 mg, 0.083 mmol) and 10-undecenoyl chloride (4.05 g, 20.0 mmol) were combined and cooled to -3 °C in an ice bath. Aqueous sodium azide solution (4 M, 5.0 mL) was added dropwise with stirring, keeping the temperature below 5 °C. The reaction mixture was stirred for a further 24 h, keeping the temperature below 0 °C for at least the first 3 h. The organic phase was diluted in 5 mL CH_2Cl_2, washed with MilliQ water (2 x 5 mL) and dried over sodium sulphate. The resulting acyl azide was reacted with trifluoroacetic acid (TFA, 2.0 mL, 26.1 mmol) under nitrogen at room temperature for 30 min then refluxed for 24 h. Washing with saturated sodium bicarbonate solution (3 x 5 mL), drying over sodium sulphate and removal of solvent under vacuum gave the crude product as a brown oil. Purification by flash chromatography on silica gel (CH_2Cl_2) afforded the pure product as a clear, colourless oil (2.38 g, 65 % yield). ^{1}H NMR (400 MHz, $CDCl_3$) δ (ppm):

6.26 (br s, 1H), 5.83 (m, 1H), 4.98 (m, 2H), 3.38 (q, *J* = 6.8Hz, 2H), 2.06 (dt, *J* = 6.9Hz, 6.7Hz, 2H), 1.60 (m, 2H), 1.45-1.27 (m, 8H). Characterisation data was consistent with previously reported results.[12]

10-Undecen-1-yl-2-pyridinecarboxamide (**3**, Figure 4.3):

2-Pyridinecarboxylic acid (0.73 g, 5.9 mmol) and tetrahydrofuran (THF, 35.0 mL) were combined under nitrogen and cooled to -5 ^{o}C in an ice bath. Triethylamine (0.82 mL, 5.9 mmol) and ethyl chloroformate (0.56 mL, 5.9 mmol) were added slowly and the resulting suspension stirred for 30 min, maintaining a temperature below -5 ^{o}C. Crude **2** (1.02 g, 6.0 mmol) was added and the reaction mixture stirred for a further 6 h, maintaining a temperature below 0 ^{o}C. The reaction mixture was filtered and the white residue rinsed with THF (10.0 mL). The solvent was removed from the combined filtrate and washings under reduced pressure to afford the crude product as a brown oil. Purification by flash chromatography on silica gel (98:2 CH_2Cl_2:MeOH), afforded the pure pyridinecarboxamide as a white crystalline solid (1.25 g, 77 % yield). m.p. 44-46 ^{o}C; MS (ESI): *m/z* 275 $[M+H]^+$; ^{1}H NMR (400 MHz, $CDCl_3$) δ (ppm): 8.54 (d, *J* = 4.1 Hz, 1H), 8.20 (d, *J* = 7.8 Hz, 1H), 8.05 (br s, 1H), 7.84 (dt, *J* = 7.8, 1.7 Hz, 1H), 7.42 (m, 1H), 5.81 (m, 1H), 4.96 (m, 2H), 3.46 (m, 2H), 2.03 (dt, *J* = 7.2, 6.8 Hz, 2H), 1.63 (m, 2H), 1.45-1.20 (m, 12H); ^{13}C NMR (100 MHz, $CDCl_3$) δ (ppm): 165.5, 151.4, 149.2, 140.7, 138.9, 127.5, 123.8, 115.5, 40.9, 35.2, 31.1, 30.9, 30.8, 30.7, 30.5, 30.3, 28.4; FTIR (ATR, neat): ν_{max} 3400, 3080, 2930, 2860, 1670, 1620, 1540, 1520, 1470, 1430, 1370, 1280, 1240, 1160, 1090, 1040, 998, 909, 820, 749, 692 cm^{-1}; Anal Calcd for $C_{17}H_{26}N_2O.0.25H_2O$: C, 73.2; H, 9.6; N 10.0. Found: C, 73.2; H, 9.7; N, 9.9.

Dibutyl 10-undecen-1-yl phosphoric acid ester (**1**, Figure 4.2):

Silver (I) oxide (2.76 g, 11.9 mmol) was added to a solution of dibutyl phosphate (5.00 g, 23.8 mmol) and 11-bromo-1-undecene (2.77 g, 11.9 mmol) in acetonitrile (36 mL). The reaction mixture was stirred vigorously at 40 ^{o}C for 24 h, then filtered. Concentration of the filtrate under reduced pressure afforded an opaque pale orange liquid which was dissolved in CH_2Cl_2 (25 mL), washed with MilliQ water (2 x 15 mL) and dried over sodium sulphate. The solvent was removed under reduced pressure to afford the crude product as an orange liquid. Purification by flash chromatography on silica gel (80:20 CH_2Cl_2:ethyl acetate) afforded the pure alkyl phosphate as a pale yellow oil (4.24 g, 98 % yield). MS (ESI): *m/z* 385 $[M+Na]^+$; ^{1}H NMR (400 MHz, $CDCl_3$) δ (ppm): 5.83 (m, 1H), 4.98 (m, 2H), 4.04 (m, 6H), 2.06 (dt, *J* = 7.3, 6.9Hz, 2H), 1.68 (m, 6H), 1.49-1.35 (m, 8H), 1.35-1.28 (m, 8H), 0.96 (t, *J* = 7.4 Hz, 6H); ^{13}C NMR (100 MHz, $CDCl_3$) δ (ppm): 139.2, 114.1, 67.7, 67.4, 33.8, 32.3, 30.3, 30.3, 29.5, 29.4, 29.1, 29.1, 28.9, 18.7, 13.6; FTIR (ATR, neat): ν_{max} 2958, 2927, 2857, 1641, 1463, 1387, 1270, 1021, 999, 907, 728 cm^{-1}; Anal Calcd for $C_{19}H_{39}O_4P$: C, 63.0; H, 10.8; P, 8.5. Found: C, 63.0; H, 11.0; P, 8.4.

4.1.3 Functionalisation of Titania Nanoparticles

Dry titania nanoparticles (0.50 g) were mixed with a dry, degassed solution of ligand (**1**, **3** or **6**) in mesitylene (0.22 M, 3.7 mL) under nitrogen. The resulting suspension was heated in

an oil bath at 115 ^{o}C for 24 h, with stirring, then filtered. The residue was washed with petroleum ether (5 mL), MeOH (5 mL) and CH_2Cl_2 (5 mL) before drying under vacuum, affording the functionalised nanoparticles as a light brown powder (0.42 g). Titania nanoparticles functionalised with ligands **1**, **3** and **6** were designated TiO_2-TBP, TiO_2-pico and TiO_2-TFAAD, respectively.

In order to prepare titania nanoparticles functionalised with a 1:10 ratio of ligand **1** and 1-decene, a dry, degassed solution of ligand **1** (0.12 g, 0.32 mmol) and 1-decene (0.52 mL, 2.7 mmol) in mesitylene (15.0 mL) was utilised to functionalise dry titania nanoparticles (1.00 g) as described above. The resulting functionalised nanoparticles were designated as TiO_2-TBP/decene.

Removal of the TFA protecting group from ligand **6** on TiO_2-TFAAD was achieved by mixing TiO_2-TFAAD (0.42 g) with a 7 wt% solution of potassium carbonate in 70:30 v/v MeOH:water (4.0 mL) and stirring at room temperature for 48 h. The reaction mixture was then filtered and rinsed with MilliQ water (5 mL) and MeOH (3 mL). Drying under vacuum afforded titania nanoparticles functionalised with ligand **2** (designated as TiO_2-NH_2) as a pale brown powder (0.36 g).

4.1.4 Sorption Methodology

Batch sorption experiments were performed in triplicate and using multiple batches of solid material with a solid-to-liquid ratio of 200, except for the americium-241 (Am-241) sorption which was performed in duplicate and using only one batch of solid material. Batch sorption experiments were performed with pH values ranging between 2 and 7 for TiO_2-NH_2, 3 and 7 for TiO_2-pico and 1 and 5 for TiO_2-TBP. In the experiments where the TiO_2-NH_2 was pre-equilibrated with nitric acid to pH 3 or 5, pH was measured both before the analyte spike was added and sorption began, as well as after filtration at the end of the 24 h sorption experiment. Since there was no significant change in pH (±0.1 pH units), the process of filtration was not considered to affect the pH.

4.2 Characterisation

4.2.1 Titania Nanoparticles

The titania nanoparticles were synthesised according to a previously described sol-gel methodology[13] and characterised using a variety of methods. The crystallinity was measured using x-ray diffraction (XRD), shown in Figure 4.4. This indicated that the titania nanoparticles contained both anatase and rutile. Using the relative intensity ratio (RIR) method,[14] the nanoparticles were shown to contain approx. 10 wt% rutile. The nanoparticle size was calculated according to the Sherrer equation,[15] using the full-width half-maximum (FWHM) of the XRD peaks, to give a value of 26 ± 6 nm.

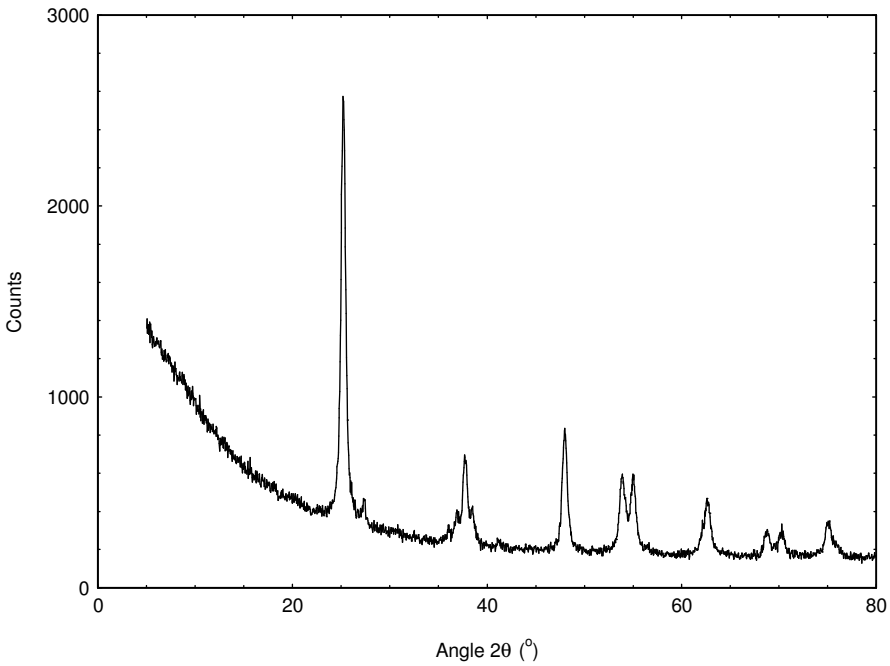

Figure 4.4: XRD pattern of titanium dioxide nanoparticles

The nitrogen adsorption-desorption isotherm for the titania nanoparticles is shown in Figure 4.5. This was a Type IV isotherm with H3 hysteresis, indicating the presence of capillary condensation in mesopores.[16] The BET surface area of the titania nanoparticles was 55 m^2/g and the pore volume was 0.09 mL/g. The t-plot had a negative y-axis intercept, indicating that there were no micropores. The inset to Figure 4.5 indicates a narrow pore size distribution (PSD) centred around 5 nm.

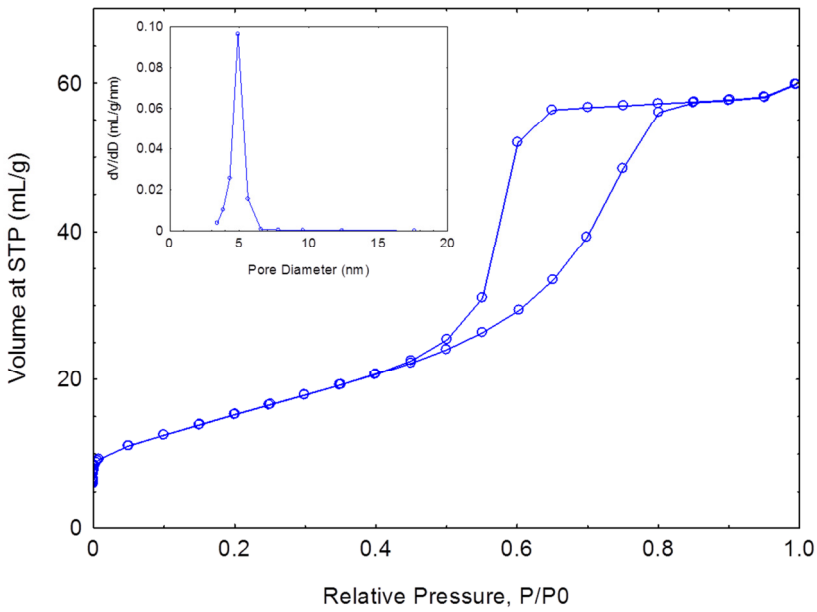

Figure 4.5: Nitrogen adsorption-desorption isotherm of titanium dioxide nanoparticles. Inset: PSD

Scanning electron microscopy (SEM) images of the titania nanoparticles are shown in Figure 4.6. The SEM images show some large particles (>10 µm) that consisted of agglomerates of much smaller titania nanoparticles. These smaller particles were approx. 20 nm in diameter, which was consistent with the particle size determined by XRD.

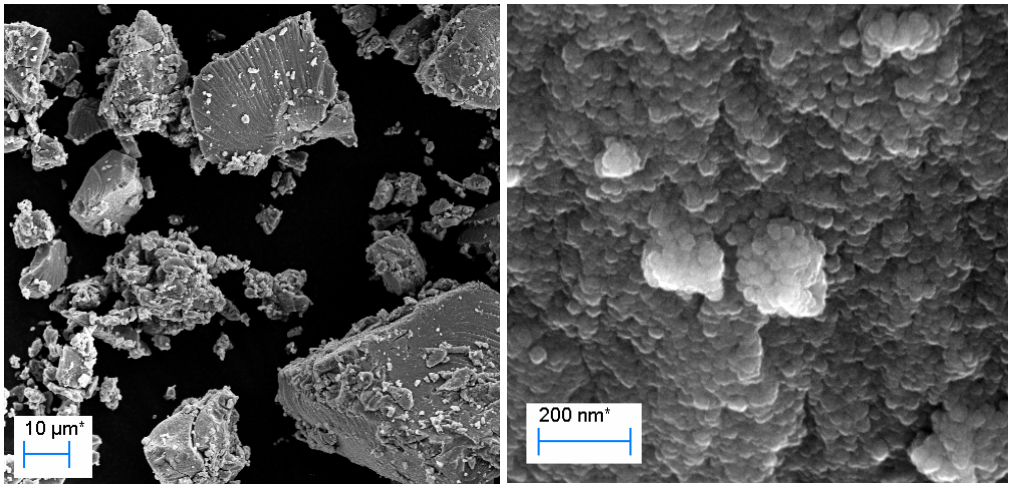

Figure 4.6: SEM images of titania nanoparticles.

Particle size was also measured using small angle x-ray scattering (SAXS) and light scattering methods. The SAXS pattern of a solution of titania nanoparticles suspended in MilliQ water is shown in Figure 4.7. This SAXS data showed a Q^{-x} dependence between 0.05 and 0.15 $Å^{-1}$ with x = -4.0, indicative of scattering from smooth three dimensional objects.[17,18] Using the Guinier approximation, a R_g of 3.3 ± 0.02 nm was calculated for these smooth, three dimensional titania nanoparticles. Thus, in addition to the 20-30 nm particles observed by XRD and SEM, smaller titania nanoparticles were also present.

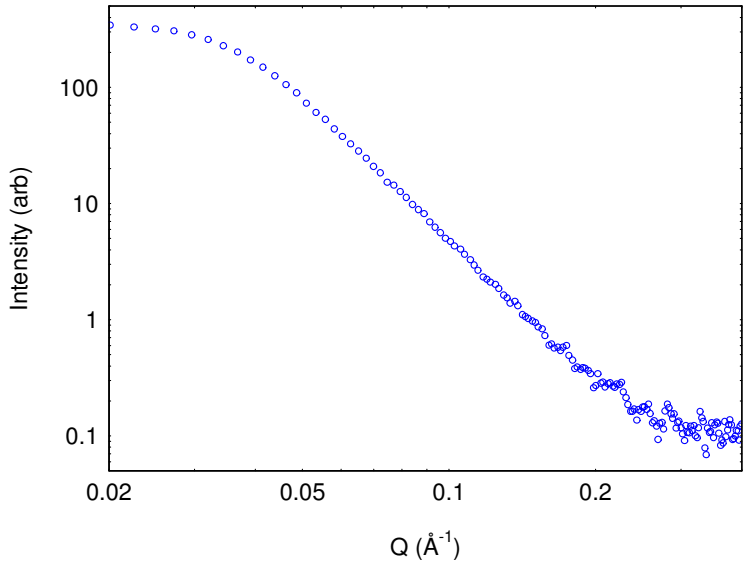

Figure 4.7: SAXS pattern of titania nanoparticles.

Measurement of the particle size using light scattering was also performed on a solution of titania nanoparticles suspended in MilliQ water. Light scattering indicated an average diameter of approx. 500 nm and a polydispersity index of 0.5. Further, the titania nanoparticle solution was observed to contain particles of two distinct sizes; one with diameter 500 ± 150 nm (30% volume fraction) and the other with diameter 120 ± 50 nm (70% volume fraction). Thus, the 20-30 nm particles measured via XRD and SEM and the approx. 3 nm particles measured via SAXS were not observed in the light scattering experiments. This was attributed to the presence of larger agglomerated particles, as was seen in the SEM images (Figure 4.6), that produced higher intensity signals in the light scattering experiments.

4.2.2 Organic Ligands

The ligands for functionalization of the titania nanoparticles consisted of an alkene terminated C_{10} alkyl chain with an amine, amide or phosphate functional head group. Characterisation data for all of the synthesised ligands is given in the experimental methods section above. Synthesis of ligands **2** and **4** were performed according to the methods of Sieval et al.,[10] with minor modifications. The other protected alkylamine ligands; **5** and **6** were synthesised according to the methods of Strother et al.[11] and Sun et al.,[12] respectively, again with minor modifications. The ligand **3** was a novel compound synthesised via a known method for coupling of 2-pyridinecarboxylic acids with amines[19] and the novel ligand **1** was synthesised using the previously reported methodology for esterification of phosphates with halides.[20]

4.2.3 Functionalised Titania Nanoparticles

Covalent attachment of the synthesised organic ligands to the titania nanoparticle surface was achieved using only heat, making this methodology simpler than previous alkene-titania functionalisations which have required the use of UV light.[5]

For functionalization with the alkylamine ligand, a protected amine functional group was used since it is known that basic amine groups can chemisorb to anatase surfaces via hydrogen bonds and lewis acid-base interactions.[21] Therefore a protected amine functional group was required to ensure that the ligand attached to the titania surface via the alkene anchor group rather than via the amine. This protecting group was then removed subsequent to functionalization of the titania nanoparticle surface to reveal the amine functional group. The phthalimide protecting group was initially considered but upon deprotection with hydrazine afforded an insoluble phthalhydrazide byproduct which could not be removed from the titania surface. Use of the *tert*-butyl carbamate (Boc) protecting group was then attempted but deprotection using 25 % TFA in CH_2Cl_2 at room temperature for 1.5 h provided incomplete cleavage, as evidenced by the presence of carbonyl stretch peak at 1680 cm^{-1} in the fourier transform infra-red (FTIR) absorption spectrum of the resulting functionalised titania. Therefore the trifluoroacetamide protecting group was finally chosen, due to its gentle deprotection conditions of 7 % potassium carbonate in MeOH/water.

To characterise the organo-functionalised titania nanoparticles, solid state ^{13}C-^{1}H cross-polarised magic angle spinning nuclear magnetic resonance (MAS NMR) spectroscopy was performed on both non-functionalised titania nanoparticles (referred to as TiO_2-NF) as well as TiO_2-NH_2, TiO2-pico and TiO_2-TBP. The results are shown in Figure 4.8. Peaks were present in the NMR spectra of TiO_2-NH_2, TiO_2-pico and TiO_2-TBP which were not present in the spectrum of TiO_2-NF, confirming that functionalization was successful. Peaks with chemical shift 10-40 ppm, due to aliphatic carbon,[22] were seen in the NMR spectra of all three functionalised titania materials as all three grafted organic molecules contain alkyl chains. The NMR spectrum of TiO_2-pico also showed peaks with chemical shifts between 110 and 160 ppm, due to aromatic –CH- groups in the picolinamide head group.[22] The peak at approx. 65 ppm in the spectrum of TiO_2-TBP was assigned as -CH_2-O groups present in the phosphonate head group.[22]

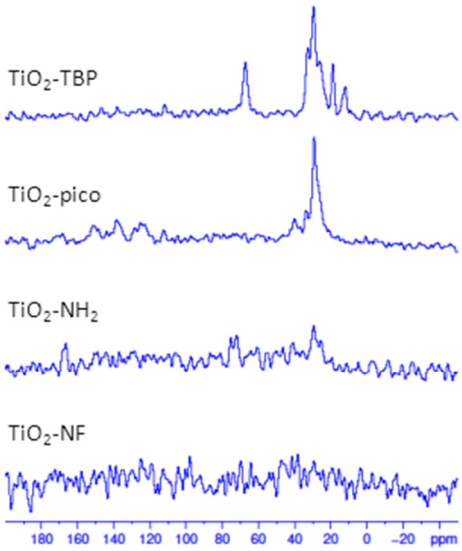

Figure 4.8: ^{13}C-^{1}H CP MAS NMR spectra of organo-functionalised and non-functionalised titania nanoparticles

The low intensity of the peaks in the NMR spectrum of TiO_2-NH_2 in Figure 4.8 resulted in the signal due to aliphatic carbon at 20-40 ppm being only just distinguishable from the background. The low intensity in this spectrum relative to TiO_2-TBP and TiO_2-pico may indicate that the level of functionalization was lower for TiO_2-NH_2 or that there was a higher level of mobility in the alkyl chains for this sample. In fact it is likely that a combination of these factors applies as high alkyl chain mobility suggests more space between the attached ligands and hence a lower level of surface coverage.

The FTIR attenuated total reflectance (ATR) spectra of TiO_2-NF, TiO_2-TFAAD, TiO_2-pico and TiO_2-TBP are shown in Figure 4.9. All of the organo-functionalised titania nanoparticles showed absorbance bands that were not present in the non-functionalised material, which was relatively featureless. This supported the NMR data in Figure 4.8 by again indicating that functionalization was successful. The FTIR spectrum of TiO_2-TFAAD had two strong absorbance bands at 1140 and 1200 cm^{-1}, as well as a weaker absorbance at 1670 cm^{-1}. These were assigned as the CF_3 symmetric stretch, CF_3 asymmetric stretch and carbonyl stretch of the amide group, respectively.[23] The FTIR spectrum of TiO_2-pico had an absorbance band at 1360 cm^{-1}, which was assigned as the C-N stretch,[24] as well as absorbing at 1670 cm^{-1} due to the carbonyl stretch of the amide group, as for TiO_2-TFAAD. The FTIR spectrum of TiO_2-TBP had a prominent absorbance band at 1090 cm^{-1}, which was assigned as the P-O-C asymmetric stretching vibration.[23] There was also a shoulder at 1487 cm^{-1} in this spectrum, which may have been due to the CH_2 scissors deformation or the CH_3 asymmetrical deformation of the n-butyl group of the TBP derivative.[23]

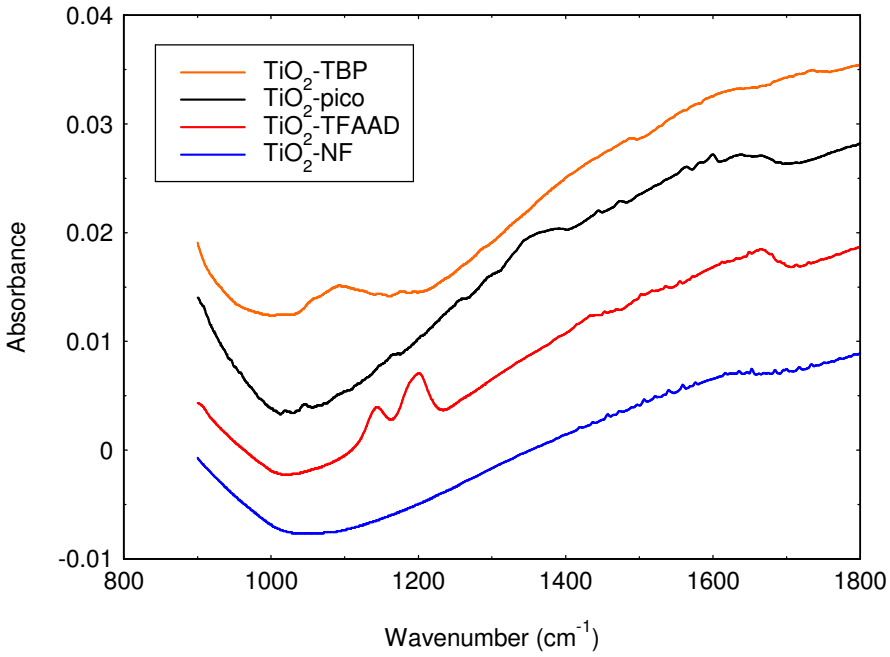

Figure 4.9: FTIR-ATR spectra of organo-functionalised and non-functionalised titania nanoparticles

The level of functionalization of TiO_2-NH_2, TiO_2-pico and TiO_2-TBP was quantitatively determined by CHN microanalysis (Table 4.1). The molecular formulae of the organic functionalised molecules and the total measured %CHN were used to determine the calculated %CHN values, which agreed with the experimentally measured values to within 0.4%. The total organic contents of the organo-functionalised titania nanoparticles was then calculated as the percentage weight of CHNOP but not including water. From this calculation it was observed that the organic contents of TiO_2-pico and TiO_2-TBP were approx. double that of TiO_2-NH_2, which was consistent with the low signal seen in the NMR spectrum of TiO_2-NH_2 (Figure 4.8). However, in terms of molar percentage, the level of functionalization was similar for TiO_2-NH_2 and TiO_2-TBP (0.006 mol%), while that of TiO_2-pico was slightly higher (0.008 mol%). The calculated area per molecule, using the measured titania nanoparticle surface area of 55 m^2/g, was 1.4 nm^2 for TiO_2-NH_2, 1.5 nm^2 for TiO_2-TBP and 1.1 nm^2 for TiO_2-pico.

Table 4.1: Elemental CHN microanalysis of functionalised titania nanoparticles (weight %)

Measured	**TiO_2-NH_2**	**TiO_2-pico**	**TiO_2-TBP**
%C	0.5	1.4	1.5
%H	0.3	0.6	0.5
%N	0.3	0.5	0.4
Total	1.2	2.5	2.3
Calculated	**$C_{10}H_{22}N.3H_2O$**	**$C_{17}H_{26}N_2O.2H_2O$**	**$C_{19}H_{39}PO_4.H_2O$**
%C	0.7	1.6	1.4
%H	0.2	0.3	0.3
%N	0.1	0.2	0.0
Total (organic)	0.9	2.2	2.2

The effect of alkylamine functionalization on the surface charge of the nanoparticles was investigated via zeta potential measurements and the results are shown in Figure 4.10. In aqueous nitrate media at a concentration of 1 mg/mL the isoelectric point for TiO_2-NF and TiO_2-NH_2 were observed at pH 4.2 and pH 5.0, respectively. The higher isoelectric point of TiO_2-NH_2 was expected given that the amino group is basic while the surface of titania itself consists of both acidic and basic reaction sites. The negative surface charge of TiO_2-NH_2 above pH 5 was attributed to excess nitrate anions surrounding the protonated TiO_2-NH_3^+ surface. Zeta potential data could not be collected for TiO_2-pico and TiO_2-TBP due to the lack of surface charge on these materials in the pH range of interest (pH 3 to 7).

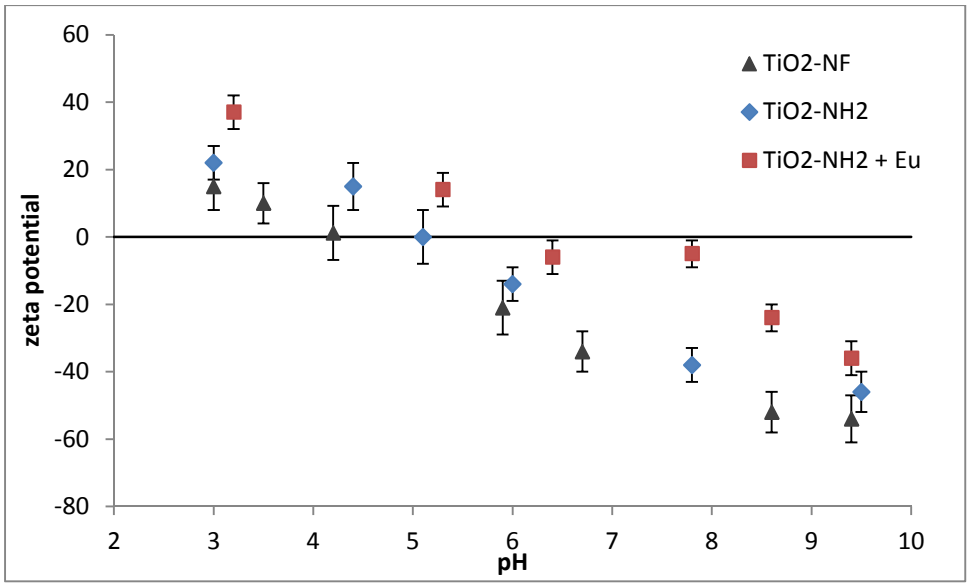

Figure 4.10: Measured zeta potential of TiO_2-NF in aqueous nitrate media and TiO2-NH_2 in aqueous nitrate media with and without 1 ppm Eu present.

4.3 Sorption Properties

4.3.1 Sorption of Individual Elements by TiO_2-NH_2

The ability of TiO_2-NH_2 to sorb Ce, Eu, Yb, Cs, Sr and U from metal nitrate solutions with initial pH ranging from 2-7 was investigated and the results are shown in Table 4.2. An unexpected decrease in sorption with increasing pH for cationic elements such as Ce, Eu, Yb and U was observed. However, it was then noted that substantial changes in the pH of the metal nitrate solutions had occurred after contact with TiO_2-NH_2 if the initial pH was 3 or higher, as shown by the measured pH values in Table 4.3. Specifically, an initial pH of 3 gave a post-contact pH of between 6 and 7 and an initial pH of 4-7 gave a post-contact pH of 8. These results indicated that the TiO_2-NH_2 removed protons from solution and that a protonated amino group (RNH_3^+) was formed. This was not surprising since alkylamine ammonium ions generally have pK_a values between 10 and 11.[25] As a result, the sorption results in Table 4.2 were not indicative of the sorption behaviour of TiO_2-NH_2 at pH 3-7.

Table 4.2: Percentage extraction of 1 ppm Ce, Eu, Yb, Cs, Sr, Mo and U (as individual elements) by TiO_2-NH_2. x = not measured.

	TiO_2-NH_2				
pH	**2**	**3**	**4**	**5**	**7**
Ce	0	≥99.8	95 ± 4	98 ± 1	85 ± 8
Eu	0	≥99.8	88 ± 2	96 ± 2	92 ± 3
Yb	0	≥99.8	89 ± 1	93 ± 3	91 ± 3
Cs	0	14 ± 10	x	27 ± 9	25 ± 9
Sr	0	98 ± 1	x	98 ± 1	98 ± 1
Mo	≥99.9	99 ± 1	51 ± 4	x	x
U	29 ± 9	99 ± 1	≥99.9	97 ± 1	98 ± 1

Table 4.3: Measured pH of metal nitrate solutions after contact with TiO_2-NH_2

Initial pH	**Ce**	**Eu**	**Yb**	**Cs**	**Sr**	**Mo**	**U**
2	1.8	1.8	2.5	2.1	2.1	2.1	2.0
3	5.8	7.3	6.4	8.1	8.3	7.0	7.8
4	7.9	8.1	8.4			7.9	7.7
5	8.0	8.1	8.1	8.3	8.3		8.0
7	8.1	8.1	8.1	8.4	8.3		8.1

To establish the effect of the alkylamine functionalization on sorption behaviour and accurately compare the behaviour of TiO_2-NF and TiO_2-NH_2, it was necessary to control the pH of the metal nitrate solutions. Therefore, sorption experiments were performed in which nitric acid solutions were pre-equilibrated with TiO_2-NH_2 to pH 3 or 5 before a 100 ppm spike of the analyte of interest was added (to give a final concentration of 1 ppm). Batch sorption was then performed for 24 h and pH was measured both before and after sorption to confirm that no substantial change in pH had taken place. The results of sorption experiments for the

non-functionalised titania nanoparticles (TiO_2-NF) and TiO_2-NH_2 with pH control are listed in Table 4.4.

Table 4.4: Percentage extraction of 1 ppm Ce, Eu, Yb, Cs, Sr and U (as individual elements) by TiO_2-NF and TiO_2-NH_2 with pH values measured post-contact. x = not measured.

TiO_2-NF					
pH	**2**	**3**	**4**	**5**	**7**
Ce	0	5 ± 9	3 ± 9	79 ± 4	≥ 99.9
Eu	1 ± 9	7 ± 9	7 ± 9	66 ± 4	≥ 99.9
Yb	0	7 ± 9	10 ± 9	47 ± 5	≥ 99.9
Cs	x	0.2 ± 10	x	1 ± 11	1 ± 10
Sr	2 ± 9	5 ± 9	x	15 ± 8	20 ± 8
Mo	≥ 99.9	≥ 99.9	≥ 99.9	x	x
U	19 ± 8	49 ± 5	x	≥ 99.9	≥ 99.9
TiO_2-NH_2					
pH	**2**	**3**	**4**	**5**	**6-7**
Ce	0	10 ± 15	x	99 ± 1	≥ 99.8
Eu	0	13 ± 18	x	≥ 99.9	≥ 99.8
Yb	0	2 ± 9	x	99 ± 2	≥ 99.8
Cs	0	0	x	0	14 ± 10
Sr	0	0	x	2 ± 9	98 ± 1
Mo	≥ 99.9	x	x	x	99 ± 1
U	29 ± 9	89 ± 15	x	≥ 99.9	99 ± 1

For TiO_2-NF, sorption of Ce, Eu and Yb (collectively referred to as Ln), Sr and U cations increased with pH (Table 4.4). This can be explained by electrostatics since the zeta potential measurements of TiO_2-NF in Figure 4.10 show that as pH was increased the titania surface charge changed from positive to negative. Thus, the metal cations in solution were repelled by the positive surface at low pH and attracted to the negative surface at high pH. Cesium was not sorbed at any pH, which was attributed to its large ionic radius relative to Ln (167pm versus <103pm)[26] and lower charge density (+1 versus +3) making it a soft Lewis base with poor affinity for the hard oxygen donors of the titania surface.[27] On the other hand, Mo was quantitatively sorbed from pH 2-4. In this pH range, the titania surface was positive according to the zeta potential data in Figure 4.10. Since Mo is present predominantly as H_2MoO_4 at pH 2-3 and as MoO_4^{2-} at pH 4,[28] sorption can again be explained by electrostatics at pH 4. At pH 2-3 the predominant Mo species was neutral but the observed quantitative sorption may be explained by the H^+ cations in H_2MoO_4 being replaced by positively charged surface groups on the titania.

Uranium was the only element, apart from Mo, sorbed more than 10 % by TiO_2-NF below its isoelectric point of pH 4.2 (Table 4.4). This may be due to the formation of anionic U nitrate complexes in solution as the nitrate concentration increased with decreasing pH.[29] The existence of inner-sphere U-titania complexes (for both rutile and anatase) has been

previously demonstrated both experimentally and theoretically.[30,31] Two surface complexes are possible as the uranyl cation is either coordinated by two bridging oxygen atoms or by one bridging and one terminal oxygen of the titania surface. The prevalence of each complex is dependent upon the conditions of sorption. However, as the acidity of solution increases, sorption becomes less energetically favourable since no stable inner sphere structures form with fully protonated surface oxygen sites.[31] This was consistent with the results of the present study which showed that U sorption decreased with pH to approx. 20 % at pH 2.

For TiO_2-NH_2, sorption of Ln was again explained by the isoelectric point. In aqueous solution below pH 6 Ln exist as trivalent cations and although at pH 7 some hydrolysis to form $LnOH^{2+}$ cations may occur, the concentration of Ln in these solutions, ≤ 0.007 mM, is so low that very little hydrolysis and no precipitation are expected.[28] Therefore, Ln cation sorption increased from < 15 % at pH 3 to ≥ 99 % at pH 5 (Table 4.4) because the surface charge of TiO_2-NH_2 changed from positive to neutral (Figure 4.10). Although at pH 5 TiO_2-NF had a slight negative charge and TiO_2-NH_2 was neutral (Figure 4.10), TiO_2-NH_2 showed higher Ln sorption than TiO_2-NF at pH 5 (Table 4.4). This indicates that the functionalization of the titania surface with the amine **2** enhanced its affinity for Ln cations. In terms of the mechanism of Ln sorption, Ln ions have previously been shown to form inner sphere nitrate complexes $[Ln(NO_3)(H_2O)_n]^{2+}$ and $[Ln(NO_3)_2(H_2O)_n]^{+}$ with between 10 and 20% relative abundance in solutions of 0.1 mM $Ln(NO_3)_3$ and 0.1 mM nitric acid.[32] These conditions are similar to the sorption conditions in this study; 0.01 mM $Ln(NO_3)_3$ and 0.0001-10 mM nitric acid (pH 2-7). Therefore it is possible that Ln sorption occurs in this system via coordination of the Ln ions to the anionic nitrate species surrounding the protonated TiO_2-NH_3^+. The zeta potential measurements in Figure 4.10 also indicate that in the presence of Eu, the surface charge of TiO_2-NH_2 was more positive at a given pH than when only water, nitrate and ammonium ions were present. This indicates that Eu was sorbed onto the surface of the TiO_2-NH_2 via outer-sphere sorption, since zeta potential measures the potential at the outside of the stationary layer of liquid surrounding the charged particle (slipping plane).[33]

For Cs and Sr, no substantial sorption occurred below pH 6-7 with TiO_2-NH_2 (Table 4.4). Cesium was the most poorly sorbed element investigated, which was again attributed to its soft Lewis base character which leads to its poor affinity for the hard oxygen donors of the nitrate anion.[27] Sorption of Sr at pH 6-7 (98 %) was much higher than for Cs (14 %) since Sr is more 'hard' than Cs, with a higher charge density and smaller ionic radius. Sorption of Mo was quantitative from pH 2-7. Below the isoelectric point of 5.0, the TiO_2-NH_2 surface was positively charged and sorption of the molybdate anion was expected, as described above for TiO_2-NF. However, at pH 7 the TiO_2-NH_2 surface was negatively charged, presumably due to the presence of nitrate anions at the surface. Therefore, the quantitative sorption of Mo at pH 7 suggests that the molybdate anion was sorbed preferentially over nitrate anions and hence replaced them at the TiO_2-NH_2 surface.

The most interesting result was the sorption of U by TiO_2-NH_2, which increased with pH from approx. 30 % at pH 2 to approx. 90 % at pH 3 and was quantitative by pH 5 (Table 4.4).

This 90 % sorption of U by TiO_2-NH_2 at pH 3 was approx. 75% higher than the extraction of any other element by TiO_2-NH_2 at pH 3, indicating TiO_2-NH_2 was selective for U at pH 3. In addition, TiO_2-NF sorbed only approx. 50 % U at pH 3, so TiO_2-NH_2 also showed enhanced affinity for U at pH 3. TiO_2-NH_2 also extracted U selectively and more efficiently than TiO_2-NF at pH 2, but to a lesser extent. When the pH was increased to 5, both TiO_2-NH_2 and TiO_2-NF demonstrated quantitative U sorption. Since at pH 2 and 3 the TiO_2-NH_2 surface was positively charged (Figure 4.10), this result suggests the uranyl cation formed a negatively charged complex with nitrate at these lower pH values where the relative concentration of nitrate was higher.[29] In fact, previous studies have shown that at the molar U:nitrate ratio present at pH 2-3 in this study, $UO_2(NO_3)_3^-$ was the predominant species in solution.[34] Thus, the observed efficient and selective sorption of U at pH 2-3 in this study can be explained by outer sphere sorption of the anionic $UO_2(NO_3)_3^-$ species to the positively charged TiO_2-NH_2 surface. Overall, the results in Table 4.4 suggest that functionalization of the titania nanoparticle surface with amine **2** altered its sorption behaviour by enhancing Ln and particularly U sorption.

4.3.2 Sorption of Individual Elements by TiO_2-pico

The ability of TiO_2-pico to sorb Ce, Eu, Yb, Cs, Sr, U and Am was investigated from pH 3-7 and the results are shown in Table 4.5. The pH of the solutions after contact with TiO_2-pico was unchanged. TiO_2-pico sorption of Ln increased with pH from 5 % or less at pH 3 to approx. 90 % at pH 7. Cesium and strontium were not sorbed at any pH while U sorption increased from 50 % at pH 3 to 99 % at pH 7. The observed trend of increasing Ln and U sorption with pH for TiO_2-pico can be explained by the increased concentration of nitrate anions in solution at lower pH, which compete with the TiO_2-pico surface to coordinate the metal cations. Thus despite the similar trend of increasing sorption with pH for TiO_2-pico and TiO_2-NH_2, the mechanism of sorption was different for TiO_2-pico since its surface was uncharged, even at pH 3. A previous study of U solvent extraction by picolinamide-based ligands showed that the U is complexed by the carbonyl group of the amide.[35] Therefore it is likely that a similar mechanism of sorption occurs for Ln and U in the present system, as they are both hard Lewis bases with a high affinity for hard oxygen donors.[27]

Table 4.5: Percentage extraction of 1 ppm Ce, Eu, Yb, Cs, Sr, U and Am (as individual elements) by TiO_2-pico at varying pH values. x = not measured.

	TiO_2-pico			
pH	**3**	**4**	**5**	**7**
Ce	1 ± 10	36 ± 7	84 ± 2	92 ± 6
Eu	5 ± 9	68 ± 6	85 ± 1	89 ± 2
Yb	3 ± 9	69 ± 4	72 ± 4	84 ± 3
Cs	2 ± 9	x	0	0
Sr	0	x	0	0
Mo	≥ 99	≥ 99	X	x
U	47 ± 5	x	99 ± 1	99 ± 1
Am	20 ± 4	x	x	x

The sorption efficiencies of TiO_2-NF and TiO_2-pico were similar at pH 3 for all elements and at pH 5 and 7 for U. However, TiO_2-pico showed higher Ln sorption at pH 4-5 and lower Ln sorption at pH 7 than TiO_2-NF. This suggests that under slightly acidic conditions, the presence of the picolinamide on the titania surface enhanced Ln sorption. However, at neutral pH when there were no protons competing for sorption, TiO_2-NF sorbed Ln more effectively than TiO_2-pico. Thus TiO_2-pico is more selective for Ln over protons than TiO_2-NF, but is also a weaker Ln sorbent. TiO_2-pico also showed lower Sr sorption than TiO_2-NF at pH 5-7, suggesting that the picolinamide functionality supressed Sr sorption.

Since calixarene based picolinamide extractants have previously been used in solvent extraction processes to achieve the challenging actinide-lanthanide separation,[9,36] it was of interest to investigate the separation factor between Am and Eu using TiO_2-pico. *N*-Butyl-2-pyridinecarboxamide was previously shown to be unable to extract Am or Eu without the use of a phase transfer agent at pH 3, but once incorporated onto the lower rim of a calix[6]arene (Figure 4.11) demonstrated a separation factor $SF_{Am/Eu}$ of 2.3, although with very low extraction efficiencies (distribution coefficient K_d <10).[36] At the same pH of 3, TiO_2-pico sorbed Am with K_d 40 ± 9 and Eu with K_d 11 ± 1, giving a separation factor $SF_{Am/Eu}$ of 3.6 ± 1.0 (mean ± standard deviation). Therefore it can be concluded that, under similar conditions, Am sorption by TiO_2-pico demonstrated superior extraction efficiency and selectivity to solvent extraction using picolinamide extractants with or without calixarene scaffolds.

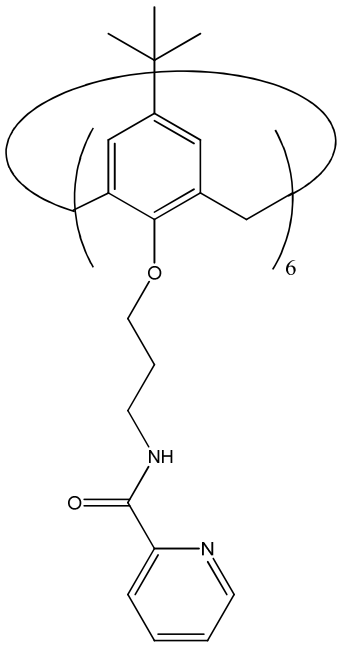

Figure 4.11: Chemical structure of as 37,38,39,40,41,42-Hexakis(3-(pyridine-2-carboxy)amino)propoxy)-*ptert*-butylcalix[6]arene

4.3.3 Sorption of Individual Elements by TiO_2-TBP

The ability of TiO_2-TBP to sorb Ce, Eu, Yb, Cs, Sr and U was investigated from pH 1-5. These sorption experiments were performed at a lower pH range than TiO_2-NH_2 and TiO_2-pico sorption experiments because TiO_2-TBP was designed as a solid-phase mimic of the TBP extractant in the PUREX process which is performed under strongly acidic conditions. However, no sorption of any element was observed at pH 1, therefore Table 4.6 shows the sorption behaviour of TiO_2-TBP from pH 2-5. The pH of the solutions after contact with TiO_2-TBP was unchanged.

Table 4.6: Percentage extraction of 1 ppm Ce, Eu, Yb, Cs, Sr and U (as individual elements) by TiO_2-TBP at varying pH values. x = not measured.

	TiO_2-TBP			
pH	**2**	**3**	**4**	**5**
Ce	x	2 ± 9	47 ± 5	51 ± 11
Eu	x	5 ± 9	79 ± 3	82 ± 3
Yb	4 ± 9	30 ± 9	94 ± 1	97 ± 1
Cs	x	0	x	2 ± 9
Sr	x	0	x	1 ± 9
Mo	52 ± 23	58 ± 28	60 ± 29	
U	10 ± 9	72 ± 3	x	99 ± 1

TiO_2-TBP sorption of Ln increased with pH from less than 5 % at pH 2 to approx. 50 % for Ce, 80 % for Eu and 95 % for Yb at pH 5. In fact, from pH 3-5, Ln sorption by TiO_2-TBP increased across the Ln series, with higher extraction efficiencies demonstrated for the

heaviest Ln Yb. The separation factors were $SF_{Yb/Ce}$ = 23.3 ± 5.2 and $SF_{Yb/Eu}$ = 6.1 ± 1.9 (mean ± standard deviation) and were reasonably consistent across the pH range 3-5. Cesium and strontium were not sorbed at any pH and U sorption was approx. 10 % at pH 2 then increased to 99 % at pH 5. This trend of increasing sorption with pH was explained similarly to TiO_2-pico since the TiO_2-TBP surface was also uncharged.

Relative to TiO_2-NF (Table 4.4), functionalization with phosphate **1** enhanced sorption of Ce at pH 4, of Eu at pH 4 and 5 and of Yb at pH 2, 3, 4 and 5. TiO_2-TBP also showed lower Sr sorption than TiO_2-NF at pH 5, suggesting that the phosphate functionality supressed Sr sorption, similar to TiO_2-pico. Functionalization with phosphate **1** also appeared to suppress sorption of Mo, which was quantitative for TiO_2-NF but only 50-60 % for TiO_2-TBP. Sorption of U was similar for TiO_2-TBP and TiO_2-NF at pH 2 and pH 5 but TiO_2-TBP showed approx. 20 % higher sorption of U at pH 3 than TiO_2-NF. It should also be noted that at pH 3 TiO_2-TBP demonstrated less selective sorption of U with respect to Yb than TiO_2-NH_2, but was more selective with respect to Mo. Therefore, the most appropriate choice of sorbent for selective U extraction would be dependent upon the other elements present in solution.

In the PUREX process, TBP is used to selectively extract U and Pu at high acid concentrations (5-6 M nitric acid) and U extraction decreases swiftly with decreasing acid concentration.[37] Therefore, sorption of U from 3 M nitric was investigated to determine whether increased nitric acid concentration would increase U sorption. However, TiO_2-TBP sorption of 1 ppm U was negligible from 3 M nitric acid (< 2 %). In order to determine the effect of increasing the nitrate concentration while maintaining an acidity of pH 1 (0.1 M H^+), sorption of U from 3 M ammonium nitrate and 0.1 M nitric acid (pH 1) was performed. TiO_2-TBP sorption of 1 ppm U was < 1 % from 0.1 M nitric acid, but increased to approx. 10 % when the nitrate concentration was increased (3 M ammonium nitrate and 0.1 M nitric acid). As such, increasing nitrate concentration did cause a modest increase in U sorption by TiO_2-TBP, suggesting that nitrate anions are involved in the mechanism of sorption. However, increasing the acid concentration concomitantly removed this effect.

One possible explanation for the low sorption of U by TiO_2-TBP was that the phosphate group of the ligand **1** was conformationally constrained when coordinated to the titania nanoparticle surface such that it could not easily coordinate metal ions from solution (Figure 4.12 'A'). This hypothesis was supported by previously performed molecular dynamics simulations, which showed that during solvent extraction the TBP in the $UO_2(NO_3)_2(TBP)_2$ complex formed was primarily coordinated to UO_2 via the P=O group.[38] The P=O group of phosphate **1** can be seen to be particularly restricted in Figure 4.12 'A'. Steric hindrance of the coordinating phosphate group of ligand **1** may also explain the selectivity of TiO_2-TBP for heavier Ln, since the smaller ionic radii of the heavy Ln (102 pm for Ce, 95 pm for Eu and 87 pm for Yb)[26] are more likely to be able to approach the sterically hindered P=O group. This hypothesis is also consistent with U being the most effectively extracted element using TiO_2-TBP, since U(VI) has an even smaller ionic radius than the Ln, of 73 pm.[26]

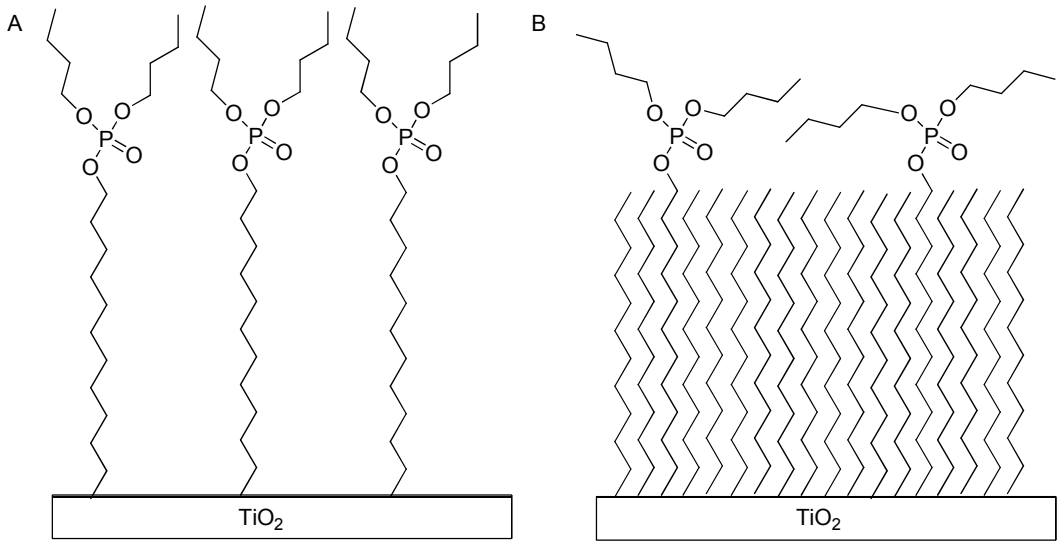

Figure 4.12: Schematic representation of TiO_2-TBP (A) and TiO_2-TBP/decene (B), illustrating that the oxygen atoms of the phosphate should be more available to coordinate metal ions from solution with TiO_2-TBP/decene.

In order to try and improve the extraction efficiency of U, titania nanoparticles were functionalised with alkylphosphate **1** and 1-decene in a 1:10 molar ratio to give TiO_2-TBP/decene. In this material the alkylphosphonate groups should have more conformational freedom (Figure 4.12 'B'). Sorption of U with TiO_2-TBP/decene gave similar extraction efficiencies to TiO_2-TBP (within error) at pH 1-2 but at pH 3 U extraction efficiencies were slightly higher with TiO_2-TBP/decene (86 ± 5 % versus 72 ± 3 %). At pH 5 both materials sorbed approx. 99 % U and thus their performances could not be distinguished. These results are still not comparable to the solvent extraction of U in the PUREX process. However, U sorption was similar or greater with TiO_2-TBP/decene than with TiO_2-TBP despite the fact that the number of phosphonate groups on the titania surface was likely to be less for TiO_2-TBP/decene as they were 'diluted' by the decene molecules (Figure 4.12). This suggests that the increased conformational freedom of the phosphonate head groups in TiO_2-TBP/decene did enhance their ability to coordinate U ions.

4.3.4 Competitive Sorption

It has been shown that TiO_2-NF, TiO_2-NH_2 and TiO_2-TBP extracted U at pH 2 but with low efficiency (approx. 20 %). Also, at pH 3, the efficiency of U extraction increased substantially for all three functionalised titania materials, but more for TiO_2-NH_2 and TiO_2-TBP than TiO_2-NF, indicating that the amine and phosphate functionalisations enhanced U sorption. It was therefore of interest to investigate whether selective U extraction could be achieved by TiO_2-NF, TiO_2-NH_2, TiO_2-TBP, and also TiO_2-TBP/decene, during competitive sorption at pH 2.5. TiO_2-pico did not demonstrate enhanced sorption of U relative to TiO_2-NF at pH 3 and was therefore not investigated further. The results of the competitive sorption experiment are shown in Figure 4.13. All four functionalised titania materials demonstrated

selectivity for U in a competitive environment, although with varying degrees of efficiency and selectivity. Molybdenum was not included in this competitive sorption experiment because as an anionic species it is not directly comparable to the other cationic species present. If necessary, uranium solutions containing Mo could be easily decontaminated using an anion exchange column.

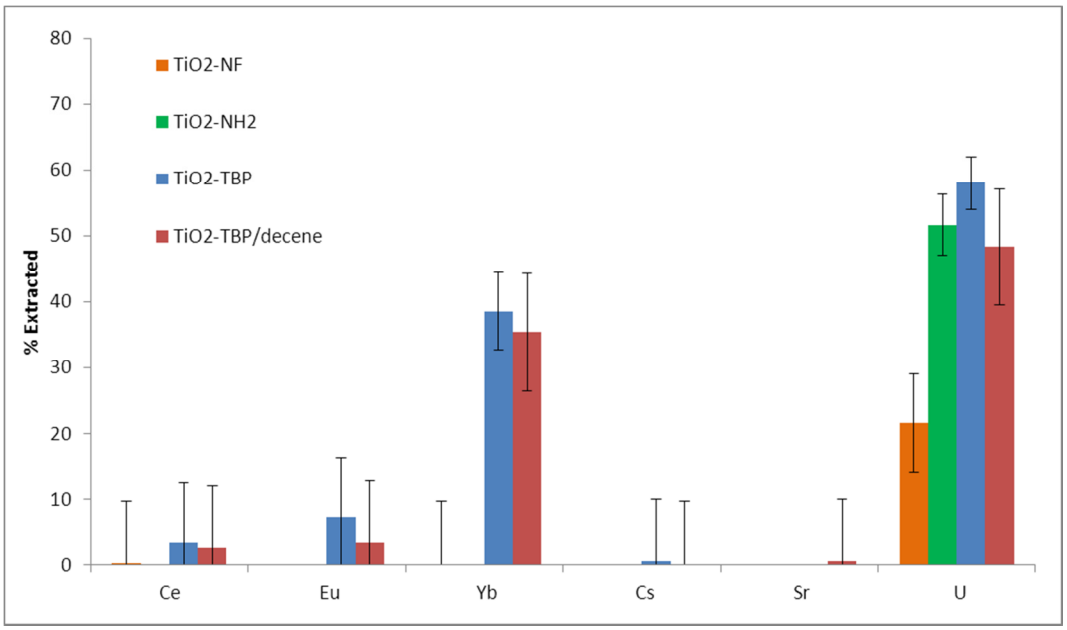

Figure 4.13: Percentage extraction of 1 ppm Ce, Eu, Yb, Cs, Sr and U (competitive) at pH 2.5 for TiO_2-NF, TiO_2-NH_2, TiO_2-TBP and TiO_2-TBP/decene.

TiO_2-NF selectively sorbed U from the solution of 1 ppm Ce, Eu, Yb, Cs, Sr and U but with a low efficiency of only approx. 20 %. TiO_2-NH_2, TiO_2-TBP and TiO_2-TBP/decene all demonstrated a higher U sorption efficiency of approx. 50 %, but only TiO_2-NH_2 combined this efficiency with complete selectivity as TiO_2-TBP and TiO_2-TBP/decene also sorbed approx. 35 % Yb. This selective sorption of U at pH 2.5 demonstrated by TiO_2-NH_2 may be of interest in applications such as decontamination of wastewater from mining[39] or dilute low level waste from nuclear processes.[40]

Although examples exist in the literature of organically functionalised titania based materials being utilised for sorption of U,[41,42] no selectivity data has previously been reported. The selectivity exhibited by TiO_2-NH_2 at pH 2.5 was superior to other polymer or silica based sorbents designed for selective U removal.[43,44] For example, a phenolic hydroxyl-functionalised polymer based chelating sorbent, during competitive sorption at pH 4.5, sorbed substantial amounts of Ln as well as U.[43] Complete U selectivity has been demonstrated by a fural functionalised mesoporous silica sorbent at pH 5.5,[45] but sorption of U decreased substantially below pH 3 and selectivity at lower pH values was not investigated. TiO_2-NH_2 may also be considered complementary to U/TEVA, a commercially available U sorbent

consisting of 40 % diamyl amylphosphonate impregnated in Amberchrom-CG (acrylic ester) resin, which effectively and selectively sorbs U from >1 M acidic solutions.[46]

4.4 Hydrolytic Stability

For separations in a nuclear context, a sorbent based on titania has the advantage of hydrolytic and radiolytic stability over silica and polymer based resins.[47,48] In order to test the hydrolytic stability of the present organo-functionalised titania nanoparticle materials, the sorption properties of TiO_2-TBP and TiO_2-TBP/decene were tested before and after leaching with 0.01 M nitric acid for 24 h. The results are shown in Figure 4.14. If functional groups were lost from the surface during leaching, it would be expected that sorption would decrease and approach the behaviour of TiO_2-NF. However, it can be seen from Figure 4.14 that the extraction efficiencies of TiO_2-TBP and TiO_2-TBP/decene for Yb and U before and after leaching were unchanged (within error). Thus, covalent functionalization of the surface of titanium dioxide via an alkene using heat provided a surface covering that was hydrolytically stable at pH 2 for 24 h. The reusability of the functionalised titania materials was not investigated since previous studies have proven the utility of disposal via ceramic wasteforms and the materials produced within this work are of appropriate compositions to be applicable.[2]

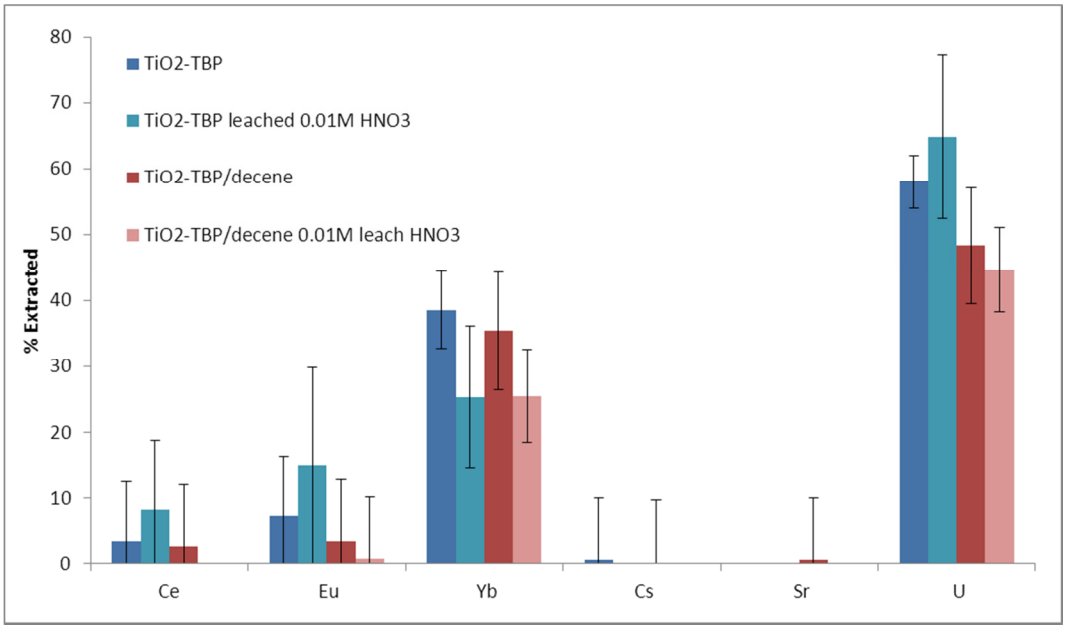

Figure 4.14: Percentage extraction of 1 ppm Ce, Eu, Yb, Cs, Sr and U (competitive) at pH 2.5 for TiO_2-TBP and TiO_2-TBP/decene before and after leaching with 0.01 M nitric acid for 24 h.

The hydrolytic stability of TiO_2-TBP and TiO_2-TBP/decene was considered superior or comparable to other organo-functionalised titania based materials that used phosphonate groups as anchors for surface functionalization. For example, treatment of mesoporous zirconium titanate frameworks functionalised with methylphosphonic acid using pH 3 nitric

acid for 24 h caused loss of approx. 10 % P.[49] On the other hand, octadecylphosphonate functionalised titania lost only 5 % of its functional groups after 1 week in a solution of 1:1 HCl/THF (pH 1).[50] Thus, materials functionalised using alkylphosphonates with longer alkyl chains demonstrated enhanced hydrolytic stability, likely due to self-assembly of a hydrophobic layer on the surface of the framework material.

4.5 Conclusions

Titania nanoparticles have been synthesised and functionalised with alkylamine **2** (TiO_2-NH_2), as well as the novel ligands alkylpicolinamide **3** (TiO_2-pico) and alkylphosphate **1** (TiO_2-TBP). Covalent functionalization of the titania nanoparticles with these organic ligands was achieved via a simple, novel heating methodology. Successful functionalization was confirmed by MAS NMR, FTIR and CHN microanalysis of the resulting materials.

The sorption behaviour of the three organo-functionalised titania materials with fission products (Ce, Eu, Yb, Cs, Sr, Mo) and actinides (U, Am) present in solutions of used nuclear fuel were explored in a wide pH range. Sorption of individual elements was initially performed and showed that the organo-functionalised titania materials had substantially different sorption properties to non-functionalised titania nanoparticles (TiO_2-NF). Most of the sorption behaviour of TiO_2-NF and TiO_2-NH_2 could be explained via electrostatics as the surface of these materials were charged. Thus, metal cation sorption increased with pH as the surface charge became negative. However, substantial sorption of U was observed at pH 2-3 despite zeta potential measurements indicating the surface charge was positive at this pH (Figure 4.10). This was attributed to the presence of anionic uranium nitrate complexes at pH 2-3.

The surfaces of TiO_2-pico and TiO_2-TBP were not charged in the pH range explored, so sorption was attributed to chelation rather than electrostatic attraction. Nevertheless, a similar trend of increasing metal cation sorption with pH was observed for these materials as competition between the metal cations and hydronium ions (H^+) decreased. TiO_2-pico also showed some selectivity for Am over Ln, which is a notoriously difficult but important separation to achieve in order to close the nuclear fuel cycle and decrease the hazards of nuclear waste. The selectivity and extraction efficiency demonstrated by the solid phase sorbent TiO_2-pico was superior to a picolinamide functionalised calixarene extractant previously used in a solvent extraction process. Thus, immobilisation of an organic ligand used for solvent extraction onto a stable, solid support provided improved separation performance in this instance. On the other hand, TiO_2-TBP showed inferior extraction efficiency and selectivity to the TBP ligand used in solvent extraction. This was attributed to the constrained conformation of alkylphosphate **1** on the surface of the titania nanoparticles. An attempt to reduce this constraint by 'diluting' the functional ligands on the surface with 1-decene (Figure 4.12) was only partially successful.

Since both TiO_2-NH_2 and TiO_2-TBP were able to selectively sorb U at low pH (2-3), their sorption was tested in a competitive environment at pH 2.5. Selectivity for U was maintained

in the competitive environment by both TiO_2-NH_2 and TiO_2-TBP, but was superior with TiO_2-NH_2. The excellent selectivity of TiO_2-NH_2 was remarkable given the simplicity of the organic ligand **2** used for functionalisation. The hydrolytic stability of TiO_2-TBP at pH 2 was also demonstrated. Overall, it has been demonstrated that titania nanoparticles can be covalently functionalised with simple organic ligands to provide simple, cost-effective, hydrolytically stable and selective solid-phase sorbents. In particular, this study was the first reported example of organically functionalised titania based sorbents for the selective removal of U from solution.

4.6 References

(1) Griffith, C. S.; De Los Reyes, M.; Scales, N.; Hanna, J. V.; Luca, V. *Acs Appl Mater Inter* **2010**, *2*, 3436.

(2) Donald, I. W.; Metcalfe, B. L.; Taylor, R. N. J. *J Mater Sci* **1997**, *32*, 5851.

(3) Soler-Illia, G. J. A. A.; Azzaroni, O. *Chemical Society Reviews* **2011**, *40*, 1107.

(4) Clifford, J. N.; Martinez-Ferrero, E.; Viterisi, A.; Palomares, E. *Chemical Society Reviews* **2011**, *40*, 1635.

(5) Li, B.; Franking, R.; Landis, E. C.; Kim, H.; Hamers, R. J. *Acs Appl Mater Inter* **2009**, *1*, 1013.

(6) Lopes, C. B. L., P.F.; Cardoso, S.P.; Pereira, E.; Duarte, A.C.; Silva, C.M. In *Ion Exchange Technology II*; Inamuddin, M. L., Ed.; Springer Science & Business Media: New York, 2012.

(7) Phillips, D. H.; Gu, B.; Watson, D. B.; Parmele, C. S. *Water Res* **2008**, *42*, 260.

(8) International Atomic Energy Agency, I. *Implications of Partitioning and Transmutation in Radioactive Waste Management*, IAEA, 2004.

(9) Galletta, M.; Baldini, L.; Sansone, F.; Ugozzoli, F.; Ungaro, R.; Casnati, A.; Mariani, M. *Dalton T* **2010**, *39*, 2546.

(10) Sieval, A. B.; Linke, R.; Heij, G.; Meijer, G.; Zuilhof, H.; Sudholter, E. J. R. *Langmuir* **2001**, *17*, 7554.

(11) Strother, T.; Hamers, R. J.; Smith, L. M. *Nucleic Acids Res* **2000**, *28*, 3535.

(12) Sun, B.; Colavita, P. E.; Kim, H.; Lockett, M.; Marcus, M. S.; Smith, L. M.; Hamers, R. J. *Langmuir* **2006**, *22*, 9598.

(13) Hanley, T. L.; Luca, V.; Pickering, I.; Howe, R. F. *J Phys Chem B* **2002**, *106*, 1153.

(14) Spurr, R. A. M., H. *Anal Chem* **1957**, *29*, 760.

(15) Patterson, A. L. *Physical Review* **1939**, *56*, 978.

(16) Sing, K. S. W., Everett, D.H., Haul, R.A.W., Moscou, L., Pierotti, R.A., Rouquerol, J., Siemieniewska, T. *Pure & Applied Chemistry* **1985**, *57*, 603.

(17) Hammouda, B.; National Institute of Standards and Technology: Gaithersburg, 2010.

(18) Higgins, J. S. B., H.C. *Polymers and Neutron Scattering*; Oxford University Press: Oxford, 1996.

(19) Gou, F. R.; Wang, X. C.; Huo, P. F.; Bi, H. P.; Guan, Z. H.; Liang, Y. M. *Org Lett* **2009**, *11*, 5726.

(20) Furuta, T.; Torigai, H.; Osawa, T.; Iwamura, M. *J Chem Soc Perk T 1* **1993**, 3139.

(21) Primet, M. P., P.; Mathieu, M-V. *The Journal of Physical Chemistry* **1971**, *75*, 1221.

(22) Bovey, F. A. J., L.; Mirau, P.A. *Nuclear Magnetic Resonance Spectroscopy*; 2nd ed.; Academic Press, Inc.: San Diego, 1988.

(23) Colthup, N. B., Daly, L.H., Wiberley, S.E. *Introduction to Infrared and Raman Spectroscopy*; Academic Press: New York, 1964.

(24) Xue, J. H.; Hua, X. H.; Yang, L. M.; Li, W. H.; Xu, Y. Z.; Zhao, G. Z.; Zhang, G. H.; Liu, K. X.; Chen, J. E.; Wu, J. G. *Crystengcomm* **2014**, *16*, 7711.

(25) McMurry, J. *Organic Chemistry*; 6th ed.; Brooks/Cole - Thompson Learning: Belmont, 2004.

(26) Greenwood, N. N. E., A. *Chemistry of the Elements*; 2nd ed.; Reed Educational and Professional Publishing Ltd: Oxford, 1997.

(27) Pearson, R. G. *J. Am. Chem. Soc.* **1963**, *85*, 3533.

(28) Baes Jr, C. F. M., R.E. *The Hydrolysis of Cations*; 1st ed.; Wiley: New York, 1976.

(29) Ikeda, A.; Hennig, C.; Rossberg, A.; Tsushima, S.; Scheinost, A. C.; Bernhard, G. *Anal Chem* **2008**, *80*, 1102.

(30) Vandenborre, J.; Drot, R.; Simoni, E. *Inorganic Chemistry* **2007**, *46*, 1291.

(31) Geckeis, H.; Lutzenkirchen, J.; Polly, R.; Rabung, T.; Schmidt, M. *Chemical Reviews* **2013**, *113*, 1016.

(32) Oikawa, T.; Urabe, T.; Kawano, S.; Tanaka, M. *J Solution Chem* **2011**, *40*, 1094.

(33) Hunter, R. J. *Zeta Potential in Colloid Science: Principles and Applications*; 3rd ed.; Academic Press Limited: London, 1988.

(34) De Houwer, S.; Gorller-Walrand, C. *Journal of Alloys and Compounds* **2001**, *323*, 683.

(35) Lapka, J. L.; Paulenova, A.; Alyapyshev, M. Y.; Babain, V. A.; Herbst, R. S.; Law, J. D. *Radiochim. Acta* **2009**, *97*, 291.

(36) Casnati, A.; Della Ca', N.; Fontanella, M.; Sansone, F.; Ugozzoli, F.; Ungaro, R.; Liger, K.; Dozol, J. F. *European Journal of Organic Chemistry* **2005**, 2338.

(37) Alcock, K. B., G.F.; Hesford, E. McKay, H.A.C. *Journal of Inorganic and Nuclear Chemistry* **1958**, *6*, 328.

(38) Ye, X. G.; Cui, S. T.; de Almeida, V.; Khomami, B. *J Phys Chem B* **2009**, *113*, 9852.

(39) Douglas, G. B.; Wendling, L. A.; Pleysier, R.; Trefry, M. G. *Mine Water Environ* **2010**, *29*, 108.

(40) Nancharaiah, Y. V.; Joshi, H. M.; Mohan, T. V. K.; Venugopalan, V. P.; Narasimhan, S. V. *Curr Sci India* **2006**, *91*, 503.

(41) Kimling, M. C.; Scales, N.; Hanley, T. L.; Caruso, R. A. *Environ Sci Technol* **2012**, *46*, 7913.

(42) Sizgek, G. D.; Griffith, C. S.; Sizgek, E.; Luca, V. *Langmuir* **2009**, *25*, 11874.

(43) Liu, J.; Li, J.; Yang, X. D.; Song, Q.; Bai, C. Y.; Shi, Y.; Zhang, L.; Liu, C. X.; Li, S. J.; Ma, L. J. *Mater Lett* **2013**, *97*, 177.

(44) Liu, Y. H.; Cao, X. H.; Hua, R.; Wang, Y. Q.; Liu, Y. T.; Pang, C.; Wang, Y. *Hydrometallurgy* **2010**, *104*, 150.

(45) Yousefi, S. R.; Ahmadi, S. J.; Shemirani, F.; Jamali, M. R.; Salavati-Niasari, M. *Talanta* **2009**, *80*, 212.

(46) Horwitz, E. P.; Dietz, M. L.; Chiarizia, R.; Diamond, H.; Essling, A. M.; Graczyk, D. *Anal Chim Acta* **1992**, *266*, 25.

(47) Chiarizia, R.; Horwitz, E. P. *Solvent Extr. Ion Exch.* **2000**, *18*, 109.

(48) Etienne, M.; Walcarius, A. *Talanta* **2003**, *59*, 1173.

(49) de los Reyes, M.; Majewski, P. J.; Scales, N.; Luca, V. *Acs Appl Mater Inter* **2013**, *5*, 4120.

(50) Marcinko, S.; Fadeev, A. Y. *Langmuir* **2004**, *20*, 2270.

Chapter 5: Simple Peptides as Ligands for Lanthanides

Covalent functionalization of titania nanoparticles with organic ligands to produce hybrid materials for selective sorption of actinides (An) has been demonstrated in *Chapter 4*. In this chapter, organic ligands for sorption of lanthanides (Ln) will be developed. Lanthanides are targeted for separation from solutions of used nuclear fuel to enable recycling and transmutation of minor actinide (MA) elements, as described previously (*Chapters 1 and 3*). Lanthanides are also of high industrial relevance due to their utility in clean energy technology,[1] catalysis[2] and as biological probes.[3] Peptides were investigated as an organic ligand for Ln because peptides with carboxyllic acid side chains, such as glutamic acid (Glu) and aspartic acid (Asp), are known to form strong and in some cases selective complexes with Ln.[3-5] These complexes form because Ln are hard Lewis acids[6] and therefore prefer to bind to hard donors such as oxygen. Lanthanide binding peptides (LnBP) are thus able to coordinate Ln ions via the oxygen atoms of carboxylic acid side chains and/or carbonyl groups on the peptide backbone.[7] LnBP are also commonly used as structural probes in biological systems[3] due to the uniquely useful properties of peptide:Ln complexes such as their luminescence, nuclear magnetic resonance (NMR) properties, and x-ray contrast.[8]

Much research has been done to develop LnBP with high affinity.[3] Optimisation of the sequence of LnBP by screening methods led to development of a 17 amino acid peptide (Ala-Cys-Val-Asp-Trp-Asn-Asn-Asp-Gly-Trp-Tyr-Glu-Gly-Asp-Glu-Cys-Ala) which showed one of the highest Ln binding constants measured and strong fluorescence.[9] The origins of these desirable properties could only be explained retrospectively after the x-ray crystal structure of the peptide-Ln complex was solved.[4] The high luminescence and selectivity were attributed to the closed-shell coordination of the Ln by the peptide so that water was excluded, hydrophobic amino acids at the C and N termini that caused the peptide to fold into a loop structure ideal for metal ion binding and the position of the Ln coordinated tryptophan residue in the peptide being optimal for sensitising luminescence. However, predictive design of efficient and selective LnBP has not yet been demonstrated to our knowledge.

Development of shorter LnBP still able to demonstrate efficient and selective Ln binding properties would be highly valuable, as this would dramatically reduce the synthetic effort required to generate LnBP. Pascale et al. designed and synthesised hexa-peptides with strong binding efficiencies using unnatural amino acid side chains (Figure 5.1).[10,11] This work demonstrated the importance of the position of the unnatural binding residue in the sequence as well as the length (*n* in Figure 5.1) and denticity of the unnatural polyaminocarboxylate side chains on the affinity and structure of the resulting Ln:peptide complexes.[10-12] However, the decrease in synthetic effort afforded by decreasing the length of the peptide chain was offset by the increased effort required for the inclusion of unnatural amino acids.

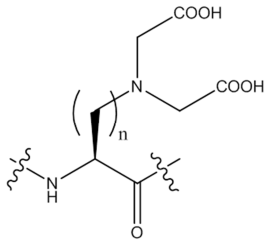

Ada_n

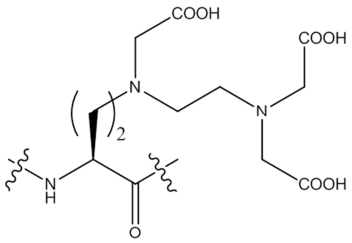

$Ed3a_2$

Hexapeptides:

$Ac - Trp - Ada_1 - Pro - Gly - Ada_2 - Gly - NH_2$

$Ac - Trp - Ed3a_2 - Pro - Gly - Ada_2 - Gly - NH_2$

Figure 5.1: LnBP with unnatural amino acids side chains.

Overall, previous studies have provided some insight into the effects of peptide structure on Ln binding properties, but the effects of simple parameters such as peptide length and stereochemistry have yet to be systematically explored. Therefore, a systematic investigation of the effects of varying the length and stereochemistry of peptides on their Ln binding properties (stoichiometry, binding affinity, complex structure) was performed. A simple model system of di-, tri- and tetra-glutamic acid (Glu) peptides were synthesised with varying stereochemistry introduced via use of both the natural "left-handed" L-Glu and the unnatural "right-handed" D-Glu enantiomers. Peptides of Glu were selected as this amino acid is a common motif in LnBP and has been observed to be involved in bidentate coordination to Ln.[4] The Eu binding properties of these peptides in neutral and acidic solutions were investigated via luminescence spectroscopy, circular dichroism (CD), small angle x-ray scattering (SAXS), NMR titrations and density functional theory (DFT) modelling. This provided insight into how the peptide length and stereochemistry affected Ln binding affinity. The information gained will assist in future design of high affinity, strongly luminescent, selective LnBP.

The peptide which displayed the strongest binding of Eu in aqueous solutions was then covalently attached to the surface of titania nanoparticles via the method described in *Chapter 4*. The solid-phase sorbent material produced was used for competitive sorption experiments with activation product aluminium (Al) and nickel (Ni), alkaline earth metal calcium (Ca), fission products strontium (Sr), cesium (Cs), lanthanum (La), neodymium (Nd), europium (Eu), holmium (Ho), ytterbium (Yb) and actinide uranium (U). These sorption experiments were performed to determine whether functionalization of the titania nanoparticles with the peptide induced selective affinity for Ln, as hoped. The pH dependence of sorption by the peptide functionalised titania nanoparticles was also investigated.

5.1 Experimental Methods

5.1.1 Synthesis of 1,3-Dioxo-1H-benz[d,e]isoquinoline-2(3H)-acetic acid (naph, 7)

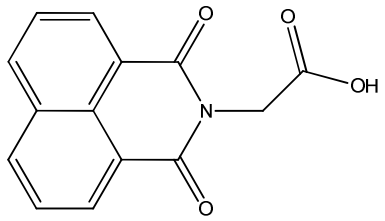

A mixture of glycine (0.28 g, 3.7 mmol) and 1,8-naphthalic anhydride (0.59 g, 3.0 mmol) in 3:1 v/v ethanol (EtOH)/water (20 mL) was heated in a pressure tube at 130 °C for 70 h. The solvent was then removed under vacuum, affording the crude product as a brown solid. The crude product was washed with EtOH and filtered. The filtrate was reduced in volume under vacuum and the resulting precipitate again filtered, washing with EtOH, to give the desired product as a light brown solid (0.63 g, 82 % yield). m.p. 272-275 °C; ^{1}H NMR (300 MHz, DMSO-d_6) δ (ppm): 8.53 (m, 4H), 7.91 (t, J = 7.8 Hz, 2H), 4.73 (s, 2H). Characterisation data was consistent with previously reported results.[13]

5.1.2 Solid Phase Peptide Synthesis

Di-, tri- and tetra-Glu peptides (Figure 5.2) with a naphthalimide tag were synthesised via solid phase peptide synthesis in polypropylene syringes equipped with Teflon filters (Torviq).

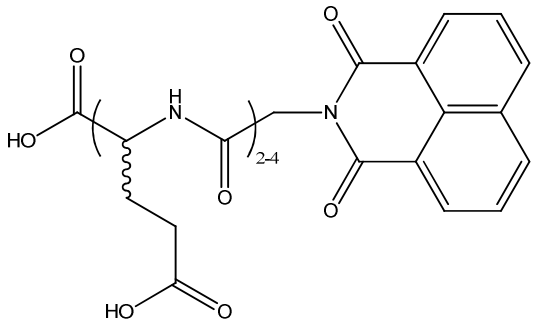

Figure 5.2: Chemical structure of di-, tri- and tetra-Glu peptides

Resin loading: Wang resin (0.10 g, 1.1 mmol/g, 0.11 mmol) was allowed to swell in dimethylformamide (DMF, 2 mL) for 30 min. Meanwhile, Fmoc-Glu(*t*Bu)-OH (0.42 g, 1.0 mmol) was dissolved in dry CH_2Cl_2 (5 mL) and *N,N'*-diisopropylcarbodiimide (DIC, 79 µL, 0.5 mmol) added. The resulting solution was immediately placed in an ice bath and stirred at 0 °C for 20 min. The solvent was then removed under vacuum to afford the asymmetric anhydride as a white solid. This residue was redissolved in DMF (4 mL) and added to the swollen Wang resin with 4-dimethylaminopyridine (DMAP, 1.2 mg, 0.01 mmol). The resin was then shaken at room temperature for 1 h before washing with DMF (5 x 3 mL), CH_2Cl_2 (5 x 3 mL) and DMF (5 x 3 mL).

Deprotection: Fmoc deprotection was performed by washing the resin three times with 1:4 v/v piperidine/DMF (3 mL) for 5-10 min. Measurement of the uv-visible absorbance of the washings at λ = 301 nm showed that the amino acid loading onto the resin was quantitative (ε = 7800 for the fulvene-piperidine adduct). The resin was then again washed with DMF (5 x 3 mL), CH_2Cl_2 (5 x 3 mL) and DMF (5 x 3 mL).

Amino acid coupling: Couplings were performed by adding a solution of either L- or D-Fmoc-Glu(*t*Bu)-OH (0.25 g, 0.6 mmol), *O*-benzotriazole-*N,N,N',N'*-tetramethyl-uronium-hexafluorophosphate (HBTU, 0.21 g, 0.5 mmol) and *N,N'*-diisopropylethylamine (DIPEA, 200 µL, 1.1 mmol) in DMF (3 mL) to the resin and shaking at room temperature for at least 1 h. The resin was then washed with DMF (5 x 3 mL), CH_2Cl_2 (5 x 3 mL) and DMF (5 x 3 mL). After the final coupling, the resin was washed with DMF (5 x 3 mL) and CH_2Cl_2 (5 x 3 mL) then dried under vacuum for 1 h before being sealed with parafilm and stored under refrigerated conditions.

Naphthalimide coupling: a solution of naphthalimide **7** (56 mg, 0.22 mmol), benzotriazol-1-yloxytri(pyrrolidino)-phosphonium hexafluorophosphinate (PyBOP, 116 mg, 0.22 mmol) and DIPEA (76 µL, 0.44 mmol) in DMF (6mL) was added to the peptide loaded resin (100 mg, 0.11 mmol). The resin was then shaken at room temperature for 2 h before washing with DMF (5 x 5 mL), CH_2Cl_2 (5 x 5 mL) and DMF (5 x 5 mL).

Cleavage: The naphthalimide tagged peptides were cleaved from the resin and the side chains concomitantly deprotected by adding a mixture of 90:5:5 v/v/v trifluoroacetic acid (TFA)/triisopropylsilane (TIS)/water (2.0 mL) to the resin (0.1 g, 0.11 mmol) and shaking at room temperature for 2 h. The cleaved products were separated from the resin by filtration and combined with TFA washings (2 x 2 mL). Addition of cold diethyl ether (50 mL) afforded a white precipitate which was extracted into distilled water (1 x 50 mL, 2 x 10 mL). After washing the aqueous phase with diethyl ether (2 x 10 mL), the volume was reduced under vacuum and the remaining liquid removed by lyophilisation to afford the modified peptides.

Naph-L-Glu(OH)-D-Glu(OH)-D-Glu(OH)-L-Glu(OH)-OH (naph-LDDL-Glu-OH, **8**) was synthesised on Wang resin utilising the general methods for solid phase peptide synthesis to give the desired tetra-peptide as a white powder (86 mg, 100%); m.p. 174-176 °C; $[\alpha]_D^{20}$ -16.0° (*c* 0.1, H_2O); ^{1}H NMR (300 MHz, DMSO-d_6) δ (ppm): 8.49 (m, 4H), 8.51 (m, 1H, NH), 8.10 (d, *J* = 8.0 Hz, 1H, NH), 8.02 (dd, *J* = 8.0, 8.2 Hz, 2H, NH), 7.89 (t, *J* = 7.8 Hz, 2H), 4.74 (s, 2H), 4.31 (m, 4H), 2.24 (m, 8H), 1.84 (m, 8H); ^{13}C NMR (125 MHz, DMSO-d_6) δ (ppm): 174.4, 174.3, 174.3, 174.1, 173.5, 171.5, 171.4, 167.5, 163.9, 162.9, 135.0, 131.8, 131.4, 128.0, 127.8, 122.4, 52.6, 52.4, 52.3, 51.5, 42.9, 30.5, 30.3, 28.3, 27.9, 27.9, 26.9 (2 signals obscured or overlapping); HRMS (ESI) calcd for $C_{34}H_{37}N_5O_{16}$ $[M+Na]^+$ *m/z* 794.2134, found 794.2128.

Naph-D-Glu(OH)-L-Glu(OH)-D-Glu(OH)-L-Glu(OH)-OH (naph-DLDL-Glu-OH, **9**) was synthesised on Wang resin utilising the general methods for solid phase peptide synthesis to give the desired tetra-peptide as a white powder (88 mg, 100%); m.p. 179-182 °C; $[\alpha]_D^{20}$ +21.5° (*c* 0.1, MeOH); ^{1}H NMR (300 MHz, MeOD) δ (ppm): 8.56 (d, *J* = 7.2 Hz, 2H), 8.35 (d, *J*

= 8.2 Hz, 2H), 7.81 (dd, *J* = 7.2, 8.2 Hz, 2H), 4.74 (s, 2H), 4.37 (m, 4H), 2.38 (m, 8H), 2.05 (m, 8H); ^{13}C NMR (100 MHz, DMSO-d_6) δ (ppm): 174.4, 174.3, 174.3, 174.1, 173.5, 171.6, 171.5, 171.4, 163.9, 162.8, 135.1, 131.8, 131.4, 128.0, 127.8, 122.4, 52.7, 52.2, 51.5, 42.9, 31.2, 30.5, 30.3, 30.2, 28.3, 27.9, 27.9, 26.9 (1 signal obscured or overlapping); HRMS (ESI) calcd for $C_{34}H_{37}N_5O_{16}$ $[M+Na]^+$ *m/z* 794.2134, found 794.2128.

Naph-L-Glu(OH)-L-Glu(OH)-L-Glu(OH)-L-Glu(OH)-OH (naph-LLLL-Glu-OH, **10**) was synthesised on Wang resin utilising the general methods for solid phase peptide synthesis to give the desired tetra-peptide as a white powder (52 mg, 61%); m.p. 200-203 °C; $[\alpha]_D^{20}$ -43.6° (*c* 0.1, MeOH) ; ^{1}H NMR (200 MHz, DMSO-d_6) δ (ppm): 8.49 (m, 4H), 8.17 (d, *J* = 7.6 Hz, 1H, NH), 8.01 (br s, 1H, NH), 7.89 (dd, *J* = 7.6, 7.9 Hz, 2H), 4.72 (s, 2H), 4.24 (m, 4H), 2.27 (m, 8H), 1.83 (m, 8H); ^{13}C NMR (100 MHz, DMSO-d_6) δ (ppm): 174.5, 174.4, 174.2, 173.5, 171.6, 171.3, 167.3, 163.8, 135.0, 131.8, 131.4, 128.0, 127.8, 122.4, 52.3, 51.7, 42.8, 30.6, 30.5, 28.0, 27.7, 26.6 (6 signals obscured or overlapping); HRMS (ESI) calcd for $C_{34}H_{37}N_5O_{16}$ $[M+Na]^+$ *m/z* 794.2134, found 794.2128.

Naph-L-Glu(OH)-D-Glu(OH)-L-Glu(OH)-OH (naph-LDL-Glu-OH, **11**) was synthesised on Wang resin utilising the general methods for solid phase peptide synthesis to give the desired tri-peptide as a white powder (69 mg, 100%); m.p. 185-191 °C; $[\alpha]_D^{20}$ -21.5° (*c* 0.1, MeOH); ^{1}H NMR (200 MHz, DMSO-d_6) δ (ppm): 8.54 (m, 4H), 8.12 (d, *J* = 8.3 Hz, 2H, NH), 7.92 (dd, *J* = 7.8, 8.3 Hz, 2H), 4.75 (s, 2H), 4.29 (m, 3H), 2.23 (m, 6H), 1.88 (m, 6H); ^{13}C NMR (100 MHz, DMSO-d_6) δ (ppm): 174.3, 174.3, 174.1, 171.4, 171.4, 167.6, 163.8, 135.0, 131.5, 131.4, 128.0, 127.8, 122.4, 52.7, 52.2, 51.5, 42.9, 30.4, 30.3, 30.2, 28.0, 27.8 (2 signals obscured or overlapping); HRMS (ESI) calcd for $C_{29}H_{30}N_4O_{13}$ $[M+Na]^+$ *m/z* 665.1708, found 665.1702.

Naph-L-Glu(OH)-L-Glu(OH)-L-Glu(OH)-OH (naph-LLL-Glu-OH, **12**) was synthesised on Wang resin utilising the general methods for solid phase peptide synthesis to give the desired tri-peptide as a white powder (51 mg, 74%); m.p. 201-207 °C; $[\alpha]_D^{20}$ -50.9° (*c* 0.1, MeOH); ^{1}H NMR (300 MHz, DMSO-d_6) δ (ppm): 8.51 (m, 4H), 8.16 (d, *J* = 7.7 Hz, 1H, NH), 7.97 (d, *J* = 7.6 Hz, 1H, NH), 7.90 (dd, *J* = 7.6, 7.7 Hz, 2H), 4.73 (s, 2H), 4.27 (m, 3H), 2.29 (m, 6H), 1.85 (m, 6H); ^{13}C NMR (100 MHz, DMSO-d_6) δ (ppm): 174.5, 174.4, 174.2, 173.5, 171.6, 171.3, 167.3, 163.8, 135.0, 131.8, 131.4, 128.0, 127.8, 122.4, 52.3, 51.7, 42.8, 30.6, 30.5, 28.0, 27.8, 26.7 (2 signals obscured or overlapping); HRMS (ESI) calcd for $C_{29}H_{30}N_4O_{13}$ $[M+Na]^+$ *m/z* 665.1708, found 665.1702.

Naph-D-Glu(OH)-L-Glu(OH)-OH (naph-DL-Glu-OH, **13**) was synthesised on Wang resin utilising the general methods for solid phase peptide synthesis to give the desired di-peptide as a white powder (41 mg, 73%); m.p. 145-148 °C; $[\alpha]_D^{20}$ +23.3° (*c* 0.1, MeOH); ^{1}H NMR (300 MHz, DMSO-d_6) δ (ppm): 8.48 (m, 4H), 8.06 (d, *J* = 8.0 Hz, 1H, NH), 7.89 (dd, *J* = 7.6, 8.0 Hz, 2H), 4.73 (s, 2H), 4.30 (m, 2H), 2.25 (m, 4H), 1.89 (m, 4H); ^{13}C NMR (100 MHz, DMSO-d_6) δ (ppm): 174.3, 174.1, 173.5, 171.5, 167.3, 163.9, 135.1, 131.8, 131.4, 128.0, 127.8, 122.4, 52.4, 51.6, 42.9, 31.2, 30.4, 28.3, 26.9; HRMS (ESI) calcd for $C_{24}H_{23}N_3O_{10}$ $[M+Na]^+$ *m/z* 536.1282, found 536.1276.

Naph-L-Glu(OH)-LGlu(OH)-OH (naph-LL-Glu-OH, **14**) was synthesised on Wang resin utilising the general methods for solid phase peptide synthesis to give the desired di-peptide as a white powder (55 mg, 97%); m.p. 188-194 °C; $[\alpha]_D^{20}$ -34.3° (*c* 0.1, MeOH); ^{1}H NMR (200 MHz, DMSO-d_6) δ (ppm): 8.54 (m, 4H), 8.21 (d, *J* = 7.4 Hz, 1H, NH), 7.92 (dd, *J* = 7.4, 7.9 Hz, 2H), 4.76 (s, 2H), 4.31 (m, 2H), 2.32 (m, 4H), 1.90 (m, 4H); ^{13}C NMR (125 MHz, DMSO-d_6) δ (ppm): 174.6, 174.3, 173.7, 171.8, 167.4, 164.0, 135.2, 132.0, 131.5, 128.1, 127.9, 122.5, 52.2, 51.9, 43.0, 30.7, 30.6, 28.3, 26.7; HRMS (ESI) calcd for $C_{24}H_{23}N_3O_{10}$ $[M+Na]^+$ *m/z* 536.1282, found 536.1276.

5.1.3 Synthesis of Undecene-L-Glu(OtBu)-D-Glu(OtBu)-D-Glu(OtBu)-L-Glu(OtBu)-OH (undecene-LDDL-Glu(tBu)-OH, 15)

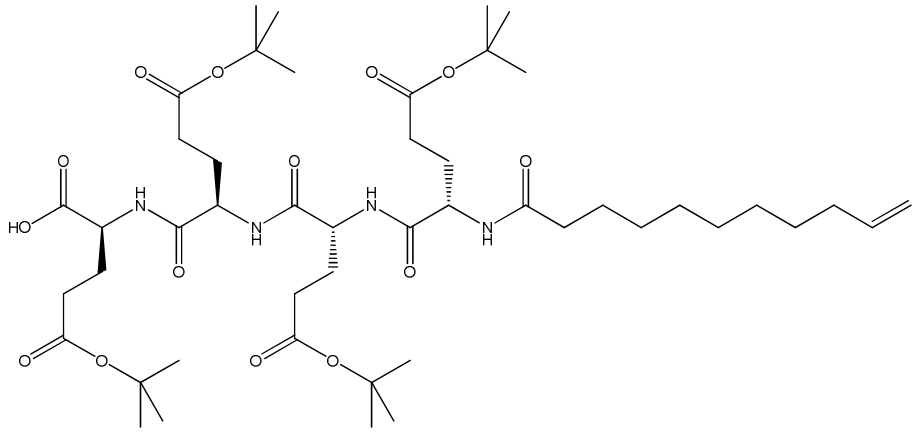

Figure 5.3: Chemical structure of undecene-LDDL-Glu(*t*Bu)-OH **15**

To load the first amino acid, 2-chlorotrityl chloride resin (0.30 g, 1.2 mmol/g, 0.36 mmol) was shaken with a solution of Fmoc-Glu(*t*Bu)-OH (0.15 g, 0.36 mmol) and DIPEA (0.25 mL, 1.4 mmol) in anhydrous CH_2Cl_2 (3 mL) at room temperature for 75 min. The resin was drained and then washed with 17:2:1 v/v CH_2Cl_2/MeOH/DIPEA (3 x 2 mL), CH_2Cl_2 (3 x 2 mL), DMF (2 x 2 mL) and CH_2Cl_2 (4 x 2 mL). Fmoc deprotection was performed as described in *section 5.1.2* and indicated a loading of 0.9 mmol/g. Coupling of the second, third and fourth Glu residues was also performed as described in *section 5.1.2* but using approx. double the amount of reagents such that L- or D- Fmoc-Glu(*t*Bu)-OH (0.62 g, 1.5 mmol), HBTU (0.54 g, 1.4 mmol) and DIPEA (0.50 mL, 2.9 mmol) in DMF (11 mL) were used. To couple undecenoic acid to the fourth Glu residue, a solution of undecenoic acid (0.11 g, 0.58 mmol), HBTU (0.22 g, 0.58 mmol) and DIPEA (0.30 mL, 1.8 mmol) in DMF (6mL) was added to the loaded resin. The resin was then shaken at room temperature for 24 h before washing with DMF (5 x 5 mL), CH_2Cl_2 (5 x 5 mL) and DMF (5 x 5 mL). To cleave the modified peptide from the resin, a mixture of 2:2:6 v/v/v acetic acid/trifluoroethanol/CH_2Cl_2 (7 mL) was added to the resin and shaken at room temperature for 4 h. The cleaved products were separated from the resin by filtration and combined with 2:2:6 v/v/v acetic acid/trifluoroethanol/CH_2Cl_2 washings (3 x

2 mL). Hexane (100 mL) was added to the product solution and the solvent subsequently removed under reduced pressure. Residual acetic acid was removed from the product by forming an azeotrope with toluene (3 x 50 mL). This afforded the desired product as a yellow oil (0.24 g, 99 %); ^{1}H NMR (400 MHz, $CDCl_3$) δ (ppm): 7.80 (d, *J* = 6.4 Hz, 1H, NH), 7.64 (d, *J* = 8.1 Hz, 1H, NH), 7.38 (d, *J* = 7.5 Hz, 1H, NH), 7.03 (d, *J* = 6.4 Hz, 1H, NH), 5.78 (m, 1H), 4.92 (m, 2H), 4.48 (m, 2H), 4.31 (m, 2H), 2.32 (m, 8H), 2.19 (m, 4H), 2.00 (m, 8H), 1.41 (s, 36H), 1.25 (m, 12H); ^{13}C NMR (400 MHz, $CDCl_3$) δ (ppm): 174.7, 173.6, 173.2, 172.8, 172.7, 172.5, 172.3, 171.8, 171.4, 139.1, 114.1, 81.2, 81.0, 80.7, 80.5, 53.9, 53.4, 52.7, 52.2, 36.0, 33.8, 31.9, 31.7, 31.7, 31.6, 29.3, 29.3, 29.1, 28.9, 28.1, 26.8, 26.7, 25.4 (6 signals obscured or overlapping); HRMS (ESI) calcd for $C_{47}H_{80}N_4O_{14}$ $[M+Na]^+$ *m/z* 947.5570, found 947.5577.

5.1.4 Functionalisation and Deprotection of Titania Nanoparticles

Data for the synthesis and characterisation of the titania nanoparticle framework material is provided in *Chapter 4*. The method of functionalization is also described in *Chapter 4* and was used without modification for functionalization with the ligand 1-undecene to produce TiO_2-alkyl. For functionalization with the peptide, titania nanoparticles (0.40 g) were suspended in a dry, degassed solution of undecene-LDDL-Glu(*t*Bu)-OH **15** (37 mg, 0.04 mmol) and 1-undecene (56 mg, 0.36 mmol) in mesitylene (4.0 mL) and heated in an oil bath at 110 ^{o}C for 24 h. The functionalised nanoparticles were then washed with petroleum ether (3 mL), MeOH (3 mL) and CH_2Cl_2 (3 mL) before drying in air overnight.

To remove the *tert*-butyl (*t*Bu) groups from the peptide after functionalization, as shown in Scheme 1, a solution of 95:2.5:2.5 TFA:TIS:water was added to the functionalised nanoparticles (0.37 g) and stirred at room temperature for 4 h. The supernantant liquid was then removed from the deprotected, functionalised nanoparticles (TiO_2-peptide) and they were washed multiple times with water until the pH of the washing solution was >4. After air drying overnight, TiO_2-peptide was afforded as an off-white solid (0.32 g).

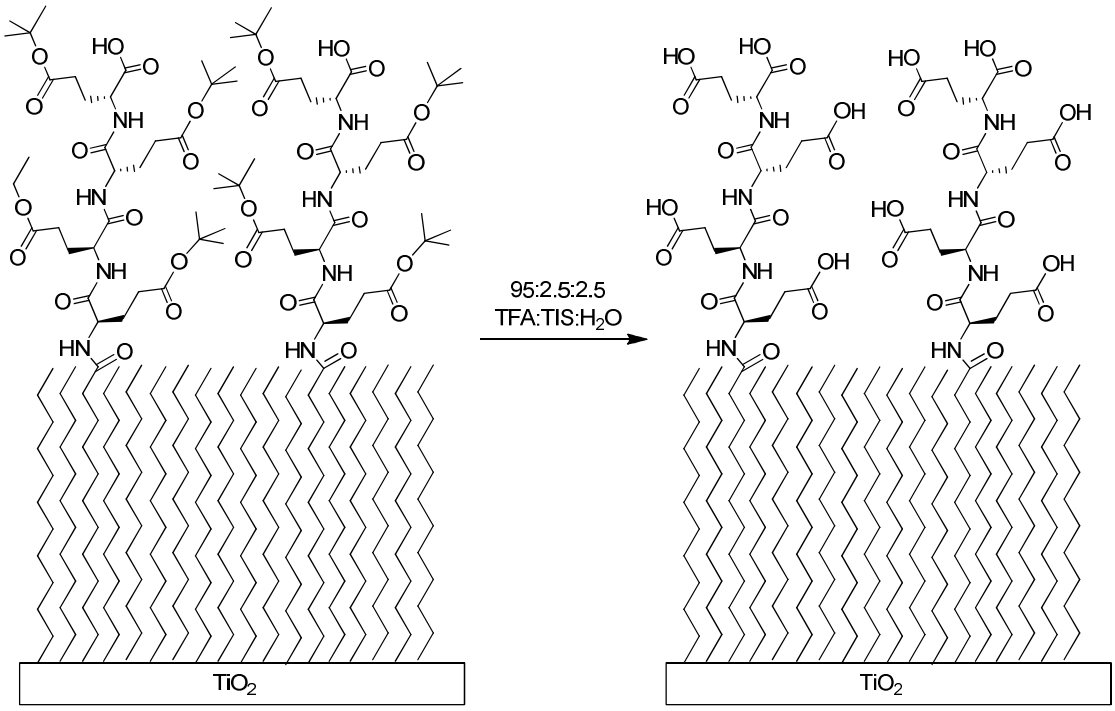

Scheme 5.1: Deprotection of undecene-LDDL-Glu(*t*Bu)-OH **15** on titania surface to give TiO_2-peptide

5.1.5 Sorption Methodology

A stock solution containing 100 ppm each of Al, Ca, Fe, Ni, Sr, Cs, La, Nd, Eu, Ho, Yb and U was prepared using metal nitrate salts of each element and MilliQ water then adjusted to pH 5 using ammonium hydroxide. Subsamples were then prepared by dilution to 1 ppm in 4-(2-hydroxyethyl)-1-piperazineethanesulfonic acid (HEPES) buffer (10 mM) and the pH of the subsamples was adjusted to 4.2 or 5.0 by the addition of nitric acid. The multi-element pH 4-5 10 mM HEPES buffer solutions were used for competitive sorption experiments with non-functionalised titania nanoparticles (TiO_2-NF) and 1-undecene functionalised titania nanoparticles (TiO_2-alkyl). The pH was measured after sorption experiments with these materials and was observed not to change significantly (± 0.2 pH units). For competitive sorption experiments with TiO_2-peptide, the organo-functionalised titania nanoparticles were pre-equilibrated with 10 mM HEPES buffer to pH 4.2 or 4.9 before a spike of the multi-element stock solution was added. The pH was also measured after sorption experiments with TiO_2-peptide and was observed not to change significantly (± 0.2 pH units).

All batch sorption experiments were performed using 0.01 g titania nanoparticles and 2.0 mL solution, giving a solid-to-liquid ratio of 200. Each experiment was performed in duplicate. Samples were shaken on a vertical mixer at a constant speed of approx. 50 rpm for a period of 24 h. Errors in the reported percentage extraction values were calculated from the largest standard deviation of the analytical results or assuming 5 % error if the standard deviation was lower than this.

5.2 Lanthanide Binding in Solution at Neutral pH

The Ln ions Eu and Tb are commonly used in biotechnological luminescence applications due to their ideal luminescence properties such as high quantum yields and long luminescence lifetimes.[14,15] For this work, the luminescent Ln Eu was chosen for luminescence titrations to monitor the formation of peptide:Ln complexes. Europium was chosen because information about the symmetry of the first coordination sphere around the Eu ion can be obtained from its luminescence spectra due to the fact that one of its two strong luminescence peaks is hypersenstitive.[15] In addition, energy transfer to Eu is more efficient at longer chromophore-Ln distances than for Tb.[15]

6.2.1 Luminescence Titrations with LLLL-Glu-OH

Titration of a non-buffered, 200 µM aqueous solution of tetra-L-Glu at pH 6 with up to 10 equiv. of 10 mM Eu nitrate was first investigated. The data in Figure 5.4 shows that the characteristic narrow emission bands of Eu phosphorescence were evident, but the complexes formed were poorly luminescent and resulted in noisy data. Direct excitation of Ln is very inefficient due to the forbidden f-f transitions of Ln,[16] hence the poor luminescence observed. Nevertheless it is clear that the luminescence increased at a decreasing rate as the Eu was added (Figure 5.4). Increasing luminescence was observed as the Eu was added to the peptide solution due to the increasing presence of luminescent peptide:Eu complexes. However, beyond addition of 1 equiv. of Eu the increases in luminescence observed were relatively small. For example, the intensity of the peak at 592 nm increased from 0 to 11 upon addition of the first equivalent of Eu but then increased only another 2 units upon addition of the second equivalent of Eu. This indicates that a larger proportion of the first added equivalent of Eu was complexed by the peptide than the subsequent Eu additions or that weaker peptide:Eu complexes were formed with the later Eu additions. Added Eu ions complexed by water molecules do not contribute to the luminescence signal because the water molecules provide a lower energy vibrational pathway for excited state relaxation.[17]

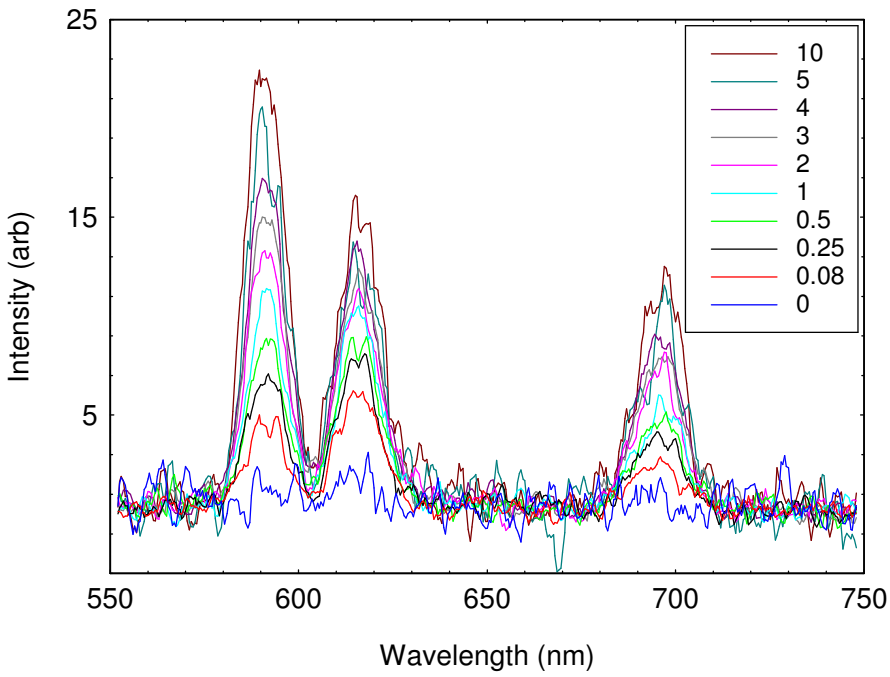

Figure 5.4: Luminescence titration using 200 µM LLLL-Glu-OH in aqueous solution at pH 6. The legend indicates the equiv. of Eu that have been added.

6.2.2 Luminescence Titrations using Peptides with a Naph Chromophore

Since the luminescence intensity was low for the unmodified peptide:Eu complexes (Figure 5.4), the strongly absorbing naph chromophore (**7**) was incorporated into the LnBPs to allow transfer of the absorbed energy of the chromophore to the Ln excited state and hence sensitise emission.[14] This is known as the "antenna effect". The naph chromophore was utilised as it is an effective sensitising antenna for both Eu and Tb and has been previously shown not to affect the affinity of peptides for Ln.[13]

Phosphoresence emission spectra were recorded upon addition of 0 to 10 equiv. of 3 mM Eu nitrate to a 30 µM solution of the naph modified peptides in pH 6.9 10 mM HEPES buffer. An excitation wavelength of 345 nm was used as it has been previously shown that the naph antenna absorbs light at this wavelength via a n-π* transition and is able to effectively transfer this absorbed energy to populate the excited state of Eu(III) ($^5D_0$ = 17200 cm^{-1}).[13] Upon excitation of the naph antenna at 345 nm in the presence of Eu, the characteristic narrow emission bands of Eu phosphorescence became evident. A typical example is shown in Figure 5.5 and clearly shows the increased strength of the luminescence signal relative to the data in Figure 5.4, despite the peptide concentration being more than six times lower for the titration shown in Figure 5.5. Thus, luminescence was substantially enhanced when Eu was complexed by peptides with the naph chromophore.

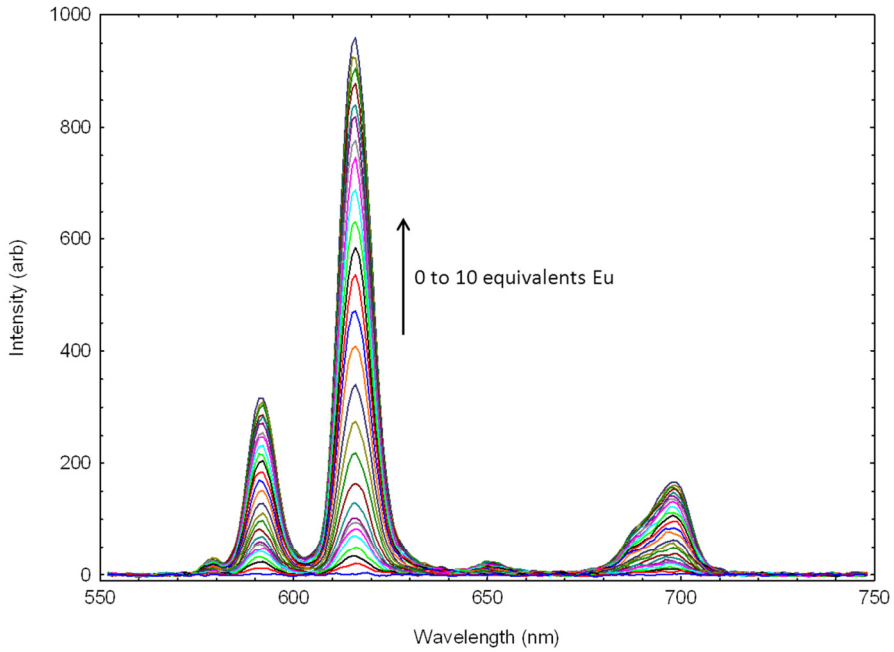

Figure 5.5: Luminescence titration of naph-DLDL-Glu-OH in pH 6.9 10mM HEPES with Eu.

The binding of Eu to the naph modified peptides was monitored using the Eu $\Delta J = 1$ transition at 592 nm since this transition has a purely magnetic dipole character. Thus, this transition is insensitive to the chemistry and symmetry of the environment of the Eu ion[16] and fluctuates based solely on the amount of Eu that is being complexed. On the other hand, the $\Delta J = 2$ transition at 615 nm is hypersensitive to electric dipole transitions, making it sensitive to the symmetry of the complex formed as well as the amount of Eu present.[16]

The integrated intensity of the $\Delta J = 1$ emission at 592 nm as Eu nitrate was added to a solution of each naph modified peptide is shown in Figure 5.6. All the titration profiles contained an inflection point, ie a second increase in luminescence occurred after a plateau had begun to develop. This indicated that in pH 6.9 10mM HEPES buffer multiple peptide:Eu complexes were formed. Similar shaped luminescence titration profiles were previously observed for Tb binding by a phosphorylated peptide fragment, for which the second increase in luminescence indicated the binding of a second Tb ion to the peptide.[18] Therefore it was assumed that polymetallic complexes also formed between the present naph modified peptides and Eu in the presence of excess Eu ions.

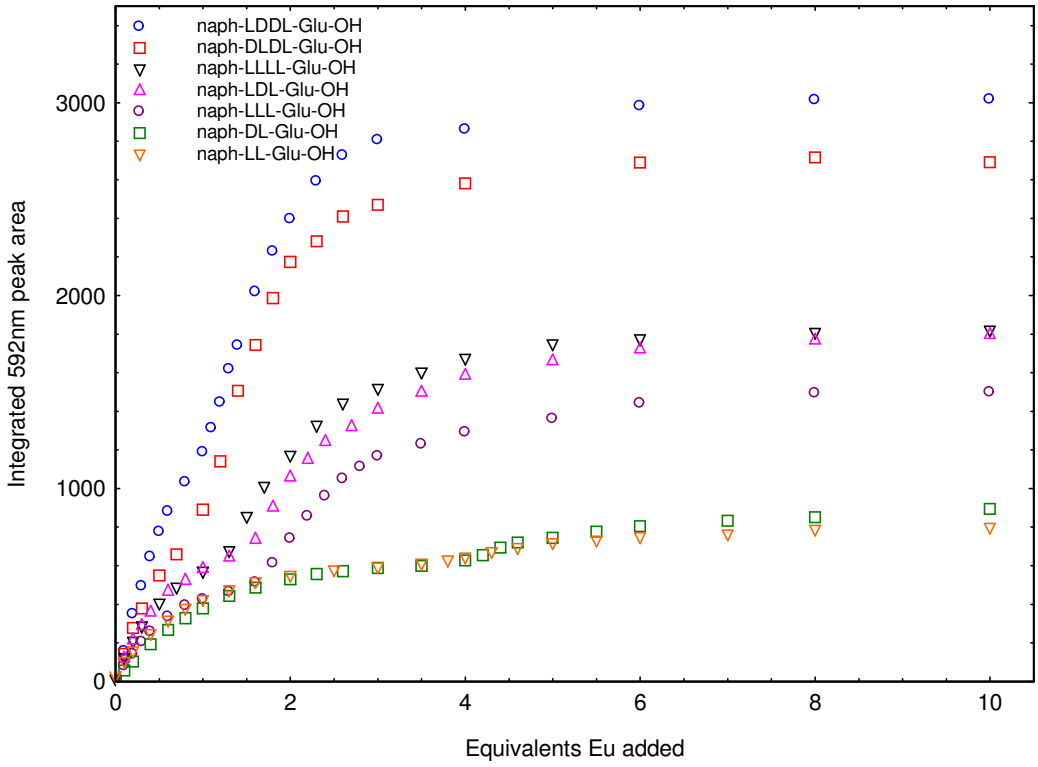

Figure 5.6: Titration profiles of all naph modified peptides in pH 6.9 10 mM HEPES buffer

Naph-LDDL- and naph-DLDL-Glu-OH showed the strongest luminescence and had an inflection point in their titration curves after addition of approx. 0.7 equiv. Eu (Figure 5.6). Naph-LLLL-, naph-LDL- and naph-LLL-Glu-OH all had similar luminescence intensities, which were lower than naph-LDDL- and naph-DLDL-Glu-OH, and the inflection points in their titration curves occurred after addition of approx. 1 to 1.5 equiv. Eu. The titration curves for naph-DL- and naph-LL-Glu-OH were also similar to each other, were lower again in intensity and their inflection points occurred after addition of approx. 4 equiv. Eu.

The luminescence titrations of all the naph modified peptides at pH 6.9 were modelled using the program HypSpec,[19] which can be used to determine binding constants and speciation. Unfortunately, fitting each luminescence titration dataset with two peptide:Eu complexes resulted in multiple models providing similar “goodness of fit” statistics. This suggests there were more than two species present in these solutions and a larger number of species could not be modelled as the number of unknown parameters was too high to obtain a unique solution. Although the exact stoichiometry and binding constants of the peptide:Eu complexes could not be determined from the HypSpec modelling, some trends were noted, as outlined in the discussion below.

Decreasing the length of the peptide chain decreased the luminescence intensity of the peptide:Eu complexes formed (Figure 5.6). The higher luminescence of the larger peptides indicates that they provided a higher denticity of coordination and hence displaced more of the water molecules that quench Eu luminescence.[15] From this, it was assumed that higher luminescence intensity indicated a higher binding affinity.[18] This was consistent with the

HypSpec modelling results which indicated that (1) binding constants for the tetra-peptides decreased in the order LDDL > DLDL > LLLL, (2) naph-LDL-Glu-OH had a similar binding strength to naph-LLLL-Glu-OH and (3) the di-peptides had similar binding strengths to each other, which was less than the tri- and tetra-peptides. The stronger luminescence of the tetra-peptides was expected given that these larger peptides had more carboxylic acid binding sites available to coordinate the Eu ions. Increasing the number of acidic residues in LnBP has previously been shown to yield increased binding constants.[20]

Decreasing the length of the peptide chain also delayed the onset of a second increase in luminescence (Figure 5.6). The second increase in luminescence observed for all of the peptides was assumed to be due to the formation of polymetallic complexes as the concentration of Eu in solution increased.[18] As such, the higher number of carboxylic acid binding sites in the larger peptides also appeared to facilitate formation of polymetallic complexes. A similar effect has been observed previously for coordination of Cr(III) with acidic peptides, although in that case bimetallic complexes did not form until more than 4 acidic residues were present.[21] Given that the pK_a of terminal carboxylic acids is on average 3.3 ± 0.8 and of glutamic acid side chains is 4.2 ± 0.9,[22,23] all of the carboxylic acids in the poly-Glu peptides are expected to be deprotonated at pH 6.9. Thus, the tetra-, tri and di-peptides had overall charges of -5, -4 and -3, respectively, since the amine terminus was replaced with a non-ionisable naph moiety. Upon binding of an Eu^{3+} cation, which is the dominant Eu species at this pH,[24] the tetra- and tri-peptide complexes would still be negative. This explains why further Eu cations were attracted to bind and form polymetallic complexes. On the other hand, a 1:1 di-peptide:Eu complex would be neutral. Therefore, the di-peptides did not form polymetallic complexes until there was a large excess (4 equiv.) of Eu present.

Both the tetra- and tri-peptide solutions increased in luminescence approx. 2.5 times in the second step of the titration while the luminescence increase upon the second step was lower (approx. 1.5 times) for the di-peptides (Figure 5.6). This may be because if multiple Eu ions were bound to a di-peptide they would be physically close enough together to cause some Ln self-quenching.[13,18] However, given that the speciation in these solutions was too complex to be modelled, further experiments would be required to confirm this hypothesis.

Although some literature examples of transition metal binding with peptides containing D-amino acid residues exist,[25-28] none could be found for Ln binding. Nevertheless, changing the stereochemistry of a single amino acid has previously been shown to have a significant effect on the binding affinities of copper,[25,27] nickel[26] and calcium[28] ions. Introducing D-amino acids such that coordinating side chains are on “opposite sides” of the molecule has previously been shown to decrease metal binding affinities in both cyclic[27] and linear[26] tetra-peptides. This was attributed to the distance and steric hindrance between coordinating groups on “opposite sides” of the molecule preventing both of the side chains from coordinating the metal ion together. It follows that alternating L- and D-amino acids, providing coordinating side chains on the “same side” of the molecule, were expected to increase metal binding. In support of this, peptides with alternating L- and D-amino acids are known to form

cation transport channels.[29,30] The data in Figure 5.6 show that for the tetra- and tri-peptides in this work, alternating L- and D-Glu residues produced complexes with higher luminescence than all L-Glu residues. Thus, peptides with alternating L- and D-Glu residues provided stronger Eu binding, as expected. This effect was more pronounced for the tetra-peptides than for the tri-peptides and was not observed at all for the di-peptides.

Overall, both the length and stereochemistry of the peptides have been shown to affect the structure of the Eu complexes formed. The tetra-peptides with alternating L- and D-Glu residues provided the most luminescent complexes and hence the strongest Eu binding. However, binding constants and speciation could not be determined due to the complex multiple equilibria present in the pH 6.9 solutions. Attempts to identify the stoichiometry of the complexes present in solution by mass spectrometry were also unsuccessful, most likely due to dissociation of the complexes upon ionisation.

To investigate the physical properties of the tetra-peptide:Eu complexes, small angle x-ray scattering (SAXS) measurements were performed on 1:1 tetra-peptide:Eu solutions at the SAXS/WAXS beamline at the Australian Synchrotron. Initially, 300 µM aqueous solutions of the tetra-peptides were used but they aggregated under the influence of the x-ray beam (Figure 5.7). Aggregation due to x-ray damage is a well-known phenomenon during SAXS of macromolecules such as proteins and peptides but can be mitigated by diluting, cooling or adding protectants to the solution.[31] Thus, measurement of 30 µM aqueous 1:1 tetra-peptide:Eu solutions was performed and high-flux synchrotron x-rays were required to characterise the complexes at this decreased concentration.

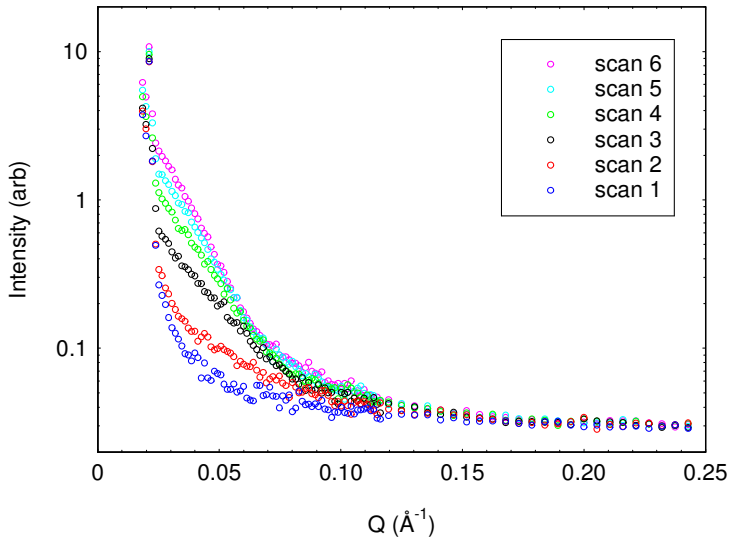

Figure 5.7: SAXS data of 300 µM naph-DLDL-Glu-OH with 1 equivalent Eu nitrate added, showing changes due to radiation effects.

The SAXS data of 30 µM 1:1 tetra-peptide:Eu aqueous solutions after background subtraction of water and the capillary are shown in Figure 5.8. No radiation effects were observed at this concentration. The SAXS data for all three tetra-peptides was very similar. In

the region from Q = 0.10 to 0.32 Å^{-1}, these curves decreased with a Q$^{-0.1}$ dependence. The fact that the SAXS data were essentially flat suggests that the solutions did not contain scattering structures of a size that was detectable in this Q range.

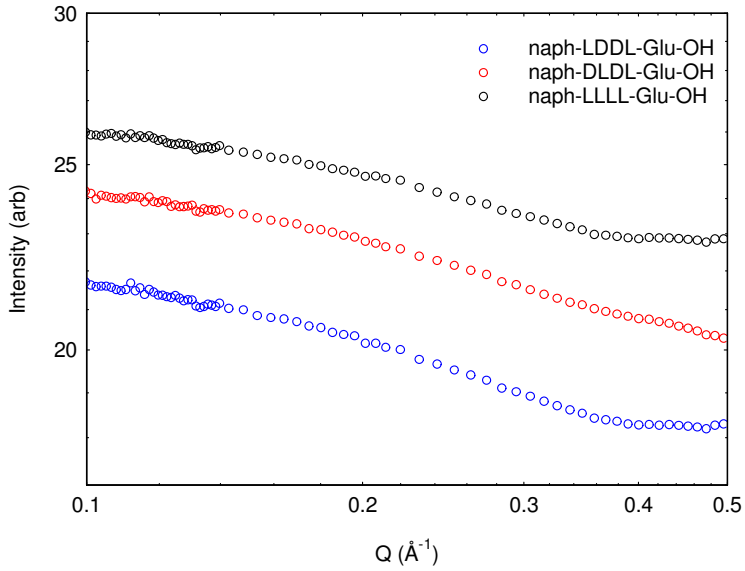

Figure 5.8: SAXS data of 30 µM 1:1 tetra-peptide:Eu complexes in aqueous solution. Traces have been offset for clarity.

To determine the kinetics of complex formation, 30 µM aqueous solutions of each tetra-peptide had 1 equivalent of aqueous Eu nitrate solution added in-situ on the SAXS/WAXS beamline using the automated multi-well plate system. Using this system, the Eu nitrate solution in one well of a 96-well plate was added to the tetra-peptide solutions in other wells then mixed by loading and unloading a 1.5 mm quartz capillary in a custom aluminium holder. The mixed sample was then loaded into the capillary for measurement. Overall the addition of Eu nitrate to the peptide solution, mixing and measurement required approx. 10 s. Since no changes in the SAXS data were seen in later measurements, this suggests that formation of the complex occurred within 10 s or less.

5.3 Lanthanide Binding in Solution at Acidic pH

Many industrial Ln separation applications including mining, industrial waste water cleanup and nuclear reprocessing, occur under acidic conditions.[32-34] Therefore, it was of interest to investigate the performance of the di-, tri- and tetra-glutamic acid LnBP under acidic conditions. Performing luminescence titrations at acidic pH produced titration profiles that were lower in intensity than those performed at neutral pH and were a single step, without an inflection point. These single step titration profiles enabled HypSpec modelling and hence calculation of binding constants $\log\beta_{xy} = [Ln_xP_y]/([Ln]^x[P]^y)$ where 'P' represents the peptide. In acidic solutions, some of the carboxylic acid side chains of the di-, tri- and tetra-

glutamic acid LnBP were protonated and thus unavailable to bind the Eu ion. In addition, since the pH was lowered using nitric acid, the concentration of nitrate anions was higher in the acidic solutions and these nitrate anions compete with the LnBP to form inner-sphere complexes with the Eu ions.[35] These two phenomena combined explain why weaker binding and hence lower luminescence intensity were observed in the binding experiments at acidic pH relative to neutral pH (*section 5.2*). They also explain why polymetallic peptide:Eu complexes did not form under acidic conditions and hence why single step luminescence titration profiles were observed.

The pH at which Ln binding experiments were performed was individually chosen for each peptide as the pH that gave a luminescence titration with a single step but still showed luminescence intensity greater than 25 at the initial step of the titrations (0.1 equiv. Eu). According to these conditions, Eu binding experiments were performed with naph-DLDL- and naph-LDDL-Glu-OH at pH 4.1, with naph-LLLL-Glu-OH at pH 4.7, with naph-LDL- and naph-LLL-Glu-OH at pH 4.9 and with naph-DL- and naph-LL-Glu-OH at pH 5.9. The shorter peptides required less acidic pH conditions to achieve single step titration profiles because they had fewer available binding sites and were hence less inclined to form polymetallic complexes, as discussed above.

5.3.1 Tetra-Peptides (pH 4.1-4.7)

Titration profiles showing the luminescence intensity evolution of the 592 and 615 nm emissions for naph-DLDL- and naph-LDDL-Glu-OH at pH 4.1 as well as speciation diagrams from HypSpec modelling are shown in Figure 5.9. The titration profiles of these two peptides were similar; luminescence increased at a decreasing rate as up to 10 equiv. Eu was added and the 615 nm emission had lower intensity than the 592 nm emission. This ratio of the emissions indicated that the symmetry surrounding the Eu ion approached a centre of inversion.[16,36]

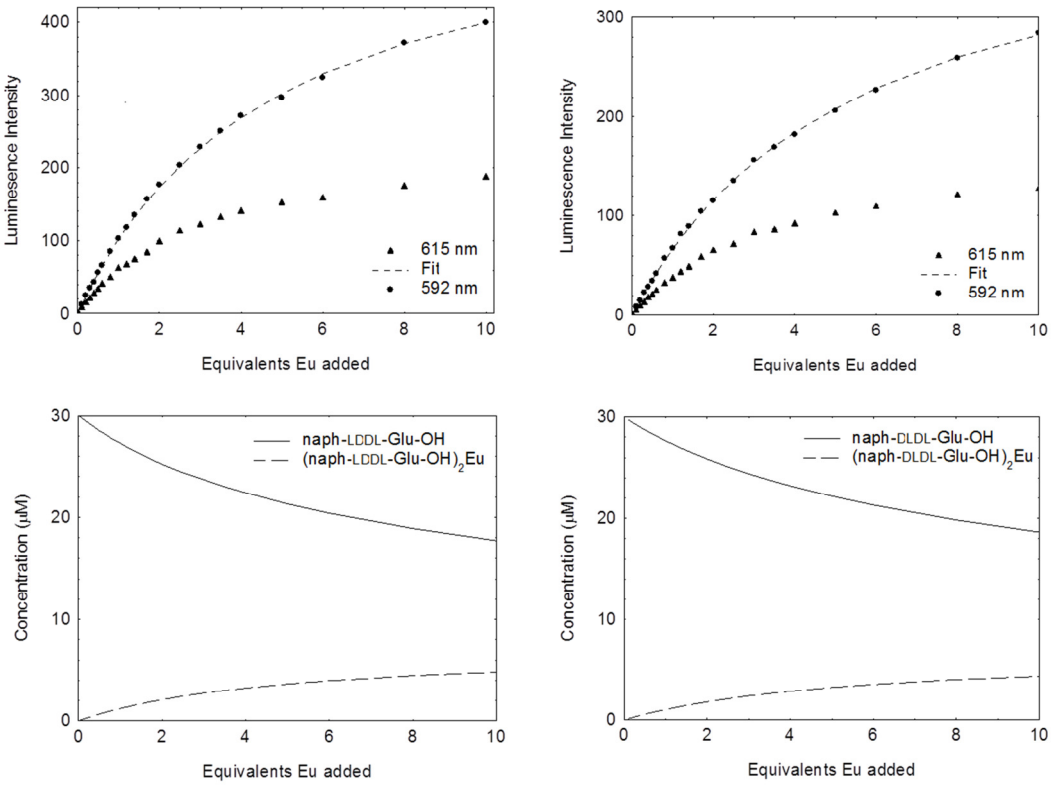

Figure 5.9: Titration profiles and speciation diagrams for naph-LDDL-Glu-OH (left) and naph-DLDL-Glu-OH (right) at pH 4.1

HypSpec fitting indicated that a 2:1 peptide:Eu complex was present for both naph-LDDL- and naph-DLDL-Glu-OH and that approx. 40 % of each peptide was complexed in the presence of 10 equiv. Eu. At pH 4.1, half of the carboxylic acid side chains (pK_a ~4.2) and the terminal carboxylic acid (pK_a ~3.3) of the tetra-peptides are expected to be deprotonated on average.[22] This would result in an overall charge of -3. Given that the predominant Eu species at this pH is Eu^{3+}, formation of the 1:1 peptide:Eu complex was expected based on charge matching. Instead, the 2:1 complex was observed. This suggested that the tetra-peptides could not effectively coordinate Eu with all three of their deprotonated carboxylic acid binding sites, because if two peptides coordinated Eu with three deprotonated carboxylic acid sites each, there would be six negative charges surrounding the Eu^{3+} ion, which would be energetically disfavoured.

The fact that only approx. 40 % of naph-LDDL- and naph-DLDL-Glu-OH were complexed with Eu even in the presence of 10 equiv. Eu suggests that the peptide:Eu binding was very weak. This was consistent with the modelled binding constants in Table 5.1, which also showed that the binding affinities for naph-LDDL- and naph-DLDL-Glu-OH were very similar. The weak binding can be attributed to the fact that the concentration of nitrate ions at pH 4.1 (approx. 100 μM) was more than three times greater than the peptide concentration. Hence, the nitrate ions provided strong competition to coordinate the Eu ions. Indeed, the fact that formation of an inner-sphere complex occurred at all at pH 4.1 is remarkable. No other reports on the binding constants of LnBP below pH 6 could be found for comparison.

Table 5.1: Binding constants for the tetra-peptides in 10 mM HEPES buffer.

Peptide	pH	Species (peptide:Eu)	$\log\beta_{21}$	Species (peptide:Eu)	$\log\beta_{11}$	σ
LDDL	4.1	2:1	7.8			0.08
DLDL	4.1	2:1	7.7			0.10
LLLL	4.7	2:1	8.7	1:1	3.6	0.09

The titration profile showing the luminescence intensity evolution of the 592 and 615 nm emissions for naph-LLLL-Glu-OH at pH 4.7 is shown in Figure 5.10. Like the other tetra-peptides, naph-LLLL-Glu-OH showed increasing luminescence at a decreasing rate up to 10 equiv. Eu. However, the relative intensity of the 592 and 615 nm emissions was reversed, suggesting that the Eu in the complex formed was not a centre of inversion. HypSpec fitting indicated the presence of both 2:1 and 1:1 peptide:Eu complexes and that more of the 1:1 complex was formed as more Eu was added, until both complexes were present at similar concentrations after addition of 10 equiv. of Eu. The speciation data also shows that approx. 76 % of naph-LLLL-Glu-OH was complexed in the presence of 10 equiv. of Eu.

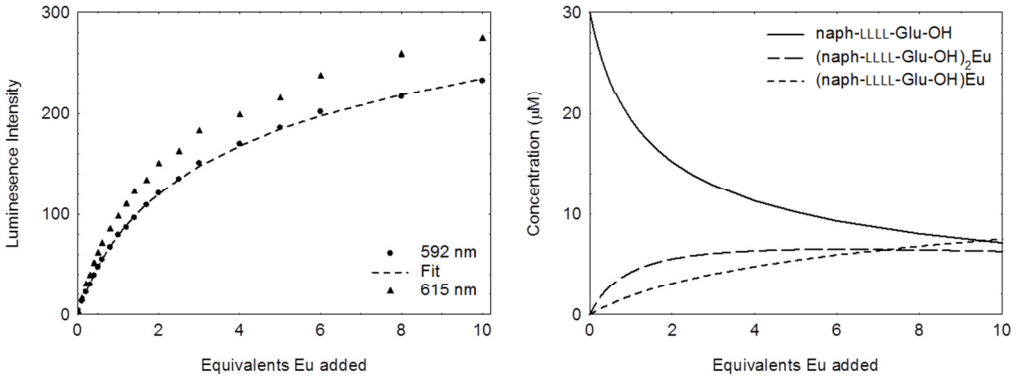

Figure 5.10: Titration profile and speciation diagram for naph-LLLL-Glu-OH at pH 4.7

The presence of the 1:1 complex and the higher degree of complexation of naph-LLLL-Glu-OH relative to the other tetra-peptides suggest that the affinity between naph-LLLL-Glu-OH and Eu at pH 4.7 was higher than between the other tetra-peptides and Eu at pH 4.1. This was consistent with the modelled binding constants in Table 5.1, which showed that the binding constant for the 2:1 naph-LLLL-Glu-OH:Eu complex at pH 4.7 was approx. one log unit higher than that of naph-LDDL- and naph-DLDL-Glu-OH at pH 4.1. This was attributed to the less acidic pH of the luminescence titration with naph-LLLL-Glu-OH and the resulting higher negative charge on this tetra-peptide. At pH 4.7, three quarters of the carboxylic acid side chains (pK_a ~4.2) and the terminal carboxylic acid (pK_a ~3.3) of naph-LLLL-Glu-OH are expected to be deprotonated on average,[22] giving an overall charge of -4. This does not however indicate that under conditions of the same pH, naph-LLLL-Glu-OH would bind Eu

more strongly than naph-LDDL- and naph-DLDL-Glu-OH. In fact, the data collected at neutral pH (Figure 5.6) suggests the opposite.

The circular dichrosim (CD) spectra of all three tetra-peptides at pH 4-4.5 in 10 mM HEPES buffer are shown in Figure 5.11. All three CD spectra were different, indicating that the differing stereochemistry of these tetra-peptides had a measurable effect on their secondary structure. Unfortunately the secondary structures of the tetra-peptides could not be assigned as α-helix or β-sheet, but this is not surprising given the shortness of the peptide chains. It has been shown in previous work that the CD spectrum of LLLL-Glu consists of a single negative band at 200 nm, assigned as random coil.[37] However, the CD spectra in Figure 5.11 did not correspond to this random coil structure, suggesting that the presence of the naph group altered the secondary structure of the LnBP. None of the tetra-peptides showed changes in their CD spectra upon addition of up to 1 equiv. Eu. This may be because the amount of peptide:Eu complex formed (< 20 %, Figures 5.9 and 5.10) was not sufficient to affect the CD spectra, or because binding Eu did not substantially change the peptide secondary structure. The first hypothesis is considered more likely given that many examples of changing CD spectra upon strong binding of Ln to peptides exist in the literature[10,13,38] and changes in the CD spectra of the tri- and di-peptides were observed upon addition of Eu (see below).

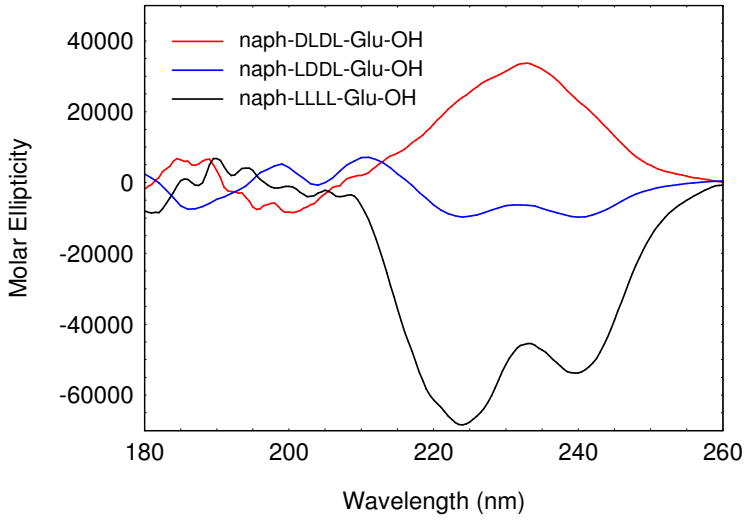

Figure 5.11: CD spectra of tetra-peptides in 10 mM HEPES buffer (naph-DLDL- and naph-LDDL-Glu-OH at pH 4, naph-LLLL-Glu-OH at pH 4.5). Below 210 nm the signal:noise ratio was too low for the data to be interpreted.

Luminescence decay rates of the tetra-peptides naph-LDDL- and naph-DLDL-Glu-OH with between 0.5 and 4 equiv. of Eu added were measured at pH 4 in 10 mM HEPES H_2O/D_2O solutions to determine the number of coordinated water molecules. This technique is based on the fact that the luminescence lifetimes of Eu ions in aqueous solution depend on the ligand environment of the Eu, in particular the number of water molecules occupying the inner coordination sphere.[15] In this work the hydration number q was calculated using equation (1)

given by Parker et al., which accounts for the contribution of closely diffusing OH and NH amide oscillators.[17]

$$q = A\left(k_{H_2O} - k_{D_2O}\right) \quad (1)$$

In equation (1), A is the proportionality constant (1.2 ms for Eu) and k is the rate constant for de-excitation. The value of Δk was corrected by a factor of -0.25 ms^{-1} to account for the effect of outer sphere water molecules on Eu and by -0.075*4 = -0.3 ms^{-1} to account for the effect of the four carbonyl-bound amide NH oscillators in the tetra-peptides.[17] The solid peptides synthesised in this work were hydrated, so the luminescence decay rate of the complex in 100% D_2O could not be directly measured and were instead extrapolated from the decay rates in solutions with increasing fractions of D_2O.

Little difference was observed in the measured lifetimes upon addition of 0.5 equiv. of Eu up to 4 equiv. For both tetra-peptides, the measured lifetimes were similar and corresponded to q_{Eu} = 9.2. Thus, there was an average of 9 water molecules coordinated to each Eu ion in solution, independent of the amount of Eu added. Given that Eu typically has a coordination number of 8-9 in solution,[15] this result suggested that most of the Eu in solution was completely hydrated. This was consistent with the speciation data in Figure 5.9, which showed that upon addition of 4 equiv. Eu to naph-LDDL- or naph-DLDL-Glu-OH, the predominant Eu species (~75 %) was 'free' and thus surrounded by water molecules.

5.3.2 Tri-Peptides (pH 4.9)

Titration profiles showing the luminescence intensity evolution of the 592 and 615 nm emissions for naph-LDL- and naph-LLL-Glu-OH at pH 4.9 are shown in Figure 5.12. The titration profiles of both tri-peptides were similar in shape and the evolution of luminescence upon addition of Eu was different for the 592 nm and 615 nm emissions. For the 592 nm emission, luminescence increased at a decreasing rate until approx. 6 equiv. Eu were added then reached a plateau. This is similar to what was observed for the tetra-peptides (Figures 5.9 and 5.10) except that the plateau was reached earlier in the titration for the tri-peptides. This could be due to the higher pH of this titration or the shorter length of the tri-peptides. Further experiments would be required to accurately determine the cause. For the 615 nm emission there was a peak in the luminescence after addition of approx. 1.5 equiv. Eu, after which luminescence began to decrease. As a result, after addition of approx. 2 equiv. Eu the luminescence intensities of the 592 and 615 nm emissions were reversed. This suggests that there was a change in the predominant peptide:Eu species present, from a species in which the first coordination sphere of the Eu ion was not highly symmetrical to a species in which the symmetry surrounding the Eu ion was approaching a centre of inversion.[16,36] Hypspec fitting suggested that these 2 species were the 2:1 and 1:1 peptide:Eu complexes, respectively.

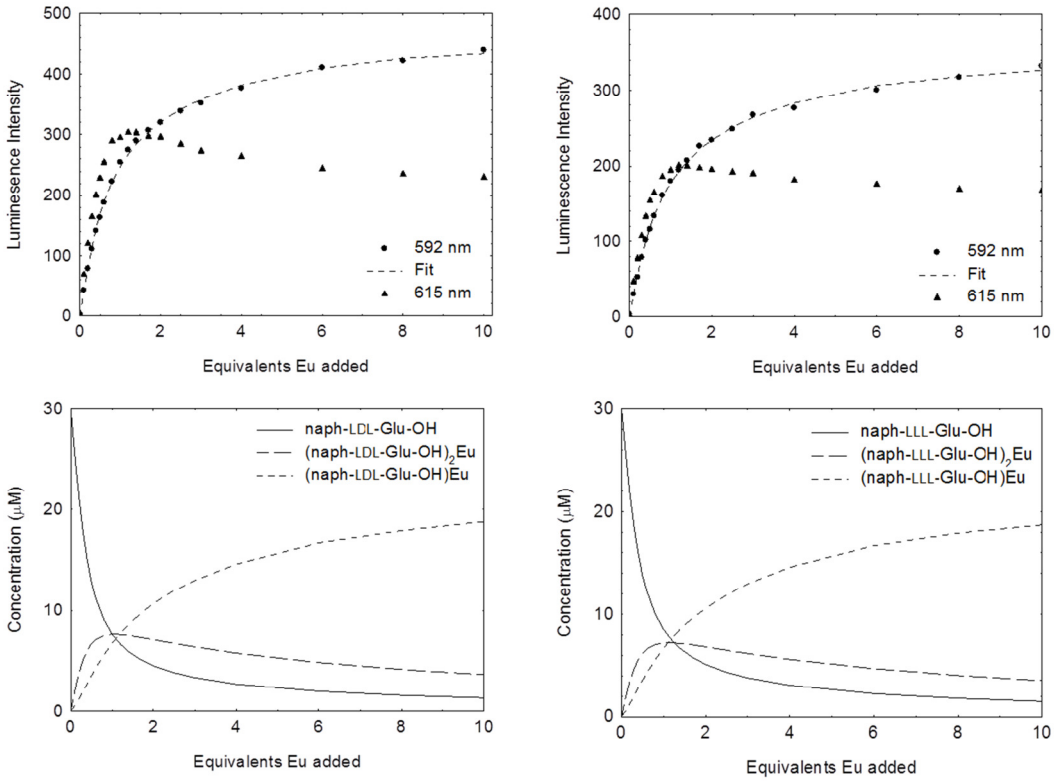

Figure 5.12: Titration profiles and speciation diagrams for naph-LDL-Glu-OH (left) and naph-LLL-Glu-OH (right) at pH 4.9

Speciation data calculated from the HypSpec model are also shown in Figure 5.12. More of the 1:1 complex formed as more Eu was added, until its concentration was more than five times that of the 2:1 complex in the presence of 10 equiv. Eu. Thus, the 1:1/2:1 complex ratio was higher in the tri-peptide titrations than in the naph-LLLL-Glu-OH titration (Figure 5.10), indicating that the stability of the 1:1 complex relative to the 2:1 complex was greater for the tri-peptides than for naph-LLLL-Glu-OH. Figure 5.12 also shows that approx. 95 % of each tri-peptide was complexed in the presence of 10 equiv. of Eu. This higher degree of complexation for the tri-peptides relative to the tetra-peptides suggests that the affinity between the tri-peptides and Eu at pH 4.9 was higher than between the tetra-peptides and Eu at pH 4.1-4.7. However, under conditions of the same pH, the tri-peptides bind Eu less strongly than the tetra-peptides, according to the data in Figure 5.6.

The data in Table 5.2 show that the modelled binding constants for the tri-peptides at pH 4.9 were both similar, so for the tri-peptides stereochemistry had little impact on binding affinity. This was also consistent with the data from luminescence titrations at neutral pH (Figure 5.6). The binding constants for the tri-peptides at pH 4.9 in Table 5.2 were also more than an order of magnitude greater than the binding constants of naph-LLLL-Glu-OH measured at a similar pH of 4.7 (Table 5.1). On the other hand, the luminescence titration data at neutral pH (Figure 5.6) indicated that the tri-peptides and naph-LLLL-Glu-OH had similar affinities for Eu when measured at the same pH. Thus, it appears that even a small

decrease in pH of 0.2 was able to cause a substantial decrease in binding affinity. Nevertheless, it is clear that simply increasing the number of Glu residues does not necessarily improve metal binding affinity. Indeed, previous work has shown that the position of charged metal binding residues is also highly influential.[10,39]

Table 5.2: Binding constants for the tri-peptides in pH 4.9 10 mM HEPES buffer.

Peptide	Species (peptide:Eu)	$\log\beta_{21}$	Species (peptide:Eu)	$\log\beta_{11}$	σ
LDL	2:1	9.9	1:1	4.8	0.10
LLL	2:1	9.8	1:1	4.7	0.09

At pH 4.9, approx. 80 % of the carboxylic acid side chains (pK_a ~4.2) and the terminal carboxylic acid (pK_a ~3.3) of the tri-peptides are expected to be deprotonated on average,[22] giving an overall charge of -3.5. Thus, the overall charge of naph-LLLL-Glu-OH at pH 4.7 (-4) was comparable to the tri-peptides at pH 4.9. This means that the higher binding constants for the tri-peptides at pH 4.9 relative to naph-LLLL-Glu-OH at pH 4.7 cannot be attributed to charge effects. Again, this indicates that simply increasing the number of binding sites in a coordinating ligand does not necessarily increase binding strength.

The CD spectra of 60 mM tri-peptide solutions in pH 4.9 10 mM HEPES buffer upon addition of 0-4 equiv. Eu are shown in Figure 5.13. Although the CD titrations were performed on 60 µM peptide solutions, CD titrations using 30 µM peptide solutions showed the same shape and molar ellipticity. Thus, the results are comparable to the luminescence titrations. The reported CD titration data was collected using 60 µM peptide solutions to improve the signal:noise ratio. Further equiv. of Eu were not added because the CD spectra underwent no further changes beyond addition of 3 equiv. Eu.

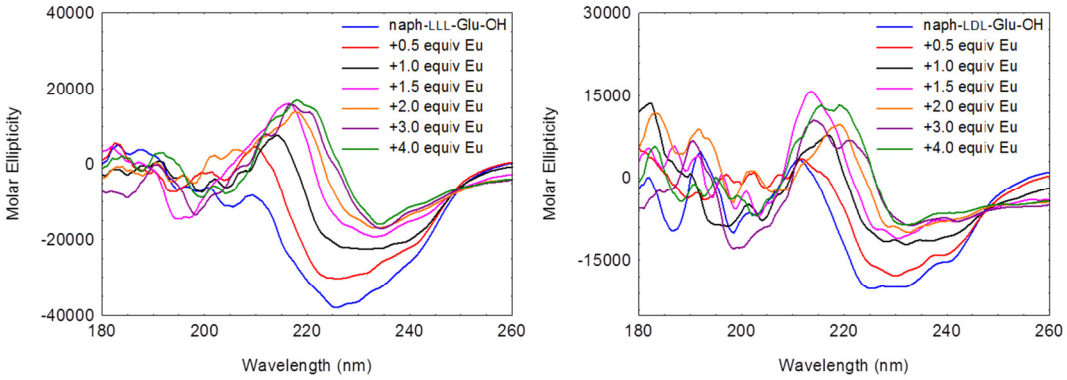

Figure 5.13: CD spectra of naph-LLL-Glu-OH (left) and naph-LDL-Glu-OH (right) in pH 4.9 10 mM HEPES buffer upon addition of Eu nitrate. Below 210 nm the signal:noise ratio was too low for the data to be interpreted.

Both tri-peptides exhibited similar shaped CD spectra in the absence of Eu, but the molar ellipticity of naph-LDL-Glu-OH was lower (Figure 5.13). The shape of the naph-LLL-Glu-OH CD

spectrum was different to that of naph-LLLL-Glu-OH (Figure 5.11), indicating that removing one L-Glu unit changed the secondary structure. The changes seen in the CD spectra during addition of Eu to the tri-peptides were similar (Figure 5.13), indicating that similar changes in their secondary structures occurred upon Eu binding. This was consistent with the fact that both tri-peptides had similar Eu binding constants (Table 5.2). The final CD spectra in Figure 5.13 were indicative of an extended structure.[37] Given that the 1:1 peptide:Eu complexes of the tri-peptides predominated in the presence of 3-4 equiv. Eu (Figure 5.12), it was assumed that these final CD spectra were representative of this 1:1 species.

5.3.3 Di-Peptides (pH 5.9)

Titration profiles showing the luminescence intensity evolution of the 592 and 615 nm emissions for naph-DL- and naph-LL-Glu-OH at pH 5.9 are shown in Figure 5.14. As for the tri-peptides, the titration profiles of both di-peptides were similar in shape and the 592 and 615 nm emissions evolved differently upon Eu addition. For the 592 nm emission, luminescence increased at a decreasing rate upon addition of up to 4 equiv. Eu then reached a plateau. Again, the point at which the data reached a plateau was earlier in the titration for these shorter peptides at higher pH relative to the tri- and tetra-peptides, but the cause of this change cannot be determined from this data. For the 615 nm emission, luminescence reached a maximum after addition of approx. 1.5 equiv. Eu and then began to decrease, as was observed with the tri-peptides. Thus, the intensity of both emissions was similar until more than 1 equiv. of Eu was added. Beyond this point, the 592 nm emission was more intense, suggesting the in-growth of a peptide:Eu species in which the symmetry surrounding the Eu ion was high.[17,37] Hypspec fitting suggested that this was the 1:1 peptide:Eu complex.

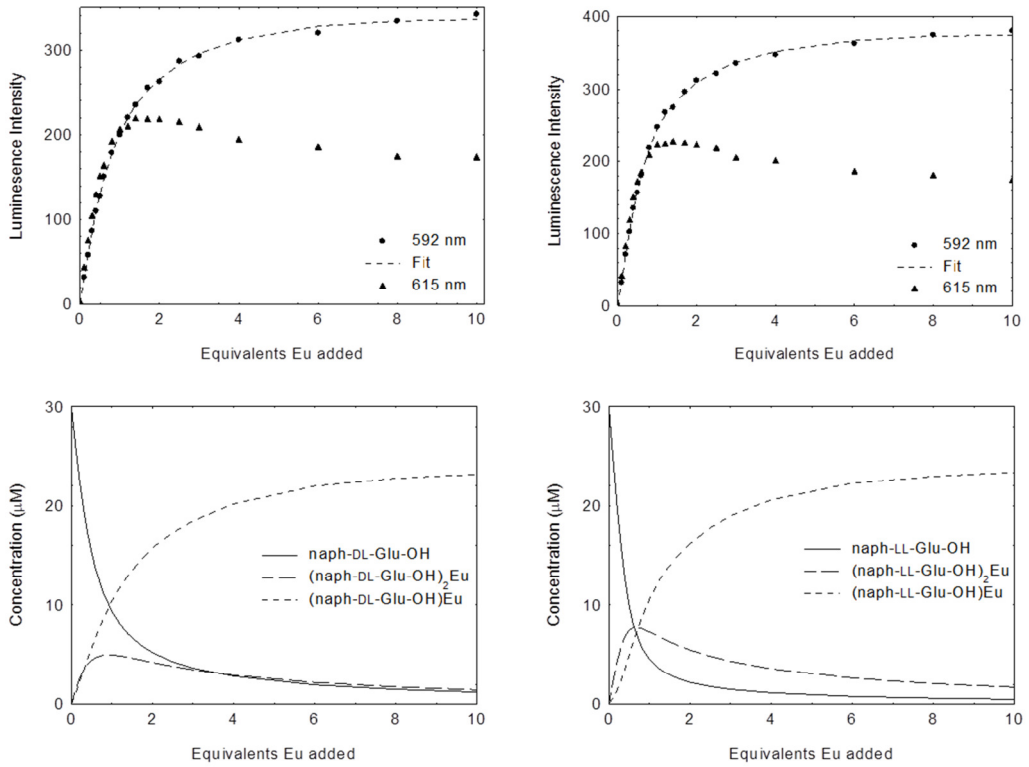

Figure 5.14: Titration profiles and speciation diagrams for naph-DL-Glu-OH (left) and naph-LL-Glu-OH (right) at pH 5.9

Speciation data from the HypSpec model are also shown in Figure 5.14. Again, more of the 1:1 complex formed as more Eu was added, until its concentration was 14-17 times that of the 2:1 complex in the presence of 10 equiv. Eu. Thus, the ratio of the 1:1/1:2 complexes in the presence of 10 equiv. Eu increased in the order di- > tri- > tetra-peptides. This trend indicated that the 1:1 complex is more favourable relative to the 2:1 complex for shorter peptide chains. One possible explanation for the increased prevalence of the 1:1 complex for the shorter peptides is that the steric bulk of the larger peptides prevents them effectively surrounding the Eu cation to form 1:1 complexes. Further experiments to explicitly characterise the structure of the coordination complexes would be required to confirm this hypothesis.

Figure 5.14 also shows that approx 95 % of naph-DL-Glu-OH and 98 % of naph-LL-Glu-OH were complexed in the presence of 10 equiv. Eu. This suggested that small but significant differences existed between the affinity of each di-peptide for Eu, which must be attributed to their differing stereochemistry. These differences were not apparent from the titration data at neutral pH (Figure 5.6). However, the modelled binding constants in Table 5.3 confirmed that the di-peptides had differing affinities for Eu at pH 5.9. Specifically, $\log\beta_{21}$ and $\log\beta_{11}$ were approx. 8 and 3 times higher for naph-LL-Glu-OH, respectively. Thus, for the di-peptides, having the carboxylic acid side chains on "opposite sides" of the molecule (naph-LL-Glu-OH) produced a higher binding affinity for Eu than having them on the "same side" (naph-DL-Glu-OH). This was the opposite effect to what was observed for the tetra-peptides. Overall, the

binding behaviour of these peptides was complex and difficult to predict, as the effect of alternating L- and D- residues was different for the di-, tri- and tetra-peptides. It may be the case that alternating L- and D- residues are beneficial only in larger peptides with four or more amino acids. Luminescence titrations with penta- and perhaps hexa-peptides of varying stereochemistry would be required to confirm this hypothesis.

Table 5.3: Binding constants for the di-peptides in pH 5.9 10 mM HEPES buffer.

Peptide	**Species (peptide:Eu)**	**logβ_{21}**	**Species (peptide:Eu)**	**logβ_{11}**	**σ**
DL	2:1	9.6	1:1	4.9	0.09
LL	2:1	10.5	1:1	5.3	0.09

The binding constants for the di-peptides at pH 5.9 (Table 5.3) were similar in magnitude to those of the tri-peptides at pH 4.9 (Table 5.2). At pH 5.9, both of the carboxylic acid side chains (pK_a ~4.2) and the terminal carboxylic acid (pK_a ~3.3) of the di-peptides are expected to be deprotonated on average,[22] giving an overall charge of -3. Thus, the overall charge of the tri-peptides at pH 4.9 (-3.5) and the di-peptides at pH 5.9 were similar and their similar binding affinities may be due simply to electrostatics.

The highest modelled binding constant for a 1:1 complex in the current work was the logβ_{11} value of 5.3 for naph-LL-Glu-OH at pH 5.9 (Table 5.3). This was lower than most recently reported binding constants for LnBP,[3] which was attributed to the short length of the peptides in this work and the fact that the binding experiments were performed under acidic conditions. The most similar binding experiment that could be found for comparison was binding of Eu by a dodecapeptide at pH 7.0 giving a logβ_{11} value of 6.8,[13] which was approx. 30 times that of naph-LL-Glu-OH at pH 5.9.

The CD spectra of 60 μM di-peptide solutions in pH 5.9 10 mM HEPES buffer upon addition of 0-2 equiv. Eu are shown in Figure 5.15. Further equiv. Eu were not added because the CD spectra underwent no further changes beyond addition of 1 equiv. Eu. Thus, the di-peptides reached equilibrium earlier in the CD titration than the tri-peptides, which required 3 equiv. Eu to be added before their CD spectra became stable (Figure 5.13). This was consistent with the luminescence titration data which also showed that equilibrium was reached at an earlier point in the titrations for the shorter peptides. The different shaped CD spectra of naph-DL- and naph-LL-Glu-OH before Eu addition in Figure 5.15 indicate that naph-DL- and naph-LL-Glu-OH had different secondary structures in solution.

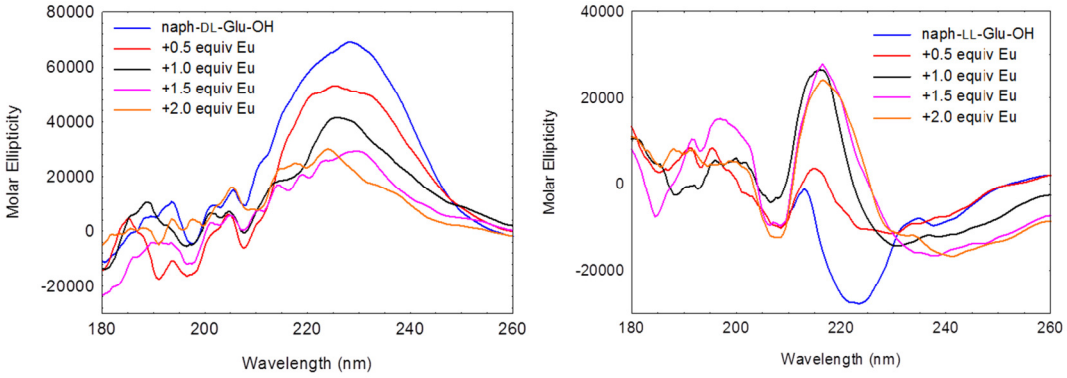

Figure 5.15: CD spectra of naph-DL-Glu-OH (left) and naph-LL-Glu-OH (right) in pH 6, 10 mM HEPES buffer upon addition of Eu nitrate. Below 210 nm the signal:noise ratio was too low for the data to be interpreted.

Upon addition of Eu, changes in the CD spectra of both di-peptides were observed, indicating a change in secondary structure upon Eu binding. Given that the predominant species of both di-peptides in the presence of 2 equiv. Eu was the 1:1 peptide:Eu complex (Figure 5.14), it was assumed that the final CD spectra in Figure 5.15 were representative of these 1:1 complexes. To further support this hypothesis, up to 4 equiv. of Eu were added to naph-DL-Glu-OH and the CD spectrum still underwent no substantial change. The final CD spectra of the di-peptides were different, suggesting different shaped 1:1 complexes. This was consistent with their different binding affinities. The final CD spectrum of naph-LL-Glu-OH also resembled the final CD spectrum of the tri-peptides (Figure 5.13), with a positive band at 215-220 nm. This suggests that the 1:1 complexes of the tri-peptides and naph-LL-Glu-OH had similar extended secondary structures.[37]

5.3.4 Characterisation of Peptide:Eu Complex Structures

In order to gain further insight into the structural characteristics required to maximise the binding affinity of LnBP, understanding of how the peptides coordinated the Eu ions in solution was desired. To achieve this, NMR titrations and density functional theory (DFT) modelling were performed. However, while the ^{1}H NMR spectra of the di-peptides showed separate signals for the methylene groups of the two side chains, the signals from the side chains of the tri- and tetra-peptides could not be distinguished. Thus, NMR titrations were only performed for the di-peptides. Similarly, DFT modelling could only be performed for the 1:1 di-peptide:Eu complexes, as the larger number of atoms in the structures of the tri- and tetra-peptides or the 2:1 complexes made the DFT calculations prohibitively slow.

The NMR titrations were performed using solutions containing 300 µM di-peptide and 10 mM HEPES buffer (pH 6) in D_2O. The concentration of 300 µM di-peptide was chosen because lower concentrations (100 µM) showed no NMR signal and higher concentrations (500 µM) precipitated upon Eu addition. At a concentration of 300 µM di-peptide, the NMR spectra were required to be collected for approx. 20 min (256 scans) in order to observe a clear signal from the peptide. To perform the titration, Eu was added as 10 mM Eu nitrate in

D_2O. The changes in the chemical shifts of the ^1H NMR signals of naph-LL-Glu-OH and naph-DL-Glu-OH upon Eu addition are shown in Figures 5.16 and 5.17, respectively. The titrations were stopped when addition of further Eu was observed to cause cloudiness in the solutions due to precipitation. This occurred upon addition of 1 equiv. Eu for naph-LL-Glu-OH and upon addition of 0.8 equiv. Eu for naph-DL-Glu-OH. Changes in the chemical shift positions of the protons at positions B and E are not given in Figures 5.16 and 5.17 because these signals were too broad and flat to accurately determine their chemical shifts.

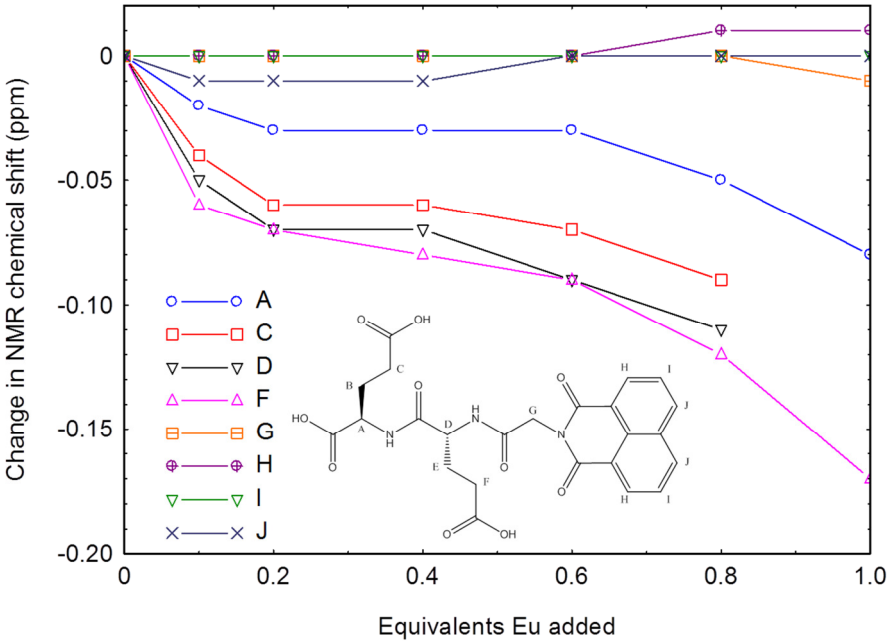

Figure 5.16: Changes in chemical shift of ^1H NMR signals from naph-LL-Glu-OH upon Eu addition.

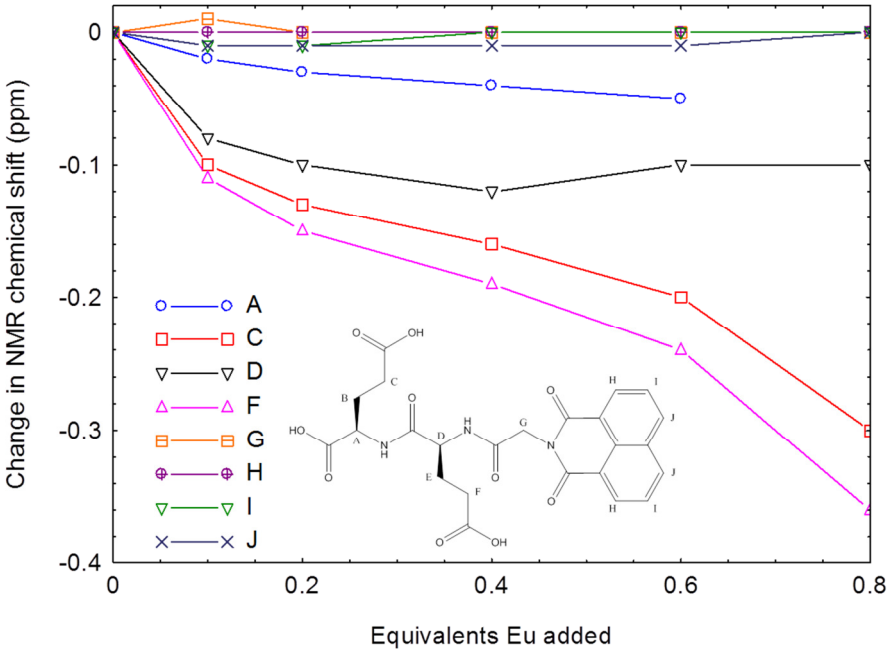

Figure 5.17: Changes in chemical shift of ^{1}H NMR signals from naph-DL-Glu-OH upon Eu addition.

The NMR titration data in Figures 5.16 and 5.17 show that none of the protons on the naphthalimide moiety of the di-peptides (G, H, I and J) shifted significantly upon Eu addition. Thus, the carbonyl groups of the naphthalimide were not involved in binding Eu. On the other hand, the methylene protons closest to the carboxylic acids of the side chains (C and F) underwent the largest upfield shifts upon Eu addition. This indicated that both of the carboxylic side chains of the di-peptides were involved in binding Eu. Further, the methine protons (A and D) also underwent downfield shifts upon Eu addition. This suggests that the terminal carboxylic acid and the carbonyl oxygen atom next to methine D were also involved in binding Eu. Unfortunately, the changes in chemical shift shown in Figures 5.16 and 5.17 were due to formation of both 2:1 and 1:1 di-peptide:Eu complexes, so the observed changes cannot be ascribed to a single complex.

The geometry of the di-peptides naph-LL- and naph-DL-Glu-OH at pH 6, when all three carboxylic acids were deprotonated, were also modelled using the DMol^{3} density functional theory (DFT) program. All calculations were performed using the conductor-like screening model (COSMO) with water as the solvent.[40] After a coarse geometry optimisation at 0 K, simulated annealing at 300 K for 0.5 ps was performed to eliminate very strained conformations.[41] This was followed by coarse and medium geometry optimisation at 0 K to refine and predict the structure and 'structural energy' of each di-peptide. In this instance, structural energy is defined as the difference between the total energy of the molecule and the combined energy of the atom fragments constituting the molecule. The geometry optimised structures for each di-peptide are shown in Figure 5.18. The structural energies of

the di-peptides were -319.45 eV for naph-LL-Glu-OH and -319.43 eV for naph-DL-Glu-OH. As such, neither isomer was more energetically favourable than the other.

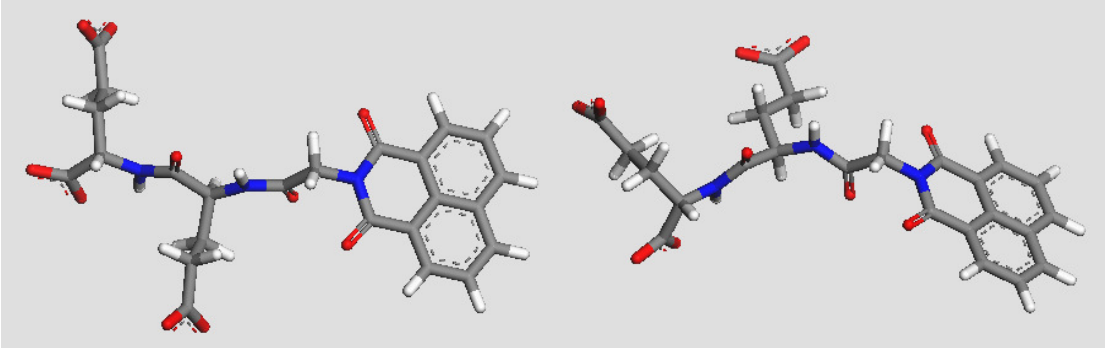

Figure 5.18: Geometry optimised structures of naph-LL-Glu-OH (left) and naph-DL-Glu-OH (right) calculated by DFT modelling

The geometry and structural energy of an Eu ion surrounded by nine water molecules was also calculated using DMol^3, with simulated annealing and geometry optimisation as described for the di-peptides above. In the final optimised structure, eight water molecules filled the first coordination sphere of Eu with Eu-O bond distances of 2.5 Å each. The structural energy of this Eu-water complex was -89.23 eV.

The geometries and structural energies of 1:1 peptide:Eu complexes with the Eu in several possible binding positions were then calculated using DMol^3. This was done by bringing together the geometry optimised structures of the Eu-water complex and one of the di-peptides, then performing simulated annealing and geometry optimisation on the resulting peptide:Eu complex as previously described. For naph-LL-Glu-OH, four possible binding positions were evaluated, as shown in Figure 5.19. For structure A, the Eu-water complex was initially placed approx. 6-7 Å from the carboxylic acid of the Glu side chain closest to the C terminus of naph-LL-Glu-OH. As can be seen from Figure 5.19, the geometry optimised structure did not show any inner coordination sphere binding between the di-peptide and the Eu ion. Instead, eight-fold coordination by the water molecules was present with two 2.5 Å and six 2.6 Å Eu-O bond distances. Nevertheless, the structural energy of complex A was -411.86 eV. Given that the sum of the structural energies of naph-LL-Glu-OH and the Eu-water complex was -408.68 eV, complex A had a binding energy of 3.18 eV.

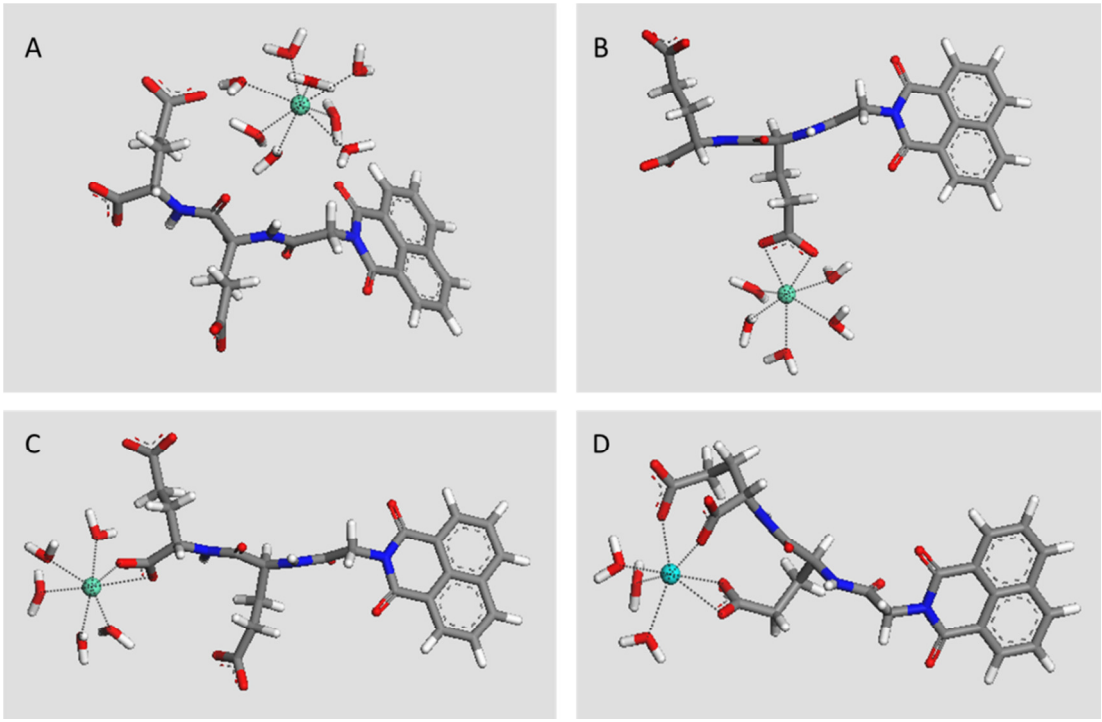

Figure 5.19: Optimised geometry of 1:1 naph-LL-Glu-OH:Eu complexes. Non-binding water molecules are not shown. Structural energy of A = -411.86 eV, B = -411.41 eV, C = -411.99 eV and D = -411.83 eV

To give structures B and C in Figure 5.19, the Eu-water complex was initially placed within 2 Å of a carboxylic acid side chain (B) or the terminal carboxylic acid (C) of naph-LL-Glu-OH. As a result, the geometry optimised structures showed inner coordination sphere binding between the di-peptide and the Eu ion. Both complexes B and C showed seven-fold coordination of the Eu ion, with two 2.5 Å bonds to the carboxylic acid of the peptide as well as four 2.5 Å and one 2.6 Å bonds to water molecules. The structural energy of complex B was -411.41 eV and of complex C was -411.99 eV. Thus, complex B had a binding energy of 2.73 eV and complex C had a binding energy of 3.31 eV. This result suggests that binding at the terminal carboxylic acid was somewhat more energetically favourable than binding at the carboxylic acid side chains. On the other hand, the NMR titration data in Figure 5.16 suggested that the carboxylic acid side chains of naph-LL-Glu-OH were involved in binding Eu, although this could have been due to the 2:1 or 1:1 peptide:Eu complex (or both).

To give structure D in Figure 5.19, the geometry optimised structures of the Eu-water complex and naph-LL-Glu-OH were not used. Instead, the peptide structure was arranged such that all three of its carboxylic acids had at least one oxygen atom within 2.5 Å of the Eu ion and nine water molecules were then added in random positions. After simulated annealing and geometry optimisation complex D (Figure 5.19) was produced. Complex D showed seven-fold coordination of the Eu ion. There were four bonds between Eu and naph-LL-Glu-OH, two 2.4 Å, one 2.5 Å and one 2.6 Å, and all three carboxylic acid groups of the di-peptide remained involved in binding. Three water molecules were also coordinated to the Eu ion,

with two 2.5 Å and one 2.6 Å bond distances. The structural energy of complex D was -411.83 eV, which meant that the binding energy for this complex was 3.15 eV.

For naph-DL-Glu-OH, four possible binding positions were also evaluated, as shown in Figure 5.20. For structure E, the Eu-water complex was initially placed between the carboxylic acids of both Glu side chains of naph-DL-Glu-OH, approx. 3-5 Å from each. As for complex A with naph-LL-Glu-OH (Figure 5.19), the geometry optimised structure did not show any inner coordination sphere binding between naph-DL-Glu-OH and the Eu ion. Instead, seven-fold coordination by the water molecules was present with four 2.5 Å and two 2.6 Å Eu-O bond distances. Thus, complex E had a lower coordination number than complex A, but a shorter average bond distance. As a result, the structural energy of complex E was -411.85 eV, almost identical to complex A. 3.19 eV. Given that the sum of the structural energies of naph-DL-Glu-OH and the Eu-water complex was -408.66 eV, complex A had a binding energy of 3.19 eV.

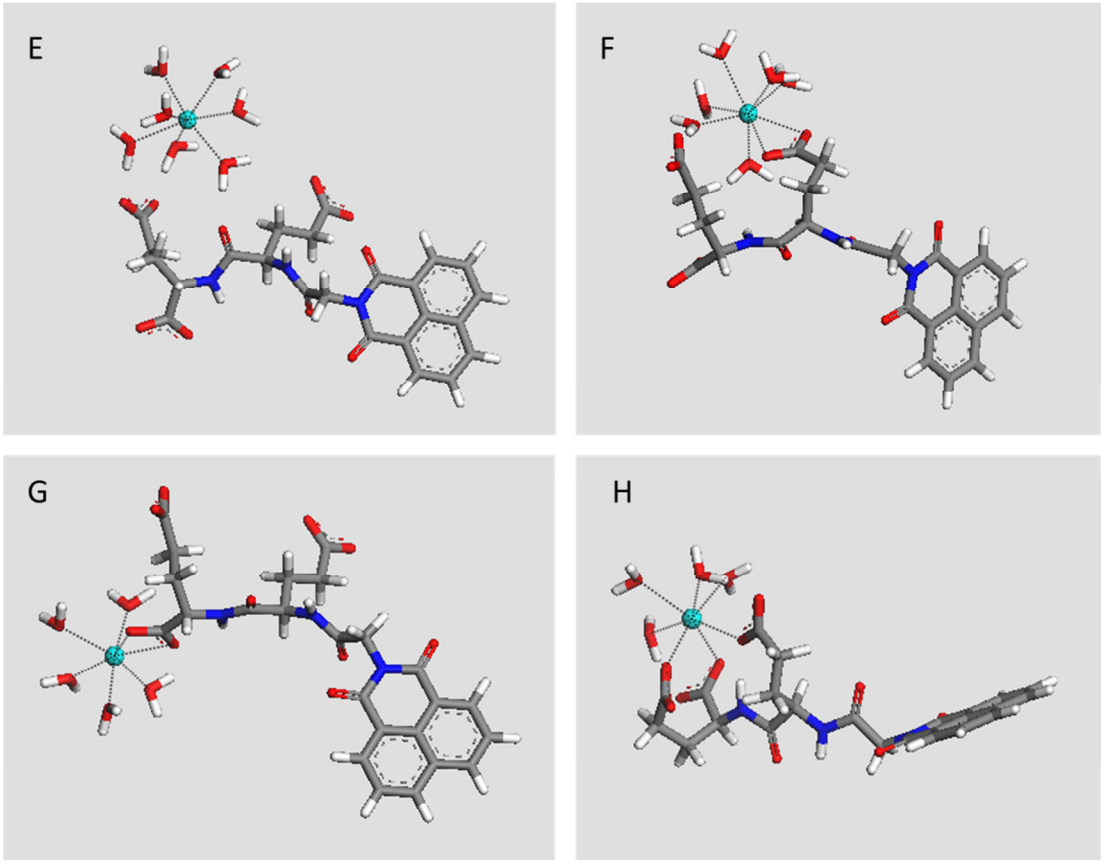

Figure 5.20: Optimised geometry of 1:1 naph-DL-Glu-OH:Eu complexes. Non-binding water molecules are not shown. Structural energy of E = -411.85 eV, F = -411.75 eV, G = -411.80 eV and H = -411.94 eV

To give structures F and G in Figure 5.20, the Eu-water complex was initially placed within 2 Å of a carboxylic acid side chain (F) or the terminal carboxylic acid (G) of naph-DL-Glu-OH. Thus, structures F and G were equivalent to structures B and C with naph-LL-Glu-OH

in Figure 5.19, respectively. Complex F showed eight-fold coordination of the Eu ion, with two 2.5 Å bonds to the carboxylic acid of the peptide as well as three 2.5 Å and three 2.6 Å bonds to water molecules. The structural energy of complex F was -411.75 eV, giving a binding energy of 3.09 eV. This was a higher coordination number and larger binding energy than was calculated for complex B (2.73 eV), indicating that binding of the Eu ion by a carboxylic acid side chain was more favourable with naph-DL-Glu-OH than naph-LL-Glu-OH. This can be explained by the proximity of the second side chain carboxylic acid to the Eu ion in complex F relative to complex B. Complex G showed seven-fold coordination of the Eu ion, with two 2.5 Å bonds to the carboxylic acid of the peptide as well as four 2.5 Å and one 2.6 Å bonds to water molecules. The structural energy of complex G was -411.80 eV, giving a binding energy of 3.14 eV. Thus, complex G had the same coordination and similar binding energy to complex C and Eu binding at the terminal carboxylic acid was similar for both di-peptides. These results also indicate that for naph-DL-Glu-OH, Eu binding at the carboxylic acid side chains was energetically similar to binding at the terminal carboxylic acid.

To give structure H in Figure 5.20, the naph-DL-Glu- structure was arranged such that all three of its carboxylic acids had at least one oxygen atom within 2.5 Å of the Eu ion and nine water molecules were then added in random positions. Thus, complex H was equivalent to complex D with naph-LL-Glu-OH in Figure 5.19. Complex H showed seven-fold coordination of the Eu ion. There was one bond to each of the carboxylic acids of naph-DL-Glu-OH, one 2.4 Å and two 2.5 Å, giving a total of three bonds to the di-peptide. Four water molecules were also coordinated to the Eu ion, with two 2.5 Å and two 2.6 Å bond distances. The structural energy of complex H was -411.94 eV, which meant that the binding energy for this complex was 3.28 eV. Thus, complex H had similar coordination and binding energy to complex D, but with one less peptide-Eu bond and one more water-Eu bond instead.

Overall, all of the 1:1 di-peptide:Eu complexes in Figures 5.19 and 5.20 had similar binding energies. Thus, it is likely that all of these possible binding positions, and others, were present to some extent in the experimental solutions. This was consistent with the NMR titration data in Figures 5.16 and 5.17, which suggested that all three carboxylic acids of the di-peptides and some of the backbone carbonyl oxygens were involved in Eu binding. It should also be noted that complexes A and E, in which the di-peptide was not directly coordinated with the Eu ion, had a similar structural energies to the other complexes in which the peptide was directly coordinated to the Eu ion. This was consistent with the weak calculated binding constants between the di-peptides and Eu (Table 5.3) and the modelled speciation data from the luminescence titrations (Figure 5.14), which suggested that not all of the added Eu was coordinated by the di-peptides.

5.4 Functionalised Titania Nanoparticles

5.4.1 Characterisation

The tetra-peptide with alternating Glu residues, naph-LDDL-Glu-OH, provided the strongest complex with Eu of all the peptides synthesised in this work, as shown in Figure 5.6. Therefore, LDDL-Glu(OtBu)-OH was appended with 1-undecanoic acid, to give compound **15**, and used to functionalise titania nanoparticles and form a solid phase sorbent material. The presence of the alkyl chain in **15** induced self-assembly on the titania surface during functionalization and the alkene enabled covalent attachment to the surface of the titania nanoparticles.[42] Due to the bulky nature of the peptide functional group, 1-undecene was also used as 'filler' between the functional molecules, so that self-assembly of the alkyl chains would not be interrupted, as shown in Scheme 5.1. After side chain deprotection, the resulting material was referred to as TiO_2-peptide.

Without protecting groups, the carboxylic acids of the Glu side chains of **15** would coordinate to the titania surface during functionalization[43] and interfere with covalent attachment of the ligands to the titania surface via the alkene. Therefore, the carboxylic acids remained protected with *tert*-butyl esters during functionalization and were deprotected only after being attached to the titania surface. During solid phase peptide synthesis of **15**, the acid-labile 2-chlorotrityl chloride resin was used, to enable cleavage of the peptide from the resin while leaving the side chain *tert*-butyl ester protecting groups intact. As a result, **15** had one unprotected carboxylic acid group at the C-terminus of the peptide backbone upon cleavage from the 2-chlorotrityl resin. It was attempted to protect the C-terminal carboxylic acid with a benzyl ester by reacting the cesium salt of **15** with benzyl chloride. However, this reaction was unsuccessful, presumably due to the steric bulk of the multiple *tert*-butyl ester protecting groups present. Therefore, functionalization of titania nanoparticles with ligand **15** was performed without a protecting group on the terminal carboxylic acid. If the C-terminal carboxylic acid of **15** coordinated to the titania surface during functionalization, the self-assembled alkyl chains would extend out towards the bulk solution. This would cause TiO_2-peptide to show the same sorption behaviour as titania nanoparticles functionalised with 1-undecene (TiO_2-alkyl). Therefore, in order to confirm that ligand **15** self-assembled with the alkene rather than the terminal carboxylic acid at the titania surface during functionalisation, the sorption behaviour of TiO_2-peptide was compared to that of TiO_2-alkyl. This also allowed differentiation between any sorption that occurred due to the 1-undecene molecule on TiO_2-peptide and sorption by the peptide ligand.

To confirm the functionalization of the titania nanoparticles, solid-state ^{13}C-^{1}H CP MAS-NMR was performed and the results are shown in Figure 5.21. Peaks were present in the NMR spectra of TiO_2-alkyl and TiO_2-peptide, which confirmed that functionalization was successful since no peaks were seen in the solid-state ^{13}C-^{1}H CP MAS-NMR spectrum of non-functionalised titania nanoparticles (Figure 4.8). Peaks with chemical shift 15-45 ppm, due to aliphatic CH_2 groups,[44] were seen in the NMR spectra of both TiO_2-alkyl and

TiO_2-peptide as both the 1-undecene and undecene-LDDL-Glu-OH ligands used for functionalisation contained alkyl chains. Since this was the only carbon containing functionality present in TiO_2-alkyl, no other peaks were seen in its NMR spectrum. However, the NMR spectrum of TiO_2-peptide also showed peaks with chemical shifts of approx. 50 and 180 ppm. These peaks were assigned as the –CH groups in the peptide backbone and the carboxylic acid or amide groups in the undecene-LDDL-Glu-OH ligand, respectively.[44,45] Thus, the ^{13}C-^{1}H CP MAS NMR spectra confirmed the presence of the undecene-LDDL-Glu-OH ligand on the surface of TiO_2-peptide.

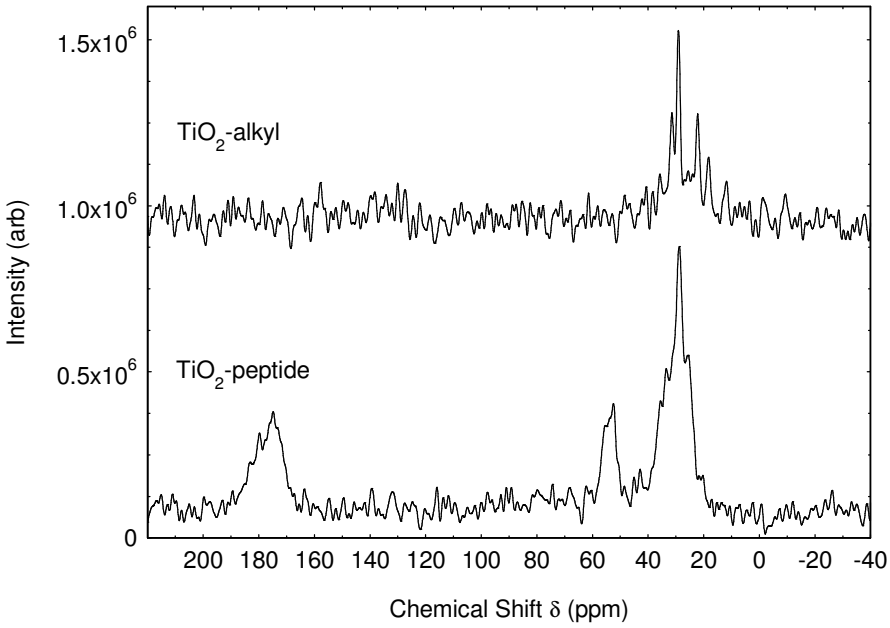

Figure 5.21: ^{13}C-^{1}H CP MAS NMR spectra of TiO_2-alkyl and TiO_2-peptide

The level of functionalization of TiO_2-peptide was quantitatively determined by CHN microanalysis (Table 5.4). It was assumed that for every molecule of undecene-LDDL-Glu-OH ($C_{31}H_{48}N_4O_{14}$) present there were nine molecules of 1-undecene ($C_{11}H_{22}$) also present, so that the overall molecular formula of the organic functional groups was $C_{130}H_{246}N_4O_{14}$. This molecular formula and the total measured %CHN were used to determine the calculated %CHN values, which agreed with the experimentally measured values to within 0.2 % (Table 5.4). However, the fact that the calculated %C was higher than measured and the calculated %N was lower than measured suggests that the ratio of undecene-LDDL-Glu-OH to 1-undecene present on the surface of the titania nanoparticles may have in fact been higher than 1:10. The total organic content of TiO_2-peptide was calculated as 1.2 % based on the percentage weight of CHNO.

Table 5.4: Elemental CHN microanalysis of TiO_2-peptide (weight %)

Measured	**TiO_2-peptide**
%C	0.7
%H	0.2
%N	0.2
Total	1.1
Calculated	**$C_{130}H_{246}N_4O_{14}$**
%C	0.9
%H	0.1
%N	0.0(3)
Total (organic)	1.2

Assuming a 1:9 undecene-LDDL-Glu-OH: 1-undecene molecular ratio on the surface of these materials, the undecene-LDDL-Glu-OH accounts for 33.6 % of the total organic mass and the 1-undecene 66.4 %. For TiO_2-peptide, this equates to 0.001 mol% undecene-LDDL-Glu-OH and 0.005 mol% 1-undecene in terms of molar percentages. The calculated area per molecule (with a titania nanoparticle surface area of 55 m^2/g) was 1.6 nm^2 for TiO_2-peptide. This was a similar molecule density to what was seen for all the organo-functionalised nanoparticles described in *Chapter 4.*

The effect of peptide functionalization on the surface charge of the titania nanoparticles was explored using zeta potential measurements, shown in Figure 5.22. In aqueous nitrate media the isoelectric point for TiO_2-NF and TiO_2-peptide were observed at pH 4.2 and pH 1.5, respectively. The lower isoelectric point of TiO_2-peptide was as expected given that the peptide functionality had five acidic carboxylic acid groups while the surface of titania consisted of both acidic and basic reaction sites.[46]

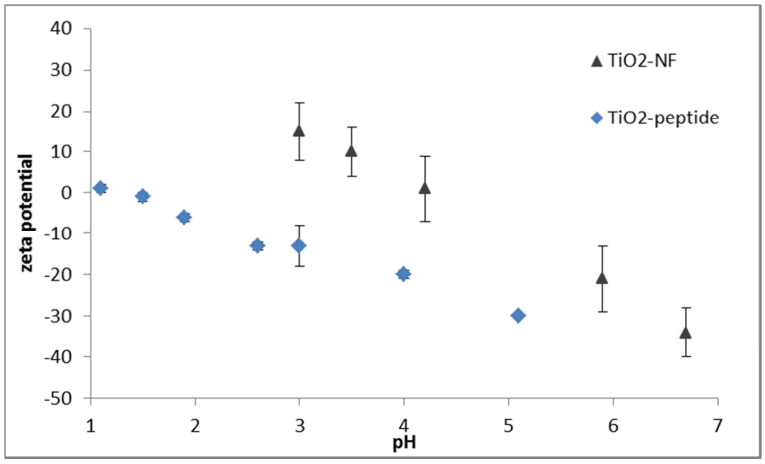

Figure 5.22: Measured zeta potential of TiO_2-NF and TiO_2-peptide in aqueous nitrate media

5.4.2 Sorption Properties

Batch sorption experiments were initially performed in water, but the pH of solution was observed to vary upon contact with TiO_2-peptide and was difficult to control. Therefore, batch

sorption experiments were instead performed in 10 mM HEPES buffer with TiO_2-NF, TiO_2-alkyl and TiO_2-peptide. However, even in the presence of 10 mM HEPES buffer, addition of 2.0 mL solution to 10 mg TiO_2-peptide caused substantial changes in pH. Therefore, pre-equilibration of the pH was required for sorption experiments with TiO_2-peptide, before spiking the equilibrated 10 mM HEPES buffer solution with the mixed analyte solution.

The results of batch sorption experiments in 10 mM HEPES buffer at pH 4.2 are given in Figure 5.23. For TiO_2-NF, the only elements sorbed were Al and U. Specifically, Al was sorbed approx. 45 % and U was sorbed approx. 98 %. This was consistent with the results of the sorption experiments with individual element solutions described in *Chapter 4*, in which Sr, Cs and Ln were not sorbed at pH 4 while U was sorbed somewhere between 50 and 100 %. Given that the isoelectric point of TiO_2-NF in aqueous nitrate media was measured to be 4.2 (Figure 5.22) and the data in Figure 5.23 was measured at pH 4.2 ± 0.1, the titania surface was expected to have negligible charge during these sorption experiments. Therefore, the affinity of Al and U for the titania surface was attributed to coordination with the hard oxygen donor atoms of the titania rather than ionic bonding. Indeed, the existence of inner-sphere U-titania complexes (for both rutile and anatase) has been previously demonstrated.[47,48] For Al, which was expected be present as unhydrolysed Al^{3+} under these conditions,[24] the sorption also cannot be attributed to electrostatic effects since the Al ion has the same charge as the Ln ions which were not sorbed. Instead, it is possible that the Al^{3+} ions were hydrolysed at the titania surface to form polynuclear species or precipitates.[49]

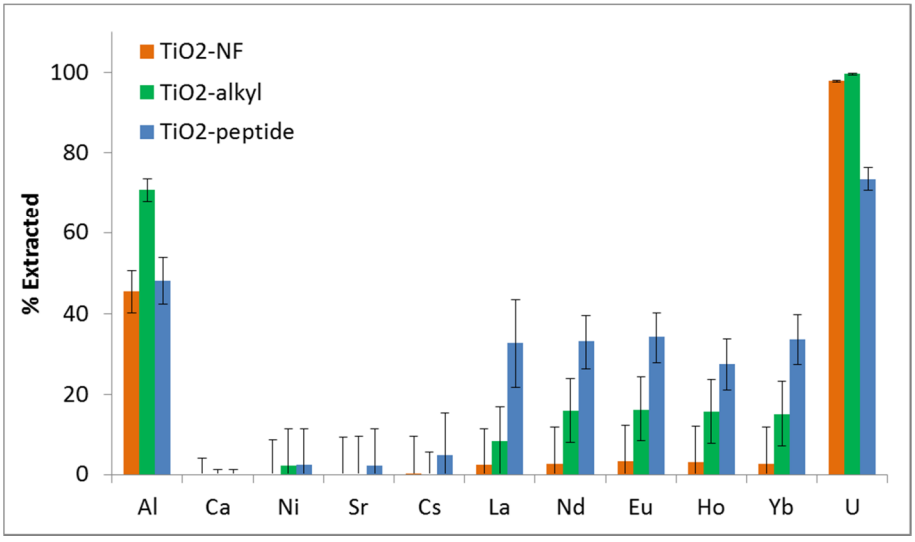

Figure 5.23: Percentage extraction of 1 ppm Al, Ca, Ni, Sr, Cs, Ln and U from pH 4.2 10 mM HEPES buffer by TiO_2-NF, TiO_2-alkyl and TiO_2-peptide.

The data in Figure 5.23 also shows the sorption results for TiO_2-alkyl at pH 4.2. As for TiO_2-NF, there was no sorption of Ca, Ni, Sr or Cs but there was some enhancement of the sorption of Al, Ln and U for TiO_2-alkyl relative to TiO_2-NF. This was attributed to the fact that the weak interactions between water and surfaces covered in hydrophobic self-assembled

monolayers create an interfacial potential and cause migration of ions to the interfacial region.[50] This effect has been suggested to be due to the suppression of dipole-moment fluctuations in surrounding water by ions in aqueous solutions, which causes the ions to be attracted to regions of water with lower relative permittivity, such as water near hydrophobes.[51] Therefore, it was assumed that the Al^{3+}, Ln^{3+} and UO_2^{2+} ions in the present work were attracted to the titania surface when it had been covered in a self-assembled monolayer of 1-undecene (TiO_2-alkyl), due to the same effect.

The sorption performance of TiO_2-peptide, also shown in Figure 5.23, indicated that the presence of the LDDL-Glu-OH moiety on the titania surface enhanced Ln sorption but decreased U sorption relative to TiO_2-NF and TiO_2-alkyl. The enhanced sorption of Ln showed that the functionalization had been successful since the affinity of the peptide moiety for Ln elements had already been demonstrated in the solution binding studies above. The Ln sorption by TiO_2-peptide was selective over Ca, Ni, Sr and Cs, which were not sorbed by any of the functionalised or non-functionalised titania nanoparticles. The sorption of U by TiO_2-peptide at pH 4.2 was approx. 75 %, which was greater than the Ln sorption of approx. 30-35 %. This was consistent with previous literature which has suggested that peptides of amino acids with carboxylic acid side chains, in particular glutamic acid, have high affinities for the uranyl cation.[52] However, U was sorbed less by TiO_2-peptide than by TiO_2-NF or TiO_2-alkyl. One possible explanation is that the higher sorption of Ln by TiO_2-peptide resulted in saturation of the nanoparticle surface such that not all the U could also be sorbed. Finally, the sorption of Al by TiO_2-peptide was approx. 50 % which was similar to that of TiO_2-NF. Given that the TiO_2-peptide surface was negatively charged at pH 4.2 (Figure 5.22), this sorption of Al^{3+} ions by TiO_2-peptide was attributed to electrostatics, rather than surface precipitation as was postulated for TiO_2-NF.

The results of batch sorption experiments in 10 mM HEPES buffer at at pH 4.8 are shown in Figure 5.24. Again, Ca, Ni, Sr and Cs were not sorbed by any of the functionalised or non-functionalised titania nanoparticle materials. For TiO_2-NF, Al and U were again the elements that were predominantly sorbed, as was seen at pH 4.2 in Figure 5.23. However, a small amount of Ln was also sorbed at this higher pH. The increased sorption of Al and U as well as the onset of a small amount of Ln sorption at pH 4.8 was presumably due to the more negative surface charge of TiO_2-NF at this higher pH (Figure 4.22). The sorption of individual element solutions with TiO_2-NF described in *Chapter 4* showed higher sorption of Sr (approx. 15 %) and Ln (45-80 %) at pH 5 than was seen in this experiment. This may be explained by the competitive sorption conditions utilised in the present work, which may have caused the titania surface to be saturated by the more strongly sorbed Al and U ions such that the Ln and Sr ions were sorbed less.

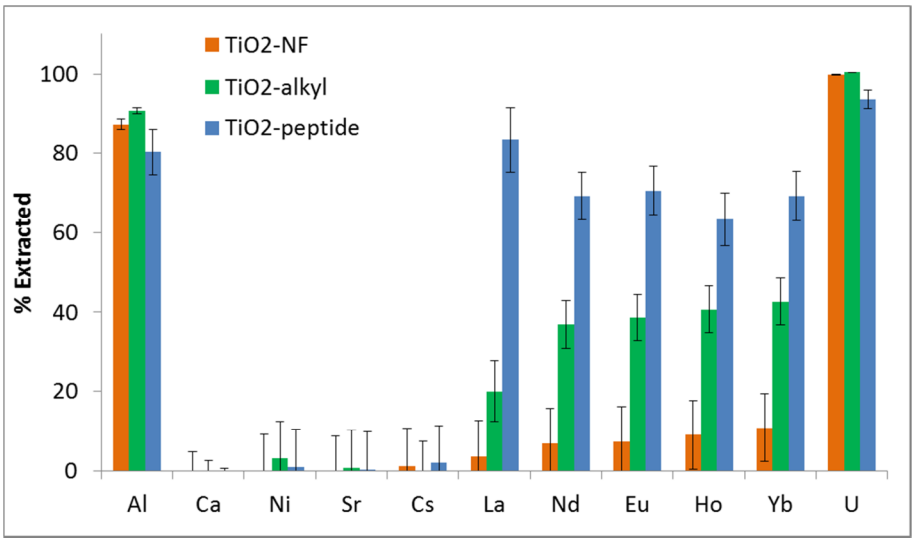

Figure 5.24: Percentage extraction of 1 ppm Al, Ca, Ni, Sr, Cs, Ln and U from pH 4.8 10 mM HEPES buffer by TiO_2-NF, TiO_2-alkyl and TiO_2-peptide.

The data in Figure 5.24 also shows the sorption results for the functionalised titania materials, TiO_2-alkyl and TiO_2-peptide, at pH 4.8. As was observed at pH 4.2 (Figure 5.23), the sorption of Al and Ln was enhanced for TiO_2-alkyl relative to TiO_2-NF, although U was similarly sorbed by both materials at pH 4.8 because sorption by TiO_2-NF was already quantitative. The sorption behaviour of TiO_2-peptide at pH 4.8 also showed the same trends relative to TiO_2-NF and TiO_2-alkene as were observed at pH 4.2. Namely, Ln sorption was enhanced, U sorption was decreased and Al sorption was similar to TiO_2-NF and less than TiO_2-alkyl. However, overall the sorption of Al, Ln and U by TiO_2-peptide were all higher at pH 4.8 than at pH 4.2. This was expected given that more of the carboxylic acid side chains of the peptide ligand would be deprotonated and capable of binding cations at this less acidic pH, as evidenced by the larger negative surface charge of TiO_2-peptide at pH 5 (Figure 5.22).

Many examples of peptides being used for functionalization of solids exist in the literature, using a variety of substrates such as Ln nanoparticles,[53] gold nanoparticles,[54,55] metal-organic frameworks,[56] silanized titanium[57] and carbon.[58] However, most of these studies have not investigated the sorbent properties of the peptide functionalised materials. Of the work that has been done investigating the utility of amino acids and peptides on solid supports as sorbents, most has focussed on remediation of heavy metals such as Pb and Cd,[59] despite the extensive literature on peptides binding Ln in solution. A few examples only exist of peptide functionalised materials being used for Ln sorption. For example, peptide coated gold nanoparticles[55] as well as poly-L-aspartic acid functionalised controlled pore glass and gold surfaces.[60,61] For the peptide coated gold nanoparticles, the selectivity of Ln sorption was not investigated.[55] However, flow through metal binding experiments using poly-L-aspartic acid immobilised on controlled pore glass showed that this material strongly bound Al, Cu and Ln at pH 7, with selectivity during competitive sorption for Al > Cu > La > Pb > Ni > Cd.[59] Sorption of Ni and Ca were also measured individually but showed minimal sorption.

This selectivity is similar to what was observed under the more acidic conditions of pH 4-5 with undecene-LDDL-Glu-OH functionalised titania nanoparticles in the present work.

5.5 Conclusions

A systematic investigation of the effects of peptide length and stereochemistry on the Ln binding properties of simple peptides was performed using a model system of di-, tri- and tetra-Glu. Covalent attachment of a naph antenna to these model peptides allowed them to effectively sensitise the luminescence of Eu such that luminescence titrations could be performed. Attachment of the naph antenna to the peptides appeared to also alter their secondary structure and impact their Ln binding capability. The longer tetra-peptides with alternating L- and D-Glu residues coordinated Ln most strongly. This was most likely due to their higher number of carboxylic acid binding sites and a higher incidence of cooperative binding when the carboxylic acid side chains were on the same side of the molecule. However, tri-peptides with alternating L- and D-Glu residues demonstrated similar binding strength to tri-peptides with all L-Glu residues and for the di-peptides naph-LL-Glu-OH in fact showed somewhat stronger binding than naph-LD-Glu-OH. Thus, the advantageous effect of alternating L- and D-Glu residues appeared to only be present for the longer peptides. Overall, it has been demonstrated that peptides based on Glu bind Ln, that increasing peptide length increased Ln affinity but stereochemistry had an inconsistent effect.

Unfortunately, the complexity of the luminescence titrations at pH 7 prevented determination of the stoichiometry and binding constants of the multiple peptide:Eu species present. However, luminescence titrations in acidic solutions were simplified and thus could be fit using HypSpec modelling software. HypSpec modelling showed that both 2:1 and 1:1 peptide:Eu complexes were present in solution and that their binding constants were strongly dependent on pH and in some cases also dependent on stereochemistry (Tables 5.1, 5.2 and 5.3). These results were generally consistent with the trends observed at neutral pH. NMR titrations and DFT modelling of the di-peptide:Eu complexes provided some insight into the mode of binding. According to the NMR titration data, both carboxylic acid side chains, the terminal carboxylic acid and possibly even backbone carbonyl groups of the di-peptides were involved in Eu binding. Similarly, DFT modelling indicated that multiple possible binding sites produced 1:1 di-peptide:Eu complexes with similar energies. Thus, it is probable that multiple modes of binding existed in the experimental solutions. Lanthanide binding by these short peptides was complex and difficult to characterise.

The LnBP that showed the highest affinity for Eu according to the luminescence titration experiments, naph-LDDL-Glu-OH, was modified with 1-undecene instead of naph to give undecene-lddl-Glu-OH **15**. This allowed self-assembly and covalent attachment of the peptide to the surface of titania nanoparticles. The resulting solid-phase sorbent material (TiO_2-peptide) was used to investigate the selectivity of the peptide for Ln over other metal cations at pH 4-5. As expected, the presence of the peptide on the titania surface enhanced the

affinity of the material for Ln across the series, even at pH 4. TiO_2-peptide also demonstrated substantial sorption of Al and U, but was selective for Ln over Ca, Ni, Sr and Cs.

5.6 References

(1) Puchy, B. *Briefing Paper: Rare Earth Elements*, Department of Environmental Quality, 2011.

(2) *Molecular Catalysis of Rare Earth Elements*; Roesky, P. W., Ed.; Springer: Berlin, 2010; Vol. 137.

(3) Ancel, L.; Niedzwiecka, A.; Lebrun, C.; Gateau, C.; Delangle, P. *Cr Chim* **2013**, *16*, 515.

(4) Nitz, M.; Sherawat, M.; Franz, K. J.; Peisach, E.; Allen, K. N.; Imperiali, B. *Angew Chem Int Edit* **2004**, *43*, 3682.

(5) Ozcubukcu, S.; Mandal, K.; Wegner, S.; Jensen, M. P.; He, C. *Inorganic Chemistry* **2011**, *50*, 7937.

(6) Pearson, R. G. *J. Am. Chem. Soc.* **1963**, *85*, 3533.

(7) Prell, J. S.; Flick, T. G.; Oomens, J.; Berden, G.; Williams, E. R. *J Phys Chem A* **2010**, *114*, 854.

(8) Allen, K. N.; Imperiali, B. *Curr Opin Chem Biol* **2010**, *14*, 247.

(9) Nitz, M.; Franz, K. J.; Maglathlin, R. L.; Imperiali, B. *Chembiochem* **2003**, *4*, 272.

(10) Niedzwiecka, A.; Cisnetti, F.; Lebrun, C.; Gateau, C.; Delangle, P. *Dalton T* **2012**, *41*, 3239.

(11) Niedzwiecka, A.; Cisnetti, F.; Lebrun, C.; Delangle, P. *Inorganic Chemistry* **2012**, *51*, 5458.

(12) Cisnetti, F.; Lebrun, C.; Delangle, P. *Dalton T* **2010**, *39*, 3560.

(13) Bonnet, C. S.; Devocelle, M.; Gunnlaugsson, T. *Org Biomol Chem* **2012**, *10*, 126.

(14) Moore, E. G.; Samuel, A. P. S.; Raymond, K. N. *Accounts Chem Res* **2009**, *42*, 542.

(15) Richardson, F. S. *Chemical Reviews* **1982**, *82*, 541.

(16) Bunzli, J.-C. G. C., G.R. *Lanthanide Probes in Life, Chemical and Earth Sciences. Theory and Practice*; Elsevier: Amsterdam, 1989.

(17) Beeby, A.; Clarkson, I. M.; Dickins, R. S.; Faulkner, S.; Parker, D.; Royle, L.; de Sousa, A. S.; Williams, J. A. G.; Woods, M. *J Chem Soc Perk T 2* **1999**, 493.

(18) Liu, L. L.; Franz, K. J. *J. Am. Chem. Soc.* **2005**, *127*, 9662.

(19) Gans, P.; Sabatini, A.; Vacca, A. *Talanta* **1996**, *43*, 1739.

(20) Marsden, B. J.; Hodges, R. S.; Sykes, B. D. *Biochemistry-Us* **1988**, *27*, 4198.

(21) Pu, D.; Vincent, J. B.; Cassady, C. J. *J Mass Spectrom* **2008**, *43*, 773.

(22) Grimsley, G. R.; Scholtz, J. M.; Pace, C. N. *Protein Sci* **2009**, *18*, 247.

(23) Bashford, D.; Case, D. A.; Dalvit, C.; Tennant, L.; Wright, P. E. *Biochemistry-Us* **1993**, *32*, 8045.

(24) Baes Jr., C. F. M., R.E. *The hydrolysis of cations*; John Wiley and Sons, Inc.: New York, 1976.

(25) Schiopu, I.; Iftemi, S.; Luchian, T. *Langmuir* **2015**, *31*, 387.

(26) Matera-Witkiewicz, A.; Brasun, J.; Cebrat, M. *Polyhedron* **2010**, *29*, 3052.

(27) Brasun, J.; Matera, A.; Oldziej, S.; Swiatek-Kozlowska, J.; Messori, L.; Gabbiani, C.; Orfei, M.; Ginanneschi, M. *J Inorg Biochem* **2007**, *101*, 452.

(28) Cusack, R. M.; Grondahl, L.; Fairlie, D. P.; Gahan, L. R.; Hanson, G. R. *J Chem Soc Perk T 2* **2002**, 556.

(29) Benke, B. P.; Madhavan, N. *Bioorgan Med Chem* **2015**, *23*, 1413.

(30) Bong, D. T.; Clark, T. D.; Granja, J. R.; Ghadiri, M. R. *Angew Chem Int Edit* **2001**, *40*, 988.

(31) Putnam, C. D.; Hammel, M.; Hura, G. L.; Tainer, J. A. *Q Rev Biophys* **2007**, *40*, 191.

(32) Paiva, A. P.; Malik, P. *J. Radioanal. Nucl. Chem.* **2004**, *261*, 485.

(33) Yantasee, W.; Fryxell, G. E.; Addleman, R. S.; Wiacek, R. J.; Koonsiripaiboon, V.; Pattamakomsan, K.; Sukwarotwat, V.; Xu, J.; Raymond, K. N. *J Hazard Mater* **2009**, *168*, 1233.

(34) (EPA), U. S. E. P. A. *Rare Earth Elements: A Review of Production, Processing, Recycling, and Associated Environmental Issues*, 2012.

(35) Andersson, S.; Eberhardt, K.; Ekberg, C.; Liljenzin, J. O.; Nilsson, M.; Skarnemark, G. *Radiochim. Acta* **2006**, *94*, 469.

(36) Silva, W. E.; Belian, M. F.; Freire, R. O.; de Sa, G. F.; Alves, S. *J Phys Chem A* **2010**, *114*, 10066.

(37) Rinaudo, M. D., A. *J. Am. Chem. Soc.* **1976**, *98*, 6360.

(38) Ende, C. W. A.; Meng, H. Y.; Ye, M.; Pandey, A. K.; Zondlo, N. J. *Chembiochem* **2010**, *11*, 1738.

(39) Lin, C. H.; Chan, F. C. H.; Hwang, J. K.; Lyu, P. C. *Protein Eng* **1999**, *12*, 589.

(40) Klamt, A.; Schuurmann, G. *J Chem Soc Perk T 2* **1993**, 799.

(41) Franzini, E.; De Gioia, L.; Fantucci, P.; Zampella, G.; Bonacic-Koutecky, V. *Inorg Chem Commun* **2003**, *6*, 650.

(42) Veliscek-Carolan, J.; Jolliffe, K. A.; Hanley, T. L. *Acs Appl Mater Inter* **2013**, *5*, 11984.

(43) Roncaroli, F.; Blesa, M. A. *Phys Chem Chem Phys* **2010**, *12*, 9938.

(44) Breitmaier, E. V., W. *Carbon-13 NMR Spectroscopy - High Resolution Methods and Applications in Organic Chemistry and Biochemistry*; 3rd ed.; VCH: Weinheim, 1987.

(45) Bovey, F. A. J., L.; Mirau, P.A. *Nuclear Magnetic Resonance Spectroscopy*; 2nd ed.; Academic Press, Inc.: San Diego, 1988.

(46) Hadjiivanov, K. I.; Klissurski, D. G. *Chemical Society Reviews* **1996**, *25*, 61.

(47) Vandenborre, J.; Drot, R.; Simoni, E. *Inorganic Chemistry* **2007**, *46*, 1291.

(48) Geckeis, H.; Lutzenkirchen, J.; Polly, R.; Rabung, T.; Schmidt, M. *Chemical Reviews* **2013**, *113*, 1016.

(49) *The environmental chemistry of aluminium*; 2nd ed.; Sposito, G., Ed.; CRC Press, Inc.: Boca Raton, 1996.

(50) Hopkins, A. J.; McFearin, C. L.; Richmond, G. L. *J Phys Chem C* **2011**, *115*, 11192.

(51) Gray-Weale, A.; Beattie, J. K. *Phys Chem Chem Phys* **2009**, *11*, 10994.

(52) Lebrun, C.; Starck, M.; Gathu, V.; Chenavier, Y.; Delangle, P. *Chem-Eur J* **2014**, *20*, 16566.

(53) Chan, C. F.; Tsang, M. K.; Li, H. G.; Lan, R. F.; Chadbourne, F. L.; Chan, W. L.; Law, G. L.; Cobb, S. L.; Hao, J. H.; Wong, W. T.; Wong, K. L. *J Mater Chem B* **2014**, *2*, 84.

(54) Lewis, D. J.; Pikramenou, Z. *Coordin Chem Rev* **2014**, *273*, 213.

(55) Savage, A. C.; Pikramenou, Z. *Chem Commun* **2011**, *47*, 6431.

(56) Katsoulidis, A. P.; Park, K. S.; Antypov, D.; Marti-Gastaldo, C.; Miller, G. J.; Warren, J. E.; Robertson, C. M.; Blanc, F.; Darling, G. R.; Berry, N. G.; Purton, J. A.; Adams, D. J.; Rosseinsky, M. J. *Angew Chem Int Edit* **2014**, *53*, 193.

(57) Dettin, M.; Zamuner, A.; Iucci, G.; Messina, G. M. L.; Battocchio, C.; Picariello, G.; Gallina, G.; Marletta, G.; Castagliuolo, I.; Brun, P. *J Pept Sci* **2014**, *20*, 585.

(58) Gaillard, C.; Girard, H. A.; Falck, C.; Paget, V.; Simic, V.; Ugolin, N.; Bergonzo, P.; Chevillard, S.; Arnault, J. C. *Rsc Adv* **2014**, *4*, 3566.

(59) Malachowski, L.; Stair, J. L.; Holcombe, J. A. *Pure Appl Chem* **2004**, *76*, 777.

(60) Gutierrez, E.; Miller, T. C.; Gonzalez-Redondo, J. R.; Holcombe, J. A. *Environ Sci Technol* **1999**, *33*, 1664.

(61) Miller, T. C.; Holcombe, J. A. *Anal Chem* **1999**, *71*, 2667.

Chapter 6: Ordered Mesoporous Titania

It has been demonstrated in *Chapters 4 and 5* that titania can be covalently functionalised with organic ligands to produce hybrid materials that selectively remove targeted elements from solutions of used nuclear fuel. In order to produce functionalised titania materials with high sorption capacity and mass transfer kinetics as well as selectivity, it was postulated that titania framework materials with an ordered mesoporous structure were required.[1,2] More broadly, mesoporous metal oxide materials have long been targets for synthesis as their high pore volumes and large surface areas make them useful for many applications in fields such as catalysis,[2-4] sorption and separations,[2,5] optics and photovoltaics,[3,6] solar cells and hydrogen production.[7,8] In particular past research has focussed on synthesis of mesoporous titania as titania is cheap, non-toxic, and photocatalytically active which makes it ideal for use in solar cells and for hydrogen production.[7,8] Since titania is also hydrolytically and radiolytically stable, ordered mesoporous titania is also a target framework material for separations at the back end of the nuclear fuel cycle.[9,10]

A common and simple way to synthesise ordered mesoporous titania is soft templating via evaporation induced self-assembly (EISA) (Figure 6.1). By this method, a mixture of inorganic precursors, surfactant, water and alcohol are allowed to evaporate under controlled conditions. As the alcohol evaporates and the concentration of the solution increases the surfactant molecules self-assemble into liquid crystal structures that act as templates for the titania precursors which are simultaneously hydrolysed and condensed by ingress of water from the atmosphere to form polymeric titania surrounding these surfactant structures.[11] Formation of ordered structures by this method requires strict control over the rate of titanium hydrolysis and condensation. The inorganic precursor titanium (IV) tetrachloride was used in this work as it is highly reactive and when mixed with ethanol and water provides the acidity required to retard the condensation of titania.[12,13] Loss of hydrochloric acid (HCl) during EISA decreases the acidity of the solution and allows titania hydrolysis to commence in a slow and controlled fashion. This method addresses both cost and simplicity of preparation to allow for easier scale up of resultant materials. Previous work on synthesis of mesoporous titania in the form of thin films or larger scale powders via EISA has shown that the structures formed are highly dependent upon the precursor solution composition[14] and age[15] as well as the temperature, humidity[16,17] and length of time over which evaporation is performed.[18] Therefore, synthesis conditions were systematically varied in his work to optimise the formation of ordered mesostructures.

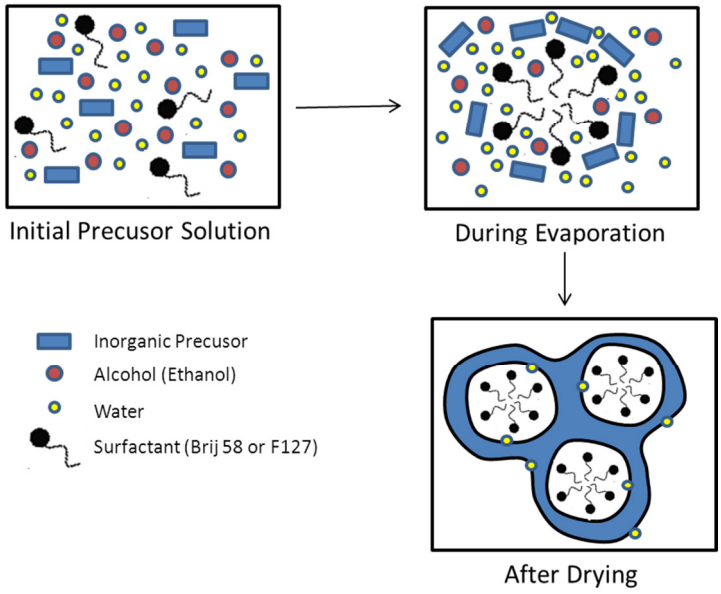

Figure 6.1: Schematic representation of Evaporation Induced Self-Assembly (EISA) process.

Although synthesis of ordered mesoporous titania thin films has been achievable for some time,[12,18,19] synthesis of ordered mesoporous titania powders in larger quantities via EISA remains challenging. The main reason for this challenge is structural collapse during thermal treatment to remove the templating polymer, which occurs due to growth of crystallites in the pore walls.[18] However, complete template removal is essential, particularly for photo-induced applications such as catalysis.[20] Thus, to prevent this collapse, additives such as ethylene diamine,[21] ammonia,[22] acetyl acetone[16,23] or sulphuric acid[24] have previously been used to stabilise the mesoporous titania structure before thermal treatment to remove the surfactant. However, such modifiers can adversely impact the performance of titania materials in their final application[25] and use of additives introduces complexity to the syntheses that in turn increases the time and cost of production. In addition, post-synthesis removal of these additives may require, for example, thermal treatment at substantially higher temperatures than are required to remove the template.[21]

Synthesis of a substantial quantity of thermally stable, ordered mesoporous titania powder without the use of stabilising additives has been achieved with only a limited number of structure directing agents; the triblock copolymers P123 ($EO_{20}PO_{70}EO_{20}$, where EO = ethylene oxide and PO = propylene oxide)[26,27] and F108 ($EO_{132}PO_{60}EO_{132}$)[27] or non-commercially available surfactants such as poly(ethyelene oxide)-block-polystyrene (PEO-*b*-PS) [19,23,28] and polyoxoethylene fluoroalkyl ether.[22] The time and cost advantages of utilising a less expensive, commercially available structure directing agent over one that must be synthesised, are compelling. Since the commercially available triblock copolymers P123 and F108 that have been used previously are structurally similar ($EO_xPO_yEO_x$), it was of interest to investigate EISA synthesis using a structurally different diblock copolymer Brij 58 ($C_{16}H_{33}EO_{20}$). A similar triblock copolymer with an EO/PO ratio intermediate between P123 and F108 was also investigated, namely F127 ($EO_{100}PO_{70}EO_{100}$). This study will therefore

allow investigation of the effects of varying both block type and length in block copolymer templates on the final materials produced, which is highly relevant when scaling the production for application.

In addition to investigating the effects of block type and length in the polymer templates, the effect of the composition and age of the precursor solution as well as the time and temperature at which EISA was performed were explored in this work. In particular, investigation of the formation of Ti structures in precursor solutions during ageing at room temperature prior to evaporation was of particular interest as it has not been previously explored. Variation of all the conditions of synthesis was observed to affect both the degree of order and the thermal stability of the resulting materials. Ordered mesoporous titania powders were synthesised under the conditions found to optimise the formation of order and thermal stability using Brij 58 or F127 templates. Following template removal, these materials were fully characterised via small angle x-ray scattering (SAXS), x-ray diffraction (XRD), transmission electron microscopy (TEM), CHN analysis and nitrogen porosimetry, to allow comparison of the different block copolymer templates.

Hierarchically porous, spherical titania beads are a morphology that is of interest due to their practical utility in applications such as sorption[5,9,29,30] and catalysis.[31] Large millimetre sized monodisperse spherical beads are desirable in particular for separations processes as they allow close packing in chromatographic columns with minimal clogging and high ease of handling.[5] Hierarchical porosity is also beneficial as the presence of macropores (>50 nm) and mesopores (2-50 nm) often improves mass transport properties and increases the number of readily available reaction sites.[9,32] More reaction sites are expected to lead to a higher level of functionalization and higher capacity for the element of interest to be sorbed.

Fabrication of porous beads using a sacrificial template, such as a cation-exchange resin[33] or polyacrylonitile (PAN) beads,[9] allows controlled introduction of macroporosity and an external spherical morphology. As such, different templates produce materials with different structures. These templates can then be removed via thermal or chemical means.[34] Spherical, millimetre sized PAN beads have been synthesised previously with a unique macroporous radial structure and imparted excellent kinetic properties to zirconium titanium oxide beads synthesised using these beads as a template.[9] Therefore, a PAN bead template was also used in this work. The PAN bead template was used to produce porous titania beads using similar precursor solution and evaporation conditions to those found to be optimal for preparation of ordered mesoporous titania powders. This provided radially macroporous millimetre sized spherical titania beads with ordered mesoporosity. These beads were also fully characterised.

6.1 Experimental Methods

Precursor solutions containing titanium tetrachloride ($TiCl_4$), ethanol (EtOH), block copolymer and water were prepared and aged statically at room temperature. These solutions

were then evaporated under conditions of controlled temperature and humidity either directly as a liquid in a petri dish to form bulk-phase powders, or after infiltration into polyacrylonitrile (PAN) beads to form hierarchically porous beads. After evaporation, the template was removed by thermal treatment as discussed in more detail in *section 6.5.2*.

6.1.1 Precursor Solution Preparation

Precursor solutions were prepared by addition of $TiCl_4$ to an ethanolic solution of block copolymer (Brij 58 or F127) in a glove box to exclude oxygen and water and allow efficient mixing of solutions prior to addition of water. After removal from the glove box, water was added in the appropriate ratios to produce a clear, colourless solution which was sealed in a pyrex Schott bottle. Dissolution of the surfactant could not be completed until after the addition of water. Precursor solutions of interest (Table 6.1) were designated PS-BXX for Brij 58 solutions or PS-FXX for F127 solutions, where XX was the molar ratio of surfactant in the precursor solution multiplied by 1000. The precursor solutions were aged statically in sealed vessels at room temperature to prevent changes in sol solvent composition. Also, overall volumes were monitored to ensure consistency.

Table 6.1: Precursor solution compositions

Solution Name	***Molar ratio***			
	$TiCl_4$	**EtOH**	**Surfactant**	**H_2O**
PS-B28	1	40	0.028 Brij 58	10
PS-B11	1	40	0.011 Brij 58	10
PS-F5	1	40	0.005 F127	10
PS-F10	1	40	0.010 F127	10

6.1.2 Polyacrylonitrile (PAN) Bead Preparation

Polyacrylonitrile (PAN) beads were generated using a 5 wt% PAN solution in dimethylsulfoxide (DMSO) and an automatic droplet generator at room temperature. To make the PAN solution, PAN (45 g) and DMSO (855 g) were mixed at 80 ^{o}C for 2 h then filtered through a 0.20 µm syringe filter. The automatic droplet generator was custom built with the capability to pass 500 mL of solution through the system in 3 min (Figure 6.2). A pyrex Schott bottle containing the PAN solution was placed in a CS-1560 Loctite pressure chamber, equipped with a pressure control knob. Pressure was generated from a HP-2.0, 2HDD air compressor. The PAN solution was passed into a specially designed polytetrafluoroethylene (PTFE) nozzle (Figure 6.3) with three needle outlets. The needle tips were 21 gauge and were broken so as to be 1-4 mm in length. A Trio CS-1560 oscilloscope was used to measure the vibrations from the nozzle. The vibrations increased the regularity of the droplets. Droplets fell into a large beaker containing approx. 4 L water and approx. 0.1 g Brij 58 to form solid beads and were stirred with an overhead paddle stirrer from Laboratory Supply P/L. The air compressor, the pressure chamber, and the nozzle were all connected with 13 mm Masterflex

tubing. The bead size was tailored by adjusting the pressure. At higher pressure a constant stream of liquid was generated from the needles in the nozzle which resulted in small approx. 0.5 mm diameter beads. At lower pressure droplets of liquid were generated from the needles in the nozzle which resulted in larger approx. 1 mm diameter beads. The beads were strained from the liquid then washed with distilled water until no surfactant foam was visible and the pH of the wash solution was that of distilled water, indicating that all of the Brij 58 had been removed.

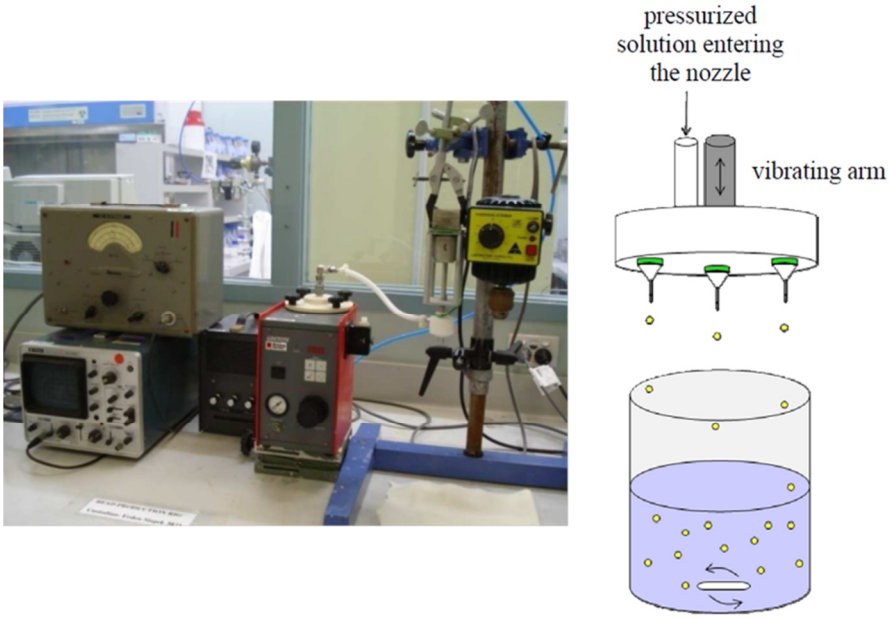

Figure 6.2: Photograph and schematic of custom made automatic droplet generator.[30]

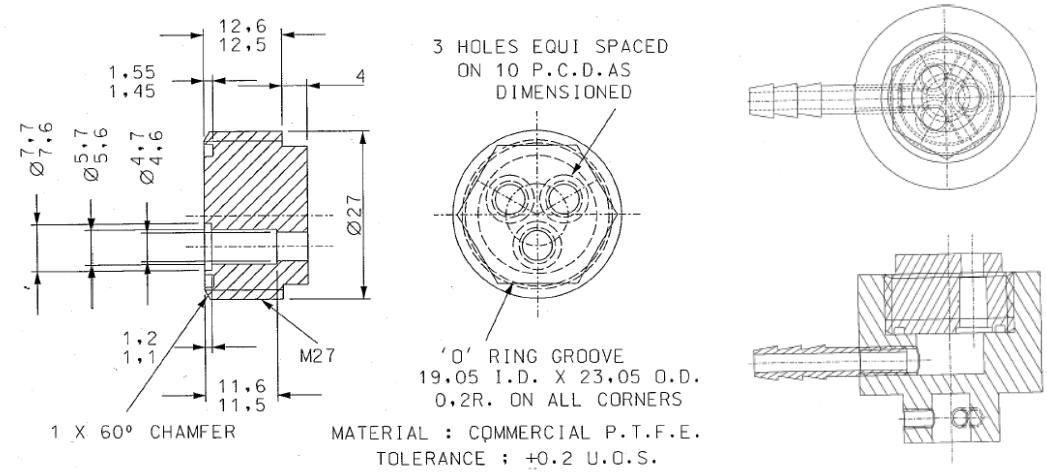

Figure 6.3: Schematic drawings of PTFE nozzle of automatic droplet generator.[30]

The PAN beads were placed in 160 mm petri dishes and underwent cross-linking in a custom made 16 L evaporation chamber with controlled flow, temperature (37 ^{o}C) and humidity (50 % relative humidity) for 3 days. The evaporation chamber was internally lined with low density polyethylene film to prevent contamination as well as adverse reactions

during evaporation. The evaporation chamber was also externally insulated using nitrile butadiene rubber/polyvinyl chloride foam. The temperature in the evaporation chamber was controlled by flowing water through the walls of the chamber on a closed loop and a Polyscience temperature control unit was used to set the temperature. The relative humidity (RH) and flow of air through the chamber were controlled using an IQI Instruquest HumiSys HF (High Flow) Relative Humidity Generator with a Watlow temperature control unit. The beads were then dried in air for a further 24 h.

6.1.3 Precursor Solution Infiltration into PAN Beads

Titania precursor solutions were prepared and aged statically at room temperature as described in *section 6.1.1*. The PAN beads were dried under vacuum for 3 h before addition of titania precursor solutions at a volume to mass ratio of 50. The PAN bead/precursor solution mixture was then degassed in a 3510E-DTH Bransonic Ultrasonic Cleaner at room temperature for 10 min and left to infiltrate for 24 h. Infiltration was evident when the PAN beads sank to the bottom of the precursor solution. After infiltration, the PAN beads were strained from the precursor solution and placed in 160 mm petri dishes lined with Whatman 42 filter paper to absorb any excess liquid.

6.1.4 Evaporation

To make bulk-phase titania powders, 4.0 mL volumes (unless specified otherwise) of precursor solution were syringed into 80 mm petri dishes and placed in the custom evaporation chamber previously described (*section 6.1.2*). To make titania beads, 160 mm diameter petri dishes containing PAN beads infiltrated with precursor solution were placed in the custom evaporation chamber immediately following straining. Both solutions and beads underwent EISA under the controlled temperature and humidity conditions of the evaporation chamber. Temperature and RH were measured periodically during evaporation using a calibrated Rotronic HygroPalm humidity probe.

After template removal, approx. 150 mg mesoporous titania powder was typically produced. It would be possible to obtain approx. 3 g of sample if the entire surface area of the evaporation chamber (900 cm^2) were utilised instead of 80 mm diameter petri dishes. The system chosen consisted of standard process engineering methodologies which enable up-scaling to produce larger material quantities. A summary of all the conditions tested for synthesis of bulk-phase titania powders is given in Table 6.2 for Brij 58 and in Table 6.3 for F127.

Table 6.2: Summary of experiments performed with Brij 58 template. All samples were prepared using 4mL volumes and evaporated at approx. 65% RH. Colours represent precursor solution composition $TiCl_4$: EtOH : Brij 58 : H_2O where red = 1:40:0.028:10, blue = 1:40:0.055:20, pink = 1:40:0.055:10, green = 1:40:0.011:10, orange = 1:40:0.028:20. Numbers in the table are the number of days each sample was evaporated.

Evaporation Temp	***Precursor solution age (days)***									
	1	**2**	**3**	**4**	**5**	**6**	**7**	**14**	**21**	**28**
25-27 °C			3 4 7			4 7 14 17 21 3 7 14	1 3 14	7 14 21		
28-30 °C	3 3 1 3 3	1	1 3	1 2 1 2 2	1 1	1 8 14 1 1 8 8	5 7 14 7 1	3 7 14 7 7	7 6 7	
37-39 °C						7 14				7

Table 6.3: Summary of experiments performed with F127 template. All samples were prepared using 4mL volumes and evaporated at approx. 50% RH. Colours represent precursor solution compositions $TiCl_4$: EtOH : F127 : H_2O where red = 1:40:0.005:10, blue = 1:40:0.01:20. Numbers in the table are the number of days each sample was evaporated.

Evaporation Temp	***Precursor solution age (days)***	
	2	**6**
26 °C (65 % RH)		14
32-35 °C		4 14
37-40 °C	18	7 14 7 14

6.2 Effect of Precursor Solution on Ordered, Mesoporous Titania Powder

6.2.1 Effect of Precursor Solution Composition

To determine the optimal precursor solution composition, mesoporous titania materials were synthesised using $TiCl_4$, EtOH, Brij 58 and water, with molar ratio 1:40:x:y, varying the amounts of Brij 58 and water. The results of SAXS measurements on the resulting materials are given in Figure 6.4. The SAXS patterns of all the as-made samples (samples after EISA but prior to template removal) contained correlation peaks, indicating the presence of mesoporous order in the samples. The d-spacings of the peaks indicated a 63-69 Å repeating unit size. As such, the d-spacing did not vary substantially for the different precursor compositions. The widths (FWHM = full width at half maximum) and relative intensities (number of counts at peak position divided by background counts at that position) of the peaks in the SAXS patterns provide an indication of the degree of order in the samples. Narrower, more intense peaks indicate a greater degree of ordering. As such, it is clear that the sample with composition 1 $TiCl_4$: 40 EtOH : 0.028 Brij 58 : 10 H_2O (designated PS-B28) was the most ordered.

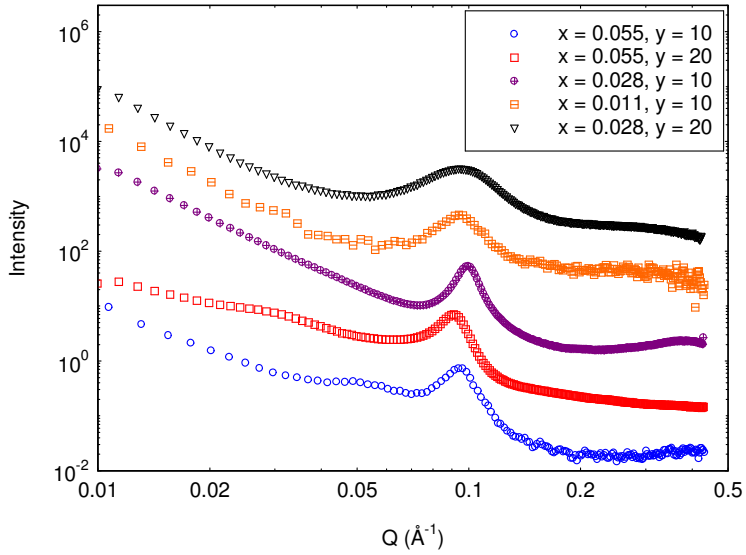

Figure 6.4: SAXS patterns of samples prepared using 4 mL volumes of 1 $TiCl_4$: 40 EtOH : x Brij 58 : y H_2O precursor solutions aged for 6 days then evaporated at 30 ^oC and approx. 65 % RH.

Decreasing the concentration of EtOH from the most ordered composition to give 1 $TiCl_4$: 37 EtOH : 0.028 Brij 58 : 10 H_2O was also investigated. However, samples prepared with this composition or with PS-B28 using 4 mL volumes of precursor solutions aged for 6 days then evaporated at 37 ^oC and approx. 65 % RH for 14 days had a similar degree of order (FWHM 0.01 and relative intensity 2). Hence, decreasing the molar ratio of EtOH in the precursor solution composition had little impact on the degree of order in the samples and

was not continued. The effect of increasing the proportion of Ti relative to Brij 58 and water to give composition 1 $TiCl_4$: 40 EtOH : 0.02 Brij 58 : 7 H_2O was also investigated as it was postulated this may produce mesoporous titania with thicker walls that would be more thermally stable.[35] Samples prepared with this composition and PS-B28 using 4 mL volumes of precursor solutions aged for 6 days then evaporated at 27 ^oC and approx. 65 % RH for 17 days again had a similar degree of order (FWHM 0.01 and relative intensity 3). However, after thermal treatment at 200 ^oC for 2 h the sample prepared using PS-B28 was more intense (relative intensity 4 versus 2). Hence, increasing the proportion of Ti relative to Brij 58 and water in the precursor solution composition actually had a somewhat detrimental effect on the thermal stability of the resulting materials.

Synthesis of bulk phase mesoporous titania with F127 template was performed using precursor solution compositions 1 $TiCl_4$: 40 EtOH : 0.005 F127 : 10 H_2O (PS-F5) or 1 $TiCl_4$: 40 EtOH : 0.01 F127 : 10 H_2O (PS-F10) as these compositions have been previously shown to produce ordered, thermally stable mesoporous titania-zirconia materials with F127.[36,37] The SAXS parameters of the resulting materials are shown in Table 6.4. PS-F10 produced a sample with similar d-spacing and width but higher relative intensity than PS-F5, indicating a higher degree of order. The sample produced using PS-F10 also demonstrated higher thermal stability and was able to maintain ordered mesoporosity after thermal treatment to 350 ^oC.

Table 6.4: d-spacings, widths and relative intensities of peaks in SAXS patterns of samples prepared using 4 mL volumes of precursor solution aged for 6 days and evaporated at 37 ^oC and approx. 50% RH for 14 days.

Precursor Solution	**100^oC**			**350^oC**		
	d-spacing (nm)	**FWHM**	**I_{rel}**	**d-spacing (nm)**	**FWHM**	**I_{rel}**
PS-F5	132 ± 10	0.01	9	part collapse, 102 ± 10	0.01	3
PS-F10	146 ± 10	0.01	10	102 ± 10	0.01	7

6.2.2 Precursor Solution Ageing

In this study, ageing of precursor solutions containing $TiCl_4$, EtOH, Brij 58 or F127 and water in a sealed vessel between 1 and 36 days was investigated. Small angle x-ray scattering was used to directly observe the formation of nanosized objects in these solutions over time, as well as to determine the degree of ordering in bulk mesoporous titania synthesised via EISA using precursor solutions of different ages.

6.2.2.1 PS-B28

Initially, the ageing of the optimal precursor solution composition, PS-B28, was investigated by SAXS and the results are shown in Figure 6.5. The scattering pattern from the Brij 58 polymer, in the absence of the titanium precursor, was measured in a solution of 4:1 EtOH:water with a Brij 58 concentration of approx. 1.5 %. Using the Guinier approximation, a

radius of gyration (R_g) of 8.9 ± 0.9 Å was calculated for the solvated Brij 58 scatterers in this solution. The Guinier plot is shown in Figure 6.6. A Debye model was also used to fit the Brij 58 block copolymer solution scattering data and resulted in R_g = 10.5 ± 0.5 Å and scale = 0.016 ± 0.0004, with the goodness of fit parameter χ^2/Npts = 0.6 (Npts = number of points in the experimental data) indicating a good fit to the experimental data. The R_g values from the Guinier analysis and Debye model were hence consistent and showed that the Brij 58 had a polymeric structure with R_g ~10 Å when in solution with 4:1 EtOH:water.

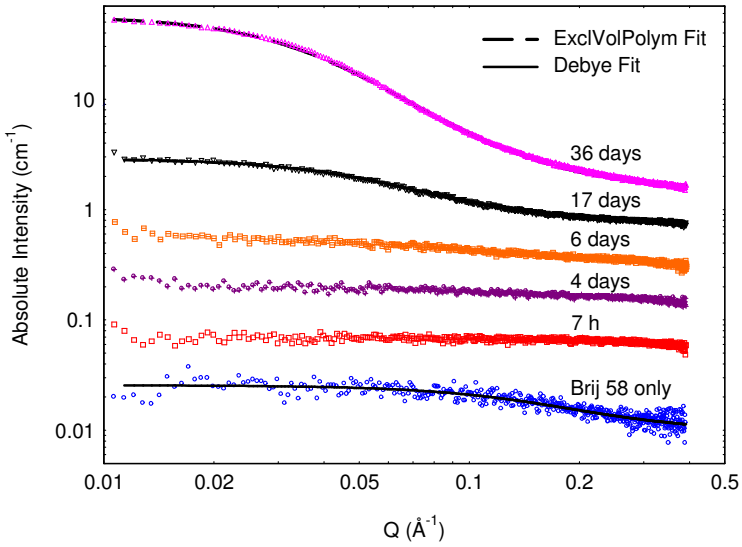

Figure 6.5: SAXS patterns of PS-B28 aged between 7 h and 36 days. Data is on an absolute scale but traces have been offset for clarity.

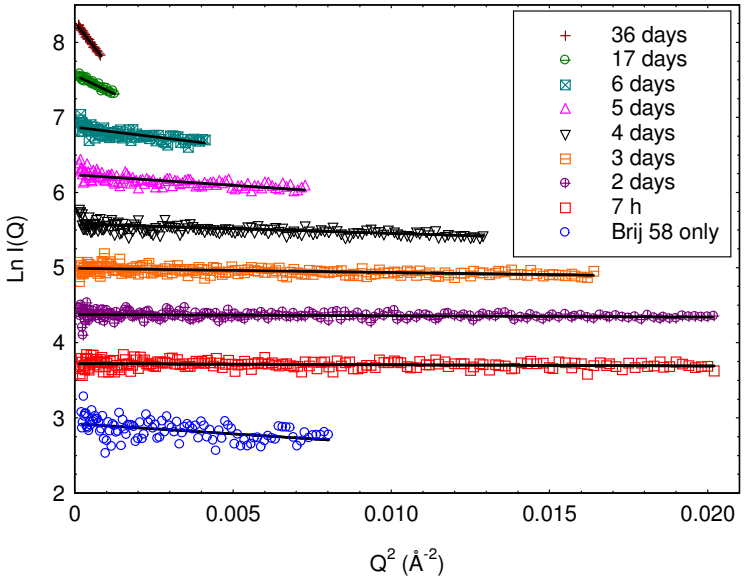

Figure 6.6: Linear Guinier plots of PS-B28 aged between 7 h and 36 days.

Figure 6.5 also displays the scattering profiles of PS-B28 aged between 7 h and 36 days in a sealed vessel. The scattering was dominated by the structure of the Ti-complexes in

solution because Ti has a much higher atomic number than the C, H and O in the Brij 58. The SAXS data of PS-B28 aged between 7 h and 6 days had a Q^{-x} dependence where x = 0.01 – 0.4. Therefore only Guinier analysis[38] was performed and the results in Table 6.5 indicate that PS-B28 contained Ti based structures that slowly increased in size over 6 days of ageing. Guinier plots are shown in Figure 6.6. Viscosity measurements of PS-B28 immediately after preparation and 6 days after preparation showed that the viscosity of the aged sol was unchanged at 4.2 ± 0.4 cP.

Table 6.5: Growth of Ti structures in precursor solutions over time. nd = not determined.

Age (days)	PS-B28 R_g (Å)	PS-B11 R_g (Å)
0.3	2.5 ± 0.3	1.5 ± 0.3
2	2.4 ± 0.3	1.5 ± 0.4
3	4.1 ± 0.3	2.4 ± 0.3
4	5.8 ± 0.3	2.8 ± 0.3
5	8.6 ± 0.4	nd
6	11.8 ± 0.6	3.8 ± 0.2
17	25-30	15.9 ± 0.5
36	41-47	35-45

When PS-B28 had been aged for 17 days, more intense scattering at low Q was observed (Figure 6.5). Guinier analysis indicated that the R_g had increased to 25.0 ± 0.8 Å. Beyond the Guinier region, the scattering decreased with a $Q^{-1.5}$ dependence, suggesting scattering behaviour intermediate between a rod and a Gaussian chain. A Debye model was used to fit the data and provided a good fit (χ^2/Npts = 1.1), indicating that the scatterers were polymeric rather than rod-like in nature. The R_g from the Debye fit of 29.6 ± 0.2 Å was similar to that calculated via Guinier analysis.

The SAXS data of PS-B28 aged for 36 days in a sealed vessel showed a substantial change in shape and increase in scattering intensity relative to the solutions aged for shorter periods of time (Figure 6.5). At low Q the scattering curve had a weak dependence on Q so a Guinier analysis was performed and indicated that R_g had again increased, to 41.4 ± 0.3 Å. A $Q^{-2.1}$ dependence was observed in the mid-high Q range for this scattering data, indicating the presence of polymeric structures in solution. However, the Debye model did not provide a good fit to the scattering data (χ^2/Npts = 13). This indicated that the polymer chains in solution did not display Gaussian statistics (that is, were not fully flexible). Therefore, a model for polymers with excluded volume was applied, as this model is able to fit SAXS data in which the power law exponent ranges from -1.6 to -3.[39,40] The excluded volume polymer fit provided a good fit to the scattering data (χ^2/Npts = 2.8) with an R_g value of 47.3 ± 0.1, consistent with that determined via Guinier analysis, and a power law of -2.4 ± 0.01. The fitted power law of -2.4 (greater than 2.0) suggested the presence of more mass inside the R_g of the polymeric structure than in a Gaussian chain. This increased density of the polymer may be due to

branching or closer packing of the polymer chains due to the initiation of self-assembly. The pair distance distribution function P(r)[41] was also calculated for this system and provided evidence that the scattering structures had an elongated shape, with R_g = 43 Å and the maximum dimension of the structure, D_{max} = 160 Å (Figure 6.7). Ab initio shape determination using simulated annealing with the software package DAMMIN[42] was not able to provide a converged solution due to the polymeric nature of the structure. However, an elongated structure was consistently produced, which supported the result of the inverse fourier transform in Figure 6.7.

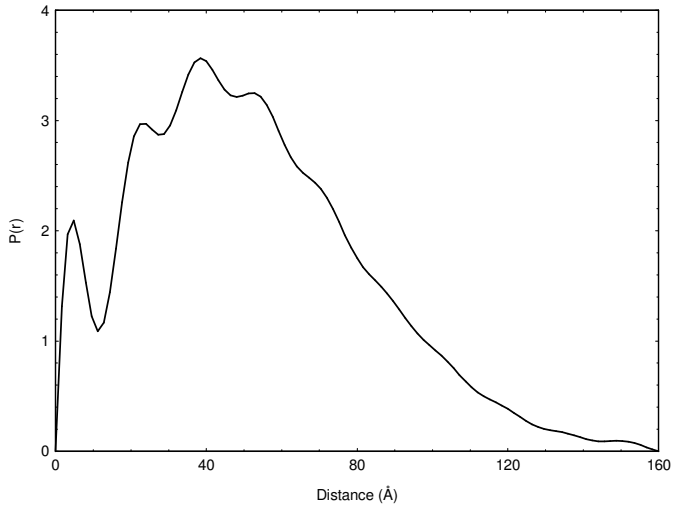

Figure 6.7: Pair distance distribution function for PS-B28 aged for 36 days.

To determine the effect of the observed changes in the precursor solutions with age on the structure of the mesoporous titania produced from these solutions, SAXS measurements were performed on as-made samples synthesised using PS-B28 that had been aged between 3 and 14 days in a sealed vessel. The results are given in Figure 6.8. It is clear from this data that between 3 and 6 days longer ageing times produced samples with a higher degree of order. Increasing the evaporation time from 1 to 7 days for 6 day aged PS-B28 caused a decrease in order as evidenced by the broadening of the correlation peak. Comparison of the SAXS data for the samples evaporated for 7 days shows that a substantially less intense peak and hence less order was present after ageing PS-B28 for 14 days rather than 6 days.

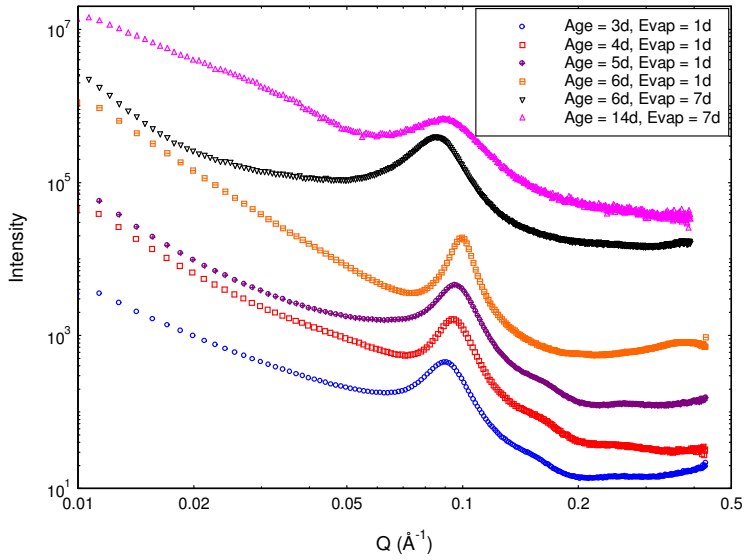

Figure 6.8: SAXS patterns of as-made samples prepared using 4 mL volumes of PS-B28 evaporated at 29 °C and approx. 65 % RH.

6.2.2.2 PS-B11

To investigate how the ageing of precursor solutions was affected by composition, specifically the amount of surfactant present, SAXS data of a precursor solution containing a lower concentration of Brij 58 (1 $TiCl_4$: 40 EtOH : 0.011 Brij 58 : 10 H_2O, designated as PS-B11) was collected over time (Figure 6.9). The SAXS data of the Brij 58 polymer in the absence of Ti is also shown in Figure 6.9, again in a solution of 4:1 EtOH:water and in this case with a concentration of approx. 0.5 %. Using the Guinier approximation, an R_g of 11.6 ± 0.9 Å was calculated for the solvated Brij 58 scatterers in this solution. The Guinier plot is shown in Figure 6.10. A Debye model was applied and provided a good fit to the experimental data (χ^2/Npts = 0.8) with R_g = 11.7 ± 1.1 Å and scale = 0.008 ± 0.0004. Thus, the R_g values from the Guinier analysis and Debye model were consistent and suggested that the Brij 58 had a polymeric structure with R_g ~12 Å when in solution with 4:1 EtOH:water. The size of these Brij 58 polymeric scatterers was within error of those in the higher concentration Brij 58 solution PS-B28 described in *section 6.2.2.1*.

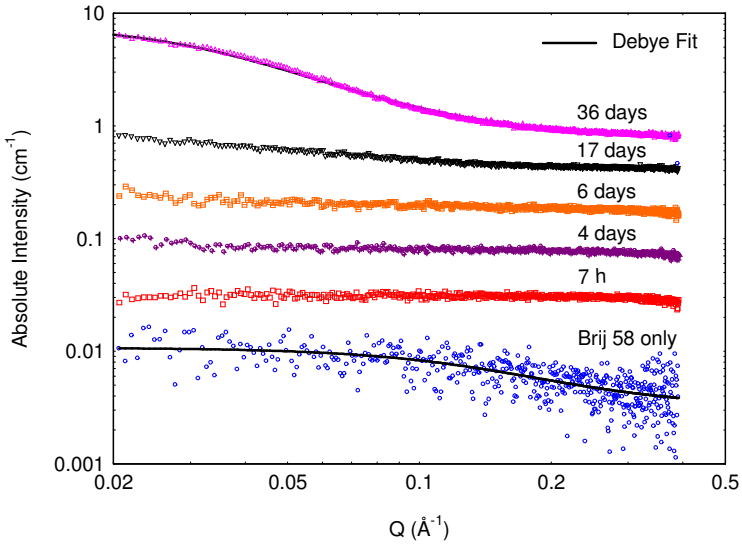

Figure 6.9: SAXS patterns of PS-B11 aged between 7 h and 36 days. Data is on an absolute scale but traces have been offset for clarity.

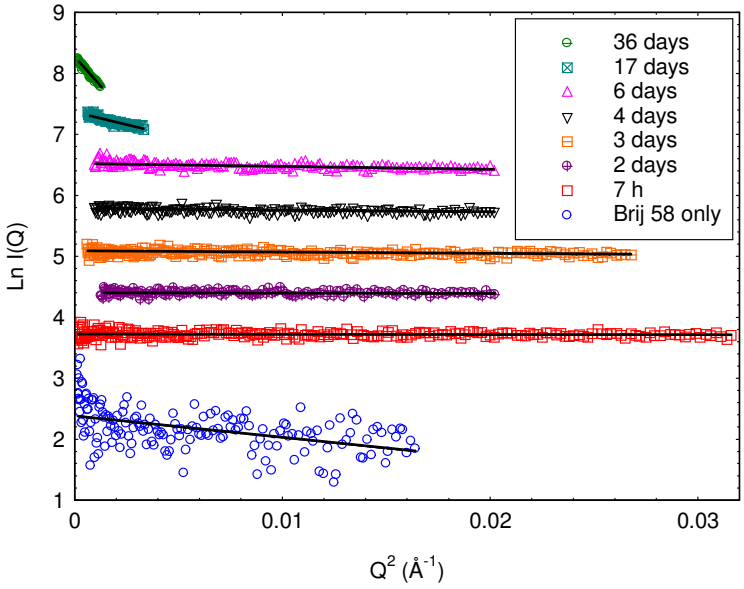

Figure 6.10: Linear Guinier plots of PS-B11 aged between 7 h and 36 days

The SAXS data in Figure 6.9 for PS-B11 aged between 7 h and 6 days in a sealed vessel had a Q^{-x} dependence where x = 0.03 – 0.2, as was seen previously for PS-B28. The R_g values from Guinier analysis of SAXS data for these samples are given in Table 6.5 and indicate the presence of Ti based structures that grew over time. The Guinier plots are shown in Figure 6.10. The intensity of scattering from PS-B11 aged for 17 days was only slightly increased relative to the 'younger' solutions. Guinier analysis of this solution indicated an R_g of 15.9 ± 0.5 Á and the scattering curve exhibited a $Q^{-1.0}$ dependence in the mid-high Q range, suggesting rod-like scattering structures. This R_g indicated further growth of the scattering

structures with increased age, as seen for PS-B28. However, the weakness of the scattering intensity for this sample prevented the possibility of further fitting.

The SAXS data of PS-B11 aged for 36 days in a sealed vessel showed a more substantial increase in scattering intensity relative to the solutions aged for shorter periods of time (Figure 6.9). At low Q the scattering curve had a weak dependence on Q so a Guinier analysis was performed and indicated that R_g was equal to 34.5 ± 0.4 Å. In the mid-high Q range the data showed a $Q^{-2.0}$ dependence, indicating scattering from polymeric structures. Therefore the Debye model was applied and provided a good fit to the experimental data (χ^2/Npts = 2.0) with R_g = 45.1 ± 0.2 and scale = 841 ± 4. This R_g was similar to that determined via Guinier analysis.

6.2.2.3 PS-F10

To determine the effect of ageing on F127 precursor solutions, SAXS patterns of PS-F10 in a sealed vessel were measured over time and the results are shown in Figure 6.11. The SAXS pattern on the left in Figure 6.11 shows the scattering profile of the solution without the Ti precursor added and gives an indication of the scattering from the F127 polymer itself. Strong scattering was evident from the solution of F127 in 4:1 EtOH:water. Using the Guinier approximation, a R_g of 19.1 ± 0.3 Á was determined for the F127 structures in this solution. The Guinier plot is shown in Figure 6.12. Beyond the Guinier region the scattering decreased with a $Q^{-2.0}$ dependence, indicative of polymeric scattering. Therefore the Debye model was applied and provided a good fit to the experimental data (χ^2/Npts = 3.2) with R_g = 21.3 ± 0.1 Á, consistent with the Guinier analysis, and scale = 269 ± 1. The indirect fourier transform of the SAXS data gave a R_g of 20 Á and D_{max} of 70 (Figure 6.13), suggesting that the scattering structures were somewhat elongated.

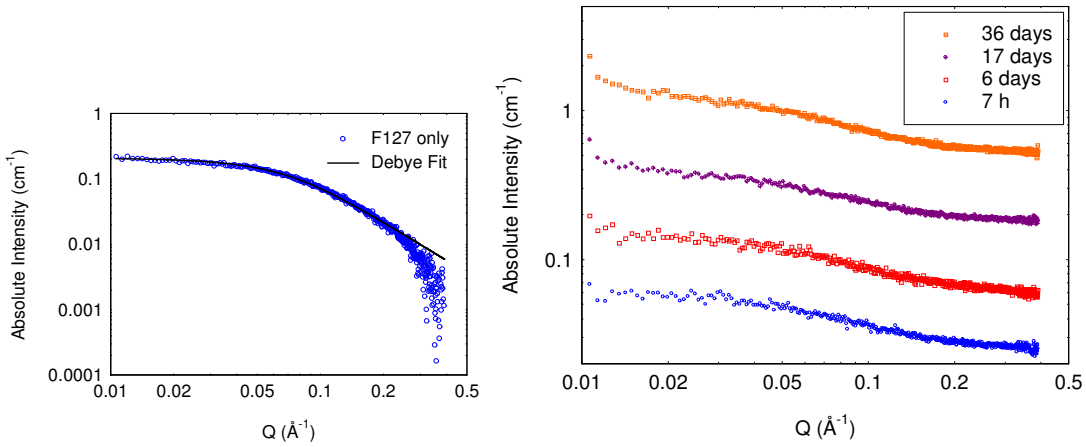

Figure 6.11: SAXS patterns of F127 in 4:1 ethanol:water before Ti addition (left) and PS-F10 aged between 7 h and 36 days (right). Data is on an absolute scale but traces have been offset for clarity.

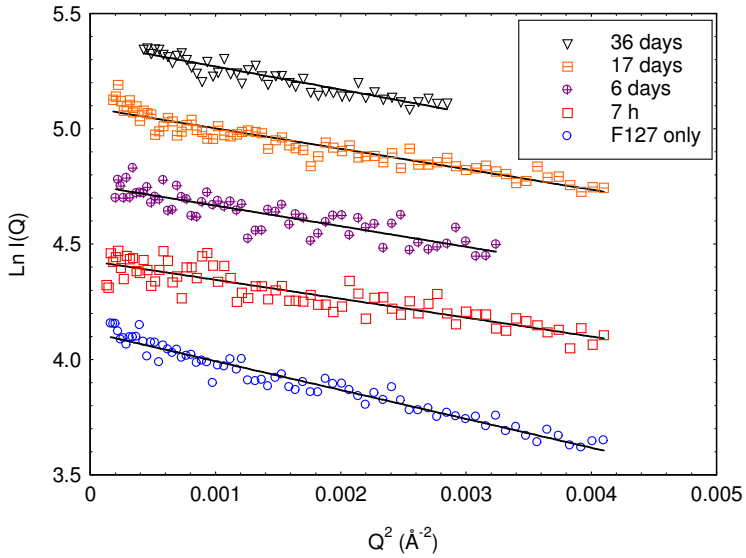

Figure 6.12: Linear Guinier plots of PS-F10 aged between 7 h and 36 days

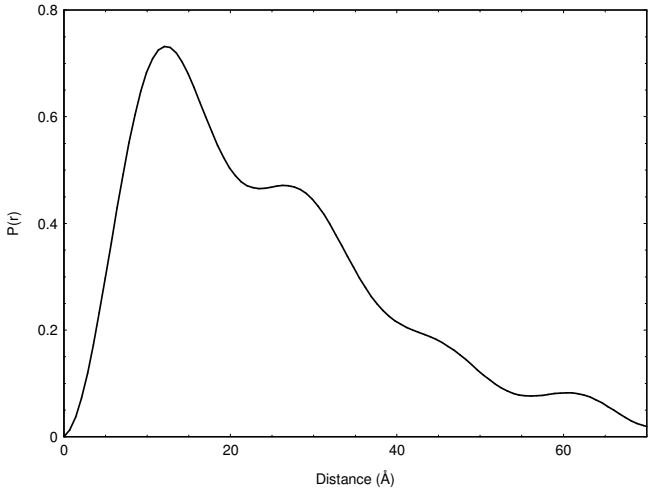

Figure 6.13: Pair distance distribution function for block copolymer F127 in 4:1 ethanol:water.

The SAXS data for PS-F10 aged from 7 hours to 36 days in a sealed vessel is also shown in Figure 6.11. These data show that addition of $TiCl_4$ to the precursor solution dramatically decreased the intensity of scattering, indicating disruption of the F127 structures previously described. As PS-F10 was aged over 36 days, its SAXS pattern remained relatively unchanged. The scattering decreased with a Q^{-x} dependence where x = 1.0-1.3 in the mid-high Q region independent of the solution age, which suggests that the scattering objects were consistently elongated or rod-like in shape. Guinier analysis also indicated that the R_g was similar at 7 h (15.8 ± 0.5 Å) and 36 days (17.1 ± 0.5 Å). Guinier plots are shown in Figure 6.12. The main observable difference in the data with age was an increase in the intensity of scattering between 6 and 17 days, suggesting an increase in the number of scattering objects present in solution between these ageing times. Viscosity measurements of PS-F10 immediately after preparation and 6 days after preparation showed that the viscosity increased a small amount from 7.6 ± 0.4 to 9.5 ± 0.4 cP upon ageing.

In order to determine the effect of precursor solution ageing on the degree of order in mesoporous titania produced by EISA of PS-F10, samples were prepared using PS-F10 aged for 2 or 6 days. The evaporation conditions were the same for both samples, specifically 14-18 days at 37 °C and approx. 50 % RH. After thermal treatment at 300 °C for 3 h, the SAXS data of both samples showed a correlation peak with FWHM 0.01 and relative intensity 7. Therefore increasing the ageing time of PS-F10 from 2 to 6 days had minimal effect on the order or thermal stability of the mesoporous titania produced by EISA of PS-F10.

6.2.3 Summary of Precursor Solution Effects

In terms of precursor composition, PS-B28 and PS-F10 produced the most ordered mesoporous titania using Brij 58 and F127, respectively. Therefore, these compositions were considered optimal and were used in further experiments to determine the evaporation conditions required to maximise the degree of order produced.

In regards to precursor solution ageing, it has been previously shown that the ordering of mesoporous titania films produced via EISA can depend on the age of the precursor solution used for spin-coating of the films.[43] Acidic precursor solutions containing inorganic Ti precursors, EtOH and block copolymers aged for 48 h at 40 °C produced less ordered films than similar precursor solutions aged 3-24 h. This was attributed to the formation of anatase nanocrystallites in the precursor solutions that grew upon ageing until they were too large to fit within the walls of the mesostructure formed during EISA. However, the ageing of similar precursor solutions at room temperature has not been investigated and is unlikely to produce crystalline material since mesoporous titania synthesised via EISA is typically amorphous prior to thermal treatment.[12,18,44] In addition, the structures formed in the precursor solutions in the present study were polymeric, whereas nanocrystals would appear as three dimensional particles when measured by SAXS.[45,46] Therefore the structures formed during precursor solution ageing at room temperature are different to those formed at 40 °C and it was of interest to determine whether ageing at room temperature would similarly affect mesostructural order.

The results of precursor solution ageing were very different for the Brij 58 and F127 systems. For the Brij 58 system, precursor solution age did affect the degree of order in mesoporous titania produced via EISA. For both PS-B11 and PS-B28, scattering structures were present that grew in size over time. However, the scattering structures in PS-B11 were consistently smaller than in PS-B28. Also, the intensity of scattering was substantially lower for PS-B11 aged for 17 and 36 days, which suggests the scattering structures were less numerous in the less concentrated Brij 58 solutions. Further, while PS-B28 contained branched or close packed polymers after ageing for 36 days, the scattering structures in PS-B11 could still be satisfactorily fit with a Debye model, indicating flexible polymer chains. These differences between PS-B11 and PS-B28 indicate that the template Brij 58 interacted with the Ti based scattering structures formed in the precursor solution, since its' concentration affected the growth of the Ti structures.

It has previously been shown that Ti oxo oligomers exist in sols containing Ti alkoxide, alcohol and aqueous acid and that they consist of R_g 20-25 Å subunits which co-condense to varying degrees depending on the water and acid content of the sol.[47] Small oligomers of mean composition $Ti(OX)_x(OH)_yO_{2-(x+y)/2}$ (X = ethyl, *iso*-propyl, *n*-butyl) which condensed into larger species over time were postulated. Changing the Ti precursor was observed to have a large impact on the composition of the oligomers formed in solution, but there was no data provided for sols containing the $TiCl_4$ precursor (used in this work). However, it is likely that similar Ti oxo oligomers are formed by hydrolysis of $TiCl_4$ in the present solutions. For PS-B28, smaller Ti oxo oligomer subunits of approx. 2 Å were initially formed, which increased in size up to approx. 45 Å over 36 days (Table 6.5). The inhibited growth of these Ti oxo oligomeric structures may be attributed to the greater acidity of a precursor solution utilising $TiCl_4$ rather than a Ti alkoxide as the inorganic precursor, since HCl rather than alcohol was produced during hydrolysis. For PS-B28, approx. 14 days of ageing was required to build Ti oxo oligomers ~25 Å in size whereas use of a Ti alkoxide precursor led to immediate formation of clusters of this size.

The previously postulated 'modulation of the hybrid interface' (MHI) mechanism, for hydrolysis and condensation of Ti precursors and PEO based templates,[13] can explain the necessity of Ti oxo oligomers in the precursor solution to achieve ordered mesoporous structures. According to the MHI mechanism the presence of excess acidic water (relative to Ti) is necessary to achieve ordered mesoporosity, as hydrophilic Ti oxo oligomers form in solution under these conditions which interact weakly (via H-bonding) with the polymer template. Evidence of interaction between the Brij 58 template and the Ti oxo oligomers has in fact been observed in the present system. This interaction allows folding and self-assembly of the template to occur during evaporation and the Ti oxo oligomers can then co-condense around these self-assembled template structures to form the ordered mesoporous titania network. Without the presence of excess water, the Ti does not form oxo oligomers. This makes the Ti more hydrophobic so it interacts more strongly with the template, causing it to unfold and leading to worm-like mesophases.[13]

The present work is consistent with the postulated MHI mechanism. The most ordered mesoporous titania materials were produced when PS-B28 was aged for 6 days. This suggests that it was beneficial to the ordering of the final material for scattering structures with a R_g of approx. 12 Å to be present before commencing evaporation. Scattering structures smaller than 9 Å or larger than 25 Å appeared to be detrimental to the formation of ordered mesoporous titania. This suggests that the presence of Ti oxo oligomers with R_g of approx. 12 Å, which can be formed by ageing the precursor solution for 6 days, are of the ideal hydrophilicity to interact appropriately with Brij 58 and encourage the formation of ordered mesoporous structures. However, there was no change in the viscosity of PS-28 after ageing for 6 days, which indicates that the formation of these small Ti oxo oligomers was not detectable via viscosity. Thus, SAXS can provide details of structural changes occurring in the sols before they become evident macroscopically.

For the F127 system, elongated Ti structures, most likely Ti oxo oligomers, appeared to form almost immediately upon preparation of PS-F10 and underwent minimal growth during 36 days of ageing. Therefore precursor solution ageing is unlikely to be a critical synthesis parameter when using F127 as a template and indeed little impact was observed upon the order of stability of materials synthesised by varying PS-F10 ageing from 2 to 6 days. A small increase in viscosity of 1-2 cP was observed in PS-F10 upon ageing for 6 days despite the SAXS data showing no change. This small increase is still well below the appreciable change in viscosity which would be required to indicate hydrolysis and gelation of a sol.[5]

The ageing behaviour of PS-F10 was very different to that of the Brij 58 solutions, which provides strong evidence of the interaction between the template and Ti in the precursor solution, since the choice of template affected the growth and structure of Ti oxo oligomers in solution. F127 appeared to interact more strongly with the Ti in the precursor solutions than Brij 58 as it quickly formed a stable structure with R_g ~16 Å whereas Brij 58 required 6 days to form comparably sized structures of R_g ~12 Å. This stronger interaction with F127 may be hypothesised to be due to its larger hydrophilic PEO blocks (EO_{100} versus EO_{20} for Brij 58) which have been previously shown to be the part of the F127 molecule that interacts with hydrophilic titania.[48] The molar ratio of Ti : EO was approx. 3:2 in PS-B28 and 1:2 in PS-F10, so the excess of Ti in the Brij 58 solution may have allowed for formation of non-associated titania structures. Further work would be required to test this hypothesis, but if true, ageing precursor solutions containing P123, which also has small EO_{20} blocks, may also improve the degree of order in mesoporous materials produced.

Before addition of $TiCl_4$, 0.5 % or 1.5 % Brij 58 in 4:1 EtOH:water solution formed polymeric structures with R_g ~10 Å. The main difference between these solutions was that the scale of the Debye fit was lower for the less concentrated solution, indicating there were fewer Brij 58 structures present. The measured R_g of ~10 Å was substantially smaller than the R_g of 30 Á reported previously for micelles present in a water solution of similar Brij 58 concentration[49] and suggests incomplete micelle formation due to the presence of ethanol. Similar phenomena upon addition of ethanol have been observed previously for the block copolymers Brij 35[50] and P123.[51]

The F127 solution before $TiCl_4$ addition consisted of approx. 8% F127, 83% ethanol and 9 % water. Therefore, no self-assembled structures were expected to form since it has been previously shown that in solutions that contain greater than 40% v/v ethanol, F127 does not form micelles.[52] However, elongated polymeric scattering structures of R_g ~20 Å were observed. As might be expected from its higher molecular weight, these F127 structures were approx. double the size of the Brij 58 micelles (R_g ~10 Á). The elongated structure suggested from the P(r) function would be consistent with solvated PEO chains extending away from a dense poly(propylene oxide) (PPO) agglomerate. The disruption of these F127 structures upon addition of $TiCl_4$ is evidence for the strong interaction between F127 and the Ti oxo structures formed. This interaction has been demonstrated previously in ordered mesoporous

thin films synthesised via EISA using F127, where the hydrophilic PEO blocks of the polymer template penetrate into the titania framework.[48]

6.3 Evaporation Conditions for Synthesis of Ordered, Mesoporous Titania Powder

Previous work has shown that the optimal RH for mesoporous titania synthesis via EISA using Brij 58 as a template was 65 %[24] and using F127 as a template was 50 %.[37] Therefore, this parameter was not varied in this work.

6.3.1 Temperature

For the Brij 58 system, PS-B28 aged 6 days was evaporated at a temperature between 25 and 37 °C for 14 days. Relative humidity was maintained as 65 % at each temperature so the absolute humidity was varied. The resulting SAXS parameters of as-made samples are shown in Table 6.6 and indicate that samples evaporated at 29 °C were more ordered than those evaporated at higher or lower temperatures.

Table 6.6: d-spacings, widths and relative intensities of peaks in SAXS patterns of samples prepared using 4 mL volumes of PS-B28 aged for 6 days and evaporated at approx. 65% RH for 14 days.

Evaporation Temp (°C)	As-made		
	d-spacing (Å)	FWHM	I_{rel}
37	68 ± 10	0.01	2
29	68 ± 10	0.01	6
25	74 ± 10	0.01	4

For the F127 system, PS-F5 aged 6 days was evaporated for 14 days at a temperature of 32 or 37 °C with a relative humidity of 50 %. It was also of interest to isolate the effect of temperature from that of humidity by preparing a sample in an environment with the same absolute humidity to 32 °C and 50 % RH but at lower temperature, namely 26 °C and 65 % RH. The resulting SAXS parameters of samples are shown in Table 6.7. Since the absolute humidity difference between samples evaporated at 65 % RH at 26 °C or 46 % RH at 32 °C, was insignificant, the increased thermal stability of the sample evaporated at 50 % RH and 32 °C must be attributed to its higher temperature of evaporation. Increasing the evaporation temperature from 32 to 37 °C while maintaining 50 % RH created an environment with a higher amount of water present. This produced as-made samples with a similar degree of order but enhanced thermal stability (Table 6.7).

Table 6.7: d-spacings, widths and relative intensities of peaks in SAXS patterns of samples prepared using 4 mL volumes of PS-F5 aged for 6 days and evaporated for 14 days.

Evaporation Temp (°C)	Relative Humidity (%)	300°C		
		d-spacing (Å)	FWHM	I_{rel}
26	65	collapsed		
32	50	Part collapse, 105 ± 10	0.01	4
37	50	104 ± 10	0.01	11

6.3.2 Evaporation Time

Mesoporous titania templated with Brij 58 were synthesised with evaporation times between 1 and 21 days and all as-made samples showed ordered mesoporosity, as indicated by correlation peaks in their SAXS patterns. To determine the effect of increasing the evaporation time, mesoporous titania samples were prepared using PS-B28 with evaporation at 29 and 37 °C for 7 versus 14 days. The results of SAXS measurements on these samples are shown in Table 6.8. Evaporation at 37 °C for 7 days produced materials with less ordered mesoporous structures than evaporation for 14 days. However, after thermal treatment at 200 °C for 2 h the structure of the shorter evaporated sample was improved whereas the longer evaporated sample was unchanged such that the degree of order in both samples was similar after this thermal treatment. The SAXS data of both these samples was also similar after thermal treatment at 300 °C. The data in Table 6.8 also indicates that although increasing evaporation time from 7 days to 14 days for samples evaporated at 29 °C had a small deleterious effect on the degree of order in as-made samples it was highly beneficial in terms of thermal stability. Increasing the evaporation time further to 28 days for samples evaporated at 29 °C had little impact on the order or thermal stability of the mesoporous titania produced. Similar behaviour was observed for samples evaporated at 26 °C, such that longer evaporation times were observed to improve thermal stability up to 14 days but 21 day evaporation provided no further stability.

Table 6.8: d-spacings, widths and relative intensities of peaks in SAXS patterns of samples prepared using 4 mL volumes of PS-B28 aged 6-7 days and evaporated at approx. 65% RH.

Evaporation Temp (°C)	Evaporation Time (days)	As-made			200 °C		
		d-spacing (Å)	FWHM	I_{rel}	d-spacing (Å)	FWHM	I_{rel}
37	7	67 ± 10	0.02	2	64 ± 10	0.01	2
37	14	68 ± 10	0.01	2	66 ± 10	0.01	2
29	7	65 ± 10	0.01	7	collapsed		
29	14	65 ± 10	0.01	6	62 ± 10	0.01	2

To determine the effect of evaporation time on F127 templated mesoporous titania, samples were synthesised using PS-F5 aged for 6 days and evaporated at approx. 50% RH and 37 °C for 7 or 14 days. The SAXS data of these samples as-made and thermally treated at 300 °C are given in Figure 6.14. Both as-made samples showed ordered mesoporosity,

although the sample with longer 14 day evaporation was more ordered. Thermal treatment at 100 °C caused partial collapse of the ordered mesoporosity in the sample evaporated for 7 days and by 300 °C structural collapse was complete. However, the sample evaporated for 14 days did not begin collapse until temperatures of 350 °C were reached.

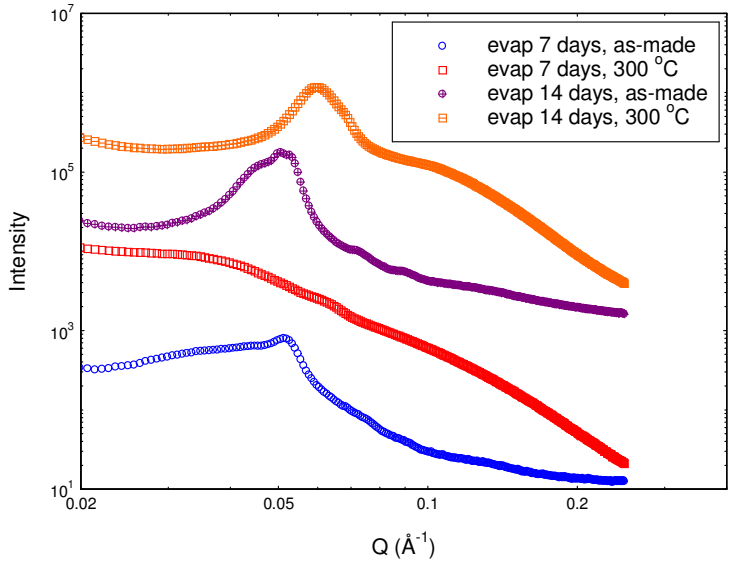

Figure 6.14: SAXS patterns of PS-F5 aged 6 days and evaporated at 37 °C and approx. 50% RH for 7 or 14 days as-made and after thermal treatment at 300 °C.

6.3.3 Summary of Effects of Varying Evaporation Conditions

The temperature at which evaporation is performed during EISA affects the rate at which the alcohol and HCl evaporate. Also, at the same RH, the absolute amount of water present in the atmosphere is greater at higher temperatures. As such, the rate of water ingress into the samples and hence the rate of Ti hydrolysis and condensation will also increase with temperature. As a result the temperature of evaporation can have a profound impact on the order and stability of the mesoporous titania produced.

Mesoporous titania with the highest degree of order was produced with evaporation at 29 °C for Brij 58 solutions and at 37 °C for F127 solutions. Higher temperature evaporation also produced F127 templated mesoporous titania with higher thermal stability. Since higher temperatures increase the rate of evaporation, this result suggests that more ordered mesostructures were formed by F127 solutions with faster rates of titania hydrolysis and condensation. Fast titania hydrolysis may “lock in” the ordered, self-assembled F127 structure as well as ensuring complete cross-linking and condensation of the titania which is beneficial to thermal stability. It should also be noted that the conditions of synthesis that produced the greatest order for the Brij 58 system (evaporation at 29 °C and 65% RH) resulted in materials that exhibited disordered wormhole mesoporosity after heating to 100 °C when replicated using PS-F5. Thus it is clear that different conditions are required to produce stable, ordered mesoporous titania with different templating polymers.

In terms of evaporation time, the precursor solution ageing data in Figure 6.8 suggested that longer evaporation times resulted in as-made samples with less order for PS-B28 solutions. However, the data in Table 6.8 and Figure 6.14 show that longer evaporation times are nevertheless beneficial in terms of thermal stability for PS-B28 solutions evaporated at 29 ^{o}C and PS-F5 solutions evaporated at 37 ^{o}C. Overall, evaporation time had no consistent effect on the degree of order in as-made samples. However, longer evaporation times were consistently beneficial in terms of thermal stability. It is likely that the observed increase in thermal stability with evaporation length occurred due to increased cross-linking of the titania during the longer evaporation, which strengthened the mesoporous structure. Previous work on ordered mesoporous titania thin films has also shown that increasing the length of evaporation of titania films from 1 to 14 days decreased the structural contraction that occurred upon thermal treatment and increased thermal stability.[18]

For PS-B28 solutions evaporated at 37 ^{o}C, hydrolysis and condensation of the titania appeared to be complete within 7 days as increasing the evaporation time to 14 days provided no stabilisation benefit. This can be attributed to the increased water ingress and faster titania hydrolysis rate at the higher temperature of 37 ^{o}C versus 29 ^{o}C. As a result, shorter evaporation times were required to complete titania hydrolysis and condensation and give thermally stable structures for higher evaporation temperatures. Increasing the evaporation time of PS-B28 from 14 to 28 days at 29 ^{o}C also did not improve thermal stability, most likely because hydrolysis and condensation of the titania was complete after 14 days of evaporation at this temperature. In the F127 system increased evaporation time improved stability even at 37 ^{o}C. This suggests that more time and more water were required for Ti condensation and cross-linking to be completed in the F127 system.

6.4 Post-EISA Treatments for Ordered, Mesoporous Titania Powder

6.4.1 Hydrothermal and Water Soaking Treatments

Hydrothermal treatment or water soaking of as-made samples were attempted as it was hypothesised this could complete the Ti hydrolysis and condensation in samples prepared with shorter evaporation times and hence enable shorter synthesis.

Hydrothermal treatment of samples of PS-B11 aged 6 days and evaporated at 28 ^{o}C and approx. 65% RH for 8 days was performed after the samples had been dried at 60 ^{o}C. The samples were hydrothermally treated at 80 ^{o}C for 1 h or 24h. The SAXS data for the untreated and treated samples are shown in Figure 6.15 and indicate that the shorter treatment of 1 h degraded the order in the sample while the 24 h treatment destroyed it completely. Similar results were seen for another sample prepared under the same conditions except aged for 4 days and evaporated for 2 days.

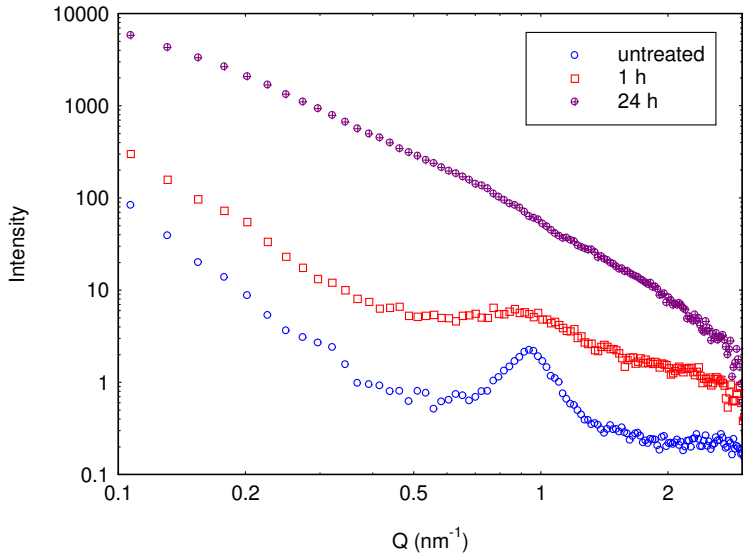

Figure 6.15: SAXS patterns PS-B11 aged 4 days and evaporated at 28 °C and approx. 65% RH for 2 days after drying at 60 °C with and without hydrothermal treatment at 80 °C.

Since hydrothermal treatment at 80 °C caused structural collapse, a less harsh hydrothermal treatment at 50 °C and soaking of the samples in water were attempted. The sample used was PS-B28 aged 14 days, evaporated at 25 °C and approx. 65 % RH for 1 week then dried at 60 °C. Hydrothermal treatment at 50 °C for 1 h on this sample caused complete collapse of the ordered mesoporous structure. Soaking the samples in 5 mL MilliQ water for 1 h caused the same loss of ordered structure. The structural collapse consistently observed upon hydrothermal treatment or water soaking was likely due to the growth of anatase crystallites catalysed by the presence of water.[53,54] Therefore it appears that for low temperature EISA, longer evaporation times are necessary and cannot be substituted by post-EISA treatments of hydrothermal treatment or water soaking.

6.4.2 Low Temperature Stabilisation

It has been demonstrated that gradually heating mesoporous titania thin films before thermal treatment at temperatures able to eliminate the template decreased the structural contraction that occurred upon template elimination and increased thermal stability.[18] Therefore, as-made mesoporous titania samples were dried at 60 °C for 24 h then thermally treated at 100-150 °C for 24 h before applying higher temperatures. It was hoped this low temperature stabilisation would complete the condensation of titania and remove excess water so as to “lock in” the ordered mesoporous structure prior to elimination of the template.

Low temperature stabilisation was investigated for PS-B28 aged 6 days and evaporated at approx. 65 % RH for 7 days at either 29 °C or 37 °C. No noticeable difference was observed between the effects of thermal treatment at 100, 125 or 150 °C. The SAXS data for thermally treated mesoporous titania produced from low-temperature (29 °C) evaporation are shown in Figure 6.16. The SAXS profiles of the samples thermally treated at 300 °C with and without low temperature stabilisation were very similar and contained no correlation peaks,

indicating loss of the ordered structure. Thus, thermal treatment at 125 °C had little effect on thermal stability at higher temperatures. Similar results were seen for samples synthesised using PS-B28 aged for 14 days and/or evaporated for 14 days. Therefore, there was no benefit in performing low temperature stabilisation at 100-150 °C on ordered mesoporous titania synthesised using PS-B28 and evaporated at 29 °C at approx. 65 % RH.

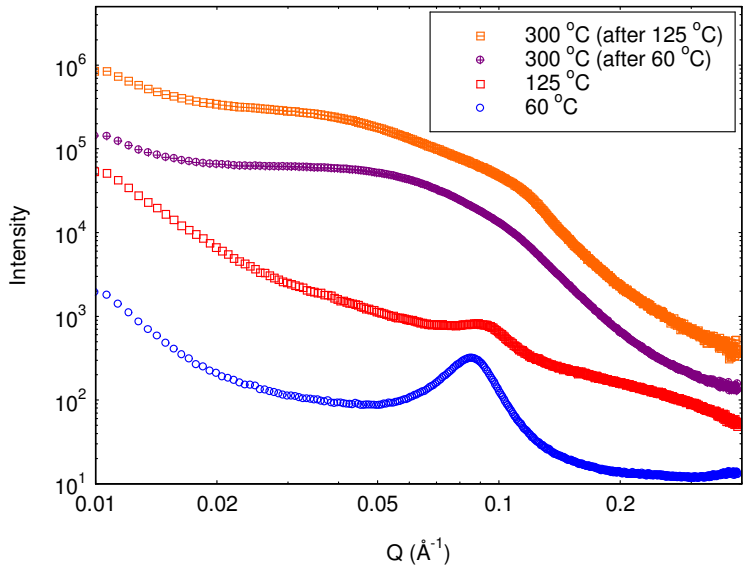

Figure 6.16: SAXS patterns of PS-B28 aged 6 days and evaporated at 29 °C and approx. 65 % RH for 7 days then thermally treated at 300 °C with or without low temperature stabilisation at 125 °C.

The SAXS data for thermally treated mesoporous titania synthesised using PS-B28 evaporated at 37 °C instead of 29 °C are shown in Figure 6.17. The SAXS profile of the sample thermally treated at 300 °C with low temperature stabilisation at 100 °C showed a prominent correlation peak indicating the presence of ordered mesopores, whereas without low temperature stabilisation, no ordered mesoporosity was evident. Therefore, low temperature thermal treatment at 100 °C prior to burn out of the polymer template did improve thermal stability relative to samples that were dried at 60 °C (or 80 °C). Figure 6.17 also shows that the sample stabilised at 100 °C had a more narrow peak and hence was more ordered than the sample dried at 60 °C. Unfortunately, template removal was still incomplete after thermal treatment at 300 °C, as evidenced by the brown colour of the sample. Thermal treatment at 350 °C was required to complete template removal but also caused collapse of the ordered mesostructure. Thus, although low temperature stabilisation of as-made mesoporous titania at 100-150 °C for 24h improved the thermal stability of samples evaporated at 37 °C, it did not enable production of bulk phase, ordered mesoporous titania with Brij 58.

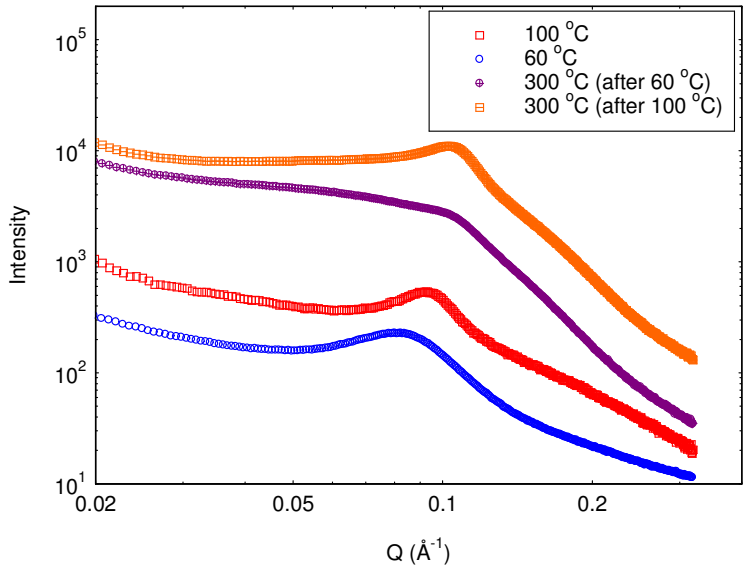

Figure 6.17: SAXS patterns of PS-B28 aged 6 days and evaporated at 37 °C and approx. 65 % RH for 7 days then thermally treated at 300 °C with or without low temperature stabilisation at 100 °C.

6.4.3 Inert Atmosphere Carbonisation

Thermal treatment under inert atmosphere to carbonise the polymer template and stabilise the mesoporous structure prior to template burn-out has proven effective in the synthesis of other mesoporous titania materials.[21,23,24,55] Therefore this methodology was used to remove the Brij 58 from an as-made ordered mesoporous titania sample synthesised using PS-B28 aged for 6 days and evaporated at 26 °C and approx. 65% RH for 14 days. The SAXS measurements of the samples after thermal treatment in an argon atmosphere showed that some order was maintained after heating to 350 °C, while thermal treatment in air to 350 °C caused total structural collapse (Figure 6.18). So, an increase in thermal stability was observed by heating under inert atmosphere. However, mesostructural collapse was evident after thermal treatment at 450 °C under an argon atmosphere (Figure 6.18).

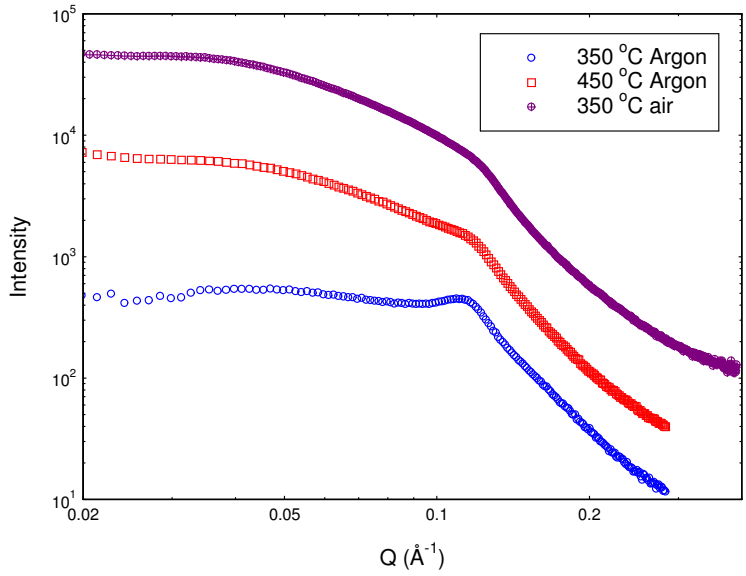

Figure 6.18: SAXS patterns of TiO_2/Brij58 ordered mesoporous materials thermally treated at 350 or 450 °C in an argon atmosphere or to 350 °C in air.

Lee et al. (2008) suggest that a template molecule must contain sp^2 hybridised carbon to avoid decomposition upon heating and instead provide a stabilising amorphous carbon layer inside the mesopores.[19] Using poly(isoprene-block-ethylene oxide) these authors were able to produce titania films that retained ordered mesoporosity after heating to 700 °C under argon. However, Robben et al. (2012) showed that thermal treatment under inert or reducing atmosphere stabilised ordered mesostructures in titania materials templated with F127, which does not contain any sp^2 hybridised carbon.[55] These authors showed that thermal treatment under inert or reducing atmosphere reduced the size of the crystallites grown in the pore walls by 2 nm. Any reduction in crystallite size in the present Brij 58 templated materials when heated to 450 °C under argon was however not sufficient to prevent mesopore collapse. It should also be noted that the materials investigated by Robben et al.[55] and other ordered, mesoporous titania materials synthesised using thermal treatment under inert atmosphere, also utilised stabilising agents such as ethylene diamine,[21] acetyl acetone[23] or sulphuric acid.[24] Therefore the thermal stability of these materials cannot be entirely attributed to the effect of the inert atmosphere. From the failure of this stabilisation method with Brij 58, it can be surmised that it is not as broadly applicable as might be assumed from its wide use.

6.5 Template Removal from Ordered, Mesoporous Titania Powder

6.5.1 Solvent Extraction

Various solvent extraction treatments were performed on Brij 58 templated as-made mesoporous titania samples after drying at 60 °C. In order to choose an organic solvent for solvent extraction, the solubility of Brij 58 in acetonitrile (ACN), diethyl ether, dimethylformamide (DMF), dimethylsulfoxide (DMSO), methanol, tetrahydrofuran (THF) and

water was tested. The solvents ACN and THF were chosen as they were able to completely solubilise 0.05 g Brij 58 with 3 mL solvent within 2 min.

Solvent extraction with THF was performed at a volume/mass ratio of 50, with shaking for 10 min at room temperature followed by decanting of the solvent from the mesoporous titania either 1 or 3 times. Similar solvent extraction was performed with ACN but with a volume/mass ratio of 70. These solvent extraction treatments had no effect on the degree of order or thermal stability of samples, but they also did not remove the need for thermal treatment or decrease the temperature required to obtain less than 5 wt% of organic material in samples. Therefore, solvent extraction at an elevated temperature of 50 or 70 ^{o}C was performed for longer periods of time. Specifically, ACN and a volume/mass ratio of 70 were used for solvent extraction at 50 or 70 ^{o}C for 1 h, 2 x 1 h, 6 h or 24 h. Again, these solvent extraction treatments did not appear to have any impact on the degree of order in the samples. However, a decrease in the thermal stability of the samples was observed after all of these elevated temperature solvent extraction experiments except for the single 1 h extraction at 50 ^{o}C. For example, after thermal treatment at 300 ^{o}C, a comparison of the SAXS data of samples with and without a single solvent extraction at 70 ^{o}C for 1 h showed that while both samples had d-spacing 6 nm, the FWHM/relative intensity of the untreated and solvent extracted samples were 0.01/4 and 0.02/2, respectively. In addition, extended periods of solvent extraction at elevated temperature still did not remove the need for thermal treatment or decrease the temperature required to obtain less than 5 wt% of organic material in samples. Therefore, solvent extraction was not continued. It is possible that the failure of solvent extraction to remove the Brij 58 template may be due to the presence of bonding between the titania surface and the PEO blocks of the template. Further experiments would be required to test this hypothesis.

6.5.2 Thermal Treatment

The ramp rate of thermal treatment, as well as the amount of time the samples were held at each temperature, were investigated to determine their effect on the structure of the mesoporous titania and minimise structural collapse. Decreasing the rate of heating during thermal treatment resulted in greater retention of ordered structures. For example, Figure 6.19 shows the SAXS patterns of the same ordered mesoporous titania heated to 200 ^{o}C either with an unspecified ‘fast’ rate by placing the sample directly at 200 ^{o}C or with a ‘slow’ ramp rate of 1 ^{o}C/min. The ordered structure in the sample was lost through ‘fast’ heating while some order was maintained in the sample heated more slowly. Decreasing the ramp rate further to 0.1 ^{o}C/minute did not substantially increase the retention of order. Therefore, a heating rate of 0.5 – 1.0 ^{o}C/min was generally employed for thermal treatment of as-made materials.

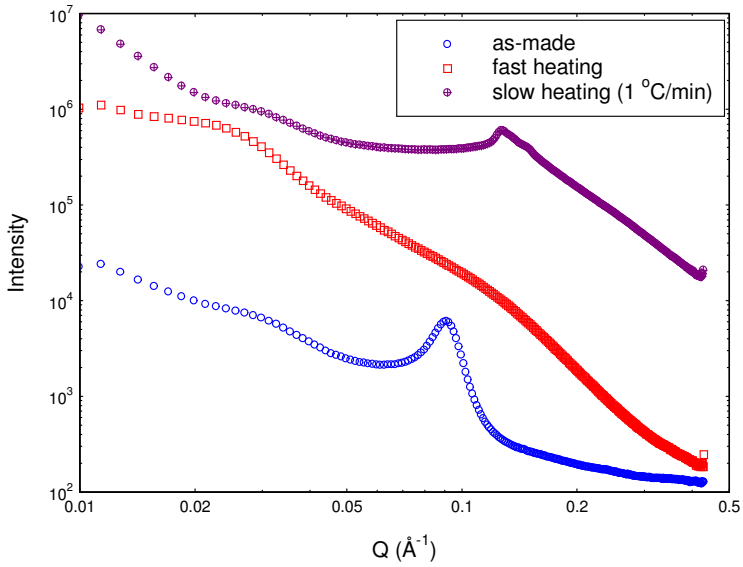

Figure 6.19: SAXS patterns of TiO_2/Brij58 ordered mesoporous materials thermally treated at 200 °C by placing the sample directly in an oven at 200 °C ("fast heating") or ramping the temperature at 1 °C/min ("slow heating").

The amount of time samples were held at 200 and 300 °C was also varied in order to establish any effects of hold time on the mesoporous structure of samples. Samples prepared using PS-B28 aged 6 days then evaporated at 28 °C and approx. 65 % RH for 14 days were held at 200 °C for 2, 8 or 24 h. The SAXS data of all three samples contained a correlation peak of d-spacing 6 nm and FWHM 0.02 but the relative intensity of the peaks decreased with increasing hold time, from 3.5 for 2 h to 3.2 for 8 h and 2.6 for 24 h. This suggests there was a decrease in the order of the samples with increasing hold time at 200 °C. Therefore, in the interest of decreasing synthesis time as well as increasing the order of the final product, a hold time of 2 h at 200 °C was generally employed for thermal treatment.

Extended hold time at 300 °C was similarly observed to decrease the degree of order in mesoporous titania samples. For example, samples prepared using 3 mL PS-B28 aged 7 days then evaporated at 29 °C and approx. 65 % RH for 7 days were held at 300 °C for 3 h or 12 h. The SAXS data of the sample held at 300 °C for 3 h contained a correlation peak of d-spacing 5 nm, FWHM 0.01 and relative intensity 3 while the SAXS data of the sample held at 300 °C for 12 h showed that the ordered mesoporous structure had collapsed. Therefore, a hold time of 3 h at 300 °C was generally employed for thermal treatment. Increasing the hold time of titania calcination has previously been shown to increase the crystallinity and crystallite size of the titania,[56] which is a likely explanation for the decrease in order observed with extended hold time at 200 and particularly 300 °C.

6.5.3 Template Removed Brij 58

The SAXS data of as-made Brij 58 templated mesoporous titania synthesised under the conditions found to maximise order (4 mL PS-B28 aged 6 days and evaporated at 29 °C and

approx. 65 % RH for 14 days) is shown in Figure 6.20. This data was fit using a power law exponent of -2.5, which is expected for any powdered system, and a Lorentzian peak with d-spacing 68 ± 10 Å and FWHM 0.028 ± 0.001 $Å^{-1}$, which indicated the presence of ordered mesoporosity. The fitted data is also shown as a solid line in Figure 6.20 and can be seen to provide an excellent fit to the experimental data (χ^2/Npts = 5.8). The relative intensity of this peak was 6. Transmission electron microscopy (TEM) was also performed on the Brij 58 templated mesoporous titania after drying at 100 °C and some of the images collected are shown in Figure 6.21. Ordered porous channels approx. 30 Å in diameter can be seen perpendicular to the edge of the titania material. Given the d-spacing of 68 Å indicated by the SAXS data, this suggests a titania wall thickness of approx. 40 Å.

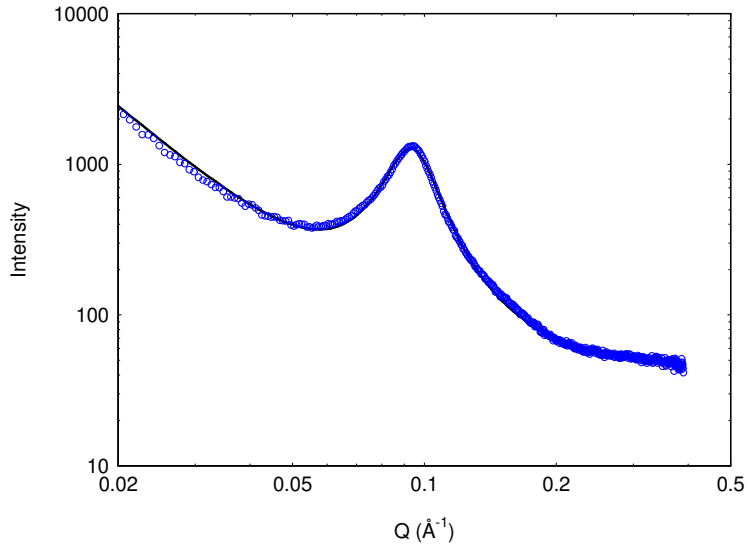

Figure 6.20: SAXS pattern of optimal, as-made Brij 58 ordered mesoporous titania. Open circles = experimental data, solid line = fitted data.

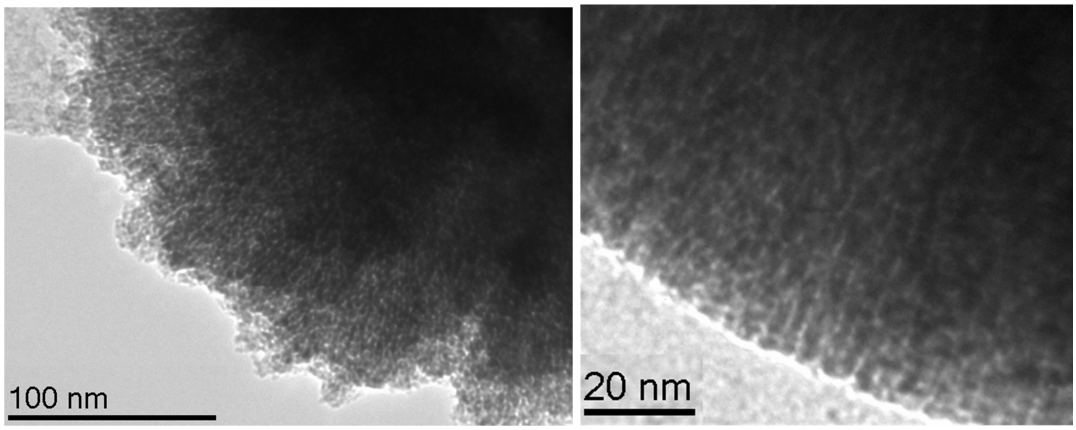

Figure 6.21: TEM images of optimal, as-made Brij 58 ordered mesoporous titania

The as-made material was ground into a fine powder using an agate mortar and pestle before thermal treatment, which decreased the temperature at which Brij 58 burnout occurred.

Thermal treatment was performed at a ramp rate of 0.5 °C/min to 200 °C for 2 h followed by 300 °C for 3 h. After thermal treatment at 200 °C, SAXS data showed a correlation peak with d-spacing 61 ± 10 Å, indicating that the mesoporous structure had shrunk by approx. 7 Å. Although typically samples were still brown in colour after thermal treatment at 300 °C, indicating that not all the polymer template had been removed, this sample was white after thermal treatment at 300 °C for 3 h. %CHN analysis of the thermally treated optimal sample confirmed that template removal was complete, as the %C measured was only 0.3 %. Therefore full characterisation of this template-free material was performed. X-ray diffraction (XRD) of the thermally treated optimal Brij 58 templated titania powder showed it to be anatase (Figure 6.22). The mean ordered crystallite size was calculated according to the Sherrer equation,[57] using the FWHM of the XRD peaks, to give a value of 183 ± 31 Å.

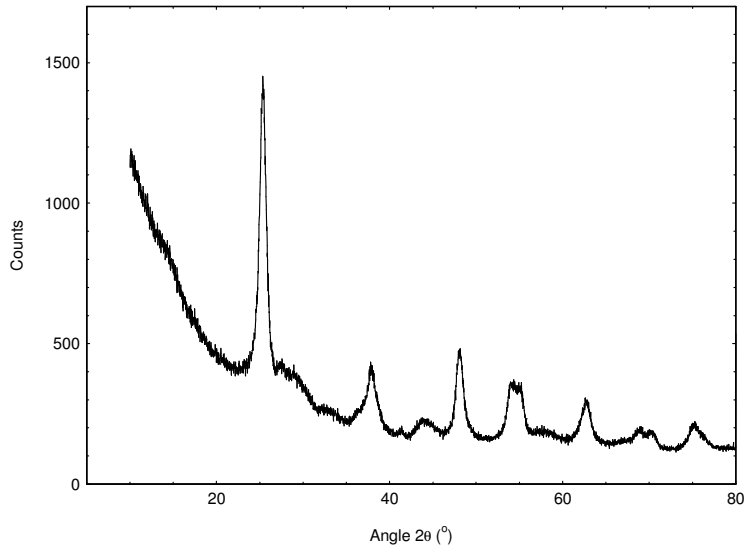

Figure 6.22: XRD pattern of optimal Brij 58 mesoporous titania after template removal via thermal treatment at 300 °C for 3 h

SAXS data of the optimal Brij 58 ordered mesoporous titania after template removal is shown in Figure 6.23. This data was fit using a power law background, a broad peak and a Gaussian peak. The fitted power law exponent was -3.5, which is expected for any powdered system. The fitted Gaussian peak had d-spacing 233 ± 10 Å and FWHM 0.087 ± 0.001 $Å^{-1}$ and dominated the SAXS data. The fitted broad peak had d-spacing 72 ± 10 Å, peak shape exponent 2.7 ± 0.02 and FWHM 0.062 ± 0.001 $Å^{-1}$. The d-spacing of this broad peak was consistent with the Lorentzian peak in the as-made material (Figure 6.20), which was attributed to the ordered mesoporous structure. However, the broad peak in the SAXS data of the optimal Brij 58 ordered mesoporous titania after template removal was wider and less intense, indicating that although some ordered mesoporosity remained after template removal, it was substantially decreased. The fitted data is shown as a solid line in Figure 6.23 and can be seen to provide a good fit to the experimental data (χ^2/Npts = 1.5).

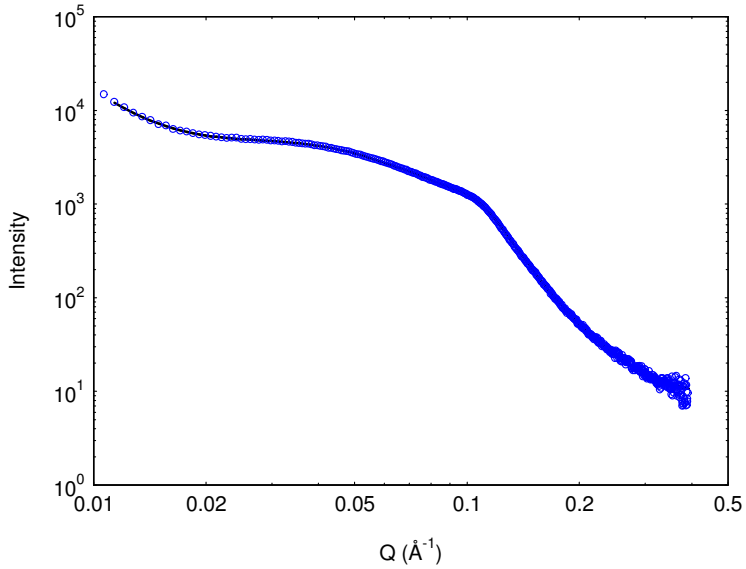

Figure 6.23: SAXS pattern of optimal Brij 58 mesoporous titania after template removal via thermal treatment at 300 °C for 3 h. Open circles = experimental data, solid line = fitted data.

An open but disordered wormhole structure with pores of approx. 30 Å and walls of approx. 40 Å can be visualised in the TEM images of the template removed sample in Figure 6.24. Some densely agglomerated areas, approx. 200 Å in size, can also be seen in the TEM images and are consistent with the crystallite size from the XRD data and with the broad Gaussian peak in the SAXS data.

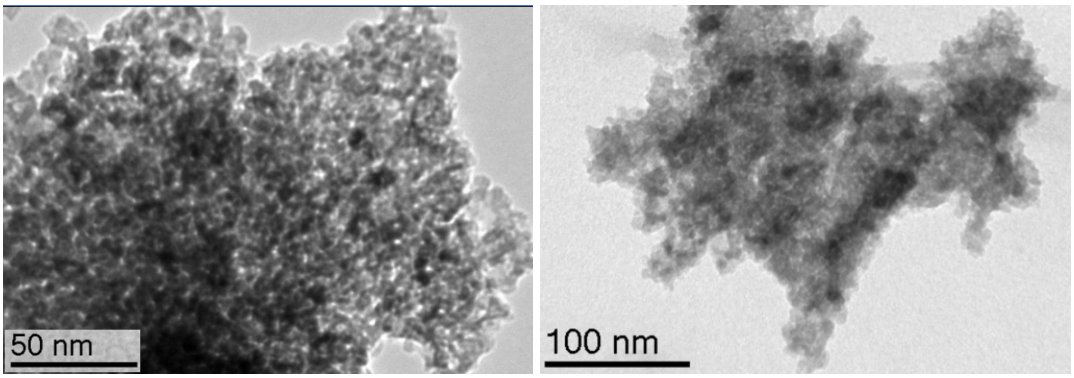

Figure 6.24: TEM images of optimal Brij 58 mesoporous titania after template removal via thermal treatment at 300 °C for 3 h

The nitrogen adsorption-desorption isotherm for the optimal Brij 58 templated mesoporous titania material after template removal is shown in Figure 6.25. The isotherm was characteristic of a type IV isotherm with H2 hysteresis, indicative of capillary condensation in mesopores. The BET surface area of this mesoporous titania material was 210 m^2/g and the pore volume was 0.16 mL/g. The t-plot had a negative y-axis intercept, indicating that there were no micropores in this material. The inset to Figure 6.25 indicates a narrow pore size

distribution (PSD) centred around 30 Å. This was consistent with the pore size seen in the TEM images in Figure 6.24.

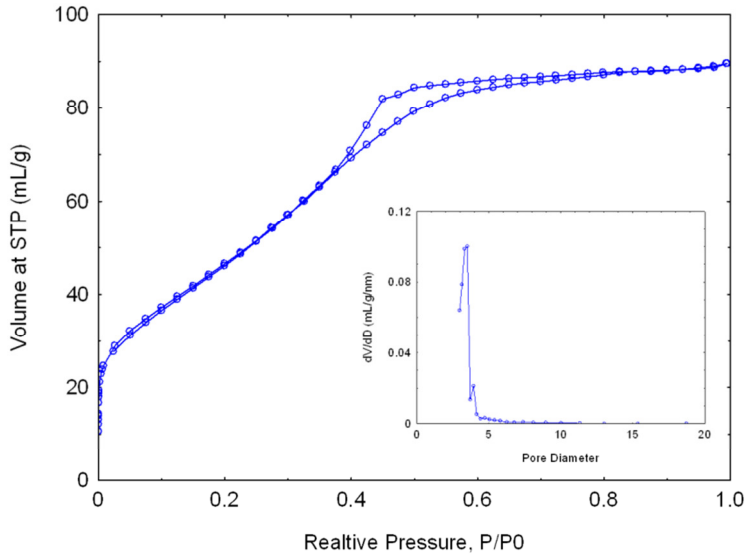

Figure 6.25: Nitrogen adsorption-desorption isotherm for optimal Brij 58 mesoporous titania after template removal via thermal treatment at 300 ^{o}C for 3 h. Inset: PSD.

6.5.4 Template Removed F127

SAXS data of as-made F127 templated mesoporous titania synthesised under the conditions found to maximise order (4 mL PS-F10 aged 6 days and evaporated at 37 ^{o}C and approx. 50 % RH for 14 days) is shown in Figure 6.26. This data was fit using a two power law background and a Lorentzian peak. From Q = 0.011 to 0.018 Å^{-1} the power law exponent was -3.2 and from 0.018 to 0.25 Å^{-1} the power law exponent was -1.1. The presence of two different power law exponents at different Q ranges indicated that there were different scattering structures at different length scales. At low Q the power law exponent was -3.2, which suggests a typical powdered structure on a large length scale. At high Q the power law was -1.1, which suggests rod-like structures, perhaps polymers of titania within the titania walls, were present on a small length scale. The prominent, narrow Lorentzian peak had d-spacing 146 ± 10 Å and FWHM 0.009 ± 0.00002 Å^{-1}. The relative intensity of this peak was 11. The fitted data is shown as a solid line in Figure 6.26 and provided a good fit to the experimental data (χ^2/Npts = 19).

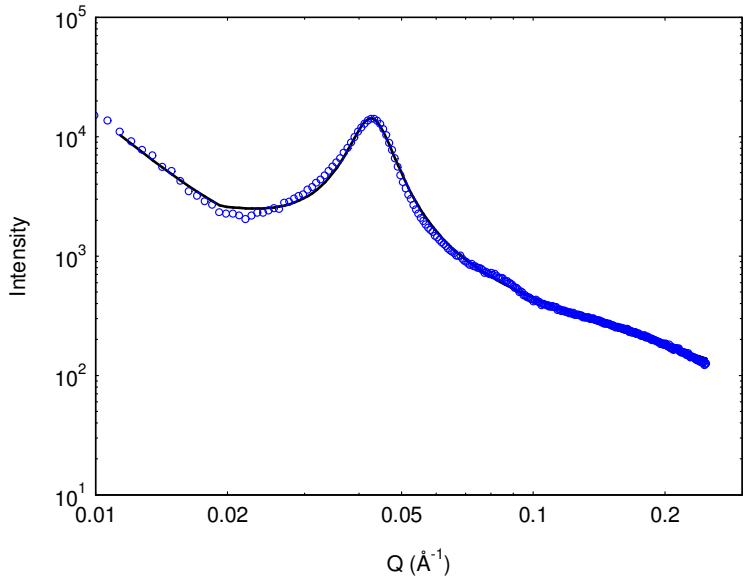

Figure 6.26: SAXS pattern of optimal, as-made F127 ordered mesoporous titania. Open circles = experimental data, solid line = fitted data.

The as-made material was ground into a fine powder using an agate mortar and pestle before thermal treatment. Thermal treatment was performed at a ramp rate of 0.5 °C/min to 300 °C for 3 h followed by 350 °C for 4 h. After thermal treatment at 350 °C template removal was complete, as confirmed by %CHN analysis in which the %C measured was only 0.5 %. Therefore full characterisation of the template-free material was performed. X-ray diffraction (XRD) of the thermally treated optimal Brij 58 templated titania powder showed it to be anatase (Figure 6.27). The mean ordered crystallite size was calculated according to the Sherrer equation,[57] using the FWHM of the XRD peaks, to give a value of 174 ± 30 Å.

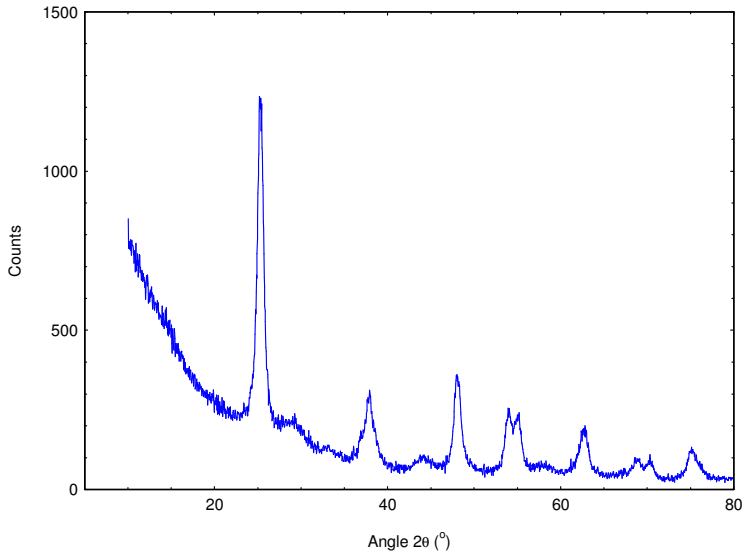

Figure 6.27: XRD patterns of optimal F127 mesoporous titania after template removal via thermal treatment at 350 °C for 4 h

After thermal treatment at 300 °C, SAXS data of the optimal F127 ordered mesoporous titania showed a correlation peak with d-spacing 114 ± 10 Å, indicating that the mesoporous structure had shrunk by approx. 32 Å. The SAXS data after template removal was complete at 350 °C is shown in Figure 6.28. This data was fit using a power law background of exponent of -2.9, which is expected for any powdered system, and 3 peaks. The peak at low Q was a broad peak with d-spacing 140 ± 10 Å and FWHM 0.044 ± 0.0001 $Å^{-1}$. This corresponded to the morphology of spherical particles of this size seen in the TEM images in Figure 6.29 and was consistent with the crystallite size determined from the XRD pattern in Figure 6.27. The mid Q-range peak in the SAXS data, which was the most intense, was a Lorentz peak with d-spacing 103 ± 10 Å and FWHM 0.012 ± 0.000004 $Å^{-1}$. The narrow width of this peak, as well as its intensity, indicate that there was still some ordered mesoporosity in this material. The d-spacing of this peak was also consistent with the shrinkage of the mesoporous structure seen after thermal treatment at 300 °C. However, the ordered mesoporosity cannot be seen in the TEM images in Figure 6.29, due to the localised nature of this characterisation technique. The final peak at high Q in the SAXS data was a low intensity Gaussian peak with d-spacing 62 ± 10 Å and FWHM 0.049 ± 0.0002 $Å^{-1}$. This peak may be a repeat unit from the peak with d-spacing 103 Å, as it is consistent with higher order peak of a hexagonal structure. The fitted data is shown as a solid line in Figure 6.28 and provided a good fit to the experimental data (χ^2/Npts = 130).

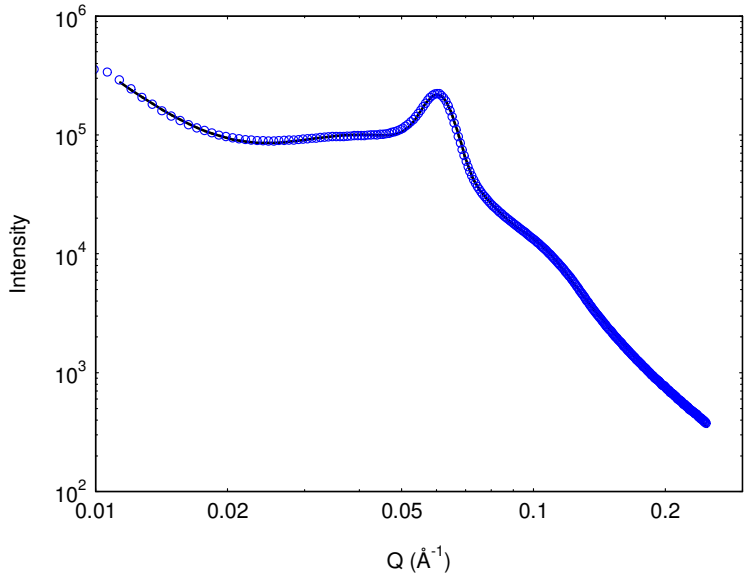

Figure 6.28: SAXS pattern of optimal F127 mesoporous titania after template removal via thermal treatment at 350 °C for 4 h. Open circles = experimental data, solid line = fitted data.

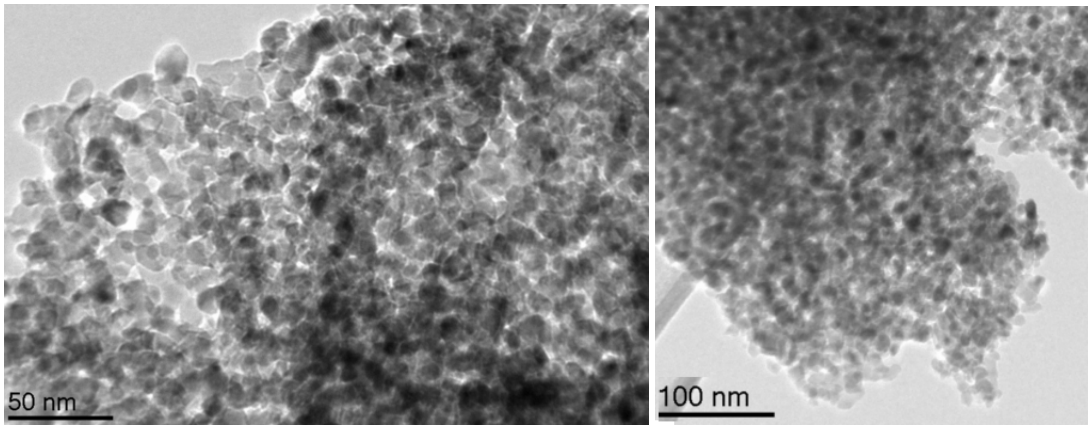

Figure 6.29: TEM images of optimal F127 mesoporous titania after template removal via thermal treatment at 350 °C for 4 h

The nitrogen adsorption-desorption isotherm for the optimal F127 templated mesoporous titania material after template removal is shown in Figure 6.30. The isotherm was characteristic of a type IV isotherm with H2 hysteresis, indicating capillary condensation in mesopores. The BET surface area of this mesoporous titania material was 190 m^2/g and the pore volume was 0.31 mL/g. The t-plot had a negative y-axis intercept, indicating that there were no micropores in this material. The inset to Figure 6.30 shows a narrow PSD centred around 50 Å. This was consistent with the pore size seen in the TEM images in Figure 6.29.

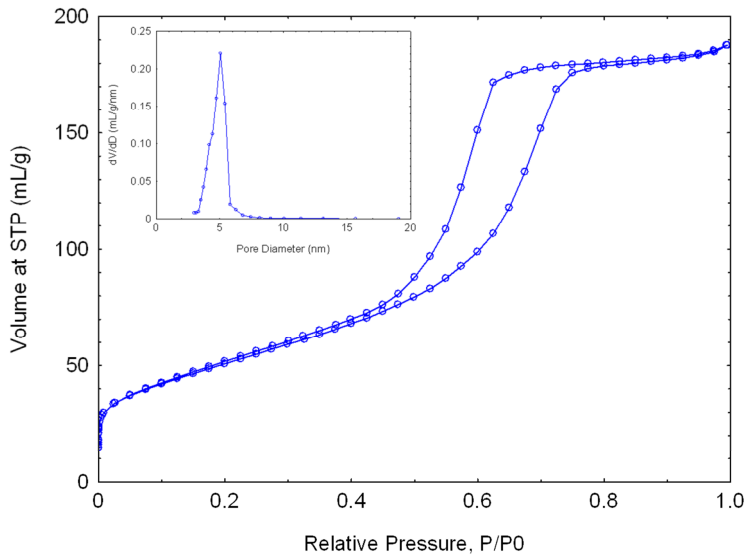

Figure 6.30: Nitrogen adsorption-desorption isotherm for optimal F127 mesoporous titania after template removal via thermal treatment at 350 °C for 4 h. Inset: PSD.

3.5.5 Comparison of Template Removed Mesoporous Titania Powders

Synthesis of large quantities of ordered mesoporous titania using Brij 58 is known to be particularly challenging as this template produces smaller pores and thinner pore walls than pluronic template materials such as F127 and P123.[18] This means that it can only

accommodate small crystallites in the pore walls and as a result typically has low thermal stability.[18,44] Several post-EISA treatments such as thermal treatment under inert atmosphere, solvent extraction, hydrothermal treatment and water soaking of as-made samples were attempted to increase thermal stability or decrease the synthesis time for Brij 58 mesoporous titania, but as described in *section 6.5* they were all unsuccessful.

The broadening of the correlation peak with d-spacing ~70 Å in the SAXS data of the Brij 58 templated mesoporous titania upon template removal indicated a loss of order due to low thermal stability, as has been seen previously. Nevertheless, mesoporous titania with pores approximately 30 Å in diameter and BET surface area 210 m^2/g has been produced. Relatively few examples of Brij 58 templated mesoporous titania materials exist for comparison. A Brij 58 templated mesoporous titania thin film demonstrated a similar pore size of 25 Å.[18] Bulk phase, Brij 58 templated ordered mesoporous titania synthesised by EISA for 24 h followed by thermal stabilisation at 60-100 ^oC produced materials with BET surface areas 90-160 m^2/g, pore volume 0.09-0.21 mL/g and 43-57 Å pore diameters.[44] Thermal stabilisation at 120 ^oC was also performed but produced materials without order. As such, it appears that the small pore size of the present materials, which is consistent with what has been observed previously in thin films, gives them greater surface area and similar pore volume to materials with shorter EISA and thermal stabilisation at 60-100 ^oC. Calcination of the literature samples at 360 ^oC for 2 h also caused the loss of the ordered structure, as was observed in the present system.

F127 has been used extensively for synthesis of mesoporous titania via EISA.[2,18,55,58] However, in this work, synthesis of bulk phase, ordered mesopous titania using F127 as a template has been achieved without the addition of a stabilising agent for the first time. This is beneficial since additives can contaminate the final titania product or increase the temperature required to obtain clean titania.[21]

The retention of order and inferred higher thermal stability of F127 templated materials was not the only difference between the Brij 58 and F127 systems. The F127 templated material had larger pores than the Brij 58 templated titania, as would be expected due to the higher molecular weight of the F127 polymer. The d-spacing of the F127 templated mesoporous titania also showed a substantial amount of shrinkage (43 Å) upon thermal treatment, while the Brij 58 templated materials did not. Similar contraction of the mesostructure upon calcination has been seen previously for F127 templated mesoporous titania films.[35] The F127 templated mesoporous titania demonstrated a similar crystallite size, nitrogen adsorption isotherm shape and BET surface area to the Brij 58 templated mesoporous titania, but with a substantially larger pore volume due to the larger pore size. This is again consistent with the larger molecular weight of the F127 block polymer relative to Brij 58.

Several examples exist in the literature of F127 templated ordered mesoporous titania materials, either as thin films or additive stabilised materials synthesised on a larger scale. Most of these materials had comparable surface areas and pore sizes to the present F127

templated titania material. For example, an ordered mesoporous titania thin film thermally treated at 350 °C demonstrated a surface area of 150 m^2/g and pore size 58 Å.[18] An ytterbium stabilised titania thin film thermally treated at 400 °C had a similar pore size of ~50 Å but lower surface area of only 110 m^2/g.[59] In terms of ordered mesoporous titania materials synthesised in larger quantities, acetic acid stabilised materials have been synthesised with surface area 190-230 m^2/g, pore volume 0.36 mL/g and pore size 50-63 Å after thermal treatment at 350 °C.[55,60] These properties are comparable to the present non-stabilised material, but the acetic acid appeared to retard the growth of anatase crystallites, which were only 70 Å in the acetic acid stabilised titania,[55] as opposed to ~170 Å in the current non-stabilised material, despite the same thermal treatment.

It was also of interest to compare the present results with those of ordered mesoporous titania materials synthesised in substantial quantities with commercially available templates and without use of stabilising additives. Using P123, ordered mesoporous titania calcined at 350 °C was produced with surface area 220 m^2/g, pore volume 0.28 mL/g and pore size 41 Å.[27] With a slightly higher calcination temperature of 400 °C, P123 templated ordered mesoporous titania with surface area 210 m^2/g and 65 Å pores was produced.[26] The crystallite size of P123 templated ordered mesoporous titania calcined at 400 °C was only 24 Å,[26] which is substantially smaller than the approximately 170 Å crystallites seen in the present system despite the lower calcination temperature of 350 °C. This accounts for the higher degree of order seen in the P123 templated titania material. Ordered mesoporous titania synthesised using F108 as a template and calcined at 350 °C also demonstrated a similar surface area, of 210 m^2/g, and pore size, of 63 Å.[27] The similar pore size values for P123, F108 and F127 suggests that the central PO block size rather than the EO block size controls this property. The smaller pore size of Brij 58 is also consistent with this hypothesis as it has a small $C_{16}H_{33}$ central block.

6.6 Titania Beads

6.6.1 F127 Versus Brij 58 Template

Titania beads synthesised using both Brij 58 and F127 based precursor solutions were prepared and their ordered mesoporus structure measured using SAXS. It was found that 0.5 mm diameter PAN beads infiltrated with F127 based precursor solution PS-F5 were more thermally stable than PAN beads infiltrated with Brij 58 solution PS-B28. As can be seen from Figure 6.31, titania beads synthesised using PS-F5 aged for 6 days and evaporated at 37 °C and approx. 65 % RH for 14 days maintained their ordered mesostructure after thermal treatment at 400 °C for 4 h whereas beads synthesised using PS-B28 under the same conditions had lost their ordered structure at this temperature. This was expected given the higher thermal stability of mesoporous titania synthesised using F127 rather than Brij 58 as a template noted earlier in this chapter.

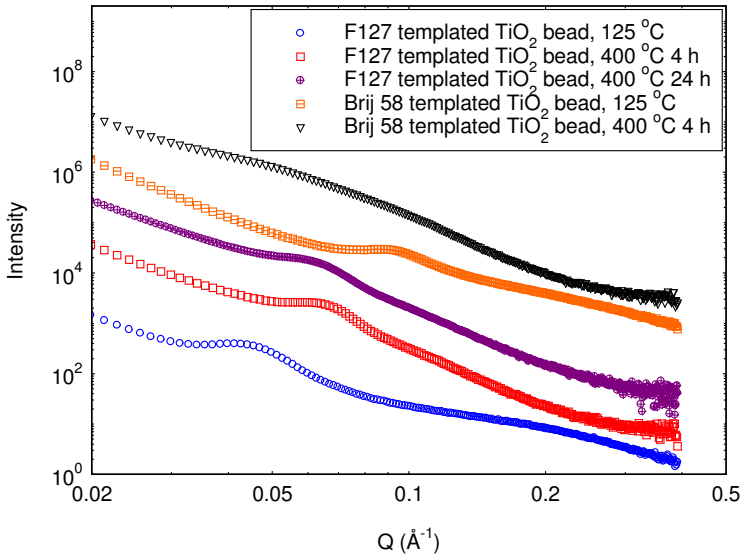

Figure 6.31: SAXS patterns of titania beads synthesised via infiltration of 6 day aged PS-F5 or PS-B28 into PAN beads followed by evaporation at 37 °C and approx. 65 % RH for 14 days

Titania beads synthesised using PS-F5 and thermally treated at 400 °C for 4 h were brown in colour, indicating not all of the F127 and PAN templates had been removed. Therefore, a longer hold time of 24 h at 400 °C was applied to these titania beads, which successfully removed the F127 and PAN templates, as evidenced by the white colour of the beads. The SAXS data in Figure 6.31 also shows that the titania beads also retained an ordered mesoporous structure after thermal treatment at 400 °C for 24 h, as a correlation peak with d-spacing 10 nm, FWHM 0.01 and relative intensity 1.5 was present.

6.6.2 Evaporation Length

The effect of evaporation length on the order and stability of titania beads was investigated using 6 day aged PS-F5 infiltrated into 0.5 mm diameter PAN beads then evaporated at 32 °C and approx. 50% RH for 7 or 14 days. The results of SAXS measurements on the resulting samples are given in Table 6.9. Although the titania beads evaporated for 7 days had a slightly more ordered mesoporous structure after drying at 100 °C, their thermal stability was substantially less than that of beads evaporated for 14 days. This increase in thermal stability with increased evaporation length was consistent with what was observed for the F127 templated mesoporous titania powders in *section 6.3.2* and can be similarly explained by the fact that the longer evaporation time allows greater cross-linking within the titania structure.

Table 6.9: d-spacings, widths and relative intensities of peaks in SAXS patterns of samples prepared using 4 mL volumes of PS-F5 aged for 6 days and evaporated at 32°C and approx. 50% RH.

Evaporation Length (days)	100 °C			300°C		
	d-spacing (Å)	FWHM	I_{rel}	d-spacing (Å)	FWHM	I_{rel}
7	121 ± 10	0.01	5	101 ± 10	0.01	7
14	125 ± 10	0.01	4	97 ± 10	0.01	10

6.6.3 Post-EISA Treatments

To test whether higher temperatures were required for template removal from bead structures than from powders, titania beads were prepared under the optimal conditions determined for F127 templated mesoporous titania powders (*section 6.5.4*) to allow direct comparison. Specifically, 0.5 and 1.0 mm diameter PAN beads were infiltrated with PS-F10 aged 6 days and evaporated at 37 °C and approx. 50 % RH for 14 days. These titania beads required thermal treatment at 350 °C for at least 12 h to remove the PAN and F127 polymer templates, whereas the powders prepared in *section 6.5.4* required only 4 h at 350 °C to remove the F127 template. This increase in the required hold time at 350 °C may be due to the presence of PAN or the increased proportion of polymer to be removed in the bead morphology relative to the powders.

It has been previously demonstrated that the use of ethylene diamine during synthesis stabilised the mesoporous structure of P123 templated bulk phase, ordered mesoporous titania powders.[21] Thus, similar ethylene diamine treatment was investigated on 1.0 mm diameter PAN beads infiltrated with PS-F5 aged 6 days then evaporated at 32 °C and approx. 50 % RH for 14 days. After thermal treatment at 200 °C for 4 h, these titania beads were refluxed in pH 11 ethylene diamine aqueous solution for 48 h. The SAXS data of the beads before and after refluxing are shown in Figure 6.32. Refluxing slightly increased the degree of mesoporous order in the titania beads, since both samples had d-spacing 10 nm and FWHM 0.01 but the sample after refluxing had relative intensity 4 rather than 3. Thermal treatment at 350 °C for 24 h was then performed to remove the PAN and F127 polymer templates. The SAXS measurements on titania beads after template removal are also shown in Figure 6.32 and indicate that refluxing in ethylene diamine aqueous solution substantially improved the stability of the beads. Without stabilisation treatment, the ordered mesoporous structure collapsed after 24 h at 350 °C. On the other hand, the ethylene diamine treated titania bead maintained an ordered mesoporous structure with d-spacing 9 nm, FWHM 0.01 and relative intensity 3 after removal of the template at 350 °C. Therefore, this stabilisation method has been shown to be effective for PAN and F127 templated titania bead structures as well as the P123 templated titania powders reported previously.

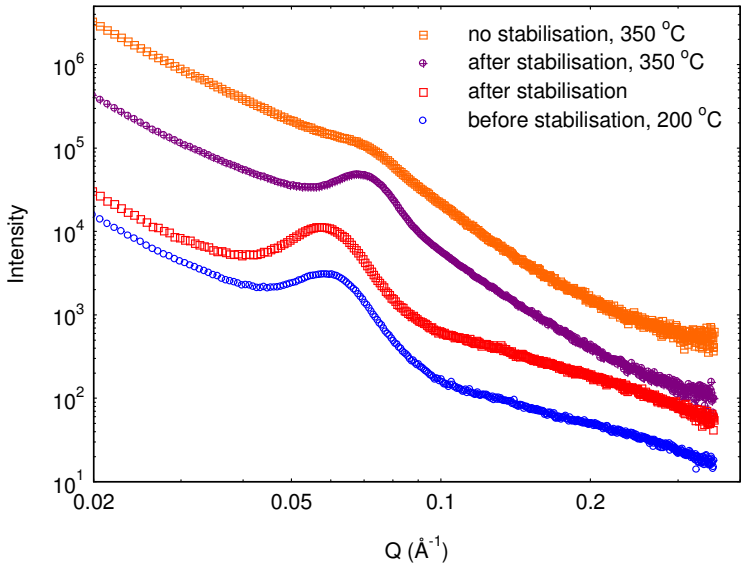

Figure 6.32: SAXS patterns of titania beads synthesised via 6 day aged PS-F5 infiltration of PAN beads followed by evaporation at 32 °C and approx. 50 % RH for 14 days with and without ethylene diamine stabilisation

Although ethylene diamine stabilisation did improve the order and thermal stability of titania beads, different conditions of synthesis using PS-F10 and an evaporation temperature of 37 °C allowed ordered mesoporous titania beads to be produced without the use of a stabilising agent. Therefore, use of ethylene diamine stabilisation was not continued.

6.6.4 Effect of Bead Diameter

Since two sizes of PAN beads were generated through varying the pressure of the air compressor in the automatic droplet generator (*section 6.1.2*), it was of interest to determine the effect of bead size on the ordered mesoporous structure of titania beads synthesised using these two different sized PAN bead templates. Figure 6.33 shows the SAXS data of titania beads synthesised using PS-F10 aged 6 days infiltrated into 0.5 mm (small) and 1.0 mm (large) diameter PAN beads and evaporated at 37 °C and approx. 50 % RH for 14 days. After drying at 100 °C, both the large and small titania beads had d-spacing 140-142 Å, FWHM 0.01 and relative intensity 2. After thermal treatment at 300 °C for 3 h, both the large and small titania beads had d-spacing 104 Å and FWHM 0.01 but the large beads had relative intensity 3 while the small beads were slightly more ordered with relative intensity 4. After 12 h at 350 °C, which was required to remove the PAN and F127 polymer templates, both the large and small titania beads again demonstrated a similar degree of order, with d-spacing 92-95 Å, FWHM 0.01 and relative intensity 2. Therefore it appears that titania beads synthesised using either 0.5 or 1.0 mm diameter PAN bead templates had a similar degree of order in their mesostructure.

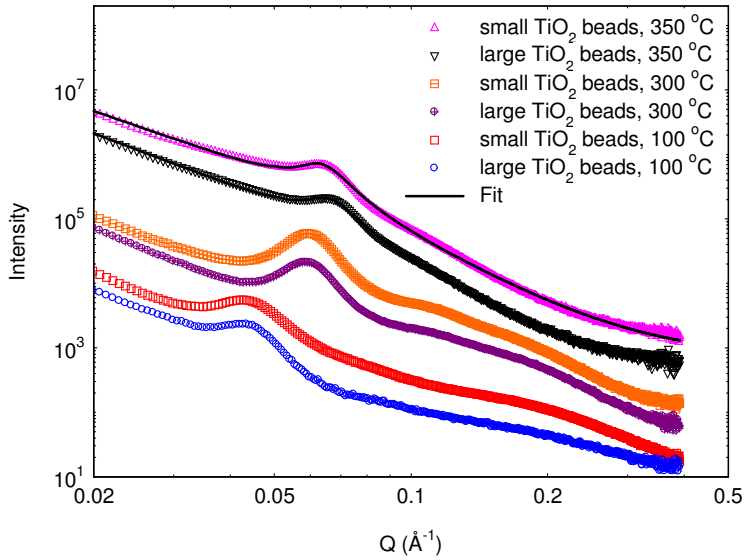

Figure 6.33: SAXS patterns of titania beads synthesised via 6 day aged PS-F10 infiltration of small and large PAN beads followed by evaporation at 37 °C and approx. 50 % RH for 14 days.

The SAXS data of the 0.5 and 1.0 mm titania beads after template removal at 350 °C for 12 h (Figure 6.33) were also fit using SASView software with two power laws and a Lorentzian peak, in order to more accurately model the data. For the 1.0 mm titania beads, a power law of exponent -2.7 was fit from Q = 0.02 to 0.05 Å^{-1} followed by a power law exponent of -3.9 from Q = 0.05 to 0.39 Å^{-1} and the Lorentzian peak had d-spacing 97 ± 10 Å and FWHM 0.020 ± 0.0001 Å^{-1}. The fitted data is shown as a solid line in Figure 6.33 and provided an excellent fit to the experimental data (χ^2/Npts = 27). For the 0.5 mm titania beads, a power law of exponent -2.5 was fit from Q = 0.02 to 0.05 Å^{-1} followed by a power law exponent of -3.8 from Q = 0.05 to 0.39 Å^{-1} and the Lorentzian peak had d-spacing 100 ± 10 Å and FWHM 0.018 ± 0.00004 Å^{-1}. The fitted data is shown as a solid line in Figure 6.33 and provided a good fit to the experimental data (χ^2/Npts = 84). From this, it is clear that both the 0.5 and 1.0 mm titania beads had a very similar SAXS profile although the smaller beads had a slightly higher degree of order. The presence of two different power law exponents at different Q ranges indicated that there were different morphologies present at different length scales, which was as expected for a hierarchically porous material such as this. X-ray diffraction of the 0.5 and 1.0 mm diameter titania beads was also performed (Figure 6.34) and showed them to be anatase. The mean ordered crystallite size was calculated according to the Sherrer equation,[57] using the FWHM of the XRD peaks, to give similar similar values of 176 ± 46 Å for the 0.5 mm beads and 184 ± 50 Å for the 1.0 mm beads.

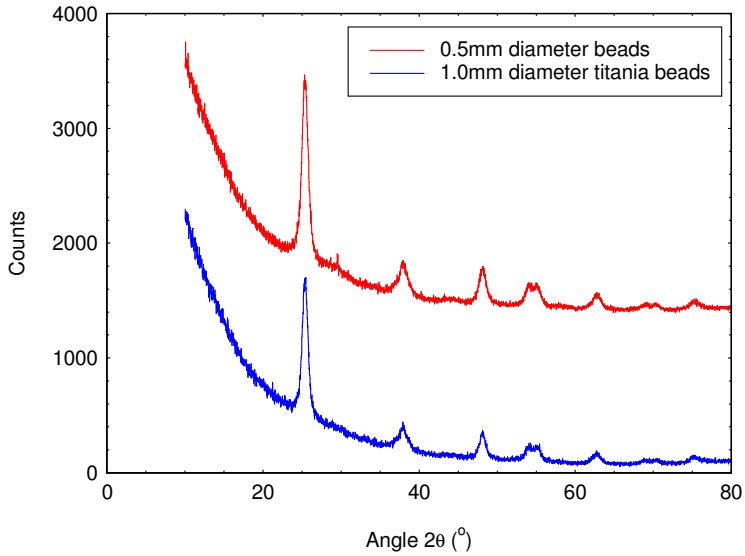

Figure 6.34: XRD patterns of 0.5 and 1.0 mm diameter hierarchically porous titania beads

The nitrogen adsorption-desorption isotherms for the PAN/F127 templated 1.0 mm and 0.5 mm titania beads are shown in Figures 6.35 and 6.36. Both isotherms had a similar shape and had characteristics of type II and type IV isotherms. The unlimited uptake at high P/P0, indicating the presence of macropores or voids, was characteristic of a type II isotherm. However, the presence of hysteresis, indicating capillary condensation in mesopores, was characteristic of a type IV isotherm. Two types of hysteresis were present in Figures 6.35 and 6.36. H2 hysteresis was present at P/P0 ~0.6, which was consistent with the nitrogen adsorption-desorption isotherm of the F127 templated titania powder in *section 6.5.4.* This suggests that the H2 hysteresis at P/P0 ~0.6 was due to the F127 templated pores, which were approx. 5 nm in diameter. H3 hysteresis was also present at P/P0 ~0.95, which was assumed to be due to pores from removal of the PAN template. H3 hysteresis typically results from agglomerates of rigidly joined plate-like particles giving rise to slit shaped pores. The presence of this morphology was confirmed by SEM images of the large and small beads, shown in Figures 6.37 and 6.38, respectively. Overall, nitrogen porosimetry demonstrated that the titania beads contained hierarchical porosity with both mesopores and macropores. This was also confirmed by the SEM images in Figures 6.37 and 6.38, which showed radial macroporosity from the PAN template as well as a wide size distribution of pore sizes in the titania walls of the beads. Porosity in the surface of the titania beads was also evident via SEM.

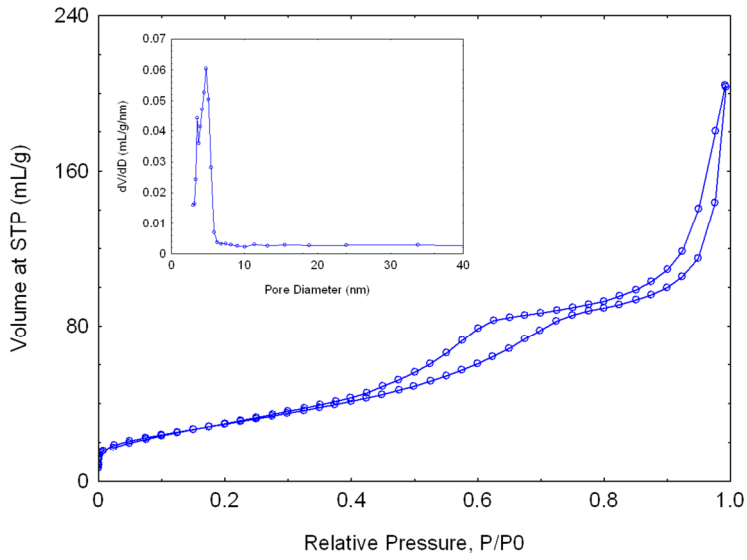

Figure 6.35: Nitrogen adsorption-desorption isotherm for PAN/F127 templated mesoporous 1.0 mm diameter titania beads. Inset: PSD.

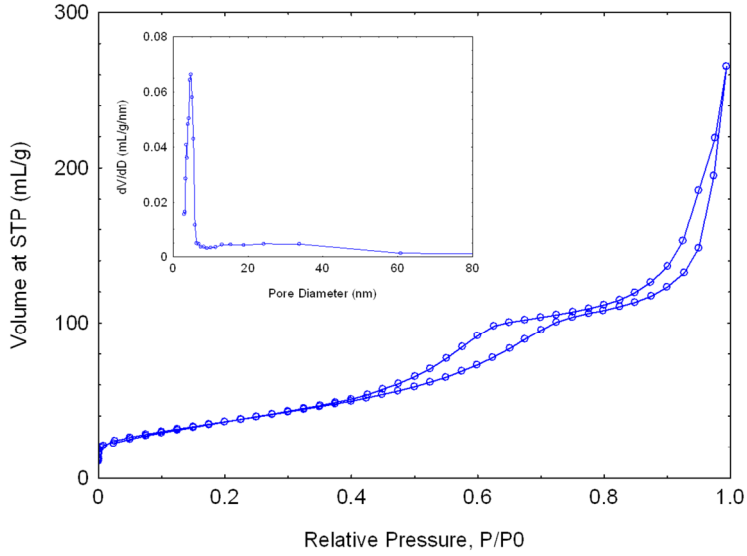

Figure 6.36: Nitrogen adsorption-desorption isotherm for PAN/F127 templated mesoporous 0.5 mm diameter titania beads. Inset: PSD.

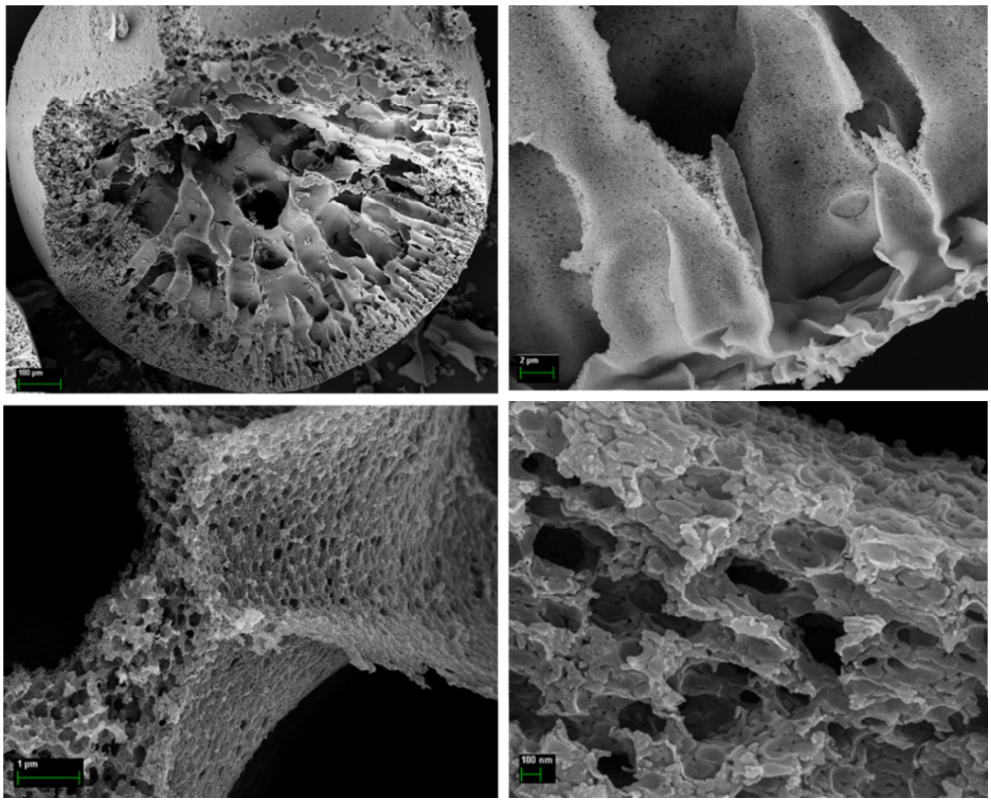

Figure 6.37: SEM images of PAN/F127 templated mesoporous 1.0 mm diameter titania beads

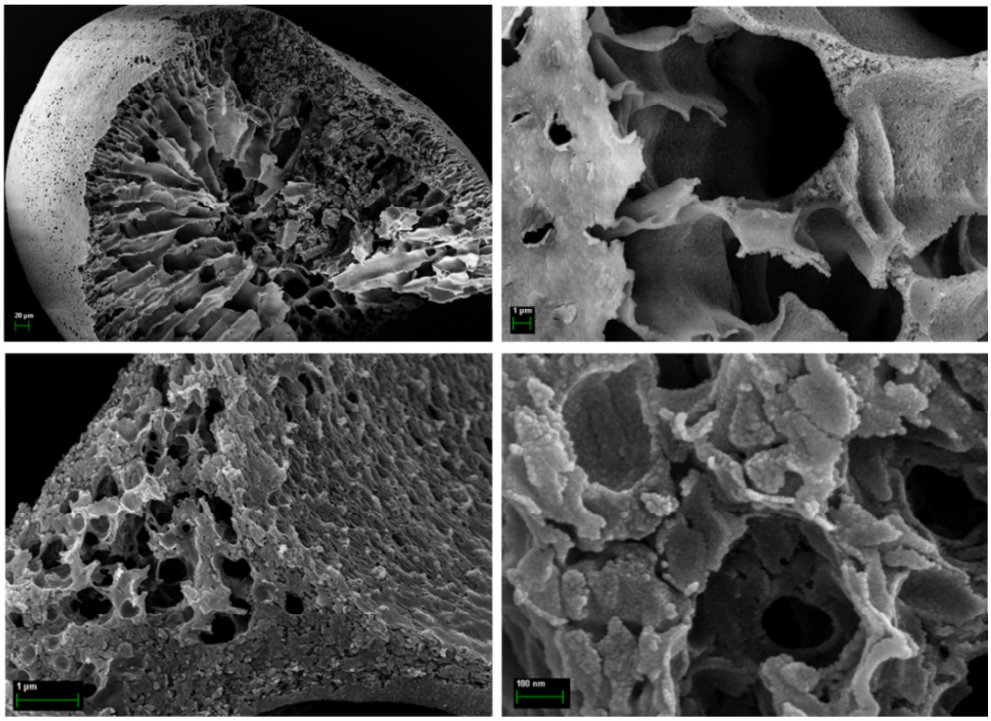

Figure 6.38: SEM images of PAN/F127 templated mesoporous 0.5 mm diameter titania beads

The BET surface area of the 1.0 mm titania beads was 110 m^2/g and the pore volume was 0.32 mL/g. For the 0.5 mm diameter beads, the BET surface area was 140 m^2/g and the pore volume was 0.41 mL/g. The t-plots for both size beads had negative y-axis intercepts,

indicating that there were no micropores. Both bead sizes also had a narrow PSD centred around 50 Å (insets of Figures 6.33 and 6.34). Overall, the 0.5 mm and 1.0 mm titania beads had similar porous structures, but the smaller 0.5 mm beads had slightly greater surface area and pore volume. In comparison with the F127 templated mesoporous titania powder material described in *section 6.5.4*, the BET surface areas of the titania beads were lower but the pore sizes were comparable and the pore volumes were similar or greater for the bead structures.

6.7 Conclusions

Titania powders and beads with ordered mesoporosity were synthesised using the commercially available block copolymer templates Brij 58 and F127 by optimising the conditions of synthesis. Precursor solution composition affected the degree of order in both Brij 58 and F127 templated titania powders, as well as the thermal stability of F127 templated materials. Precursor solution ageing at room temperature was explored for the first time and showed very different behaviour for the Brij 58 and F127 systems. This was a particularly important result given that it provides the first ever evidence of time-dependent Ti structure formation in EISA precursor solutions. Brij 58 precursor solution ageing had a large impact on the order of the structures formed after EISA, with ageing of 6 days producing Ti oxo oligomers of ~12 Å in the precursor solution which were the optimal size to interact with the Brij 58 template so as to form ordered mesostructures. On the other hand, F127 templated systems were unaffected by precursor solution age. This is strong evidence that the choice of template affects the growth and structure of Ti oligomers in the precursor solution, possibly due to the size of the EO blocks in the block copolymer templates.

The optimal evaporation temperature during EISA to produce ordered, stable mesoporous titania powders was also dependent on the choice of template. When using Brij 58, evaporation at 29 ^{o}C produced samples with the greatest order but when using F127, higher temperature evaporation at 37 ^{o}C produced more thermally stable materials. Evaporation time on the other hand had similar effects for Brij 58 and F127 templated materials. That is, increasing evaporation length up to 14 days improved thermal stability in both systems. Optimisation of all these conditions of synthesis enabled production of a substantial quantity of ordered mesoporous titania powder using commercially available block copolymer template F127 without the use of any stabilising additives and with a clean final product for the first time.

As for the mesoporous titania powder materials, the F127 template produced titania beads with greater thermal stability than the Brij 58 template. Using PAN beads and the synthesis conditions found to be optimal for production of ordered mesoprous titania powders, two sizes of titania beads, 0.5 and 1.0 mm in diameter, were produced. These beads demonstrated a hierarchically porous structure with radial macroporosity from the PAN template and ordered mesopores approx. 50 Å in diameter. Therefore these beads, when functionalised, are expected to demonstrate enhanced sorption capacity and mass transfer

kinetics relative to the functionalised titania nanoparticles described in *Chapters 4 and 5*. This, combined with their granular morphology should make the functionalised titania beads of great utility as materials for extraction chromatography.

Overall, a deeper understanding of the factors that control creation of ordered mesoporous titania structures and thermal stability has been achieved. It has been demonstrated that the formation of ordered, thermally stable mesoporous titania is highly sensitive to the choice of template as well as the conditions of synthesis.

6.8 References

(1) Wang, J. G.; Bian, Z. F.; Zhu, J.; Li, H. X. *J Mater Chem A* **2013**, *1*, 1296.

(2) Gu, D.; Schuth, F. *Chemical Society Reviews* **2014**, *43*, 313.

(3) Boettcher, S. W.; Fan, J.; Tsung, C. K.; Shi, Q. H.; Stucky, G. D. *Accounts Chem Res* **2007**, *40*, 784.

(4) Cao, S. W.; Zhu, Y. J. *J Phys Chem C* **2008**, *112*, 6253.

(5) Sizgek, G. D.; Sizgek, E.; Griffith, C. S.; Luca, V. *Langmuir* **2008**, *24*, 12323.

(6) Li, W.; Wu, Z. X.; Wang, J. X.; Elzatahry, A. A.; Zhao, D. Y. *Chem Mater* **2014**, *26*, 287.

(7) Orilall, M. C.; Wiesner, U. *Chemical Society Reviews* **2011**, *40*, 520.

(8) Lianos, P. *J Hazard Mater* **2011**, *185*, 575.

(9) Sizgek, G. D.; Griffith, C. S.; Sizgek, E.; Luca, V. *Langmuir* **2009**, *25*, 11874.

(10) Griffith, C. S.; De Los Reyes, M.; Scales, N.; Hanna, J. V.; Luca, V. *Acs Appl Mater Inter* **2010**, *2*, 3436.

(11) Grosso, D.; Cagnol, F.; Soler-Illia, G. J. D. A.; Crepaldi, E. L.; Amenitsch, H.; Brunet-Bruneau, A.; Bourgeois, A.; Sanchez, C. *Adv Funct Mater* **2004**, *14*, 309.

(12) Grosso, D.; Soler-Illia, G. J. D. A. A.; Babonneau, F.; Sanchez, C.; Albouy, P. A.; Brunet-Bruneau, A.; Balkenende, A. R. *Adv Mater* **2001**, *13*, 1085.

(13) Soler-illia, G. J. D.; Sanchez, C.; Lebeau, B.; Patarin, J. *Chemical Reviews* **2002**, *102*, 4093.

(14) Hung, I. M.; Wang, Y.; Huang, C. F.; Fan, Y. S.; Han, Y. J.; Peng, H. W. *J Eur Ceram Soc* **2010**, *30*, 2065.

(15) Elgh, B.; Yuan, N.; Cho, H. S.; Nilsson, E.; Terasaki, O.; Palmqvist, A. E. C. *J Phys Chem C* **2013**, *117*, 16492.

(16) Samie, L.; Beitollahi, A.; Faal-Nazari, N.; Nejad, M. M. A.; Vinu, A. *J Mater Sci-Mater El* **2011**, *22*, 273.

(17) Luca, V.; Drabarek, E.; Griffith, C. S.; Hanley, T. L. *Chem Mater* **2010**, *22*, 3832.

(18) Crepaldi, E. L.; Soler-Illia, G. J. D. A.; Grosso, D.; Sanchez, M. *New Journal of Chemistry* **2003**, *27*, 9.

(19) Lee, J.; Orilall, M. C.; Warren, S. C.; Kamperman, M.; Disalvo, F. J.; Wiesner, U. *Nat Mater* **2008**, *7*, 222.

(20) Sun, Y.; Ndifor-Angwafor, N. G.; Riley, D. J.; Ashfold, M. N. R. *Chem Phys Lett* **2006**, *431*, 352.

(21) Zhou, W.; Sun, F. F.; Pan, K.; Tian, G. H.; Jiang, B. J.; Ren, Z. Y.; Tian, C. G.; Fu, H. G. *Adv Funct Mater* **2011**, *21*, 1922.

(22) Zimny, K.; Ghanbaja, J.; Carteret, C.; Stebe, M. J.; Blin, J. L. *New Journal of Chemistry* **2010**, *34*, 2113.

(23) Zhang, J. Y.; Deng, Y. H.; Gu, D.; Wang, S. T.; She, L.; Che, R. C.; Wang, Z. S.; Tu, B.; Xie, S. H.; Zhao, D. Y. *Adv Energy Mater* **2011**, *1*, 241.

(24) Zhang, R. Y.; Tu, B.; Zhao, D. Y. *Chem-Eur J* **2010**, *16*, 9977.

(25) Barksdale, J. *Titanium: Its Occurrence, Chemistry and Technology*; 2nd ed.; Ronald Press: New York, 1966.

(26) Yang, P. D.; Zhao, D. Y.; Margolese, D. I.; Chmelka, B. F.; Stucky, G. D. *Nature* **1998**, *396*, 152.

(27) Tian, B. Z.; Yang, H. F.; Liu, X. Y.; Xie, S. H.; Yu, C. Z.; Fan, J.; Tu, B.; Zhao, D. Y. *Chem Commun* **2002**, 1824.

(28) Hwang, J.; Kim, J.; Ramasamy, E.; Choi, W.; Lee, J. *Micropor Mesopor Mat* **2011**, *143*, 149.

(29) *Synlett* **2011**.

(30) Drisko, G. L.; Kimling, M. C.; Scales, N.; Ide, A.; Sizgek, E.; Caruso, R. A.; Luca, V. *Langmuir* **2010**, *26*, 17581.

(31) Ma, T. Y.; Lin, X. Z.; Yuan, Z. Y. *Chem-Eur J* **2010**, *16*, 8487.

(32) Kimling, M. C.; Caruso, R. A. *J Mater Chem* **2012**, *22*, 4073.

(33) Moller, T.; Bestaoui, N.; Wierzbicki, M.; Adams, T.; Clearfield, A. *Appl Radiat Isotopes* **2011**, *69*, 947.

(34) Bellezza, F.; Cipiciani, A.; Costantino, U.; Marmottini, F. *Langmuir* **2006**, *22*, 5064.

(35) Li, H.; Wang, J. S.; Li, H. Y.; Yin, S.; Sato, T. *Mater Lett* **2009**, *63*, 1583.

(36) Luca, V.; Soler-Illia, G. J. A. A.; Angelome, P. C.; Steinberg, P. Y.; Drabarek, E.; Hanley, T. L. *Micropor Mesopor Mat* **2009**, *118*, 443.

(37) Yuan, Q.; Liu, Y.; Li, L. L.; Li, Z. X.; Fang, C. J.; Duan, W. T.; Li, X. G.; Yan, C. H. *Micropor Mesopor Mat* **2009**, *124*, 169.

(38) Guinier, A. F., G. *Small angle scattering of X-rays*; Wiley: New York, 1955.

(39) Benoit, H. *Comptes Rendus* **1957**, *245*, 2244

(40) Hammouda, B. *Adv Polym Sci* **1993**, *106*, 87.

(41) Glatter, O. K., O. *Small Angle X-ray Scattering*; Academic Press: London, 1982.

(42) Svergun, D. I. *Biophys J* **1999**, *77*, 2896.

(43) Nisson, E.; Sakamoto, Y.; Palmqvist, A. E. C. *Chem Mater* **2011**, *23*, 2781.

(44) Herregods, S. J. F.; Mertens, M.; Van Havenbergh, K.; Van Tendeloo, G.; Cool, P.; Buekenhoudt, A.; Meynen, V. *J Colloid Interf Sci* **2013**, *391*, 36.

(45) *Handbook of Nanophysics: Nanoaparticles and Quantum Dots*; Sattler, K. D., Ed.; Taylor and Fracid Group: Boca Raton, 2010.

(46) Borchert, H.; Shevehenko, E. V.; Robert, A.; Mekis, I.; Kornowski, A.; Grubel, G.; Weller, H. *Langmuir* **2005**, *21*, 1931.

(47) Blanchard, J.; Ribot, F.; Sanchez, C.; Bellot, P. V.; Trokiner, A. *J Non-Cryst Solids* **2000**, *265*, 83.

(48) Neyshtadt, S.; Jahnke, J. P.; Messinger, R. J.; Rawal, A.; Peretz, T. S.; Huppert, D.; Chmelka, B. F.; Frey, G. L. *J. Am. Chem. Soc.* **2011**, *133*, 10119.

(49) Schefer, J.; Mcdaniel, R.; Schoenborn, B. P. *J Phys Chem-Us* **1988**, *92*, 729.

(50) Tomsic, M.; Bester-Rogac, M.; Jamnik, A.; Kunz, W.; Touraud, D.; Bergmann, A.; Glatter, O. *J Colloid Interf Sci* **2006**, *294*, 194.

(51) Soni, S. S.; Brotons, G.; Bellour, M.; Narayanan, T.; Gibaud, A. *J Phys Chem B* **2006**, *110*, 15157.

(52) Sarkar, B.; Ravi, V.; Alexandridis, P. *J Colloid Interf Sci* **2013**, *390*, 137.

(53) Assaker, K.; Carteret, C.; Durand, P.; Aranda, L.; Stebe, M. J.; Blin, J. L. *J Phys Chem C* **2013**, *117*, 16500.

(54) Assaker, K.; Carteret, C.; Lebeau, B.; Marichal, C.; Vidal, L.; Stebe, M. J.; Blin, J. L. *Acs Sustain Chem Eng* **2014**, *2*, 120.

(55) Robben, L.; Ismail, A. A.; Lohmeier, S. J.; Feldhoff, A.; Bahnemann, D. W.; Buhl, J. C. *Chem Mater* **2012**, *24*, 1268.

(56) Zhang, B. L.; Clearfield, A. *J. Am. Chem. Soc.* **1997**, *119*, 2751.

(57) Patterson, A. *Physical Review* **1939**, *56*, 978.

(58) Weng, W.; Higuchi, T.; Suzuki, M.; Fukuoka, T.; Shimomura, T.; Ono, M.; Radhakrishnan, L.; Wang, H. J.; Suzuki, N.; Oveisi, H.; Yamauchi, Y. *Angew Chem Int Edit* **2010**, *49*, 3956.

(59) Li, Z. X.; Shi, F. B.; Zhang, T.; Wu, H. S.; Sun, L. D.; Yan, C. H. *Chem Commun* **2011**, *47*, 8109.

(60) Fan, J.; Boettcher, S. W.; Stucky, G. D. *Chem Mater* **2006**, *18*, 6391.

Chapter 7: Titania Nanoparticles and Beads Covalently Functionalised with Bistriazinylpyridine (BTP) Ligands

Covalent functionalization of titania nanoparticles to induce selectivity has been achieved in *Chapters 4 and 5* and hierarchically porous titania beads with ordered mesoporosity were developed in *Chapter 6*. Therefore, in this chapter, covalent functionalization of titania beads will be performed and their sorption performance will be compared to that of titania nanoparticles functionalised with the same organic ligand. The higher surface area and hierarchical porosity, including ordered mesoporosity, of the titania beads relative to nanoparticles is expected to improve the capacity and mass transport properties of sorption.[1,2] In addition, bead morphologies are considered desirable for solid phase sorption materials as they allow close packing in chromatographic columns with minimal clogging and high ease of handling.[3]

The ligand to be used for covalent functionalization is a bistriazinylpyridine (BTP). This functional group was chosen because the highest minor actinide (MA)-lanthanide (Ln) separation factors (SF) achieved under realistic nitric acid nuclear reprocessing conditions were seen with the BTP ligand $CyMe_4$-BTP (Figure 7.1), with $SF_{Am/Eu}$ ~5600.[4] The MA-Ln separation is important because it is required in order to transmutate the long-lived and radiotoxic MA in used nuclear fuel into stable isotopes so that the hazards associated with long-term storage of used nuclear fuel are substantially reduced.[5] In solvent extraction, the high Am distribution coefficient of $CyMe_4$-BTP (K_d ~500) makes stripping difficult. In addition, the extraction is slow and BTP ligands are susceptible to radiolysis.[6] Immobilisation of the ligand on a titania based solid support framework should ameliorate these effects. For example, stripping is no longer necessary as the MA loaded functionalised titania sorbent can be used as a transmutation matrix or wasteform. In this scenario the sorbent would be single use only, so the detrimental effect of radiolysis of the extractant would also be largely defunct. In addition, the slow kinetics of solvent extraction with BTP ligands is due to their surface inactivity at the aqueous-organic interface,[7] where the chemical complexation reaction takes place.[8] This interface does not exist for a separation using a solid phase sorbent. Therefore the kinetics of extraction may be expected to be substantially improved for a functionalised solid phase sorbent.

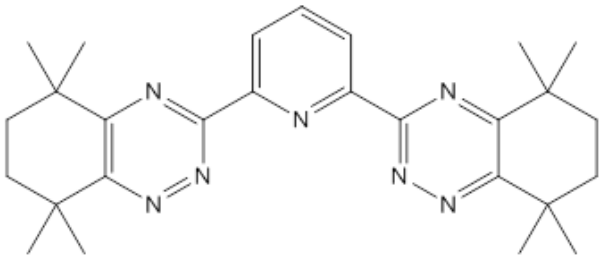

Figure 7.1: Chemical structure of $CyMe_4$-BTP ligand for MA-Ln separation

Since radiolysis of the organic extractant is of minimal concern for a once-through process using a functionalised solid sorbent, a BTP extractant with methyl substituents (Me-BTP) rather than $CyMe_4$ groups at the 5,6 positions of the triazinyl rings was chosen for functionalization. The method for synthesis of 5,6 triazinyl substituents ($CyMe_4$ or methyl) on the BTP ligand is shown in Scheme 7.1. Using methyl substituents substantially decreases the synthetic effort required since the 3,3,6,6-tetramethyl-cyclohexane-1,2-dione required to make the $CyMe_4$ substituents is produced via a three step synthesis[9] whereas the 2,3-butanedione required to make the methyl substitutents is commercially available.

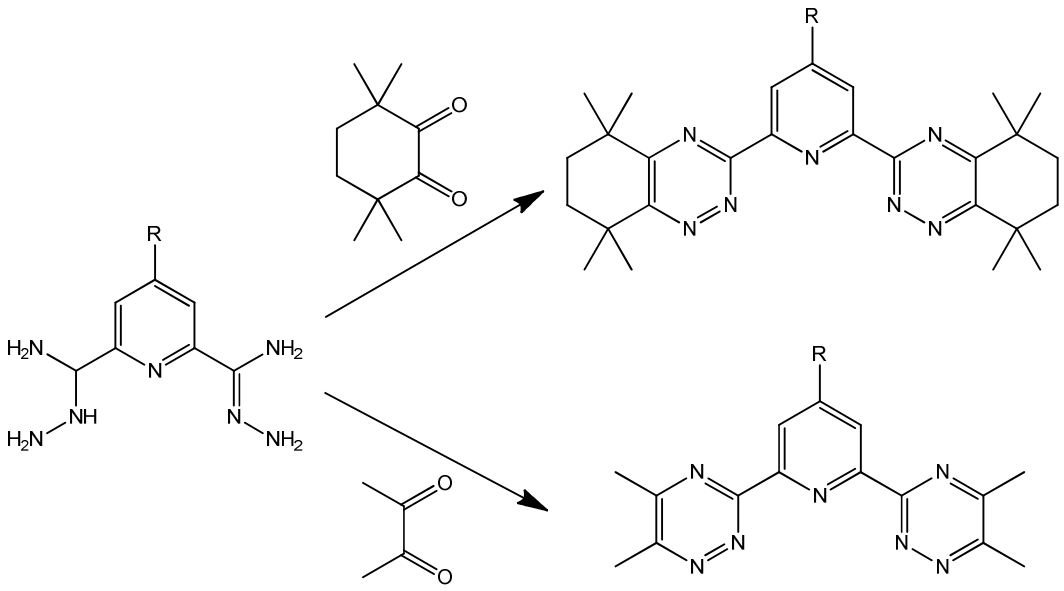

Scheme 7.1: Formation of 5,6 triazinyl substitutents on BTP. Reaction conditions: 4 equiv. dione, 1.3 equiv Et_3N, THF, reflux.

In order to attach the Me-BTP ligand to a surface, modification at the R position shown in Scheme 7.1 was required. This modification has been described previously in the only other example of covalent functionalization with a BTP molecule, which was onto a gold surface to be used as a Ln sensor.[10] For the gold surface functionalization, butylamine modified BTP was covalently linked to 11-mercaptoundecanoic acid that had been previously self-assembled on the gold surface, as shown in Scheme 7.2. For the titania functionalization in

the present work, R was chosen to be an O-undecene substituent, to give 4-(11-undecen-1-yloxy)-2,6-bis(5,6-dimethyl-1,2,4-triazin-3-yl)pyridine (Me-BTP-O-undecene), shown in Figure 7.2. The alkene terminated aliphatic alkyl chain was introduced in order to induce self-assembly and enable covalent attachment at the titania surface, as described in *Chapter 4*. The oxygen atom was introduced because previous work has shown that increasing the BTP ligand basicity by introducing a methoxy group at the R position increased the distribution coefficient and the $SF_{Am/Eu}$ it could achieve.[11,12]

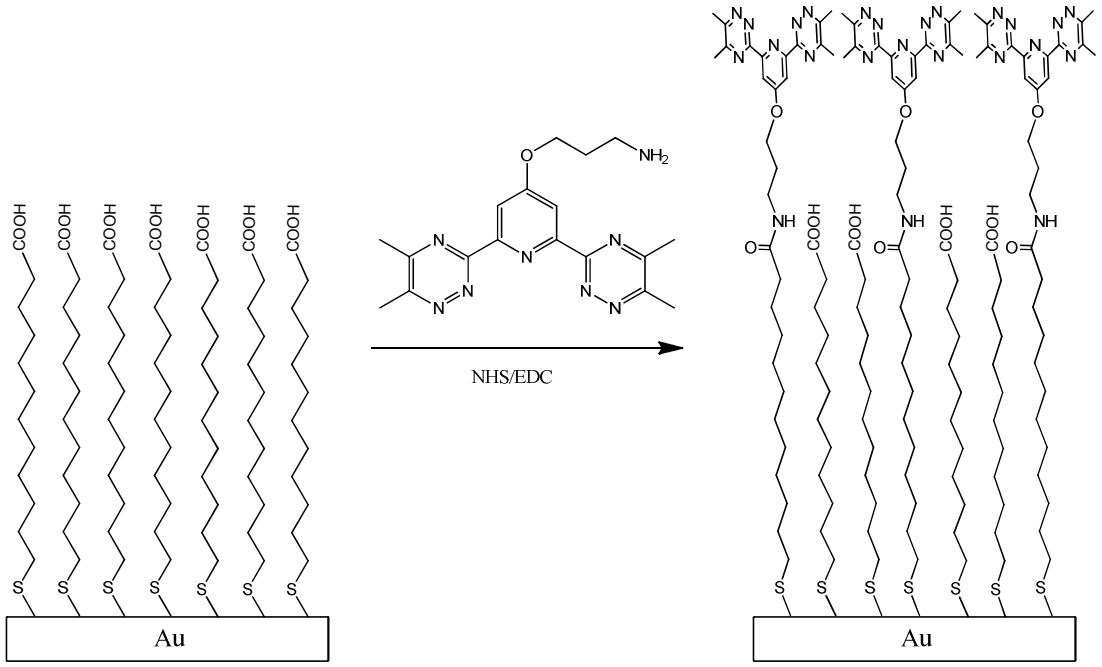

Scheme 7.2: Functionalisation of gold surface with butylamine modified BTP.[10]

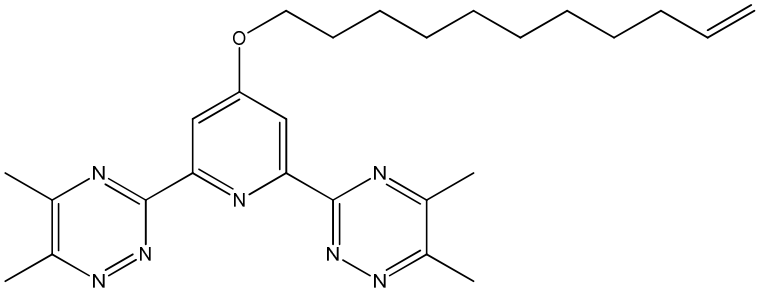

Figure 7.2: Chemical structure of the Me-BTP-O-undecene ligand

During functionalization of titania nanoparticles and beads, 1-undecene was used to 'fill' between the Me-BTP-O-undecene molecules, as shown in Figure 7.3. This 'filler' was intended to prevent interruption of the self-assembly of the alkyl chains that might occur due to the steric of the BTP functional group. Functionalisation with three different ratios of Me-BTP-O-undecene to 1-undecene was performed on the titania nanoparticles in order to determine the optimal packing density; 1:2 (NP-BTP2), 1:4 (NP-BTP4) and 1:8 (NP-BTP8). The optimal ratio was then used for functionalization of the titania beads.

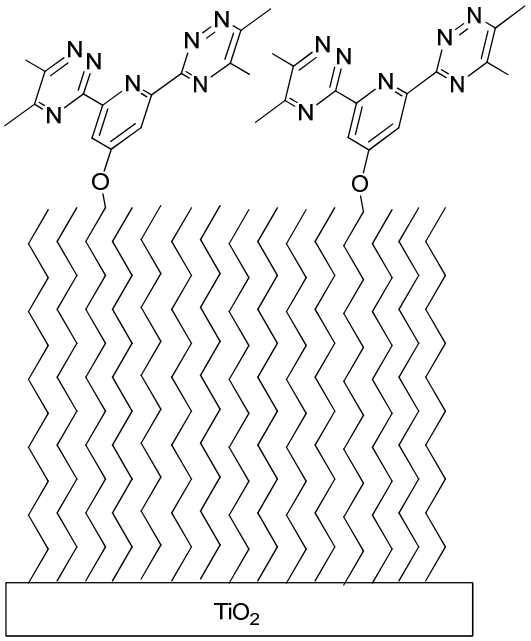

Figure 7.3: Titania functionalised with Me-BTP-O-undecene and 1-undecene in a 1:8 ratio.

In this chapter, the synthesis and characterisation of the Me-BTP-OH ligand and its modification with a long-chain alkene to allow grafting to the titania surface are described. Details of the functionalisation of the titania nanoparticles and hierarchically porous titania beads with the resulting Me-BTP-O-undecene ligand are also provided. Finally, sorption experiments will be performed using the functionalised titania nanoparticles and beads with the MA americium (Am) and the Ln europium (Eu) in 0.01-0.1 M nitric acid. The selectivity, capacity and kinetics of sorption using the functionalised titania nanoparticles and beads are compared to elucidate whether the more complex porous bead framework provides enhanced performance, as expected. Also, the MA-lanthanide separation achieved by these BTP functionalised titania materials is compared to other materials and solvent extraction processes using similar BTP ligands.

7.1 Experimental Methods

7.1.1 Synthesis of 2,6-Bis(5,6-dimethyl-1,2,4-triazin-3-yl)-4-hydroxypyridine (Me-BTP-OH, 22)

The synthesis of the BTP derivative Me-BTP-OH described by Mercier et al. (2010)[10] was reproduced and is represented in Scheme 7.3.

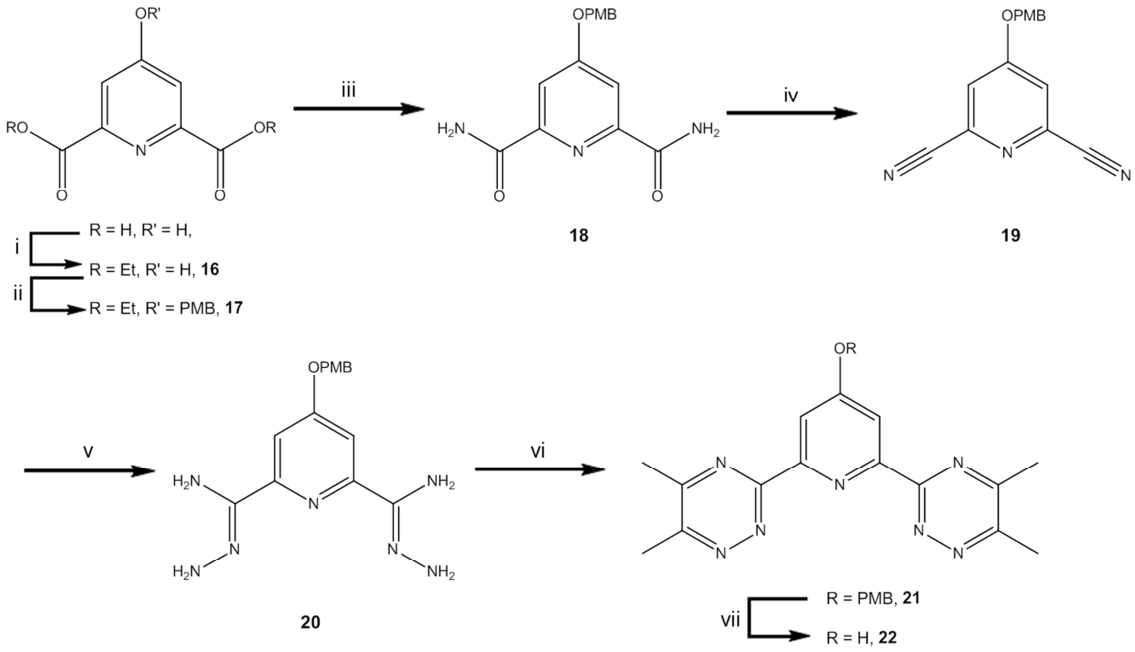

Scheme 7.3: Synthesis of Me-BTP-OH. Conditions: (i) H_2SO_4, EtOH; (ii) K_2CO_3, *p*-methoxybenzyl chloride, CH_3CN; (iii) aqueous ammonia, MeOH; (iv) pyridine, trifluoroacetic acid, CH_2Cl_2; (v) hydrated hydrazine, EtOH; (vi) 2,3-butanedione, Et_3N, tetrahydrofuran; (vii) anisole, trifluoroacetic acid, CH_2Cl_2.

Diethyl-4-hydroxypyridine-2,6-dicarboxylate (**16**)

Chelidamic acid monohydrate (10.1 g, 50.2 mmol) was reacted with concentrated sulphuric acid (0.2 equiv.) in ethanol (EtOH, 300 mL) under reflux for 25 h then worked up as described previously. The crude product was purified by flash chromatography on silica gel (95:5 CH_2Cl_2:MeOH) to afford pure compound **16** as a white, crystalline solid (9.83 g, 82 % yield). ^{1}H NMR (400 MHz, MeOD) δ (ppm): 7.58 (s, 2H), 4.46 (q, *J* = 7.0 Hz, 4H), 1.45 (t, *J* = 7.0 Hz, 6H). Characterisation data was consistent with previous results.

Diethyl-4-(4-methoxybenzyloxy)pyridine-2,6-dicarboxylate (**17**)

A solution of **16** (3.8 g, 16.1 mmol), potassium carbonate (5.0 equiv.) and *p*-methoxybenzyl chloride (1.1 equiv.) in acetonitrile (ACN, 190 mL) was refluxed under inert atmosphere with vigorous stirring for 41 h. After workup of the reaction as described previously, purification by flash chromatography on silica gel (98:2 CH_2Cl_2:MeOH) afforded pure compound **17** as a white solid (5.0 g, 87 % yield). ^{1}H NMR (400 MHz, $CDCl_3$) δ (ppm): 7.82 (s, 2H), 7.35 (d, *J* = 8.8 Hz, 2H), 6.94 (d, *J* = 8.8 Hz, 2H), 5.13 (s, 2H), 4.47 (q, *J* = 7.2 Hz, 4H), 3.82 (s, 3H), 1.45 (t, *J* = 7.2 Hz, 6H). Characterisation data was consistent with previous results.

4-(4-Methoxybenzyloxy)pyridine-2,6-dicarboxamide (**18**)

A suspension of **17** (2.72 g, 7.57 mmol) and aqueous ammonia (20.0 equiv.) in MeOH (23 mL) was stirred at room temperature for 24 h then filtered and dried as described previously afforded compound **18** as a white solid (1.5 g, 64 % yield). ^{1}H NMR (400 MHz,

DMSO-d_6) δ (ppm): 8.81 (br s, NH), 7.70 (s, 2H), 7.39 (d, *J* = 8.7 Hz, 2H), 6.96 (d, *J* = 8.7 Hz, 2H), 5.24 (s, 2H), 3.73 (s, 3H). Characterisation data was consistent with previous results.

2,6-dicyano-4-(4-methoxybenzyloxy)pyridine (**19**)

A suspension of **18** (1.0 g, 3.3 mmol), pyridine (4.4 equiv.) and trifluoroacetic anhydride (2.2 equiv.) in CH_2Cl_2 (125 mL) was stirred under inert atmosphere at room temperature for 21 h (dissolution was apparent after approx. 2 h). The reaction mixture was worked up as described previously to afford the crude product as a light brown solid. Purification by flash chromatography (CH_2Cl_2 then 85:15 CH_2Cl_2:ethyl acetate) afforded pure compound **19** as a white solid (0.70 g, 78 % yield). ^{1}H NMR (400 MHz, $CDCl_3$) δ (ppm): 7.43 (s, 2H), 7.34 (d, *J* = 8.8 Hz, 2H), 6.98 (d, *J* = 8.8 Hz, 2H), 5.17 (s, 2H), 3.87 (s, 3H). Characterisation data was consistent with previous results.

(4-Methoxybenzyloxy)pyridine-2,6-biscarbamidrazone (**20**)

A solution of **19** (1.1 g, 4.1 mmol) in EtOH (70 mL) at 60 °C was mixed with hydrated hydrazine (34.4 equiv.) then cooled to room temperature. After stirring under inert atmosphere for 27 h the resulting white precipitate was filtered and the residue rinsed with EtOH (approx. 10 mL) to afford pure compound **20** as a white solid (1.2 g, 86 % yield). ^{1}H NMR (400 MHz, DMSO-d_6) δ (ppm): 7.41 (s, 2H), 7.37 (d, *J* = 8.7 Hz, 2H), 6.95 (d, *J* = 8.7 Hz, 2H), 5.10 (s, 2H), 3.76 (s, 3H). Characterisation data was consistent with previous results.

2,6-Bis(5,6-dimethyl-1,2,4-triazin-3-yl)-4-(4-methoxybenzyloxy)pyridine (**21**)

A solution of **20** (0.72 g, 2.2 mmol), triethylamine (1.3 equiv.) and 2,3-butanedione (3.0 equiv.) in tetrahydrofuran (THF, 16 mL) was refluxed for 6 h then cooled, filtered and washed as described previously to afford BTP **21** as an off-white solid (0.81 g, 89 % yield). ^{1}H NMR (400 MHz, $CDCl_3$) δ (ppm): 8.46 (s, 2H), 7.47 (d, *J* = 8.7 Hz, 2H), 6.98 (d, *J* = 8.7 Hz, 2H), 5.33 (s, 2H), 3.86 (s, 3H), 2.81 (s, 6H), 2.76 (s, 6H). Characterisation data was consistent with previous results.

2,6-Bis(5,6-dimethyl-1,2,4-triazin-3-yl)-4-hydroxypyridine (Me-BTP-OH, **22**)

A solution of **21** (0.50 g, 1.2 mmol), anisole (10 equiv.) and trifluoroacetic acid (5.1 equiv.) in CH_2Cl_2 (21 mL) was stirred at room temperature, under inert atmosphere, for 4 h. The reaction mixture was worked up as described previously to afford pure BTP **22** (Me-BTP-OH) as an orange solid (0.31 g, 84 % yield).). ^{1}H NMR (400 MHz, DMSO-d_6) δ (ppm): 7.80 (s, 2H), 2.72 (s, 6H), 2.64 (s, 6H). Characterisation data was consistent with previous results.

7.1.2 Synthesis of 4-(11-undecen-1-yloxy)-2,6-bis(5,6-dimethyl-1,2,4-triazin-3-yl)pyridine (Me-BTP-O-undecene, 23)

1-Bromo-11-undecene (81 mg, 0.35 mmol) and potassium carbonate (0.24 g, 1.7 mmol) were added to a solution of 2,6-bis(5,6-dimethyl-1,2,4-triazin-3-yl)-4-hydroxypyridine (0.11 g, 0.34 mmol) in dimethylformamide (DMF, 12 mL). The reaction mixture was stirred under reflux for 4 h. The solvent was then removed under reduced pressure and the resulting dark green solid resuspended in CH_2Cl_2 before filtration. The residue was rinsed with CH_2Cl_2

(approx. 10 mL) and the filtrate then removed under reduced pressure to afford the crude product as a dark green oil. Purification by flash chromatography (CH_2Cl_2 then 98:2 CH_2Cl_2:MeOH) afforded pure **23** (Me-BTP-O-undecene) as a yellow oil (46 mg, 29 % yield). HRMS (ESI) calcd for $C_{26}H_{35}N_7O$ $[M+Na]^+$ *m/z* 484.2801, found 484.2796. ^{1}H NMR (400 MHz, $CDCl_3$) δ (ppm): 8.33 (s, 2H), 5.81 (m, 1H), 4.97 (m, 2H), 4.25 (t, *J* = 6.6 Hz, 2H), 2.79 (s, 6H), 2.71 (s, 6H), 2.05 (dt, *J* = 7.2, 6.8 Hz, 2H), 1.89 (tt, *J* = 7.4, 6.6 Hz, 2H), 1.50 (m, 2H), 1.45-1.20 (m, 10H). ^{13}C NMR (100 MHz, $CDCl_3$) δ (ppm): 167.3, 161.3, 159.7, 157.2, 154.9, 139.2, 114.1, 111.9, 68.8, 33.8, 29.5, 29.4, 29.3, 29.1, 28.9, 25.9, 21.9, 19.7 (1 signal obscured or overlapping). IR (ATR, neat): ν_{max} 3362, 3074, 2922, 2851, 1675, 1640, 1591, 1571, 1535, 1426, 1388, 1359, 1333, 1308, 1240, 1194, 1161, 1128, 1091, 1033, 1010, 991, 976, 905, 872, 831, 796, 735 cm^{-1}.

7.1.3 Functionalisation

Functionalisation of titania nanoparticles with 1-undecene to give 'NP-alkyl', or with Me-BTP-O-undecene : 1-undecene at a ratio of 1:2, 1:4 or 1:8 to give 'NP-BTP2', 'NP-BTP4' and 'NP-BTP8', respectively, was performed as described in *Chapter 4*. For example, to synthesise NP-BTP4, dry titania nanoparticles (0.21 g) were mixed with a dry, degassed solution of Me-BTP-O-undecene (19 mg, 0.041 mmol) and 1-undecene (25 mg, 0.18 mmol) in mesitylene (2.0 mL) under nitrogen. The resulting suspension was heated in an oil bath at 115 ^{o}C for 24 h, with stirring, then filtered. The residue was washed with petroleum ether (approx. 3 mL), MeOH (approx. 3 mL) and CH_2Cl_2 (approx. 3 mL) before drying under vacuum, affording the functionalised nanoparticles (NP-BTP4) as a light brown powder (0.19 g).

Functionalisation of hierarchically porous titania beads with 1:4 Me-BTP-O-undecene : 1-undecene was performed similarly to the titania nanoparticles, but without stirring to prevent mechanical degradation of the bead structures. Titania beads of diameter 0.5 mm (52 mg) or 1.0 mm (80 mg) were first contacted with a degassed solution of Me-BTP-O-undecene (9 mg, 0.019 mmol) and 1-undecene (12 mg, 0.078 mmol) in mesitylene (1.0 mL) under nitrogen atmosphere at room temperature for 5 h. Infiltration of the beads was evident as they sunk in the mesitylene solutions. The bead suspensions were then heated in an oil bath at 110 ^{o}C for 22 h. The solution was then decanted from the beads via glass pipette and the titania beads washed with petroleum ether (approx. 3 mL), MeOH (approx. 3 mL) and CH_2Cl_2 (approx. 3 mL). This afforded functionalised small 0.5 mm diameter titania beads (51 mg), designated as 'SB-BTP', as well as functionalised large 1.0 mm diameter titania beads (85 mg), designated as 'LB-BTP', both of which were pale brown in colour.

7.1.4 Sorption Methodology

To prepare 10 ppb Am-241 solutions, 28 µL aliquots of a Am-241 stock solution (2.1 MBq/mL, 3 M nitric acid, specific activity Am-241 = 118.4 MBq/mg) were diluted to 50 mL with either 0.1 M (pH 1) or 0.01 M (pH 2) nitric acid. To prepare the pH 2 10 ppb Eu solution,

a 3.6 mL spike of Eu-152 stock solution (1.0 kBq/mL, specific activity Eu-152 = 6.7 GBq/mg) and 20 µL of 10 ppm carrier Eu were diluted to 20 mL with 0.01 M nitric acid. Individual element sorption experiments were performed with pH 1-2 Am-241 solutions and with pH 2 spiked Eu-152 solutions. For NP-BTP, SB-BTP and LB-BTP, batch sorption experiments were performed using 0.005 g of beads and 1.0 mL solution, giving a solid-to-liquid ratio of 200. Each experiment was performed in duplicate. Samples were shaken on a vertical mixer at a constant speed of approx. 10 rpm for a period of 24 h. Errors in the reported partition coefficient (K_d) values were calculated from the standard deviation of the gamma counting results. If the standard deviation was less than 1 % of the measured K_d, an error of 1 % was applied. If the error for a K_d was larger than the K_d itself (for example 0.4 ± 3.0), the K_d value was reported as 1 since this was considered the minimum measurable K_d given the accuracy of a gamma counter measurement.

7.2 Characterisation

Synthesis and characterisation of the titania nanoparticles and the hierarchically porous titania beads used as framework materials for functionalization are described in *Chapters 4 and 6*, respectively.

To confirm the functionalisation of the titania nanoparticles and beads, solid-state ^{13}C-^{1}H CP MAS-NMR was performed on NP-alkyl, NP-BTP4 and SB-BTP and the results are shown in Figure 7.4. Peaks were present in the NMR spectra of all three functionalised titania materials, which confirmed that functionalization was successful since no peaks were seen in the solid-state ^{13}C-^{1}H CP MAS-NMR spectrum of non-functionalised titania nanoparticles (see *Chapter 4*). Peaks with chemical shift 15-45 ppm, due to aliphatic CH_2 groups,[13] were seen in the NMR spectra of NP-alkyl, NP-BTP4 and SB-BTP as both the 1-undecene and Me-BTP-O-undecene ligands used for functionalisation contained alkyl chains. Since the alkyl chain was the only carbon containing functionality present in NP-alkyl, no other peaks were seen in its NMR spectrum. However, the NMR spectrum of NP-BTP4 and SB-BTP also showed a peak with a chemical shift of approx. 70 ppm, which was assigned as the CH_2-O moiety in the Me-BTP-O-undecene ligand.[13] Therefore the ^{13}C-^{1}H CP MAS NMR spectra also confirmed the presence of the Me-BTP-O-undecene ligand on the surface of NP-BTP4 and SB-BTP.

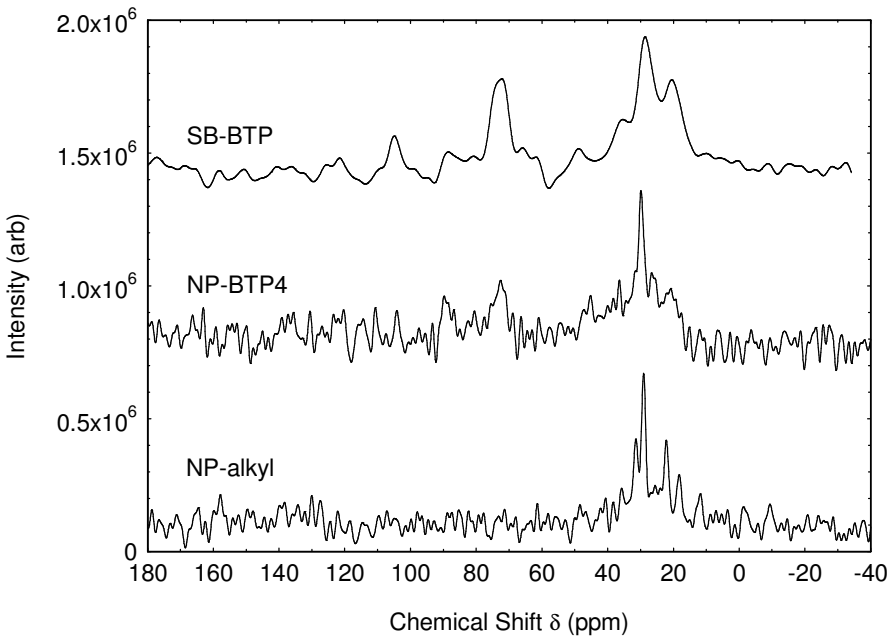

Figure 7.4: ^{13}C-^{1}H CP MAS NMR spectra of NP-alkyl and NP-BTP4

The level of functionalization of NP-BTP4, SB-BTP and LB-BTP was quantitatively determined by CHN microanalysis (Table 7.1). It was assumed that for every molecule of Me-BTP-O-undecene ($C_{26}H_{35}N_7O$) present there were 4 molecules of 1-undecene ($C_{11}H_{22}$) also present, so that the overall molecular formula of the organic functional groups was $C_{70}H_{123}N_7O$. The molecular formulae of the organic functionalised molecules and the total measured %CHN were used to determine the calculated %CHN values, which agreed with the experimentally measured values to within 0.2 %. The total organic content of the Me-BTP-O-undecene functionalised titania nanoparticles and beads were then calculated as the percentage weight of CHNO. CHN analysis was not performed for NP-BTP2 and NP-BTP8 because with a total organic content of 1.7 %, the difference in the percentage of C, H and N would be less than 0.1 % for the different Me-BTP-O-undecene : 1-undecene ratios and hence would be undetectable.

Table 7.1: Elemental CHN microanalysis of Me-BTP-O-undecene functionalised titania nanoparticles and beads (weight %)

Measured	**NP-BTP4**	**SB-BTP**	**LB-BTP**
%C	1.1	2.6	2.4
%H	0.3	0.5	0.4
%N	0.3	0.2	0.2
Total	1.7	3.3	3.0
Calculated	**$C_{70}H_{123}N_7O$**	**$C_{70}H_{123}N_7O$**	**$C_{70}H_{123}N_7O$**
%C	1.3	2.6	2.3
%H	0.2	0.4	0.3
%N	0.2	0.3	0.3
Total (organic)	1.7	3.4	3.0

Assuming a 1:4 Me-BTP-O-undecene : 1-undecene molecular ratio on the surface of NP-BTP4, the Me-BTP-O-undecene should account for 42.8 % of the total organic mass and the 1-undecene 57.2 %. For NP-BTP, this equates to 0.002 mol% Me-BTP-O-undecene and 0.006 mol% 1-undecene in terms of molar percentages. For comparison, the picolinamide functionalised titania nanoparticles (TiO_2-pico) described in *Chapter 4*, which were also designed for MA-Ln separation, had 0.008 mol% organic content. Thus, the level of functionalization of the Me-BTP-O-undecene ligand itself was lower than was seen for TiO_2-pico, but the overall level of functionalization of NP-BTP4 was similar. The calculated area per molecule (with a titania nanoparticle surface area of 55 m^2/g) was 1.2 nm^2 for NP-BTP4. This was a similar molecular density to what was seen for the organo-functionalised titania nanoparticles described in *Chapter 4.*

For the functionalised titania beads, the percentage organic content was approx. double that of the functionalised titania nanoparticles, indicating that the titania beads had a higher level of functionalisation. This explains the fact that the NMR spectrum of SB-BTP in Figure 7.4 was substantially less noisy than that of NP-BTP4. For SB-BTP, the level of functionalization was 0.003 mol% Me-BTP-O-undecene and 0.013 mol% 1-undecene. For LB-BTP, the level of functionalization was 0.003 mol% Me-BTP-O-undecene and 0.011 mol% 1-undecene. Therefore the average level of functionalization in the titania beads was 0.015 ± 0.001 mol%, approx. double what was seen for NP-BTP4. Since the surface areas of the titania beads (110 m^2/g for the large beads and 140 m^2/g for the small beads) was also approx. double that of the titania nanoparticles (55 m^2/g), a similar molecular density was expected for the functionalised nanoparticles and beads. This was confirmed as the calculated area per molecule was 1.5 nm^2 for SB-BTP and 1.3 nm^2 for LB-BTP.

7.3 Sorption Properties

7.3.1 BTP Functionalised Titania Nanoparticles (NP-BTP)

A comparison of the Am and Eu sorption performance of titania nanoparticles with and without organic functionalization is given in Table 7.2. At pH 1, sorption of Am was negligible with the non-functionalised nanoparticles (NP-NF), NP-alkyl and NP-BTP4. Even in the presence of 10% EtOH, the Am K_d was not increased above 1 for NP-BTP4. At pH 2, NP-NF and NP-alkyl still showed no appreciable sorption of Am. However, NP-BTP4 demonstrated an Am K_d of 28 and $SF_{Am/Eu}$ 28 at pH 2, as Eu was not sorbed. Since TiO_2-NF and TiO_2-alkyl were unable to sorb Am at pH 2, it was inferred that the Me-BTP-O-undecene molecules on the surface of NP-BTP4 were responsible for the selective Am sorption observed, as expected. The observed decrease in Am sorption with pH for NP-BTP4 was contrary to the usual behaviour of BTP extractants in solvent extraction, which is that extraction increases with acidity.[8] It can however be explained by the higher basicity of the Me-BTP-O-undecene ligand relative to BTP itself, due to the electron withdrawing substitutent which has been added at the 4-position of the pyridine ring.[11]

Table 7.2: Partition coefficients (K_d) for sorption of 10 ppb Am and Eu by NP-BTP. x = not measured.

Sorbent	***Solution***	***Am (K_d ± SD)***	***Eu (K_d ± SD)***	***$SF_{Am/Eu}$***
NP-NF	**pH 1**	1	x	
	pH 2	1	1	1
NP-alkene	**pH 1**	1	x	
	pH 2	1	1	1
NP-BTP4	**pH 1**	1	x	
	pH 2	28 ± 4	1	28
	pH 1 + 10% EtOH	1	1	1
	pH 2 + 10% EtOH	56 ± 5	1	56
NP-BTP2	**pH 2 + 10% EtOH**	64 ± 5	1	64
NP-BTP8	**pH 2**	36 ± 5	x	
	pH 2 + 10% EtOH	54 ± 8	1	54
NP-pico	**pH 2**	6.1 ± 4.2	1	6
	pH 2 + 10% EtOH	6.5 ± 4.2	x	

Adding 10 % EtOH to the aqueous Am and Eu solutions at pH 2 increased the K_d for Am by nearly double for NP-BTP4 (Table 7.2). This was initially assumed to be due to improved contact between the hydrophobic organo-functionalised surface and the Am in solution when 10 % EtOH was present. On the other hand, Eu was still not appreciably sorbed by NP-BTP4

when the solution consisted of 10 % EtOH at pH 2. As such, addition of EtOH also increased the separation factor between Am and Eu ($SF_{Am/Eu}$) achieved by NP-BTP4 by nearly double.

The ratio of Me-BTP-O-undecene to 1-undecene in the functionalization solution was both doubled (1:2, NP-BTP2) and halved (1:8, NP-BTP8) to determine if this had any impact on the sorption properties of the material. However, both NP-BTP2 and NP-BTP8 showed similar Am K_d and separation factor values to NP-BTP4 (Table 7.2). One possible explanation for this result is that the ratio of Me-BTP-O-undecene to 1-undecene that actually assembled on the surface of the titania nanoparticles was independent of the ratio that was present in the functionalization solution. Although varying the Me-BTP-O-undecene to 1-undecene did not provide a material with improved sorption properties, it did demonstrate that a lower 1:8 ratio can provide equally high K_d and SF values while using less of the valuable Me-BTP-O-undecene ligand. This was considered a valuable result.

The results in Table 7.2 are all equilibrium measurements from contact times of 24 h. The kinetics of sorption of Am with and without 10 % EtOH using NP-BTP8 are shown in Figure 7.5. From this data it is clear that, in the presence of 10 % EtOH, equilibrium was reached within 1 h and after only 5 min approx. 40 % of the total sorption had occurred. In purely aqueous solution, Am K_d values were consistent with those for the 10 % EtOH solutions until they reached a maximum at 1 h. This indicated that the presence of 10 % EtOH did not improve the kinetics of Am sorption and hence that the presence of EtOH did not in fact improve contact with the NP-BTP surface, as previously thought. The kinetics data in Figure 7.5 also shows that at longer contact times (≥ 8 h), the Am K_d from aqueous solution decreased. Similar kinetic behaviour was also seen in aqueous solution for NP-BTP4, that is sorption was decreased below the maximum upon long contact times. One possible explanation for the loss of Am extraction performance over time in aqueous solution is radiolytic damage or loss of the functional ligands on the titania surface. The fact that there was no performance loss in the 10 % EtOH solutions may be due to the hydroxyl radical scavenging properties of EtOH.[14,15]

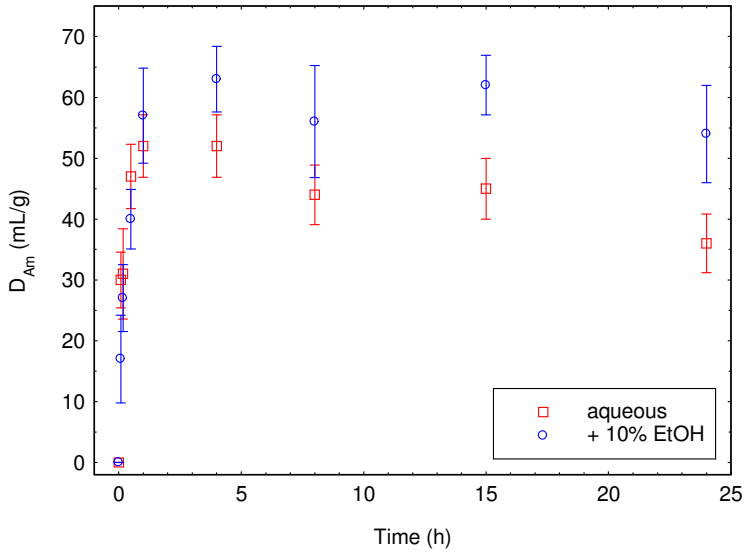

Figure 7.5: Sorption of Am over time at pH 2, with or without 10 % EtOH, using NP-BTP8.

7.3.2 BTP Functionalised Hierarchically Porous Titania Beads

The data in Table 7.3 show the results of Am and Eu sorption experiments with SB-BTP and LB-BTP from solutions both with and without 10 % EtOH. From purely aqueous pH 2 solution, there was a small increase in the Am K_d for LB-BTP relative to SB-BTP. However, there was no significant difference between the large and small beads in terms of Am extraction from pH 2 solutions containing 10 % EtOH. Decreasing the pH to 1 in the presence of 10 % EtOH decreased the Am K_d by approx. an order of magnitude for LB-BTP, but measurable extraction of Am was still possible at pH 1 with the titania beads. There was no significant extraction of Eu for SB-BTP or LB-BTP under any of the conditions tested. Therefore, $SF_{Am/Eu}$ increased linearly with Am K_d.

Table 7.3: Partition coefficients (K_d) for sorption of 10 ppb Am and Eu by SB-BTP and LB-BTP. x = not measured.

Sorbent	***Solution***	***Am (K_d ± SD)***	***Eu (K_d ± SD)***	***$SF_{Am/Eu}$***
SB-BTP	**pH 2**	64 ± 5	1	64
	pH 2 +10% EtOH	159 ± 11	1	159
LB-BTP	**pH 2**	80 ± 6	1	80
	pH 1 +10% EtOH	9.2 ± 4.2	x	
	pH 2 +10% EtOH	163 ± 9	1	163

The functionalised, hierarchically porous titania beads were expected to exhibit higher capacity than the functionalised titania nanoparticles due to their higher surface areas. For sorption experiments from both the aqueous and ethanolic solutions, the K_d for Am doubled with the bead morphology relative to the nanoparticles. However the K_d for Eu remained negligible, so that $SF_{Am/Eu}$ also increased by approx. a factor of two with the bead morphology relative to the nanoparticles. The BET surface area of the titania nanoparticles (55 m^2/g) was

approx. half that of the titania beads (140 and 110 m^2/g for the 0.5 mm and 1.0 mm diameters beads, respectively). Therefore, Am sorption increased proportionally with surface area. This suggests that all of the internal surface area of the titania beads was functionalised, without significant pore blockages, which have previously been shown to occur during functionalization with strong, non-reversible grafting reactions.[16] Overall, the bead morphology was considered superior to the nanoparticles since their higher surface area resulted in higher Am K_d values without any loss of selectivity. Also, as a granular morphology, beads are preferable for solid phase sorption materials as they allow packing in chromatographic columns with minimal clogging and high ease of handling.[3]

The kinetics of Am sorption using the titania beads was also explored. Sorption of Am from pH 2 10 % EtOH solutions was performed for 5 and 30 min using SB-BTP and for 30 min using LB-BTP. For SB-BTP, after 5 min the Am K_d was 97 ± 9 and after 30 min the Am K_d was 166 ± 22. Since the Am K_d for SB-BTP after 24 h under these conditions was 159 ± 11 (Table 7.3), this indicated that approx. 80 % of the total sorption occurred within the first 5 min and sorption equilibrium was reached within 30 min using SB-BTP. For LB-BTP, after 30 min the Am K_d was 139 ± 15. Since the Am K_d for LB-BTP after 24 h under these conditions was 163 ± 9 (Table 7.3), equilibrium was also reached within 30 min using LB-BTP. This demonstrated that the titania bead morphology had faster kinetics of sorption relative to NP-BTP, which required 1 h to reach equilibrium (Figure 7.5). The higher rates of mass transport in the titania beads were attributed their hierarchical and ordered porous structure. Sorption of Am from fully aqueous pH 2 solution was also performed for 30 min using SB-BTP and the measured Am K_d was 182 ± 16. This Am K_d value was nearly three times higher than the value measured after sorption for 24 h (Table 7.3). Thus, the loss of Am extraction performance over time in aqueous solution that was observed for NP-BTP (Figure 7.5), was also present for the functionalised titania beads.

7.3.3 Comparison with Other Processes for MA-Ln Separation using BTP Ligands

For reprocessing of used nuclear fuel, MA-Ln separation is typically required after a group extraction of both MA and Ln from other fission products using a TRUEX or DIAMEX solvent extraction process.[5] Since stripping of the extracted MA and Ln from the loaded organic phase after TRUEX or DIAMEX processing is recommended to be carried out using nitric acid with pH ≥ 1,[17] a MA-Ln separation process that performs well at low acidity may be considered preferable. In terms of solvent extraction, 0.01 M Me-BTP-OMe (**A** in Figure 7.6) in 7:3 kerosene : 1-octanol extracted Am with K_d 61 and $SF_{Am/Eu}$ 61 (assuming a minimum measurable K_d for Eu of 1) from 0.01 M nitric acid + 1 M ammonium nitrate solution.[11] SB-BTP and LB-BTP were able to provide similar performance to this, without the need for any organic solvents or addition of ammonium nitrate to the aqueous phase. In addition, this solvent extraction with Me-BTP-OMe required 90 min to reach equilibrium,[11] whereas SB-BTP and LB-BTP required less than 30 min. Therefore the present solid phase sorbent materials were considered superior to solvent extraction with Me-BTP-OMe.

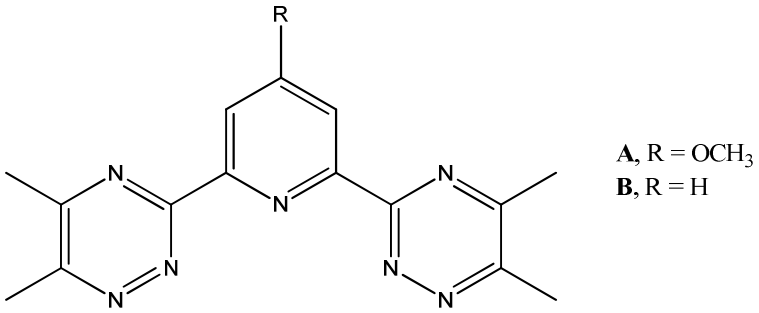

Figure 7.6: Chemical structure of Me-BTP-OMe (A) and Me-BTP (B), which have previously been used for MA-Ln separation via solvent extraction

Without modification of the pyridine ring with an electron withdrawing oxygen substitutent, BTP ligands extract MA more effectively from more acidic solutions.[18,19] This is why 0.01 M Me-BTP (**B** in Figure 7.6) in 7:3 kerosene : 1-octanol extracted Am with a K_d of only 2.1 from 0.01 M nitric acid + 1 M ammonium nitrate solution after 90 min.[11] Ligands that perform MA-Ln separation best at high acidity could be of use for direct extraction of Am from the PUREX raffinate, which is approx. 3 M nitric acid,[20] if selectivity over fission products was also demonstrated. The BTP ligand which has demonstrated the highest $SF_{Am/Ln}$ of ~5600, $CyMe_4$-BTP (Figure 7.1), in n-octanol extracted Am with K_d ~500 from 0.5 M nitric acid after only 15 min when used in conjunction with a malonamide.[6] However, without the malonamide to improve contact between the aqueous and organic phases, $CyMe_4$-BTP extracted Am with a K_d of only 3.9 after 60 min under the same conditions and had still not reached equilibrium.[6] Thus, the BTP functionalised titania materials developed in this work, SB-BTP and LB-BTP, demonstrated more effective, selective and faster Am extraction than solvent extraction using BTP ligands unless a phase modifier was used in the solvent extraction process.

Solid phase materials functionalised with BTP based ligands including $CyMe_4$-BTPhen, $CyMe_4$-BTP and *i*Bu-BTP (Figure 7.7) have previously been used for MA-Ln separation and a summary of the performance of these materials is given in Table 7.4. The first material for comparison is *i*Bu-BTP impregnated into styrene-divinylbenzene polymer which was in turn embedded into porous silica particles (SiO_2-P-*i*BuBTP, **A**). This material demonstrated an Am K_d of approx. 500 and $SF_{Am/Eu}$ of approx. 100 from 0.1 M nitric acid (Table 7.4).[21,22] When the aqueous solution was 3 M nitric acid, the Am K_d increased nearly 2 orders of magnitude but the $SF_{Am/Eu}$ decreased to approx. 25.[21] Therefore at high acidity sorbent **A** demonstrated very high Am extraction but relatively poor selectivity while at low acidity Am extraction was medium and selectivity was high. The kinetics and stability of sorbent **A** have only been investigated in 0.01 M nitric acid and showed that equilibrium was reached within 30 min and that less than 1.5 % of *i*Bu-BTP leaked from the material with an irradiation dose of 130 kGy.[23] Other BTP ligands with different R groups (such as isohexyl,[24] isoheptyl[25] and n-butyl[21,26]) have also been impregnated into SiO_2-P materials, but showed slower kinetics and/or lower chemical stability than sorbent **A**.

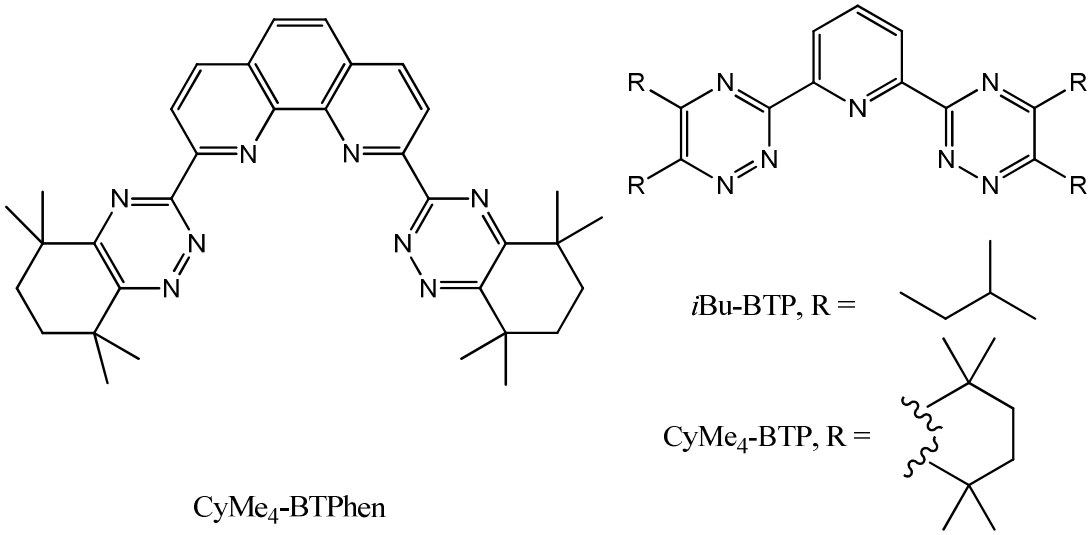

Figure 7.7: Chemical structures of BTP based ligands that have previously been used to functionalise solid phase sorbent materials for MA-Ln separations.

Table 7.4: Partition coefficiencts (K_d) for sorption of Am and Eu by BTP functionalised materials

	Sorbent Material	[HNO_3] (M)	Am (K_d ± SD)	Eu (K_d ± SD)	$SF_{Am/Eu}$
A	SiO_2-P-*i*BuBTP	0.1	~500	~5	~100
A	SiO_2-P-*i*BuBTP	3	~20000	~800	~25
B	Amberchrom-*i*BuBTP	0.1	80	~3	~27
B	Amberchrom-*i*BuBTP	2	3800	20	190
C	XAD-7-$CyMe_4$BTP	0.1	~2500	6	~400
D	SiFeNP-$CyMe_4$BTPhen	0.001	1163 ± 79	701 ± 32	2
D	SiFeNP-$CyMe_4$BTPhen	0.1	1857 ± 154	101 ± 2	18
D	SiFeNP-$CyMe_4$BTPhen	1	623 ± 31	10 ± 1	65
D	SiFeNP-$CyMe_4$BTPhen	4	55 ± 2	1*	55*

*assuming a minimum measurable K_d for Eu of 1

Both *i*Bu-BTP and $CyMe_4$-BTP ligands (Figure 7.7) have been used to functionalise polymeric extraction chromatography resins. For example, *i*Bu-BTP has been used to impregnate acrylic ester polymer Amberchrom CF-71 M to a weight loading of approx. 15 % (Amberchrom-*i*BuBTP, **B**)[27] and the MA-Ln separation results using this resin are reproduced in Table 7.4. Both the Am K_d and $SF_{Am/Eu}$ of sorbent **B** were maximised at 2 M nitric acid but the kinetics and radiation stability of this material were not specifically investigated. Similarly, $CyMe_4$-BTP has been impregnated into the macroporous cross-linked acrylic ester polymer XAD-17 and the resulting material (XAD-7-$CyMe_4$BTP, **C**) used for extraction chromatography.[28] A $CyMe_4$-BTP loading of 1.5 wt% was found to maximise $SF_{Am/Eu}$ and so was utilised for sorption experiments from 0.1 M nitric acid with a contact time of 1 h. The results are reproduced in Table 7.4 and show high Am K_d as well as $SF_{Am/Eu}$ values. However,

the kinetics of extraction were quite slow as 8 h was required to achieve the maximum K_d, approx. 2 % of the $CyMe_4$-BTP leached from the polymer resin after 1 h and the Am could not be eluted from the resin after sorption. Finally, since methacrylate polymers are generally not radiolytically stable,[29] it is also likely that there would be leaching of the BTP ligands from both sorbents **B** and **C** due to radiolysis. In addition, the loaded resin would not be an appropriate wasteform or transmutation matrix.

The last material for comparison is silica coated magnetic nanoparticles functionalised with the $CyMe_4$-BTPhen ligand (SiFeNP-$CyMe_4$BTPhen, **D**).[22] This ligand was designed to improve the extraction kinetics and K_d of MA-Ln separation relative to the similar $CyMe_4$-BTBP ligand, as described in *Chapter 1*. To functionalise the magnetic nanoparticles they were coated in silica then modified with 3-iodopropyl-trimethoxysilane before being linked with the 5-(4-hydroxyphenyl) modified $CyMe_4$-BTPhen ligand. Thus the present Me-BTP-O-undecene functionalised titania beads SB-BTP and LB-BTP are much simpler to synthesise as the functionalization is a simple one step method. It should also be noted that in sorbent **D** the ligand was coordinated to the surface via silane bonds which are not hydrolytically or radiolytically stable.[30,31] This may reduce the practicality of this material as a sorbent for reprocessing of used nuclear fuel. From the data in Table 7.4, the $SF_{Am/Eu}$ for sorbent **D** in 0.01 M nitric acid can be inferred to be between 2 and 18. Therefore, SB-BTP and LB-BTP provided $SF_{Am/Eu}$ values approx. an order of magnitude higher than sorbent **D** in 0.01 M nitric acid. However, the Am K_d was at least an order of magnitude lower for SB-BTP and LB-BTP than for sorbent **D** at this acidity. This was attributed to the fact that SB-BTP and LB-BTP contained a much lower percentage of the extractant ligand (3 % versus 20 %). Overall, sorbent **D** and SB-BTP/LB-BTP were considered to be complementary in their extraction abilities since the best selectivity and extraction performances were achieved at 1-4 M nitric acid for sorbent **D** and at 0.01 M nitric acid for SB-BTP and LB-BTP. As such, sorbent **D** would be suited for direct extraction of Am from highly acidic PUREX raffinate solutions, while SB-BTP and LB-BTP would be preferable for MA-Ln separation of TRUEX or DIAMEX strip solutions.

7.4 Conclusions

Titania nanoparticles and heirarchically porous titania beads were successfully covalently functionalised with the novel BTP derivative **23** and 1-undecene, as indicated by MAS NMR and CHN microanalysis. The resulting materials selectively extracted Am over Eu from 0.01 M nitric acid solutions and varying the ratio of BTP derivative **23** to 1-undecene during functionalization did not affect the sorption performance. The BTP functionalised titania sorbents extracted Am more efficiently from solutions containing 10 % EtOH relative to purely aqueous solutions when the contact time between the sorbent and solution was long (≥ 4 h) but not when it was short. This was hypothesised to be due to hydroxyl radical scavenging by EtOH reducing the rate of radiolysis of the BTP ligand on the titania surface.

However, given that maximum sorption was achieved within 1 h or less for the BTP functionalised titania nanoparticles and beads, addition of EtOH is unlikely to be necessary in an industrial setting.

A greater level of functionalization was achieved for the titania beads (approx. 3%) than for the nanoparticles (1.5%), presumably due to the higher surface area of the porous beads. This higher level of functionalization of the titania beads correlated with a higher Am extraction efficiency. The kinetics of sorption were also faster for the functionalised titania beads than for the nanoparticles. Thus, the more complex porous titania bead framework fulfilled its intended purpose of providing enhanced capacity and mass transport kinetics relative to the titania nanoparticles.

The extraction efficiencies, selectivity factors and kinetics of extraction achieved by SB-BTP and LB-BTP were comparable if not better than those reported for other solvent extraction processes or sorbent materials designed for MA-Ln separation. As solid phase materials, SB-BTP and LB-BTP also have advantages over solvent extraction processes including a lack of organic solvents and use of less complex extractant ligands. The faster kinetics of Am extraction with SB-BTP and LB-BTP relative to solvent extraction with BTP ligands was particularly beneficial because although radiolysis of the BTP ligands still occurred after contact times of ≥ 4 h, this had no detrimental effect on sorption which was complete within 30 min. Considering the superior stability of the present titania based materials in comparison to polymer and/or silica based sorbents, the potential to directly covert a titania based sorbent material into a ceramic wasteform or transmutation matrix, as well as the practical advantages of a bead-like morphology for extraction chromatography purposes, this result represents a substantial breakthrough in the development of solid-phase materials for the important and challenging MA-Ln separation.

7.5 References

(1) Sizgek, G. D.; Griffith, C. S.; Sizgek, E.; Luca, V. *Langmuir* **2009**, *25*, 11874.
(2) Kimling, M. C.; Caruso, R. A. *J Mater Chem* **2012**, *22*, 4073.
(3) Sizgek, G. D.; Sizgek, E.; Griffith, C. S.; Luca, V. *Langmuir* **2008**, *24*, 12323.
(4) Ekberg, C.; Fermvik, A.; Retegan, T.; Skarnemark, G.; Foreman, M. R. S.; Hudson, M. J.; Englund, S.; Nilsson, M. *Radiochim. Acta* **2008**, *96*, 225.
(5) Hudson, M. J.; Harwood, L. M.; Laventine, D. M.; Lewis, F. W. *Inorganic Chemistry* **2013**, *52*, 3414.
(6) Hudson, M. J.; Boucher, C. E.; Braekers, D.; Desreux, J. F.; Drew, M. G. B.; Foreman, M. R. S.; Harwood, L. M.; Hill, C.; Madic, C.; Marken, F.; Youngs, T. G. A. *New Journal of Chemistry* **2006**, *30*, 1171.
(7) Benay, G.; Schurhammer, R.; Wipff, G. *Phys Chem Chem Phys* **2010**, *12*, 11089.
(8) Weigl, M.; Geist, A.; Mullich, U.; Gompper, K. *Solvent Extr. Ion Exch.* **2006**, *24*, 845.

(9) Lewis, F. W.; Harwood, L. M.; Hudson, M. J.; Drew, M. G. B.; Desreux, J. F.; Vidick, G.; Bouslimani, N.; Modolo, G.; Wilden, A.; Sypula, M.; Vu, T. H.; Simonin, J. P. *J. Am. Chem. Soc.* **2011**, *133*, 13093.

(10) Mercier, D.; Leconte, N.; Methivier, C.; Suzenet, F.; Guillaumet, G.; Wuillaume, A.; Pradier, C. M. *Phys Chem Chem Phys* **2010**, *12*, 6099.

(11) Trumm, S.; Wipff, G.; Geist, A.; Panak, P. J.; Fanghanel, T. *Radiochim. Acta* **2011**, *99*, 13.

(12) Benay, G.; Schurhammer, R.; Desaphy, J.; Wipff, G. *New Journal of Chemistry* **2011**, *35*, 184.

(13) Breitmaier, E. V., W. *Carbon-13 NMR Spectroscopy - High Resolution Methods and Applications in Organic Chemistry and Biochemistry*; 3rd ed.; VCH: Weinheim, 1987.

(14) Kopoldova, J. V., V. *Journal of Labelled Compounds and Radiopharmaceuticals* **1984**, *21*, 679.

(15) Ingelman-Sundberg, M. J., I. *The Journal of Biological Chemistry* **1984**, *259*, 6447.

(16) Angelome, P. C.; Soler-Illia, G. J. D. A. A. *Chem Mater* **2005**, *17*, 322.

(17) Ansari, S. A.; Pathak, P.; Mohapatra, P. K.; Manchanda, V. K. *Sep. Purif. Rev.* **2011**, *40*, 43.

(18) Panak, P. J.; Geist, A. *Chemical Reviews* **2013**, *113*, 1199.

(19) Lewis, F. W.; Hudson, M. J.; Harwood, L. M. *Synlett* **2011**, 2609.

(20) Wilden, A.; Schreinemachers, C.; Sypula, M.; Modolo, G. *Solvent Extr. Ion Exch.* **2011**, *29*, 190.

(21) Hoshi, H.; Wei, Y. Z.; Kumagai, M.; Asakura, T.; Morita, Y. *Journal of Alloys and Compounds* **2006**, *408*, 1274.

(22) Afsar, A. H., L.M.; Hudson, M.J.; Distler, P.; John, J. *Chem Commun* **2014**, *50*, 15082.

(23) Xu, Y. L.; Kim, S. Y.; Ito, T.; Hitomi, K.; Kuraoka, E.; Usuda, S.; Ishii, K. *J. Radioanal. Nucl. Chem.* **2014**, *299*, 149.

(24) Liu, R. Q.; Wang, X. P.; Wei, Y. Z.; Shi, W. Q.; Chai, Z. F. *Radiochim. Acta* **2014**, *102*, 93.

(25) Usuda, S.; Wei, Y. Z.; Liu, R. Q.; Li, Z.; Xu, Y. L.; Wu, Y.; Kim, S. *Sci China Chem* **2012**, *55*, 1732.

(26) Wei, Y. Z.; Hoshi, H.; Kumagai, M.; Asakura, T.; Morita, Y. *Journal of Alloys and Compounds* **2004**, *374*, 447.

(27) Klug, C.; Sudowe, R. *Separation Science and Technology* **2013**, *48*, 2567.

(28) Deepika, P. S., K.N.; Srinivasan, T.G.; Vasudeva Rao, P.R. *Separation Science and Technology* **2014**, *48*, 2020.

(29) Dong, L. M.; Hill, D. J. T.; ODonnell, J. H.; Pomery, P. J.; Hatada, K. *J Appl Polym Sci* **1996**, *59*, 589.

(30) Iler, R. K. *The Chemistry of Silica: Solubility, Polymerisation, Colloid and Surface Properties and Biochemistry of Silica*; Wiley-Interscience: New York, 1979.

(31) Etienne, M.; Walcarius, A. *Talanta* **2003**, *59*, 1173.

Chapter 8: Conclusions and Future Work

Novel hybrid inorganic-organic solid phase materials have been developed and studied for their ability to selectively separate targeted elements from solutions of used nuclear fuel with high capacities and fast kinetics. Selective elemental separations are important at the back end of the nuclear fuel cycle to enable recycling of key actinide elements (An) that can be re-used as nuclear fuel.[1] This recycling of An to close the nuclear fuel cycle increases the number of years that nuclear power will be a viable option for power generation. In addition, closing the nuclear fuel cycle decreases the hazardous nature of nuclear waste requiring long-term storage, which in turn decreases risk to the environment and human health, decreases cost of waste storage, and improves the public perception of nuclear technology. Commercial reprocessing of used nuclear fuel and the majority of research into separations at the back end of the nuclear fuel cycle use solvent extraction technology.[2] However, the research in this thesis has instead focussed on developing solid phase materials to perform radiochemical separations at the back end of the nuclear fuel cycle. Solid phase materials provide several advantages over solvent extraction. For example, they do not require use of organic solvents or phase transfer agents, they can provide faster extraction kinetics and they do not suffer from third phase formation.

This thesis described the preparation of porous metal oxide framework materials as well as functionalization of those framework materials with organic ligands. The relationship between the porous structure of the framework materials and their sorption capacity and kinetics was investigated. Two different strategies were used to introduce organic ligands into the framework materials; co-condensation of the inorganic framework with the organic ligands (*Chapter 3*) and covalent grafting of the organic ligands onto the surface of framework materials post synthesis (*Chapters 4, 5 and 7*). Organic ligand functionalization using both methodologies successfully imparted selectivity for the targeted An or lanthanide (Ln). Thus, this work provides the first example of a covalently functionalised metal oxide material, specifically titania, being used for radiochemical separations. Previously, materials used for separations relevant to the back end of the nuclear fuel cycle have been predominantly based on silica or polymer resins.[3-5]

Porous titania and zirconia framework materials were synthesised and characterised. The synthesis methods used to make the titania and zirconia framework materials were different; titania based materials were synthesised via evaporation induced self-assembly (EISA) with block copolymer and/or polyacrylonitrile templates (*Chapter 6*) while zirconia based materials were synthesised via hydrothermal methods without the use of templating agents (*Chapter 3*). Thus, it has been demonstrated that porous materials can be generated with or without the use of templates. However, the use of polymer templates in the synthesis of ordered mesoporous titania provided increased control over and flexibility in the porosity generated. For example, the choice of block copolymer template controlled pore size. It was hypothesised that the size of the more hydrophobic propylene oxide (PO) block in the block copolymer templates controlled the size of the pores generated. To

prove this hypothesis, further work on synthesis of mesoporous oxides using block copolymer templates with systematically varying block sizes would be required.

For both the titania and zirconia systems, a thorough investigation of the effects of the synthesis parameters on the structure and composition of the final material was performed. Synthesis parameters that were investigated included the chemistry of the precursors used, ratios of chemical precursors, pH, temperature and time. All of these parameters affected the structure and sorption properties of the resulting materials. In terms of the chemical nature of precursors used, the zirconium organophosphonate (ZrP) materials produced using the zirconium propoxide precursor had lower surface area, smaller pores and could not incorporate as high a percentage of phosphorus as ZrP materials synthesised using the zirconium chloride precursor. As a result, the ZrP materials synthesised using the chloride precursor had higher sorption capacities. With respect to the ratio of chemical precursors used during synthesis, this affected the degree of order in mesoporous titania powder samples and increasing the amount of phosphonate added during synthesis of ZrP materials increased their sorption capacity. Increasing the pH of synthesis also increased the sorption capacity of ZrP materials. Finally, the temperature and time of evaporation during EISA to produce ordered mesoporous titania affected both the degree of order and the thermal stability of the materials produced. The optimal temperature was different depending on the template used but increasing evaporation time increased thermal stability under all the conditions tested, presumably due to increased cross-linking of the titania. Understanding how the conditions of synthesis affected the structure and properties of the materials produced allowed informed choice of the synthesis conditions such that the desired characteristics were obtained. As a result, ordered mesoporous titania powder templated with block copolymer F127 was synthesised without the use of any stabilising additives and with a clean final product for the first time (*Chapter 6*) and ZrP materials with high selectivity and capacity as well as fast kinetics of sorption were developed (*Chapter 3*).

Another synthesis parameter that was investigated for the production of ordered mesoporous titania was precursor solution ageing prior to evaporation (*Chapter 6*). This parameter has never been investigated previously, despite the extensive literature available on production of ordered mesoporous titania.[6-8] Titanium oxo oligomers were shown to grow in precursor solutions containing the block copolymer template Brij 58 over time, with sizes dependent on the Brij 58 concentration (Figure 8.1). However, the Ti structures observed in precursor solutions containing another block copolymer template F127 did not change over time. Thus, the Ti structures formed were dependent on the type and concentration of block copolymer template present. This proved that the Ti precursors interacted with the block copolymer templates in the sealed precursor solution vessels even before evaporation began. It was hypothesised that the interaction between the Ti and block copolymer templates was dependent on the size of the ethylene oxide (EO) blocks in the templates, but again further work would be required to confirm this. For the Brij 58 system in which the Ti structures in the precursor solution grew over time, the age of the precursor solution also affected the degree of order in the mesoporous titania powders produced via EISA of those solutions. The optimal age for the 1.5 % Brij 58 precursor solution was 6 days, which corresponded to structures with a radius of gyration of approx. 12 Å (Figure 8.1).

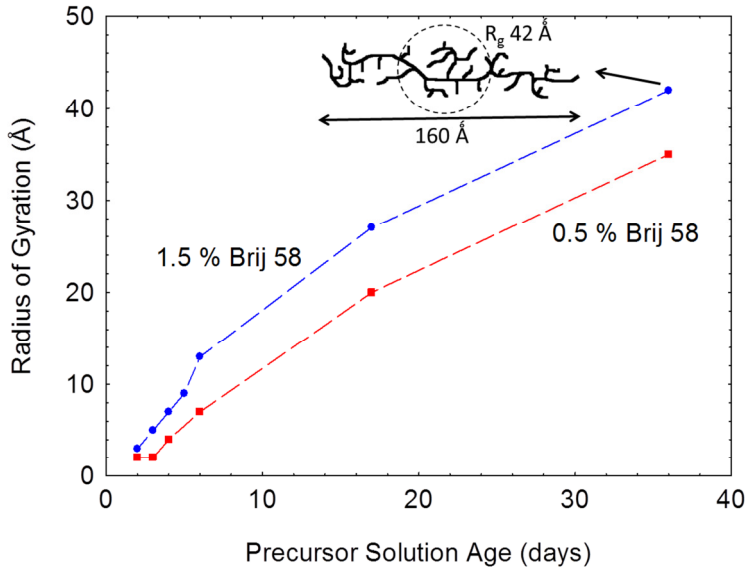

Figure 8.1: Growth of Ti/Brij 58 structures in precursor solutions for synthesis of ordered mesoporous titania powders.

Another important result from the synthesis and characterisation of the metal oxide framework materials was that the ZrP materials with the highest surface areas, as measured by nitrogen porosimetry, did not provide the highest sorption capacities (*Chapter 3*). This contradicts conventional wisdom which suggests that materials with higher surface areas have more surface active sites at which sorption, catalysis or some other reaction can occur.[9] Small angle x-ray scattering (SAXS) provided an explanation for this phenomenon as it indicated that the structure of the ZrP materials with low BET surface areas and high sorption capacities changed when they were wet. When these ZrP materials were present as a slurry with nitric acid, the SAXS patterns indicated wormhole mesoporosity. This result shows that low nitrogen porosimetry surface area measurements should not be used to discount the utility of a material as a sorbent. Rather than surface area, the relative ratio of phosphonate groups in the ZrP materials had the greatest effect on their sorption capacities. This suggests that sorption occurred via the phosphonate groups, which was supported by the FTIR and NMR data.

Functionalisation of the metal oxide materials was performed via co-condensation with an organophosphonate in the case of zirconia (*Chapter 3*) or via post-synthetic organic grafting in the case of titania (*Chapters 4, 5 and 7*). The functionalization via co-condensation was performed simultaneously with synthesis of the zirconia framework and has already been described above. In terms of post-synthetic grafting, several different organic ligands were used to functionalise either titania nanoparticles or hierarchically porous titania beads. All of these ligands consisted of a functional group with a known affinity for the metal ion targeted for separation, modified with an alkyl chain to induce self-assembly on the titania surface and an alkene for covalent attachment to the surface. Although covalent functionalization of titania via an alkene has been demonstrated previously,[10] in this work it was shown that it is possible to achieve this covalent functionalization

simply using heat rather than uv irradiation. It should be noted that although covalent functionalization was assumed due to the hydrolytic stability of the functionalised materials, explicit characterisation of Ti-O-C bonds at the titania surface could not be achieved. To obtain direct evidence of covalent functionalization via FTIR or NMR, materials with a higher level of functionalization than the 1-3 % achieved in this work must be obtained.

Functionalisation of titania via post-synthetic grafting successfully imparted selectivity for targeted An and Ln elements. For example, titania nanoparticles functionalised with a simple amine functional group were able to selectively separate uranium (U) from a multi-element solution at pH 2.5 (*Chapter 4*). This was the first example of organically functionalised titania being used as a sorbent for selective An separation. Also, titania nanoparticles and hierarchically porous titania beads functionalised with an alkyl modified bistriaziylpyridine (BTP) ligand (Figure 8.2) were able to achieve the challenging but important minor actinide (MA)-Ln separation (*Chapter 7*). The BTP functionalised titania beads showed higher extraction efficiency and selectivity for MA over Ln as well as faster sorption kinetics than similarly functionalised titania nanoparticles. The improved capacity of the titania beads was attributed to their higher surface area and their improved kinetics was attributed to the macropores and ordered mesopores in the titania beads, while the titania nanoparticles had only disordered mesopores. Synthesis of BTP functionalised titania beads with macroporosity but disordered mesopores in future would allow determination of whether the macropores or ordered mesopores were responsible for the improved kinetics of the titania beads relative to the nanoparticles.

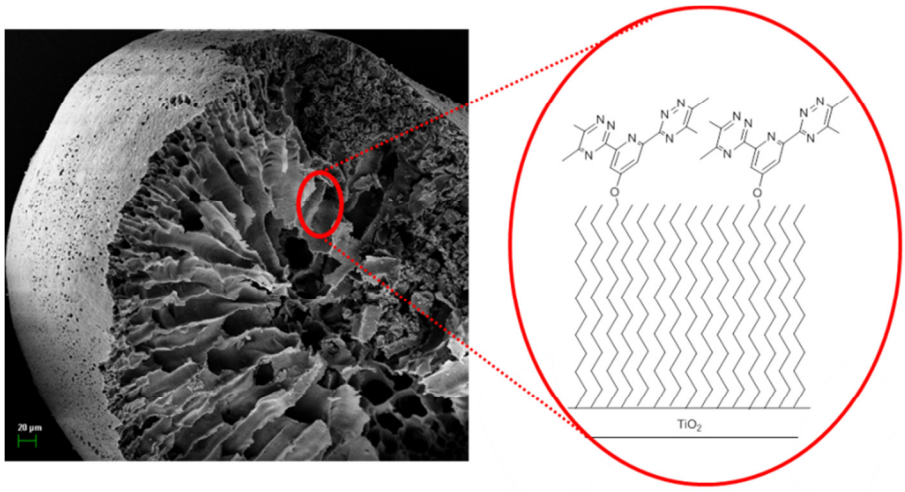

Figure 8.2: Hierarchically porous titania bead functionalised with alkyl modified BTP.

In some cases, the titania materials were functionalised with ligands based on organic extractants from solvent extraction processes and performed better than those solvent extraction processes. For example, picolinamide functionalised titania nanoparticles demonstrated higher extraction efficiejncies (K_d) and MA-Ln separation factors (SF) than calixarene based picolinamide extractants in solvent extraction (*Chapter 4*). Also, BTP functionalised titania beads demonstrated similar K_d and SF values but faster kinetics than a solvent extraction process using a similar BTP

ligand (*Chapter 7*). These solid phase sorbents also have the advantage of not requiring organic solvents or any other additives to achieve separations. In other cases, organic ligands performed better in solvent extraction than on titania sorbents. For example, alkyl phosphate functionalised titania nanoparticles did not sorb U from strongly acidic solutions although tributyl phosphate can achieve this separation via solvent extraction (*Chapter 4*). This was hypothesised to be due to a loss of conformational freedom in the ligands upon surface attachment. In an attempt to increase conformational freedom and ensure complete surface coverage, 1-undecene was used as a 'spacer' between the functional groups on the titania surface, as shown in Figure 8.2, with limited success. The optimal ratio of functional ligand to 1-undecene on the titania surface was not determined because it could not be explicitly measured with the characterisation methods used and the low level of functionalization present. In future, materials with a higher level of functionalization may allow optimisation of this ratio.

As well as functionalization of titania with ligands based on extractants from solvent extraction, peptide based ligands were developed (*Chapter 5*). Peptides are known to form strong complexes with Ln, as these complexes are commonly used as bioprobes.[11] Thus, peptides were considered to have potential as ligands to separate Ln fission products from solutions of used nuclear fuel. Systematic structure variation of peptides based on glutamic acid showed that longer peptides with alternating L- and D- residues had the strongest affinity for Ln in solution studies. However, the effects of the peptide stereochemistry, which have not previously been investigated, were complex and dependent on peptide length. The mode of binding between the peptides and Ln was also complex and binding at multiple carboxylic acid sites on the peptides was evident. Titania nanoparticles were then functionalised with an alkyl modified version of the peptide with the strongest Ln affinity and the resulting material also demonstrated selectivity for Ln.

Functionalization via co-condensation versus post-synthetic grafting had different advantages and disadvantages. Functionalisation via post-synthetic grafting allowed more flexibility and control in the choice of functional group, while co-condensation allowed a higher level of functionalization and hence led to materials with higher sorption capacities. Both the titania nanoparticles and beads showed a similar level of functionalization, independent of the organic ligand used, of approx. 1 molecule/nm^2. On the other hand, the ZrP material with the highest capacity and kinetics contained approx. 40 organophosphonate molecules/nm^2. The level of functionalization achieved via post-synthetic grafting in this work was also lower than the 2-3 molecules/nm^2 that has been observed previously upon functionalization of titania with an alkylphosphonate or via an alkene with uv activation.[10,12] This suggests that monolayer coverage was not achieved with post-synthetic grafting in this work. Further work to optimise the conditions of functionalization and improve surface coverage, for example via reflectometry experiments on a model titania thin film system, should be performed in future.

Although sorbent materials were developed based on group IV metal oxides titania and zirconia because of their chemical stability and ability to be converted to a wasteform or transmutation matrix, these attributes were not extensively tested in this work. Although limited hydrolytic stability testing was performed (*Chapter 4*), experiments to test the stability of the functionalised porous metal oxide

materials under more acidic conditions and in the presence of radiation fields are still needed. Understanding the effect of temperature on the stability and performance of these materials would also be of interest. Some work has also begun into converting the ZrP materials described in this work into a ceramic wasteform (*Chapter 3*). However, further research should investigate conversion of the functionalised titania sorbent materials to ceramic wasteforms or transmutation matrices. Production of viable wasteforms would require further development of the functionalised titania materials to increase their sorption capacities. This could be achieved by increasing the surface area of the framework materials to be functionalised and/or improving surface coverage as described above.

All of the sorption experiments in this thesis were performed via a batch method. However, to determine the practicality of the sorbents for use on a commercial scale, flow through experiments in chromatographic columns are required.[13] In particular, flow through column sorption experiments should be performed in future with the BTP functionalised titania beads, as the bead morphology was chosen specifically to optimise packing in chromatographic columns. In terms of the MA-Ln separation targeted by the BTP functionalised titania beads, competitive sorption experiments from solutions containing an excess of Ln should also be performed in future to more closely mimic realistic processing conditions.[14]

Whether Australia invests in nuclear power in the future or not, Australia already has radioactive waste from medical isotope production and mining activities in Australia that require treatment and safe storage. In addition, research into materials for selective elemental separations at the back end of the nuclear fuel cycle allows Australia to contribute to advanced nuclear fuel cycles internationally. This research has shown that by combining porous inorganic framework materials with organic functionalization it is possible to create hybrid sorbent materials with high capacity, fast kinetics and selectivity for elements relevant to the back end of the nuclear fuel cycle (An and Ln). In addition, these materials have the potential to be converted into wasteforms or used as transmutation matrices. Thus these materials could be used to enable actinide recycling or safe storage of nuclear waste. The materials described in this thesis represent a new and exciting approach for separations at the back end of the nuclear fuel cycle, relative to the traditionally used solvent extraction processes and polymer/silica materials.

8.1 References

(1) Feiveson, H. M., Z.; Ramana, M.V.; von Hippel, F. *Managing Spent Fuel from Nuclear Power Reactors: Experience and Lessons from Around the World*, The International Panel on Fissile Materials (IPFM), 2011.

(2) *Advanced Separation Techniques for Nuclear Fuel Reprocessing and Radioactive Waste Management*; Nash, K. L. L., G.J., Ed.; Woodhead Publishing Limited: Cambridge, 2011.

(3) Fryxell, G. E.; Mattigod, S. V.; Lin, Y. H.; Wu, H.; Fiskum, S.; Parker, K.; Zheng, F.; Yantasee, W.; Zemanian, T. S.; Addleman, R. S.; Liu, J.; Kemner, K.; Kelly, S.; Feng, X. D. *J Mater Chem* **2007**, *17*, 2863.

(4) Shi, W. Q.; Yuan, L. Y.; Li, Z. J.; Lan, J. H.; Zhao, Y. L.; Chai, Z. F. *Radiochim. Acta* **2012**, *100*, 727.

(5) Mokhodoeva, O. B. M., G.V.; Zakharchenko, E.A. *Radiochemistry* **2011**, *53*, 35.

(6) Gu, D.; Schuth, F. *Chemical Society Reviews* **2014**, *43*, 313.

(7) Li, W.; Wu, Z. X.; Wang, J. X.; Elzatahry, A. A.; Zhao, D. Y. *Chem Mater* **2014**, *26*, 287.

(8) Orilall, M. C.; Wiesner, U. *Chemical Society Reviews* **2011**, *40*, 520.

(9) Lehman, S. E.; Larsen, S. C. *Environ-Sci Nano* **2014**, *1*, 200.

(10) Li, B.; Franking, R.; Landis, E. C.; Kim, H.; Hamers, R. J. *Acs Appl Mater Inter* **2009**, *1*, 1013.

(11) Ancel, L.; Niedzwiecka, A.; Lebrun, C.; Gateau, C.; Delangle, P. *Cr Chim* **2013**, *16*, 515.

(12) Gao, W.; Dickinson, L.; Grozinger, C.; Morin, F. G.; Reven, L. *Langmuir* **1996**, *12*, 6429.

(13) Raju, C. S. K.; Subramanian, M. S. *J Hazard Mater* **2007**, *145*, 315.

(14) Hudson, M. J.; Harwood, L. M.; Laventine, D. M.; Lewis, F. W. *Inorganic Chemistry* **2013**, *52*, 3414.

Appendix A: Supplementary Data on Zirconium Organophosphonate Materials

A1 Nitrogen porosimetry

All the zirconium organophosphonate materials synthesised, as described in *Chapter 3*, are listed again in Table A1. Nitrogen porosimetry data for series #1 (ZrPA), #5 (ZrPB) and #8 (ZrPC) are given in *Chapter 3*. For the remaining series (#2, #3, #4, #6 and #7), the calculated BET surface area, pore volume and pore diameters from nitrogen porosimetry are given in Table A2. It should be noted that for series #4, the samples prepared with molar P/Zr ratios of 1:4 and 1:8 did not form precipitates upon hydrothermal treatment and hence their properties could not be determined.

Table A1. Synthesis conditions for ZrP materials.

series #	sample name	Zr precursor	Temp (°C)	pH adjust*	Zr:P stoichiometries
1	ZrPA	chloride	120	N (~1)	1:1, 3:4, 1:2, 1:3, 1:4
2		chloride	120	Y (4-5)	1:1, 3:4, 1:2, 1:4
3		chloride	160	Y (4-5)	1:1, 3:4, 1:2, 1:4
4		chloride	160	Y (6-7)	1:1, 1:2, 1:4, 1:8
5	ZrPB	propoxide	120	N (1-2)	1:1, 3:4, 1:2, 1:3, 1:4
6		propoxide	120	Y (<1)	1:1, 3:4, 1:2, 1:4
7		propoxide	160	N (1-2)	1:2, 1:4, 1:8, 1:10
8	ZrPC	propoxide	160	Y (4-5)	1:1, 3:4, 1:2, 1:3, 1:4, 1:8

*N = No, Y = Yes

Table A2: Physicochemical properties of zirconium organophosphonate samples

Sample (#series, Zr:P)	*BET Surface Area (m^2/g)*	*Pore Volume (mL/g)*	*Pore Diameter (nm)*
#2, 1:1	241	0.43	~20
#2, 3:4	296	0.70	~30
#2, 1:2	266	0.76	~50
#2, 1:4	114	0.41	~40
#3, 1:1	323	0.70	~25
#3, 3:4	316	0.73	~30
#3, 1:2	279	0.60	~50
#3, 1:4	193	0.38	~40
#4, 1:1	72	0.19	~20
#4, 1:2	47	0.04	-
#6, 1:1	270	0.73	~25
#6, 3:4	333	0.95	~30
#6, 1:2	375	1.40	~45
#6, 1:4	111	0.89	~60
#7, 1:2	97	0.30	~60
#7, 1:4	29	0.16	~60
#7, 1:8	128	0.52	<3
#7, 1:10	110	0.41	<3

A2 Preliminary sorption experiments

Preliminary sorption experiments using La, Nd and Gd at a concentration of 0.1 mM each in 0.1 M nitric acid were performed on all the zirconium organophosphonate materials synthesised (Table A1). Single batch competitive sorption experiments were performed using a constant volume-to-mass ratio of 100. Initial and final concentrations were analysed by x-ray fluorescence. The results are given in Table A3.

Table A3: Lanthanide sorption properties of zirconium organophosphonate samples

Sample (#series, Zr:P)	*La K_d*	*Nd K_d*	*Gd K_d*
#1, 1:1	15 ± 21	13 ± 9	6 ± 8
#1, 3:4	2 ± 20	7 ± 9	1 ± 8
#1, 1:2	-13 ± 18	-7 ± 7	-3 ± 8
#1, 1:4	1240 ± 460	>1914	1430 ± 741
#2, 1:1	72 ± 28	117 ± 19	164 ± 25
#2, 3:4	483 ± 103	781 ± 92	993 ± 232
#2, 1:2	>1575	>1914	>1600
#2, 1:4	>1814	>2250	>1600
#3, 1:1	25 ± 22	22 ± 8	19 ± 9
#3, 3:4	120 ± 33	135 ± 21	200 ± 31
#3, 1:2	>570	>1663	>1291
#3, 1:4	>1240	>1914	>1600
#4, 1:1	>1118	>1182	>1175
#4, 1:2	191 ± 52	253 ± 32	303 ± 39
#5, 1:1	-1 ± 20	2 ± 8	7 ± 9
#5, 3:4	3 ± 16	22 ± 9	31 ± 10
#5, 1:2	103 ± 50	213 ± 43	292 ± 49
#5, 1:4	81 ± 31	161 ± 25	226 ± 36
#6, 1:1	-4 ± 19	1 ± 8	4 ± 8
#6, 3:4	-9 ± 18	-5 ± 7	-8 ± 7
#6, 1:2	-8 ± 15	4 ± 9	-3 ± 8
#6, 1:4	>1814	2250 ± 1300	>1813
#7, 1:2	25 ± 13	62 ± 12	101 ± 16
#7, 1:4	29 ± 12	68 ± 12	104 ± 17
#7, 1:8	1118 ± 382	1914 ± 906	>1600
#7, 1:10	>1575	>2250	>1600
#8, 1:1	235 ± 76	327 ± 44	467 ± 69
#8, 1:2	>1575	>1914	>1430
#8, 1:4	>1389	1467 ± 867	>1600
#8, 1:8	>1575	1663 ± 671	1430 ± 741

A3 EXAFS

The EXAFS spectrum of ZrPA-3 (shape 'B') was background subtracted with a R_{bkg} value of 0.79 using the data processing program Athena. A Fourier transform was then applied to the aligned and background subtracted data in the k-range 2.0 to 7.3 using a Hanning window with a window sill width (dk) of 1.2, to give χ(R). Finally, the R-range 0.8 to 3.3 Å was fit to the theoretical model using Artemis software. The number of independent points in the fit was 8 and the number of variables in the fit was 6. The best calculated fit (R-factor 0.005, χ_v^2 5239) is shown in Figure A1 and the fit parameters are given in Table A4.

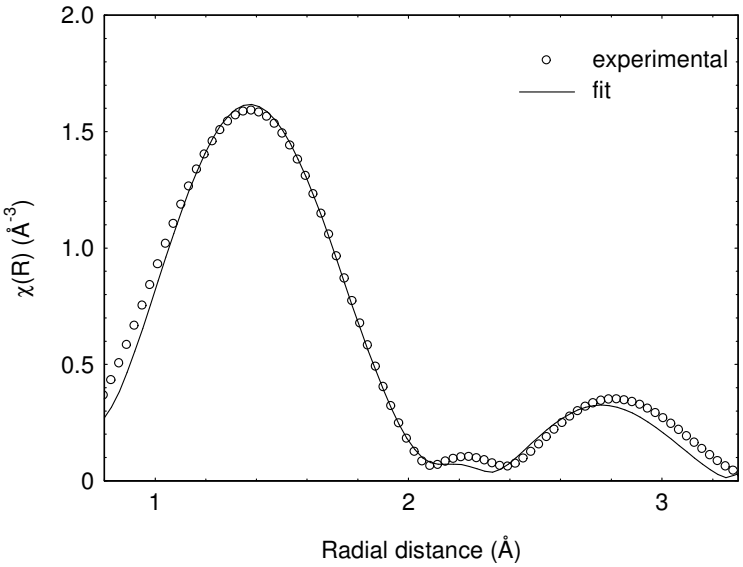

Figure A1: Experimental and calculated Fourier transforms of ZrPA-3 EXAFS from FEFF code for $Zr(HPO_4)_2(H_2O)$ with single scattering from inner-shell O and P.

Table A4: Fitting parameters of Zr EXAFS for ZrP materials

Sample	Path	S_0^2	E_0	N	R (Å)	σ^2 (Å^2)
ZrPA-3	Zr-O	1.1 ± 0.2	-4.8 ± 1.5	6	2.04 ± 0.01	0.005 ± 0.002
	Zr-P			6	3.62 ± 0.04	0.017 ± 0.006
ZrPB-1	Zr-O	1.7 ± 0.4	-9.8 ± 2.5	4	2.10 ± 0.02	0.006 ± 0.003
	Zr-P			2	3.06 ± 0.19	0.040 ± 0.039
ZrPB-4	Zr-O	1.2 ± 0.3	-9.6 ± 2.6	4	2.05 ± 0.02	0.003 ± 0.004
	Zr-P			2	3.08 ± 0.09	0.020 ± 0.017
ZrPC-1	Zr-O	1.2 ± 0.3	-9.0 ± 2.1	4	2.09 ± 0.02	0.002 ± 0.003
	Zr-P			2	3.15 ± 0.14	0.030 ± 0.029
ZrPC-2	Zr-O	0.9 ± 0.3	-4.3 ± 2.5	4	2.11 ± 0.02	0.000 ± 0.005
ZrPC-3	Zr-O	0.9 ± 0.2	-9.0 ± 2.2	4	2.06 ± 0.02	0.002 ± 0.004
ZrPC-5	Zr-O	0.8 ± 0.2	-4.2 ± 1.9	6	2.03 ± 0.02	0.001 ± 0.003
	Zr-P			6	3.58 ± 0.05	0.016 ± 0.009

The EXAFS spectrum of ZrPB-1 (shape 'A') was background subtracted with a R_{bkg} value of 0.82 using the data processing program Athena. A Fourier transform was then applied to the aligned and background subtracted data in the k-range 1.8 to 8.4 using a Hanning window with a window sill width (dk) of 1.5, to give χ(R). Finally, the R-range 0.8 to 3.5 Å was fit to the theoretical model using Artemis software. The number of independent points in the fit was 11 and the number of variables in the fit was 6. The best calculated fit (R-factor 0.035, χ_v^2 16736) is shown in Figure A2 and the fit parameters are given in Table A4.

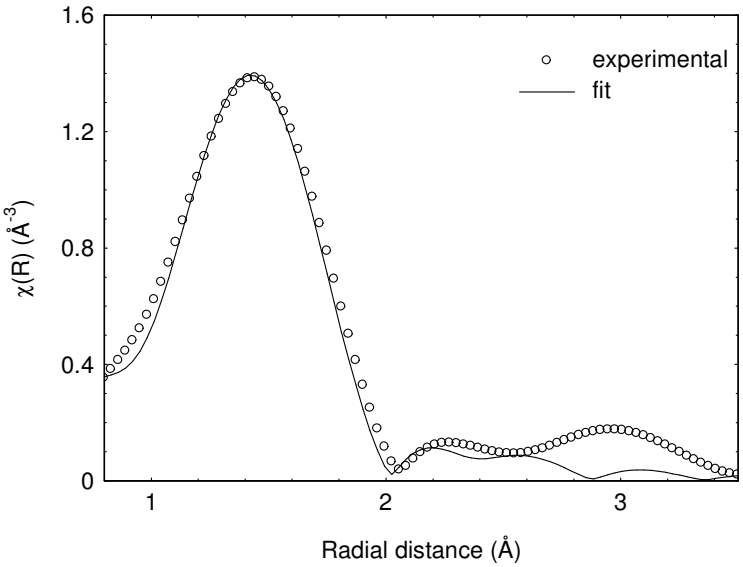

Figure A2: Experimental and calculated Fourier transforms of ZrPB-1 EXAFS from FEFF code for $Zr(HPO_4)_2(H_2O)$ with single scattering from inner-shell O and P.

The EXAFS spectrum of ZrPB-4 (shape 'A') was background subtracted with a R_{bkg} value of 0.80 using the data processing program Athena. A Fourier transform was then applied to the aligned and background subtracted data in the k-range 1.8 to 7.5 using a Hanning window with a window sill width (dk) of 1.3, to give χ(R). Finally, the R-range 0.8 to 3.2 Å was fit to the theoretical model using Artemis software. The number of independent points in the fit was 8 and the number of variables in the fit was 6. The best calculated fit (R-factor 0.017, χ_v^2 5667) is shown in Figure A3 and the fit parameters are given in Table A4.

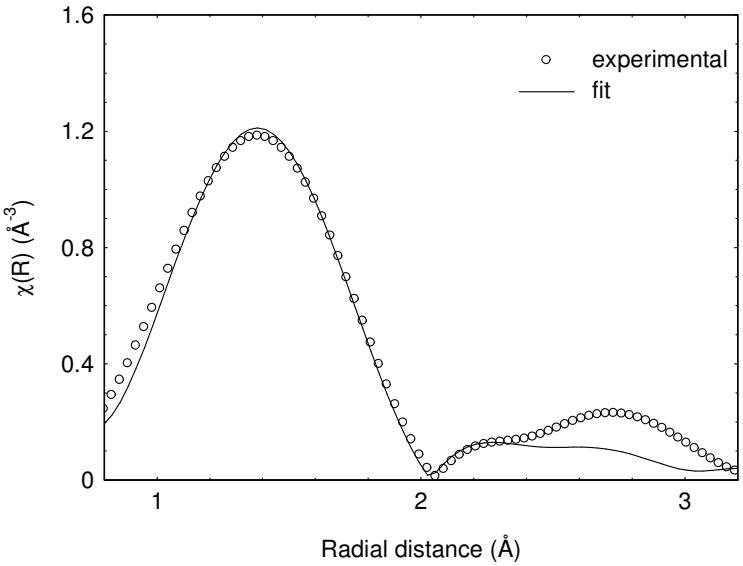

Figure A3: Experimental and calculated Fourier transforms of ZrPB-4 EXAFS from FEFF code for $Zr(HPO_4)_2(H_2O)$ with single scattering from inner-shell O and P.

The EXAFS spectrum of ZrPC-1 (shape 'A') was background subtracted with a R_{bkg} value of 0.80 using the data processing program Athena. A Fourier transform was then applied to the aligned and background subtracted data in the k-range 1.7 to 7.4 using a Hanning window with a window sill width (dk) of 1.3, to give χ(R). Finally, the R-range 0.8 to 3.5 Å was fit to the theoretical model using Artemis software. The number of independent points in the fit was 10 and the number of variables in the fit was 6. The best calculated fit (R-factor 0.021, χ_v^2 5210) is shown in Figure A4 and the fit parameters are given in Table A4.

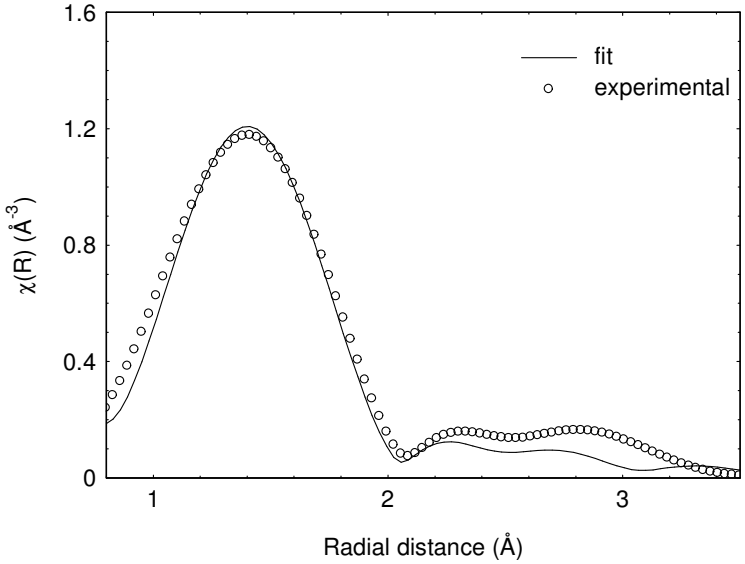

Figure A4: Experimental and calculated Fourier transforms of ZrPC-1 EXAFS from FEFF code for $Zr(HPO_4)_2(H_2O)$ with single scattering from inner-shell O and P.

The EXAFS spectrum of ZrPC-2 (shape 'A') was background subtracted with a R_{bkg} value of 0.90 using the data processing program Athena. A Fourier transform was then applied to the aligned and background subtracted data in the k-range 2.0 to 6.4 using a Hanning window with a window sill width (dk) of 1.4, to give χ(R). Finally, the R-range 0.9 to 3.0 Å was fit to the theoretical model using Artemis software. The number of independent points in the fit was 6 and the number of variables in the fit was 4. The best calculated fit (R-factor 0.010, χ_v^2 6666) is shown in Figure A5 and the fit parameters are given in Table A4. An acceptable fit could not be achieved if the Zr-P path was included, possibly because the k range only extended to 6.4.

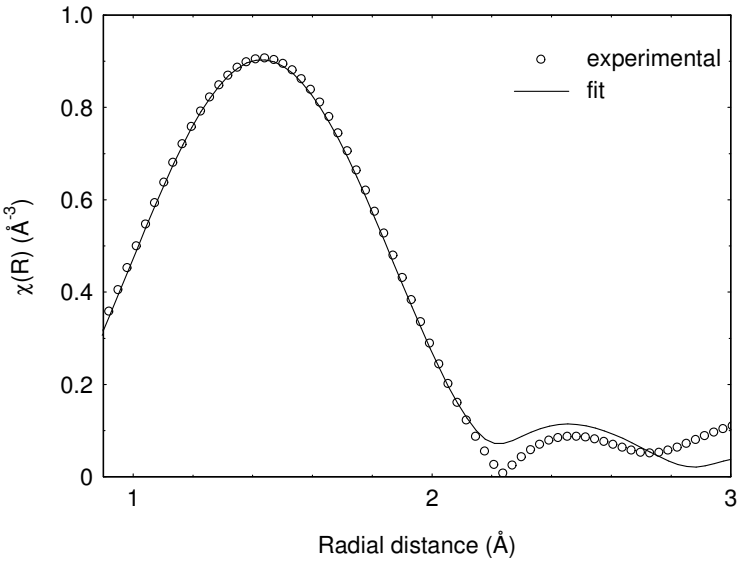

Figure A5: Experimental and calculated Fourier transforms of ZrPC-2 EXAFS from FEFF code for $Zr(HPO_4)_2(H_2O)$ with single scattering from inner-shell O and P.

The EXAFS spectrum of ZrPC-3 (shape 'A') was background subtracted with a R_{bkg} value of 0.80 using the data processing program Athena. A Fourier transform was then applied to the aligned and background subtracted data in the k-range 2.0 to 6.4 using a Hanning window with a window sill width (dk) of 1.8, to give χ(R). Finally, the R-range 0.8 to 3.7 Å was fit to the theoretical model using Artemis software. The number of independent points in the fit was 8 and the number of variables in the fit was 4. The best calculated fit (R-factor 0.015, χ_v^2 662) is shown in Figure A6 and the fit parameters are given in Table A4. An acceptable fit could not be achieved if the Zr-P path was included, possibly because the k range only extended to 6.4.

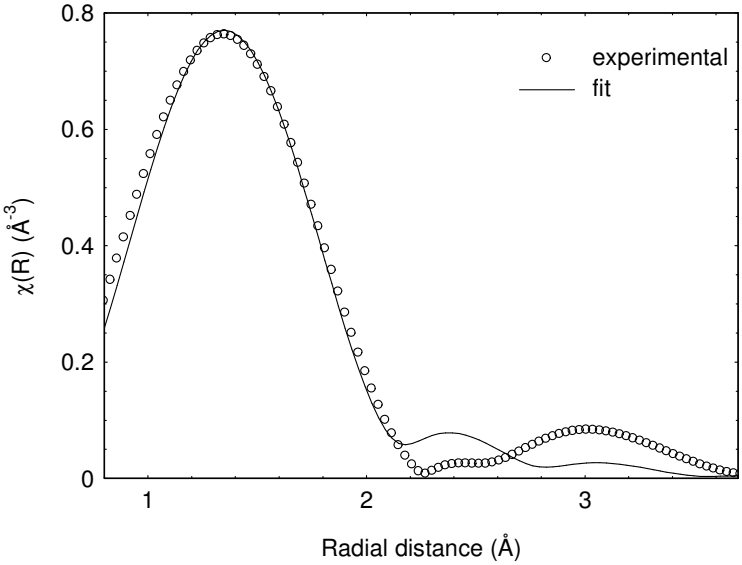

Figure A6: Experimental and calculated Fourier transforms of ZrPC-3 EXAFS from FEFF code for $Zr(HPO_4)_2(H_2O)$ with single scattering from inner-shell O and P.

The EXAFS spectrum of ZrPC-5 (shape 'B') was background subtracted with a R_{bkg} value of 0.80 using the data processing program Athena. A Fourier transform was then applied to the aligned and background subtracted data in the k-range 2.2 to 6.8 using a Hanning window with a window sill width (dk) of 1.5, to give χ(R). Finally, the R-range 0.8 to 3.6 Å was fit to the theoretical model using Artemis software. The number of independent points in the fit was 8 and the number of variables in the fit was 6. The best calculated fit (R-factor 0.006, χ_v^2 2080) is shown in Figure A7 and the fit parameters are given in Table A4.

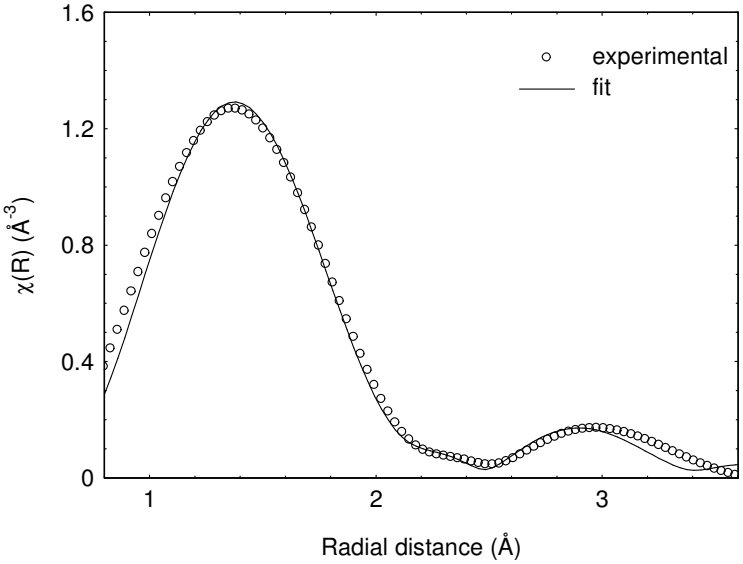

Figure A7: Experimental and calculated Fourier transforms of ZrPC-5 EXAFS from FEFF code for $Zr(HPO_4)_2(H_2O)$ with single scattering from inner-shell O and P.